Fakultät für Physik
Institut für Theorie der Kondensierten Materie

Mesoscopic effects and magnetoresistance in graphene devices

Zur Erlangung des akademischen Grades eines
DOKTORS DER NATURWISSENSCHAFTEN (Dr. rer. nat.)

von der KIT-Fakultät für Physik
des Karlsruher Instituts für Technologie (KIT)
genehmigte

Dissertation

von
M. Sc. Vanessa Gall
aus Calw

Tag der mündlichen Prüfung: 15.07.2022
Referent: PD Dr. Igor V. Gornyi
Korreferent: Prof. Dr. Alexander D. Mirlin

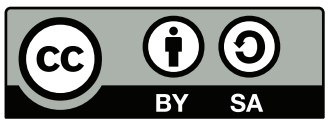

Ich erkläre hiermit, dass ich die vorliegende Arbeit selbständig verfasst, keine anderen als die angegebenen Quellen und Hilfsmittel verwendet habe und alles kenntlich gemacht wurde, das aus Arbeiten anderer unverändert oder mit Abänderungen entnommen ist.

Karlsruhe, den 29. September 2022

Vanessa Gall

Chapter 4 of this thesis is based on the following already published article:

- **V. Gall, R. Kraft, I. V. Gornyi, and R. Danneau** (2022). Spin and valley degrees of freedom in a bilayer graphene quantum point contact: Zeeman splitting and interaction effects. *Phys. Rev. Research*, **4**, 023142.

Chapter 5 of this thesis is based on the following already published article:

- **M. Kamada, V. Gall, J. Sarkar, M. Kumar, A. Laitinen, I. Gornyi, and P. Hakonen** (2021). Strong magnetoresistance in a graphene Corbino disk at low magnetic fields. *Phys. Rev. B*, **104**, 115432.

Chapter 6 of this thesis is based on the following preprint:

- **V. Gall, B. N. Narozhny, I. V. Gornyi** (2022). Electronic viscosity and energy relaxation in neutral graphene. *Preprint*, **arxiv:2206.07414**

Introduction

While pencils with graphite core have existed since the 16th century [1], it was long believed that this core actually consisted of lead, terming their German name "Bleistift". Only much later it was realized that graphite, just like diamond, is a naturally occurring modification of polymorph carbon atoms [2]. Unlike in diamond, carbon atoms in graphite are organized in two-dimensional layers, which are stacked on top of each other in different variations [3]. In each of these layers, they are arranged on a honeycomb lattice, forming a trigonal Bravais lattice with a two atomic basis. Based on this special spatial arrangement and the fact that graphite is indeed porous enough to serve as a writing instrument, people soon started to wonder whether it was possible to fabricate a single of these graphite layers: graphene. The expected behavior of electrons in such a material had already been proposed in 1947 in Ref. [2], but the existence of a true purely two-dimensional material seemed to be at odds with the Mermin-Wagner theorem, stating that long range order in two dimensions should be impossible due to the present thermal fluctuations. This did however not stop Andre Geim and Konstantin Novoselov from pulling away few-layer, including monolayer graphene, from a high quality graphite sample in 2004 by mechanical exfoliation, fittingly dubbed the scotch-tape technique [4].

As already proposed in the theoretical prediction Ref. [2], monolayer graphene possesses a linear, Dirac like spectrum without a band gap. In reciprocal space, these linear-band touching points occur exactly at the corners of the honeycomb Brillouin zone. Neighboring corners correspond to a different sublattice, meaning that at low energies electrons close to one of these don't talk to each other, thus forming two non-equivalent valleys, which introduces an additional quantum degree of freedom, on top of spin [5].

Graphene can be fabricated very cleanly and external gates can be used to tune the electronic density. Due to its special spectrum, electron-electron interaction effects in graphene show a very special behavior as well [6]. In a Galilean invariant system, where energy bands are parabolic in momentum, the ratio between kinetic energy and Coulomb energy per electron scales with the density and thus screening is very effective and Fermi-liquid behavior a fitting description above a certain minimum density. The linear (Lorentz invariant) band spectrum in graphene however means that this ratio, the unitless interaction constant α, is independent of the density. Moreover, since the density of states vanishes at the Dirac point, screening of the long-range Coulomb interaction is much less effective in charge neutral graphene, especially, since α can actually be of the order of unity [6]. The one remaining problem of graphene is the impossibility of opening a band-gap, which means that electrostatic gating cannot be used to form devices like quantum wires or quantum point contacts.

This changes fundamentally, if one places two graphene layers on top of each other, without introducing a twist. The resulting material, bilayer graphene (BLG), possesses a quadratic band spectrum for low energies, while the presence of two inequivalent valleys is not changed [7], the finite distance between the two layers allows one to induce a displacement field leading to a gate tunable band gap [8]. By using two gates, a back and a top gate, one can thus tune both the band gap and the total density, which enables the fabrication of a plethora of electronic devices.

The most easily realizable experimental setup, which still enables an observation of electronic behavior and the role of different mechanisms, is a conductance measurements in a two-terminal setup. One

attaches two leads at the area of interest, and measures the current I flowing through the sample at a fixed voltage U or vice versa. The resulting conductance $G = U/I$, which in general depends on the dimensions of the measured sample, is determined as $G = \sigma W/L$ in a sufficiently large two-dimensional sample. Here σ is the conductivity, which is a material property and independent of the size of the system and W and L are the width and length of a rectangular sample respectively. This behavior is called ohmic and only occurs, if there are no internal length scales that are much larger than the dimensions of the sample [9–11].

There are different scenarios, in which this is indeed not the case. If a sample is exceptionally clean, the mean free path, which is the typical length an electron can move without scattering off of an impurity, can be of the order or larger than 100 nm, which is a length scale that can be easily undershot by modern hetero structures [12]. If one for example places two electronic fingergates with a distance shorter than that on top of bilayer graphene and additionally uses an overall top and bottom gate, one may tune the bands in such a way, to prohibit transport underneath the finger gates, leaving only a small passageway. This setup is called a quantum point contact (QPC) [13]. As mentioned above, this violates the requirements for ohmic transport, instead quantum effects become very apparent. While electrons can still move freely along one direction, they are strongly confined along the other and one has to take into account their wave nature, leading to a quantization of momentum and thus energy in the transverse direction. This quantization directly translates into the quantization of the measured conductance, which shows clear steps at integer values of $\frac{e^2}{h}$ [14]. The integers in front of this universal conductance quantum are determined by the degeneracies that are present in the system. For a material, where only spin is degenerate, one find steps of $2 \times \frac{e^2}{h}$; due to their additional valley degeneracy graphene and bilayer graphene show steps at multiples of $4 \times \frac{e^2}{h}$. The sharpness of these conductance steps is determined by temperature, among other things.

While the role of disorder can be neglected in such a setup, interaction effects may still play a role. A very prominent example for this is the appearance of an additional shoulder below the first conductance plateau, which is seen over a wide range of samples and up to temperatures, where the conductance steps themselves are no longer resolved. This feature is called the 0.7 anomaly, since, in systems with spin-degeneracy, it appears close to the conductance value of $0.7 \times 2 \times \frac{e^2}{h}$ [15]. Since this feature continuously moves into the Zeeman split plateau under the application if an in-plane magnetic field, it was soon connected with spin. However, there is still no microscopic explanation for all of its features that is commonly accepted. The situation is even more advanced, if one considers a material like BLG, where the additional valley degree of freedom could be involved in the interaction effects.

If one turns to systems, where the typical dimensions of the sample are of the order of several μm, but temperatures are still low, i.e. of the order of a few Kelvin, transport in monolayer graphene is dominated by disorder scattering. In low magnetic fields, these systems can be described by semi-classical approaches, like the Boltzmann equation [16], which is a non-linear differential equation for the distribution function. For finite disorder, quantum states require a finite lifetime τ_q, which is obtained from the imaginary part of the self-energy in the Green's function formalism. This time can also be obtained from a golden-rule calculation, which can also be used to find the transport scattering rate τ_{tr} that describes the relaxation of momentum. In the semi-classical regime, the Boltzmann equation can be used to determine the conductivity and thus the conductance of the sample. For high magnetic fields this semi-classical description fails, since quantum effects like Landau levels cannot be included. In this situation, one may still calculate the conductivity by means of perturbation theory, which in the case of low magnetic fields simplifies exactly to the Drude result obtained before. By performing this calculation and including the disorder scattering in the self consistent Born approximation, one

realizes that it is exactly τ_{tr} that should enter the Boltzmann equation, which is obtained after including corrections from the velocity vertex.

For finite magnetic fields, conductivity obtains a matrix structure and its inverse, the resistivity, is needed to obtain the magnetoresistance of the system. From the dependence of the resistance on magnetic field and electronic density, on can infer information on the type of scattering processes occurring inside the sample. In the typical, rectangular Hall bar setup, the magnetoresistance as obtained from the Boltzmann equation actually vanishes. For this reason, one turns towards a different geometry, the Corbino disk, which is essentially a flat donut, where current flows between the inner and outer radius. Due to the polar symmetry, magnetoresistance is determined by the longitudinal conductivity alone in this setup and thus quadratic in the simple Boltzmann equation calculation. This simple functional form can be used to analyze the role of different scatterers in the system, since their transport times have different density dependencies.

If one considers the same sample at elevated temperatures, electron-electron interaction becomes more important and in very clean samples one reaches the regime, where ℓ_{ee}, the length scale related to electron-electron interaction, is shorter than the mean free path between disorder scattering events as well as electron-phonon and quasiparticle recombination processes [17]. This regime is called hydrodynamic regime, since due to the relatively strong interaction effects, electrons form a strongly correlated liquid and show collective behavior. In this regime, the Boltzmann equation is still applicable, but by integrating with different weights and taking into account the conservation properties of all different scattering events, one can obtain a set of continuity equations. Hydrodynamic behavior is specified by assuming a local equilibrium, which is established by electron-electron collisions. In this local equilibrium the electronic fluid is characterized by a collective hydrodynamic drift velocity, for which one finds an equation of the form of a generalized Navier-Stokes equation from the continuity equation for momentum [18].

Structure of this Thesis

This thesis consists of two main parts. The first part, comprising Chapters 1,2 and 3 summarizes the already well known results, on which the Chapters 4, 5 and 6 extend.

In Chapter 1 I start with an introduction to the electronic properties of mono and bilayer graphene. I especially present the eigensystems of monolayer graphene in vanishing and high magnetic fields.

In the following Chapter 2 I give a general introduction describing why two-terminal electric measurements of the conductance or resistance of a system already reveal a lot about the internal processes and discuss different methods of describing transport in mesoscopic systems. The first one is the semi-classical Boltzmann equation discussed in Sec. 2.1 and shown in Eq. (2.1), the second one is perturbation theory by means of a diagrammatic Green's function approach, which is discussed in Sec. 2.2 and ultimately leads to the Kubo formula of conductivity shown in (2.97). The Chapter ends with two methods, that can be deduced from these two formalisms in special limits. For temperature ranges, where the average distance between electron-electron interaction events is larger than the system size but the distance between impurity scatterers is smaller, one can use the scattering matrix theory and the resulting Landauer-Büttiker formula (2.164) discussed in Sec. 2.3 to describe the conductance of the system. If one turns to elevated temperatures and larger systems, one can reach the limit where the elastic mean free path is the smallest length scale of the system, in which the hydrodynamic approach discussed in Sec. 2.4 is applicable, especially the set of hydrodynamic equations (2.206), (2.208), (2.209), (2.210).

The first part finishes with Chapter 3, where I discuss effect that occur on special device geometries. The first geometry is the quantum point contact (QPC) discussed in Sec. 3.1, where I apply the Landauer-Büttiker formula (2.164), to show that conductance in such a system is quantized, as visualized in Fig. 3.2. I also discuss the effect of an in-plane magnetic field on such a device in Sec. 3.1.1 and present an introduction to an interaction-based phenomenon- the 0.7 effect- in such systems in Sec. 3.1.2. This chapter ends with an overview on the Corbino geometry in Sec. 3.2.
The second main part contains the results I obtained during my PhD.

Interaction effects in bilayer graphene quantum point contacts In Chapter 4 I present two interaction induced features, that were observed in a bilayer graphene (BLG) QPC in parallel magnetic field. After a summary of the experimental results 4.2 obtained in Ref. [19] I discuss how these results can be explained, based on the effective two-band model of BLG in Sec. 4.3. An important building block is the gate-tunability of the gap, that is discussed in Sec. 4.3.2 and leads to the conductance quantization presented in Sec. 4.3.5. The main message of this chapter is that one can indeed observe interaction effects in such a system. To motivate this conclusion, I discuss the screening effects in this specific device in Sec. 4.3.3. The first interaction induced effect is the 0.7 anomaly discussed in Sec. 4.4. I propose to use a phenomenological model [20] and extend it to the additional valley degree of freedom of BLG. This phenomenological model can be motivated by combining the free energy obtained in Sec. 3.1.2.3 with the observations of the more involved model summarized in Sec. 3.1.2.2. The second interaction induced effect is an enhancement of the Landé g-factor in parallel magnetic field, which is also discussed in Sec. 4.3.3. This chapter ends with a discussion in Sec. 4.7, concluding that the additional conductance shoulder in the experiment can be explained based on the proposed phenomenological model by assuming a spin-splitting and degenerate valley degree of freedom.

Disorder dominated transport in a graphene Corbino disk In Chapter 5 I show that in the disorder dominated transport regime, the magnetoresistance measured in a monolayer graphene Corbino disk at low temperatures can be used to characterize and distinguish the role of short range and charged impurity scattering. The experiment, on which this analysis is performed is introduced in Sec. 5.2. In the following Sec. 5.3 I present the theoretical background, including the Drude conductivity (2.1.1) with the transport time determined in (2.8). In Sec. 5.3.1 I argue that also in this disorder dominated regime, one can use the Boltzmann equation to derive an equation for the current density, that has the form of a generalized Navier-Stokes equation and can be used to find the magnetoresistance in a graphene Corbino disk at low magnetic fields (5.49). Subsequently I show in Sec. 5.3.2 that scattering off of charged impurities can be treated in the same formalism but the resulting transport time has a different density or energy dependence, which can be used to distinguish it from short range disorder, if one measures the density of voltage dependence of magnetoresistance. Since the experimental data includes measurement close to the Dirac point, I detail the expected saturation behavior in Sec. 5.3.3. I discuss finite temperature effects in Sec. 5.3.4 and effects due to electron-electron interaction in Sec. 5.3.5. From these ingredients I develop a fitting procedure, which allows the extraction of parameters characterizing the two types of disorder and the true bulk resistance. Since this is a very clean system, the contact resistance is larger than the true bulk resistance, and thus a naive extraction of the mobility is too low. This analysis is presented in Sec. 5.4 and supplemented by a discussion of the role of finite temperature and electron-electron interaction for the specific parameters of the system in Sec. 5.4.1. I conclude in Sec. 5.6 that one indeed has to perform the more involved fitting procedure proposed here

to extract the true bulk mobility of clean devices but that by doing so one automatically gets access to the details of disorder scattering in the sample.

Hydrodynamic transport in a graphene Corbino disk While interaction effects could be disregarded in Chapter 5 and only lead to additional features in Chapter 4, I concentrate on the strongly interacting regime in Chapter 6. Here I show, how the hydrodynamic approach discussed in Sec. 2.4, where the smallest legthscale of the problem ℓ_{ee} is due to electron-electron interaction, can be used, to describe the electric and heat transport in a graphene Corbino disk at charge neutrality. The charge neutral setup is of special interest here, since recombination processes mean that the densities within both conductance and valence band are not conserved individually. Moreover, the energy and charge transport, which for finite densities are both carried by the hydrodynamic velocity $\mathbf{u}$ and simply proportional, decouple at the Dirac point and the electrical current becomes fully dissipative. On the other hand, Corbino disks are an ideal experimental setup to observe hydrodynamic effects, since they naturally show non-uniform flow and one could potentially observe these effects in the exact same device investigated in Chapter 5. This chapter starts with an introduction and motivation in Sec. 6.1. The hydrodynamic equations, that are generally used to describe this system, are introduced in Sec. 6.2. I restrict ourselves to the charge neutral case in zero magnetic field and to linear order in the external drive. The resulting equations are listed and solved in Sec. 6.3. In Sec. 6.4 I discuss, how the dissipation obtained from the kinetic energy can be used to find the jump of the potential at the interface. This chapter end with a discussion in Sec. 6.5 and a summary and conclusion in Sec. 6.6

This thesis ends with a conclusion and outlook in Chapter 7.

Main statements

1. Interaction effects visibly influence the conductance in a narrow bilayer graphene quantum point contact. An effective spin splitting (rather than valley splitting) is consistent with the experimental observations and would be expected in every material, where spin and valley degree of freedom are degenerate without interaction effects.

2. The Corbino disk geometry is especially suited to characterize disorder in a sample by measuring the low magnetic field magnetoresistance. This is true for graphene and also holds for other two-dimensional electron gases.

3. Hydrodynamic effects influence the temperature and potential profile of charge neutral graphene Corbino disks in a measurable way. These effects are dominated by energy relaxation over viscosity.

Publications

In the following my relevant publications and their bibliography reference in this thesis are listed:

- Ref. [21]: R. Kraft, I. V. Krainov, V. Gall, A. P. Dmitriev, R. Krupke, I. V. Gornyi, and R. Danneau, *Valley subband splitting in bilayer graphene quantum point contacts*, Physical Review Letters **121** 257703, 2018.
- Ref. [12]: M. Kamada, V. Gall, J. Sarkar, M. Kumar, A. Laitinen, I. Gornyi, and P. Hakonen, *Strong mag- netoresistance in a graphene Corbino disk at low magnetic fields*, Physical Review B **104**, 115432, 2021.
- Ref. [19]: V. Gall, R. Kraft, I. V. Gornyi, and R. Danneau, *Spin and valley degrees of freedom in a bilayer graphene quantum point contact: Zeeman splitting and interaction effects*, Physical Review Research **4**, 023142, 2022.
- Ref. [22]: V. Gall, B. N. Narozhny, and I. V. Gornyi, *Electronic viscosity and energy relaxation in neutral graphene*, arxiv:2206.07414, 2022.

Acknowledgments

First of all, I want to express my deepest gratitude to my PhD advisor Igor V. Gornyi for his constant support, his patience and guidance through all the ups and downs of the last years. His motivation and help contributed tremendously to the successful completion of this work.

I would like to extend my sincere thanks to my second reviewer Alexander D. Mirlin for giving me the opportunity to work in his group and his feedback on this manuscript.

I am very grateful to my collaborators Romain Danneau, Rainer Kraft, Pertti Hakonen and Masahiro Kamada, since this work relied heavily on their nice experimental data. Moreover I am indebted to Boris Narozhny, who greatly influenced and advanced the hydrodynamic project.

I also want to thank Yuli Nazarov, who hosted me for two weeks at TU Delft and the KIT Networking grant for financing my stay.

Special thanks go to:
Jonas Karcher for proof-reading of this thesis and general emotional support
Charlie Steward for proof-reading
My partner and my family

Finally I want to thank all my current and former colleagues for their company, support and suggestions.

Contents

1 Chapter 1
Graphene

All devices investigated in this thesis consist of either mono- or bilayer graphene. In this chapter we introduce the basic properties of these two materials. The main result is, that both systems can, for low energies, effectively be described by a two band model. In the case of monolayer graphene, low energy modes have a Dirac spectrum, for bilayer graphene it is quadratic.

The eigensystem of monolayer graphene will be used in Sec. 2.2.5 to derive the conductivity perturbatively and in Sec. 2.1 based on the Boltzmann equation. These results are used in Chapter 5 to find the magnetoresistance in a monolayer graphene Corbino disk. The linear spectrum is also relevant for the hydrodynamic approach introduced in Sec. 2.4 and applied in Chapter 6 to a graphene Corbino disk at elevated temperatures. Corbino disks are introduced in Sec. 3.2.

Bilayer graphene is investigated in the shape of a quantum point contact in Chapter 4. There we need its spectrum and the presence of its additional valley degeneracy. The gate tunability and some effects of electron-electron interaction in bilayer graphene are also discussed there. An introduction into quantum point contacts is given in Sec. 3.1.

Monolayer graphene is a one atom thick material consisting of carbon atoms arranged on a honeycomb lattice. Its band structure was first theoretically predicted in 1947 in Ref. [2], but was only experimentally found in 2004 [4]. Low energy states in graphene are massless, chiral Dirac fermions and in charge neutral graphene the chemical potential sits exactly at the Dirac point, where the chiral bands cross. Half filled bands are an important ingredient for strong correlation effects, since Coulomb energies can be very large in such systems [23]. Due to this peculiar band structure, electrons in graphene mimic the physics of quantum electrodynamics, except that the speed of light should be replaced with the Fermi-velocity.

This leads to several interesting phenomena, like the anomalous integer quantum Hall effect in high, perpendicular magnetic fields [24, 25], where graphene shows step heights of $4\frac{e^2}{h}$ without any Hall plateau at $N = 0$. Another peculiarity is the Klein paradox discussed in Refs. [26, 27], which allows electrons to get transmitted through classically forbidden regions with unit probability. While disorder can never be avoided, graphene can be fabricated exceptionally clean, and under certain conditions localization effects can be completely absent [28]. Due to its truly two dimensional nature, graphene shows a special kind of disorder, called ripples [29–33], which have a similar effect as charged impurities [34]. Also due to its two-dimensional nature, graphene hosts special out-of-plane vibrational modes called flexural phonons [35]. Due to its honeycomb lattice structure, graphene has two distinct types of clean edges, armchair and zigzag, which lead to different behavior [36], but are quite hard to control

on mesoscopic samples. Finally, graphene possesses two valleys, which can be used as an additional quantum degree of freedom in a field called valleytronics [37]. For all of these reasons, graphene is a very interesting candidate for mesoscopic transport setups [38, 39]. For an overview on all of these topics see Ref. [5] and references therein.

However one problem of graphene is the impossibility to electrostatically open a band gap, which is a requirement for electrostatic confinement in devices like quantum point contacts (QPCs) and quantum dots. This is fundamentally different in bilayer graphene (BLG) [40–42]. While there are different ways of stacking two graphene sheets on top of each other, including the introduction of a finite twisting angle [43], we will only consider Bernal-stacked bilayer graphene. Low energy excitations of bilayer graphene (BLG) are massive chiral quasiparticles with a parabolic spectrum [44]. The integer quantum Hall effect in BLG is again anomalous [45], but while in graphene the whole staircase was shifted symmetrically away from 0 with constant step heights of $4\frac{e^2}{h}$, the zeroth Landau level in BLG gives rise to a lowest step spanning from $-4\frac{e^2}{h}$ to $4\frac{e^2}{h}$, i.e. has a double the height of all others due to the eightfold degeneracy of the zeroth Landau level. On top of the parabolic low energy spectrum, one observes trigonal warping [46], due to the broken rotational invariance of the trigonal Bravais lattice and for large band gaps Mexican hat features [47]. Since BLG does not have a linear dispersion and in most cases a finite band gap, interaction effects are expected to be very similar to normal two dimensional Fermi liquids at finite densities. Both carrier density and the energy band gap can be controlled by electrostatic gates or doping [44, 48], where one should take into account the screening of the two graphene planes as discussed in Ref. [8]. This allows for the construction of BLG quantum point contacts, that were for example studied in [21, 49].

In this section we discuss monolayer graphene in Sec. 1.1, which also shows the behavior in a perpendicular magnetic field, and the low energy theory of BLG in Sec. 1.2.

1.1 Monolayer graphene

Monolayer graphene consists of carbon atoms, that are arranged on a honeycomb lattice. This corresponds to a triangular Bravais lattice with a bi-atomic basis, that is pictured in Fig. 1.1.

The triangular lattice is formed by sp^2 hybridization between one s and two p orbitals, which form σ bonds with a separation of 1.42Å leaving one p orbital unaffected. Thus each carbon atoms contributes one electron to the overall π band formed by the covalently bound p orbitals, which is consequently exactly half filled [5]. From the two basis atoms we also find two non-equivalent point in momentum space, which are known as the K and K' Dirac point. Using a tight binding approximation, where one includes next neighbors from the opposite sublattice and next nearest neighbors from the original one and looking at momenta close to one of the Dirac points, as discussed in Refs. [5, 50], one can find a many-body Hamiltonian of the form

$$H = -iv_g \int \mathrm{d}x\mathrm{d}y \left[\hat{\mathbf{\Psi}}^\dagger_+(\mathbf{r})\sigma \cdot \nabla \hat{\mathbf{\Psi}}_+(\mathbf{r}) + \hat{\mathbf{\Psi}}^\dagger_-(\mathbf{r})\sigma^* \cdot \nabla \hat{\mathbf{\Psi}}_-(\mathbf{r}) \right], \tag{1.1}$$

where $\xi = +, -$ corresponds to the K, K' point respectively and $v_g \approx 1 \times 10^6$ m/s is the Fermi velocity of electrons in graphene. The field operators are vectors in the sublattice space. For small momenta, the two Dirac points do not couple to each other, and we can restrict ourselves to momenta close to one of them, i.e. restrict ourselves to one of the two valleys. The many-body Hamiltonian (1.1) is

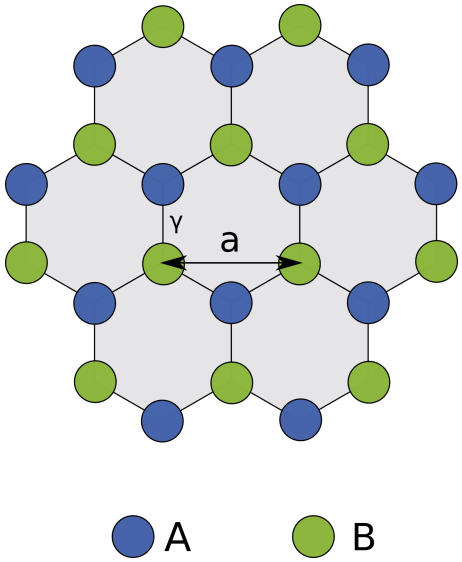

Figure 1.1: Monolayer graphene lattice, showing the two sublattices A and B with the lattice constant a. The hopping parameter γ between neighboring carbon atoms, that belong to opposite sublattices, determines the Fermi velocity in graphene $v_g = \sqrt{3}a\gamma/(2\hbar)$.

non-interacting and contains the single-particle Hamiltonian

$$\check{H}_0\mathbf{F} = \varepsilon\mathbf{F}, \tag{1.2}$$

$$\check{H}_0 = v_g\xi \begin{pmatrix} 0 & \hat{\pi}^\dagger \\ \hat{\pi} & 0 \end{pmatrix}, \tag{1.3}$$

which again acts on the sublattice space. Here the generalized momentum operator

$$\hat{\pi} = \xi\hat{p}_x + i\hat{p}_y, \quad \hat{\pi}^\dagger = \xi\hat{p}_x - i\hat{p}_y, \tag{1.4}$$

$$\hat{\mathbf{p}} = -i\hbar\nabla + e\hbar\mathbf{A}/c \tag{1.5}$$

has been introduced and $\mathbf{A}$ is the vector potential with a vectors structure in real space. For vanishing magnetic field $B = 0$ the eigensystem can be easily found and is

$$\check{H}_0\mathbf{F}_{s,\mathbf{k}}(\mathbf{r}) = \varepsilon_{s,\mathbf{k}}\mathbf{F}_{s,\mathbf{k}}(\mathbf{r}), \tag{1.6}$$

$$\varepsilon_{s,\mathbf{k}} = s\hbar v_g k, \tag{1.7}$$

$$\mathbf{F}_{s,\mathbf{k}}(\mathbf{r}) = \frac{1}{\sqrt{2}}e^{i\mathbf{kr}} \begin{pmatrix} s \\ e^{i\theta} \end{pmatrix}, \tag{1.8}$$

where $\mathbf{k} = k(\cos\theta, \sin\theta)$. The band index $s = \pm$ labels two linear bands, that touch exactly at the corresponding Dirac point. The problem is not diagonal in the sublattice basis but in this $s = \pm$ basis.

1.1.1 Finite perpendicular magnetic field

For the situation $\mathbf{B} = B\mathbf{e}_z$ we show in Appendix A.1, how one can obtain the eigensystem. One finds the unified eigenenergies

$$\varepsilon_n = \mathrm{sign}(n)\hbar\Omega\sqrt{2|n|}, \tag{1.9}$$
$$\mathrm{sign}(n) = \begin{cases} 1 & n > 0, \\ 0 & n = 0, \\ -1 & n < 0, \end{cases}$$
$$\Omega = v_g\sqrt{\frac{eB}{\hbar c}},$$

and the correctly normalized eigenstates

$$\mathbf{F}_{n,k_y,+}(\mathbf{r}) = C_n e^{-ik_y y}\begin{pmatrix}\mathrm{sign}(n)h_{|n|-1}\\ h_{|n|}\end{pmatrix}, \tag{1.10}$$
$$C_n = \begin{cases} 1 & n = 0 \\ 1/\sqrt{2} & n \neq 0 \end{cases},$$
$$h_{|n|} = \frac{i^{|n|}}{\sqrt{2^{|n|}|n|!\sqrt{\pi}l}} e^{-\frac{1}{2}\left(\frac{x-l^2k_y}{l}\right)^2} H_{|n|}\left(\frac{x-l^2k_y}{l}\right),$$

where $l = \sqrt{c\hbar/eB}$ is the magnetic length and $H_{|n|}$ are the physicist's Hermite polynomials. Notably n can be negative in this formulation.

1.2 Bilayer graphene

Bilayer graphene is obtained, by stacking two layer of monolayer graphene on top of each other while placing an atom of sublattice A on top of one of sublattice B in the other layer, without introducing a relative twist, as pictured in Fig. 1.2.

This system is reviewed in Ref.[7, 50]. Here we will reproduce the most important properties.

In the setups considered in this work energies are low compared to the lower band edges of the systems. For this reason it is sufficient, to restrict ourselves to an effective low-energy descriptions for bilayer graphene.

Starting again from a tight binding approach, one can obtain again a single particle Hamiltonian for both the K and K' valley, which decouple for low energies. The presence of two sublattices led to a 2×2 single particle Hamiltonian in monolayer graphene (1.3). The additional layer degree of freedom in bilayer graphene thus leads to a 4×4 matrix in sublattice and layer space. This full four-band Hamiltonian is given by

$$\check{H}_0 = \begin{pmatrix} \varepsilon_{A1} & v\hat{\pi}^\dagger & -v_4\hat{\pi}^\dagger & v_3\hat{\pi}, \\ v\hat{\pi} & \varepsilon_{B1} & \gamma_1 & -v_4\hat{\pi}^\dagger, \\ -v_4\hat{\pi} & \gamma_1 & \varepsilon_{A2} & v\hat{\pi}^\dagger, \\ v_3\hat{\pi}^\dagger & -v_4\hat{\pi} & v\hat{\pi} & \varepsilon_{B2} \end{pmatrix}, \tag{1.11}$$

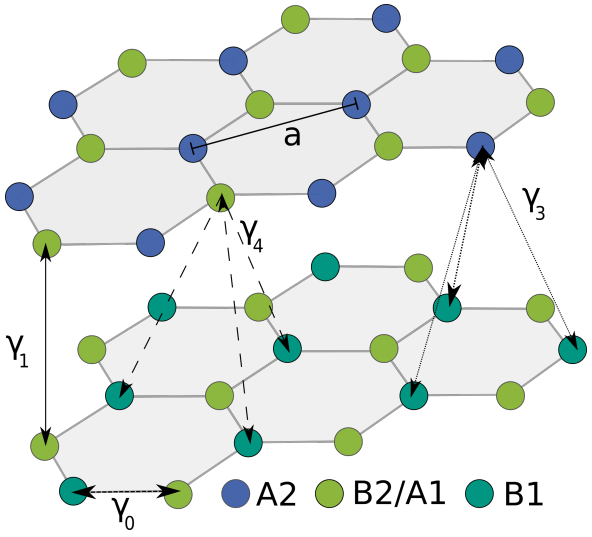

Figure 1.2: Bilayer graphene lattice, showing the two graphene layers with sublattices $A1$, $B1$ and $A2$, $B2$ respectively. In the considered Bernal stacking, $B2$ is directly on top of $A1$. The hopping parameters γ_i determine different velocities $v_i = \sqrt{3}a\gamma_i/(2\hbar)$.

where

$$\varepsilon_{A1} = \frac{1}{2}(-U + \delta_{AB}), \tag{1.12}$$

$$\varepsilon_{B1} = \frac{1}{2}(-U + 2\Delta' - \delta_{AB}), \tag{1.13}$$

$$\varepsilon_{A2} = \frac{1}{2}(-U + 2\Delta' + \delta_{AB}), \tag{1.14}$$

$$\varepsilon_{B2} = \frac{1}{2}(U - \delta_{AB}), \tag{1.15}$$

as derived in Ref. [7] and the momentum operators $\hat{\pi}, \hat{\pi}^\dagger$ are again given by Eq. (1.4). This operator acts on the four-component wave-function according to

$$\mathcal{H} \begin{pmatrix} \psi_{A1} \\ \psi_{B1} \\ \psi_{A2} \\ \psi_{B2} \end{pmatrix} = E \begin{pmatrix} \psi_{A1} \\ \psi_{B1} \\ \psi_{A2} \\ \psi_{B2} \end{pmatrix}. \tag{1.16}$$

We can include the spin degree of freedom by writing

$$\check{H}_i = \check{H}_0 \otimes \check{s}_0 \tag{1.17}$$

in the spin-degenerate sector, and for Zeeman splitting we introduce

$$\check{H}_Z = \Delta E_Z \, \check{\mu}_0 \otimes \check{\sigma}_0 \otimes \check{s}_z, \tag{1.18}$$

where $\check{\mu}, \check{\sigma}$ and $\check{s}$ are the Pauli matrices in layer, sublattice, and spin space, respectively. Finally, we can include spin-orbit coupling, where according to [51], two types of intrinsic spin-orbit interaction

are allowed by the symmetry of the problem

$$\check{H}_1^{\mathrm{so}} = \xi\lambda_1 \check{\mu}_0 \otimes \check{\sigma}_z \otimes \check{s}_z, \tag{1.19}$$

$$\check{H}_2^{\mathrm{so}} = \xi\lambda_2 \check{\mu}_z \otimes \check{\sigma}_0 \otimes \check{s}_z, \tag{1.20}$$

where $\xi = \pm$ corresponds to valley K (K'). Following [52], we additionally introduce an extrinsic spin-orbit interaction of the form

$$\check{H}_3^{\mathrm{so}} = \xi\,\mathrm{diag}(\lambda_u, -\lambda_u, \lambda_d, -\lambda_d) \otimes \check{s}_z. \tag{1.21}$$

Following the procedure presented in Appendix A.2 one obtains an effective, low energy two band Hamiltonian. Here, we are not interested in a perpendicular magnetic field, but rather in an in-plane one. Moreover we want to include the gate-tunable band gap U and thus consider the Hamiltonian

$$\check{H}_0 = \left(-\frac{1}{2m} \begin{pmatrix} 0 & (\hat{\pi}^\dagger)^2 \\ \hat{\pi}^2 & 0 \end{pmatrix} - \frac{U}{2} \begin{pmatrix} 1 & 0 \\ 0 & -1 \end{pmatrix} \right) \otimes \hat{s}_0 + \frac{\Delta E_z}{2} \begin{pmatrix} 1 & 0 \\ 0 & 1 \end{pmatrix} \otimes \hat{s}_z, \tag{1.22}$$

that acts on the low-energy non-dimer states

$$(\psi_{A1}, \psi_{B2})^T \tag{1.23}$$

where we neglect effects like the Mexican hat feature and trigonal warping, that are discussed in Refs. [46]. The direct effect of an in-plane magnetic field on the band structure via minimal coupling is negligible for magnetic fields below several hundred teslas [53]. Intrinsic spin-orbit coupling in graphene is very weak. This Hamiltonian has the eigenvalues

$$\varepsilon_{\sigma,s,k} = \frac{\sigma\Delta E_z}{2} + s\frac{\sqrt{k^4 m^2 \hbar^4 + 4m^4 U^2}}{2m^2}. \tag{1.24}$$

1.3 Summary and conclusions

In summary we see, that in zero magnetic field monolayer graphene has a Dirac like dispersion with spinor eigenstates in sublattice space (1.8) and a unusual Landau level spectrum in magnetic field (1.10). In the non-interacting limit, both graphene and bilayer graphene have two valleys with a large separation in momentum space, which can be described separately.

In Sec. 2.1 we will use the zero magnetic field dispersion relation to derive the conductivity in small perpendicular magnetic fields within the Boltzmann equation approach. The relaxation time entering the disorder relaxation of the distribution function is defined in Eq. (2.6) and evaluates to Eq. (2.8). Due to its spinor wavefunction, which have a non trivial dependence on the angle of the momentum, the transport scattering time τ_{tr} and the quantum scattering time τ_q differ by a factor of two in monolayer graphene. In the case of large perpendicular magnetic fields, one has to perform a full perturbative treatment, to obtain the conductivity, as done in Sec. 2.2. These results will then be applied in Chapter 5 to describe the magnetoresistance in a graphene Corbino disk at small perpendicular magnetic fields and at low temperatures.

If one turns to higher temperatures, electron-electron interaction becomes more important and a perturbative treatment like Sec. 2.2 is no longer valid. Instead, the hydrodynamic approach discussed in Sec. 2.4 can be applied and electrons in graphene can be describes similarly to a classical fluid, since

strong correlations induce a collective behavior. This will be applied to the same graphene Corbino disk, however at elevated temperatures, in Chapter 6, where we strongly rely on the linear dispersion discussed here.

For low energies, BLG has a quadratic spectrum, with a band gap and spinor eigenstates in sublattice/layer space (1.24). This band gap can be opened by a combination of gates and especially used, to electrostatically confine the electron gas and construct a quantum point contact, which is investigated in Chapter 4. In Sec. 2.3 we use Landauer theory to find the conductivity of such a system, where a scattering matrix theory approach is valid. The general aspects of quantum point contacts, which form the basis of Chapter 4 are discussed in Sec. 3.1.

2 Chapter 2
Methods in quantum transport

In this chapter we discuss different formalisms to describe electronic transport at the meso-scale. We start with the Boltzmann equation, deriving the magnetoresistance in monolayer graphene (2.29) *and* (2.30)*. Then we show, how the linear response conductivity can be found in the Green's function formalism by means of the Kubo formula* (2.97) *and how the non-interacting Green's function look for the case of disordered monolayer graphene* (2.58)*. These results are relevant for Chapter 5, where we apply them to a graphene Corbino disk in small perpendicular magnetic field at low temperature. This device geometry is discussed in Sec. 3.2. We also discuss the Landauer-Büttiker formula* (2.164)*, which is a special limit of the Kubo formula and will be applied in Chapter 4. Finally we present, how and when the Boltzmann equation* (2.167) *can be used, to derive a set of hydrodynamic equations in graphene* (2.206)*,* (2.208)*,*(2.209)*,*(2.210)*, which is used in Chapter 6 to describe the same graphene Corbino disk, but at elevated temperatures.*

Transport in electronic systems strongly depends on the hierarchy of length scales involved in the given setup. The systems we consider, can all be characterized by a generally finite conductance $G = I/U$, which gives the ratio between the current I passing through the system over the applied voltage U. If a conducting two dimensional system is large enough, then this conductance is given by $G = \sigma W/L$, where σ is the conductivity, which is a material property and independent of the dimensions, and W and L are width and length of the system respectively. This behavior is called ohmic and only occurs, if both of these length scales are much larger than inherent length scales, that characterize the sample. Usually these length scales are the quantum mechanical coherence length ℓ_ϕ, over which the phase of the wavefunction stays well defined, the energy relaxing mean free path ℓ_{in}, the momentum relaxing mean free path ℓ_{p} and the Fermi wavelength λ_F. All of these depend on external properties like the temperature or applied magnetic fields, but also on internal properties of the sample, like its band structure and disorder. A good review on the behavior in different length hierarchies is given in [9–11].

In the following we will give an overview on two methods of describing electronic transport. The first method is the Boltzmann equation, which is a semiclassical non-linear differential equation for the distribution function 2.1. It is applicable, if excitations have long wavelengths and low frequencies. Disorder and interaction effects are usually treated on the golden rule level, which is a result of perturbation theory to first order. As long as disorder and interaction effects are weak, they can be taken into account in a perturbative expansion, but this expansion becomes better, if we can include

relevant higher order corrections as well. This is archieved in the Green's function formalism introduced in Section 2.2. Starting from free electrons, we include the most relevant interaction or disorder induced corrections, and calculate the conductivity in linear response. The chapter ends with two special limits of these two methods. The first is the Landauer-Büttiker formula of conductance discussed in Sec. 2.3, which is essentially the much simplified first order result of the linear response conductivity obtained in the Green's function formalism. Finally we end with a special application of the Boltzmann equations, which can be used to derive conservation laws in the form of hydrodynamic equations in graphene discussed in Sec. 2.4.

2.1 Boltzmann equation

One way of describing the response of a system to external fields is the semiclassical Boltzmann equation, which is discussed in Refs. [16, 54, 55] and was first derived by Ludwig Boltzmann in 1872. For excitations with sufficiently long wavelengths ($\lambda \gg 2\pi/k_F$) and low frequencies ($\omega \ll 2E_F/\hbar$) the distribution function $f(\mathbf{r}, \mathbf{k}, t)$ of the electron gas obtains additional dependencies compared to the bare Fermi-Dirac distribution function $f_0(\varepsilon) = \Big(1 + \exp\Big((\varepsilon - \mu)/k_B T\Big)\Big)^{-1}$. These are described by the Boltzmann equation

$$\left[\partial_t + \frac{\mathrm{d}\mathbf{p}}{\mathrm{d}t} \cdot \nabla_{\mathbf{p}} + \frac{\mathrm{d}\mathbf{r}}{\mathrm{d}t} \cdot \nabla_{\mathbf{r}}\right] f(\mathbf{r}, \mathbf{p}, t) = S\{f\}(\mathbf{r}, \mathbf{p}, t), \tag{2.1}$$

where $\frac{\mathrm{d}\mathbf{r}}{\mathrm{d}t} = \mathbf{v} = \nabla \varepsilon_p$ is the velocity and $\frac{\mathrm{d}\mathbf{p}}{\mathrm{d}t} = \mathbf{F}(\mathbf{r}, \mathbf{p}, t)$ is the total force acting on the electrons. The functional $S\{f\}$ is known as collision integral and originates from potential variations on the scale k_F^{-1}, which lead to momentum changes of the particles. Assuming, that the scattering rates $W_{\mathbf{k},\mathbf{q}}$ describe the probability per unit time of scattering from a state with momentum $\mathbf{k}$ into one with momentum $\mathbf{q}$, this collision integral can be expressed as

$$S\{f\}(\mathbf{r}, \mathbf{k}, t) = -\int \frac{(\mathrm{d}^d q)}{(2\pi)^2} \left(W_{\mathbf{q},\mathbf{k}} f_{\mathbf{q}} - W_{\mathbf{k},\mathbf{q}} f_{\mathbf{k}}\right), \tag{2.2}$$

i.e. it's given by the difference of states scattering out of the state $f_{\mathbf{k}}$ (which need to be filled, so are weighted by $f_{\mathbf{q}}$) and those that are scattered out of the state with $f_{\mathbf{k}}$. Notably, the scattering rates usually also depend on the distribution function, so this is a non-linear integro-differential equation. In the limit of low energies, most scattering events occurs due to scattering off of impurities, which conserves momentum and is thus elastic. Then the scattering rates can be found from the Fermi golden rule in the Born approximation. A common way of simplifying this even further is to assume, that the scattering potential is actually independent of the transfered momentum, in which case one may write

$$S\{f\}(\mathbf{r}, \mathbf{k}, t) = \frac{f - \langle f \rangle}{\tau_{\mathrm{tr}}(\epsilon_k)}, \tag{2.3}$$

where $\tau_{\mathrm{tr}}(\epsilon_k)$ is the momentum relaxation time and $\langle f \rangle$ is the angular average. The momentum relaxation time is also called transport scattering time τ_{tr} and for graphene it can be found as

$$\frac{1}{\tau_{\mathrm{tr}}(\mathbf{k})} = \frac{2\pi}{\hbar} n_{\mathrm{imp}} \int_0^{2\pi} \mathrm{d}\theta \int_0^{\infty} \frac{k' \mathrm{d}k'}{(2\pi)^2} S(\mathbf{k}, \mathbf{k}')(1 - \cos\theta), \tag{2.4}$$

$$S(\mathbf{k}, \mathbf{k}') = |U_{\mathbf{k}'\mathbf{k}}|^2 \frac{1}{\hbar v_g} \delta(k' - k), \tag{2.5}$$

$$U_{\mathbf{k}'\mathbf{k}} = \int \mathrm{d}\mathbf{r} \psi^{\dagger}_{s,\mathbf{k}'}(\mathbf{r}) \check{U}(\mathbf{r}) \psi_{s,\mathbf{k}}(\mathbf{r}), \tag{2.6}$$

where $\check{U}(\mathbf{r})$ is the scattering potential of a single impurity at the origin, $\psi_{s,\mathbf{k}}(\mathbf{r})$ are the spinor wavefunctions of graphene shown in Eq. 1.8 and n_{imp} is the density of impurities. This approximation is known as relaxation time approximation. This should be contrasted with inelastic scattering from electron-electron or electron-phonon interactions, where energy is not conserved and distribution function of different energies thus get mixed.

For the simplest example of a potential

$$\check{V}(\mathbf{r}) = \delta(\mathbf{r} - 0) u_0 \begin{pmatrix} 1 & 0 \\ 0 & 1 \end{pmatrix}, \tag{2.7}$$

we find with the zero magnetic field wavefunctions from Eq. (1.8)

$$\tau_{\mathrm{tr}}(\epsilon_k) = \frac{2\gamma\hbar}{|\epsilon_k|}, \quad \gamma = \frac{2\hbar^2 v_g^2}{n_{\mathrm{imp}} u_0^2}. \tag{2.8}$$

2.1.1 Static linear response in constant perpendicular magnetic field

Let us consider a setup, where we apply a perpendicular magnetic field $\mathbf{B}$ and a static electric field $\mathbf{E}$ and want to find the response of the current density $\mathbf{j}$ to linear order in $\mathbf{E}$, which gives access to the conductivity σ through

$$\mathbf{j} = \sigma \mathbf{E}. \tag{2.9}$$

Restoring all units of $\hbar$ and specifying the electromagnetic force we want to consider

$$\frac{\partial f}{\partial t} + \frac{\partial \mathbf{k}}{\partial t} \nabla_{\mathbf{k}} f + \frac{\partial \mathbf{r}}{\partial t} \nabla_{\mathbf{r}} f = S\{f\}(\mathbf{r}, \mathbf{k}, t), \tag{2.10}$$

$$\frac{\partial \mathbf{r}}{\partial t} = \mathbf{v}_k = \frac{1}{\hbar} \nabla_{\mathbf{k}} \epsilon_k, \tag{2.11}$$

$$\frac{\partial \mathbf{k}}{\partial t} = -\frac{e}{\hbar} \mathbf{E} - \frac{e}{\hbar c} \mathbf{v}_k \times \mathbf{B}. \tag{2.12}$$

The current density is then found by

$$\mathbf{j}(t, \mathbf{r}) = -e \sum_k f(t, \mathbf{r}, \mathbf{k}) \mathbf{v}_k. \tag{2.13}$$

We will assume, that this situation only slightly deviates from the free problem, i.e. $f(t, \mathbf{r}, \mathbf{k}) = f_0(\mathbf{k}) + g(t, \mathbf{r}, \mathbf{k})$, where f_0 is the spatially homogeneous and time independent Fermi-Dirac distribution

function and g is a small deviation. We will further assume spatial homogeneity and use a relaxation time approximation $S\{f\}(\mathbf{r},\mathbf{k},t) = -\frac{g}{\tau_{\mathrm{tr}}(\epsilon_k)}$. Furthermore we consider monolayer graphene with a dispersion

$$\epsilon_k = \hbar v_g k. \tag{2.14}$$

Then we get

$$-i\omega g - \frac{e}{\hbar}\mathbf{E}\left(\nabla_{\mathbf{k}} g + \frac{\partial f_0}{\partial \epsilon_k}\hbar\mathbf{v}_k\right) - \frac{e}{\hbar}\left(\frac{1}{c}\mathbf{v}_k \times \mathbf{B}\right)\nabla_{\mathbf{k}} g = -\frac{g}{\tau_{\mathrm{tr}}(\epsilon_k)}. \tag{2.15}$$

To linear order in the external electric field this means

$$-e\frac{\partial f_0}{\partial \epsilon_k}\mathbf{E}\cdot\mathbf{v}_k - \frac{e}{\hbar c}(\mathbf{v}_k \times \mathbf{B})\cdot\nabla_{\mathbf{k}} g = \left(i\omega - \frac{1}{\tau_{\mathrm{tr}}(\epsilon_k)}\right) g, \tag{2.16}$$

which can be solved using the ansatz

$$g = \mathbf{A}(\epsilon_k)\cdot\mathbf{k} \Rightarrow \nabla_{\mathbf{k}} g = \mathbf{A}(\epsilon_k) + \left(\frac{\partial \mathbf{A}}{\partial \epsilon_k}\cdot\mathbf{k}\right)\nabla_{\mathbf{k}}\epsilon_k = \mathbf{A}(\epsilon_k) + \left(\frac{\partial \mathbf{A}}{\partial \epsilon_k}\cdot\mathbf{k}\right)\hbar\mathbf{v}_k. \tag{2.17}$$

Since $\mathbf{v}_k \times \mathbf{B}$ is orthogonal to $\mathbf{v}_k$, the second gradient does not contribute and we get

$$-e\frac{\partial f_0}{\partial \epsilon_k}\mathbf{E}\cdot\mathbf{v}_k - \frac{e}{\hbar c}(\mathbf{v}_k \times \mathbf{B})\cdot\mathbf{A}(\epsilon_k) = \left(i\omega - \frac{1}{\tau_{\mathrm{tr}}(\epsilon_k)}\right)\mathbf{A}(\epsilon_k)\cdot\mathbf{k}. \tag{2.18}$$

Next we use, that $\mathbf{v}_k = v_g\mathbf{e}_k = \frac{v_g}{k}\mathbf{k}$ compare the coefficients of v_k^α to find

$$-e\frac{\partial f_0}{\partial \epsilon_k}E^\alpha = \left[\delta_{\alpha\gamma}\frac{k}{v_g}\left(i\omega - \frac{1}{\tau_{\mathrm{tr}}(\epsilon_k)}\right) + \epsilon_{\alpha\beta\gamma}\frac{e}{\hbar c}B^\beta\right]A^\gamma(\epsilon_k), \tag{2.19}$$

$$\Gamma_{\alpha\gamma} = \left[\delta_{\alpha\gamma}\frac{k}{v_g}\left(i\omega - \frac{1}{\tau_{\mathrm{tr}}(\epsilon_k)}\right) + \epsilon_{\alpha\beta\gamma}\frac{e}{\hbar c}B^\beta\right] \tag{2.20}$$

$$\Leftrightarrow -e\frac{\partial f_0}{\partial \epsilon_k}\mathbf{E} = \Gamma\mathbf{A}(\epsilon_k) \tag{2.21}$$

$$\Rightarrow g = -e\frac{\partial f_0}{\partial \epsilon_k}(\Gamma^{-1}\mathbf{E})\cdot\mathbf{k}. \tag{2.22}$$

Let us choose $\mathbf{B} = B\mathbf{e}_z$, then we have

$$\Gamma_{\alpha\gamma} = \frac{k}{v_g}(i\omega - \frac{1}{\tau_{\mathrm{tr}}(\epsilon_k)})\left(\delta_{\alpha\gamma} + \epsilon_{\alpha z\gamma}\frac{\omega_c(\epsilon_k)}{i\omega - \frac{1}{\tau_{\mathrm{tr}}(\epsilon_k)}}\right), \qquad \omega_c(\epsilon) = \frac{eBv_g^2}{\epsilon c}. \tag{2.23}$$

The current density is then

$$j^\alpha = e^2\sum_k \frac{\partial f_0}{\partial \epsilon_k}k^\gamma\Gamma^{-1}_{\gamma\beta}E^\beta v_k^\alpha, \tag{2.24}$$

and using the definition $j^\alpha = \sigma_{\alpha\beta}E^\beta$ we get the conductance

$$\sigma_{\alpha\beta} = e^2 \sum_k \frac{\partial f_0}{\partial \epsilon_k} k^\gamma \Gamma^{-1}_{\gamma\beta} v_k^\alpha = e^2 \sum_k \frac{\partial f_0}{\partial \epsilon_k} k^\gamma \Gamma^{-1}_{\gamma\beta} \frac{v}{k} k^\alpha \tag{2.25}$$

Since both the Fermi function at equilibrium and the matrix Γ only depend on the absolute value of k, the the angular part of the integral is only concerned with the expression $k^\alpha k^\gamma$, but in both two and three dimensions, this angular integral vanishes for $\alpha \neq \gamma$, so we may write $k^\alpha k^\gamma = \delta_{\alpha\gamma}\frac{k^2}{d}$, where d is the dimension, which can be seen by considering the trace. Thus

$$\begin{aligned}\sigma_{\alpha\beta} &= e^2 \sum_k \frac{\partial f_0}{\partial \epsilon_k} \Gamma^{-1}_{\alpha\beta} \frac{v}{k} \frac{k^2}{d} \\ &= \frac{e^2 v_g^2}{d} \sum_k \frac{\partial f_0}{\partial \epsilon_k} \frac{1}{i\omega - \frac{1}{\tau_{\mathrm{tr}}(\epsilon_k)}} \left(\begin{pmatrix} 1 & 0 \\ 0 & 1 \end{pmatrix} + \frac{\omega_c(\epsilon_k)}{i\omega - \frac{1}{\tau_{\mathrm{tr}}(\epsilon_k)}} \begin{pmatrix} 0 & -1 \\ 1 & 0 \end{pmatrix} \right)^{-1}_{\alpha\beta}.\end{aligned} \tag{2.26}$$

From this we get for $\omega = 0$

$$\sigma_{xx} = -\frac{e^2 v_g^2}{d} \sum_k \frac{\partial f_0}{\partial \epsilon_k} \frac{\tau_{\mathrm{tr}}(\epsilon_k)}{1 + \Big(\omega_c(\epsilon_k)\tau_{\mathrm{tr}}(\epsilon_k)\Big)^2} = \int \mathrm{d}\epsilon \left(-\frac{\partial f_0}{\partial \epsilon} \right) \frac{e^2 v_g^2 \tau_{\mathrm{tr}}(\epsilon)\nu(\epsilon)}{d} \frac{1}{1 + \Big(\omega_c(\epsilon)\tau_{\mathrm{tr}}(\epsilon)\Big)^2}, \tag{2.27}$$

$$\sigma_{xy} = -\frac{e^2 v_g^2}{d} \sum_k \frac{\partial f_0}{\partial \epsilon_k} \frac{\omega_c(\epsilon_k)\tau_{\mathrm{tr}}(\epsilon_k)^2}{1 + \Big(\omega_c(\epsilon_k)\tau_{\mathrm{tr}}(\epsilon_k)\Big)^2} = \int \mathrm{d}\epsilon \left(-\frac{\partial f_0}{\partial \epsilon} \right) \frac{e^2 v_g^2 \tau_{\mathrm{tr}}(\epsilon)\nu(\epsilon)}{d} \frac{\omega_c(\epsilon)\tau_{\mathrm{tr}}(\epsilon)}{1 + \Big(\omega_c(\epsilon)\tau_{\mathrm{tr}}(\epsilon)\Big)^2}. \tag{2.28}$$

At zero temperature this simplifies to

$$\sigma_{xx} = \sigma_0 \frac{1}{1 + \Big(\omega_c(\mu)\tau_{\mathrm{tr}}(\mu)\Big)^2}, \tag{2.29}$$

$$\sigma_{xy} = \sigma_0 \frac{\omega_c(\mu)\tau_{\mathrm{tr}}(\mu)}{1 + \Big(\omega_c(\mu)\tau_{\mathrm{tr}}(\mu)\Big)^2} \tag{2.30}$$

For the disorder potential introduced in Eq. (2.7) one finds

$$\sigma_0 = \frac{e^2 v_g^2}{d} \tau_{\mathrm{tr}}(\epsilon)\nu(\epsilon) = \frac{2e^2 v_g^2 \hbar}{n_{\mathrm{imp}} u_0^2 \pi}. \tag{2.31}$$

2.1.2 Summary

The semi-classical Boltzmann equation was one of the earliest theories, that could connect microscopic details, like the band structure of a system, with macroscopic, measurable quantities like the conductivity. In this section we have introduced this semi-classical Boltzmann equation and shown its application to graphene in a non-quantizing perpendicular magnetic field. One obtains the conductivity shown in Eqs. (2.29), (2.30). This result, combined with the perturbative calculation of the same quantity performed in Sec. 2.2.5 will be used in Chapter 5 to describe the magnetoresistance of a graphene Corbino disk at low temperatures. The special properties of the Corbino geometry are discussed in Sec. 3.2. A special limit of the Boltzmann equation is the hydrodynamic description of collective modes in graphene at elevated temperatures discussed in Sec. 2.4, which is applied to the same graphene Corbino disk at elevated temperatures in Chapter 6.

2.2 Perturbation theory

Transport measurements, that are performed in samples of mesoscopic size are not sensitive to the individual motion of electrons and holes in the system, but only to collective properties. In the systems considered in this section, the Coulomb interaction between electrons and the scattering from random impurities, that are always present in any sample, is considered to be weak. In this limit, one can essentially perform an expansion in small parameters related to the interaction and disorder scattering. To this end, one introduces Green's function, which are discussed in this section. We summarize the general properties of Green's functions and how to incorporate weak disorder scattering and weak electron-electron interaction. We also reproduce, how the linear response conductance is found in this formalism and what it looks like in monolayer graphene with a perpendicular magnetic field in particular. Since we will focus on the Corbino geometry (Sec. 3.2) later on, we restrict ourselves to the σ_{xx} component of the conductivity tensor.

2.2.1 Many-body Green's functions

In order to describe mesoscopic properties of weakly interacting electrons in mono- or bilayer graphene we use a diagrammatic Green's functions approach. Following Ref. [10] we here reproduce the most important results adapted to our needs.

The many body Green's function $\check{G}(\mathbf{r}_1, t_1; \mathbf{r}_2, t_2)$ is defined via

$$G_{ij}(\mathbf{r}_1, t_1; \mathbf{r}_2, t_2) = -i \left\langle \phi_0 | \mathcal{T} \hat{\Psi}_i(\mathbf{r}_1, t_1) \hat{\Psi}_j^\dagger(\mathbf{r}_2, t_2) | \phi_0 \right\rangle, \tag{2.32}$$

with the time ordering operator $\mathcal{T}$ acting according to

$$\mathcal{T} \hat{\Psi}_i(\mathbf{r}_1, t_1) \hat{\Psi}_j^\dagger(\mathbf{r}_2, t_2) = \Theta(t_1 - t_2) \hat{\Psi}_i(\mathbf{r}_1, t_1) \hat{\Psi}_j^\dagger(\mathbf{r}_2, t_2) - \Theta(t_2 - t_1) \hat{\Psi}_j^\dagger(\mathbf{r}_2, t_2) \hat{\Psi}_i(\mathbf{r}_1, t_1). \tag{2.33}$$

The indices i, j can in general label any matrix structure of the free Hamiltonian, in the case of monolayer graphene they will specifically label the sublattice space. For bilayer graphene they could either label the full sublattice and layer space and thus run over $A1$, $A2$, $B1$ and $B2$ if one uses the full 4×4 Hamiltonian, or run over $A1$ and $B2$ only for the effective low energy Hamiltonian discussed in Sec. 1.2.

Similarly one defines the retarded (R) and advanced (A) many-body Green's functions

$$G_{ij}^{(R)}(\mathbf{r}_1, t_1; \mathbf{r}_2, t_2) = -i\theta(t_1 - t_2) \left\langle \phi_0 | \left[\hat{\Psi}_i(\mathbf{r}_1, t_1) \hat{\Psi}_j^\dagger(\mathbf{r}_2, t_2) \right]_{B/F} | \phi_0 \right\rangle, \tag{2.34}$$

$$G_{ij}^{(A)}(\mathbf{r}_1, t_1; \mathbf{r}_2, t_2) = i\theta(t_2 - t_1) \left\langle \phi_0 | \left[\hat{\Psi}_i(\mathbf{r}_1, t_1) \hat{\Psi}_j^\dagger(\mathbf{r}_2, t_2) \right]_{B/F} | \phi_0 \right\rangle, \tag{2.35}$$

$$\left[\hat{A}, \hat{B} \right]_{F/B} = \begin{cases} \left[\hat{A}, \hat{B} \right] = \hat{A}\hat{B} - \hat{B}\hat{A}, & \text{bosons(B)} \\ \left\{ \hat{A}, \hat{B} \right\} = \hat{A}\hat{B} + \hat{B}\hat{A}, & \text{fermions(F)} \end{cases}. \tag{2.36}$$

The field operator $\hat{\mathbf{\Psi}}$ is defined as

$$\hat{\mathbf{\Psi}}(\mathbf{r}, t) = \sum_\alpha \mathbf{F}_\alpha(\mathbf{r}) \hat{a}_\alpha(t), \tag{2.37}$$

where α labels single-particle states and $\mathbf{F}_\alpha(\mathbf{r})$ are the eigenstates of the single-particle Hamiltonian, which in our case will have a vector structure in sublattice space labeled by indices $i, j, ...$, thus $\check{G}$ is a matrix with entries labeled by i, j. For monolayer graphene without a magnetic field, one could use Eq. (1.8), in which case the label $\alpha = (s, \mathbf{k})$ would label the eigenstates and both $\hat{\mathbf{\Psi}}$ and $\mathbf{F}_\alpha(\mathbf{r})$ are vectors in sublattice space.

In the interaction representation used in perturbation theory, operators evolve with the free dynamics determined by the non-interacting part of the Hamiltonian. Thus the time dependence of the field operators is fully determined by the eigenenergies of the single particle Hamiltonian and one finds the expressions

$$\hat{\Psi}(\mathbf{r}, t) = \sum_\alpha \mathbf{F}_\alpha(\mathbf{r})\hat{a}_\alpha e^{-i\varepsilon_\alpha t}, \quad \hat{\mathbf{\Psi}}^\dagger(\mathbf{r}, t) = \sum_\alpha \mathbf{F}^H_\alpha(\mathbf{r})\hat{a}^\dagger_\alpha e^{+i\varepsilon_\alpha t}, \tag{2.38}$$

where the superscript $()^H$ notes the conjugate transpose. Restricting ourselves to a free problem, where no interacting part of the Hamiltonian is present, the ground state $|\phi_0\rangle$ moreover consists of all single particle states below the Fermi level, thus we find generally

$$\check{G}^{(0)(R/A)}(\mathbf{r}_1; \mathbf{r}_2; \omega) = \sum_\alpha \frac{\mathbf{F}_\alpha(\mathbf{r}_1)\mathbf{F}^H_\alpha(\mathbf{r}_2)}{\omega - \varepsilon_\alpha \pm i0} = \sum_\alpha \mathbf{F}_\alpha(\mathbf{r}_1)\mathbf{F}^H_\alpha(\mathbf{r}_2)G^{(0)(R/A)}_\alpha(\omega), \tag{2.39}$$

where $+i0$ applies for the retarded case, and $-i0$ for the advanced.

2.2.2 Matsubara Green's function

At finite temperature T the expectation value of an operator $\hat{A}$ in the grand canonical ensemble is given by

$$\langle \hat{A} \rangle = \sum_n \frac{e^{-\beta E'_n}}{Z_G}\langle n|\hat{A}|n\rangle = \sum_n \langle n|e^{\beta(\Omega - \hat{H} + \mu\hat{N})}\hat{A}|n\rangle = \mathrm{Tr} e^{\beta(\Omega - \hat{H} + \mu\hat{N})}\hat{A}, \tag{2.40}$$

$$Z_G = \mathrm{Tr} e^{-\beta(\hat{H} - \mu\hat{N})} = \exp(-\beta\Omega), \tag{2.41}$$

with $\beta = 1/T$, where n labels the eigenstates and eigenenergies E_n of the Hamiltonian $\hat{H}$ and $E'_n = E_n - \mu N_n$. The grand canonical potential is obtained as $\Omega = \log(Z_G)/\beta$. Thus we define the imaginary time $t = -i\tau$ with $\tau \in [0, \beta]$ and the temperature-dependent, imaginary time Matsubara Green's function

$$\mathcal{G}_{ij}(\mathbf{r}_1, \tau_1; \mathbf{r}_2, \tau_2) = -\left\langle \mathcal{T}_\tau \Psi_{MH,i}(\mathbf{r}_1, \tau_1)\bar{\Psi}_{MH,j}(\mathbf{r}_2, \tau_2)\right\rangle, \tag{2.42}$$

$$\Psi_{MH}(\mathbf{r}, \tau) = e^{\hat{H}\tau}\hat{\Psi}(\mathbf{r})e^{-\hat{H}\tau}, \tag{2.43}$$

where $\mathcal{T}_\tau$ is the imaginary time ordering operator with

$$\mathcal{T}_\tau \Psi_{MH}(\tau_1)\bar{\Psi}_{MH}(\tau_2) = \begin{cases} \Psi_{MH}(\tau_1)\bar{\Psi}_{MH}(\tau_2) & \tau_1 > \tau_2, \\ \mp\bar{\Psi}_{MH}(\tau_2)\Psi_{MH}(\tau_1) & \tau_1 < \tau_2 \end{cases} \tag{2.44}$$

and the upper/lower sign holds for fermions/bosons respectively. The most important property of the Matsubara Green's function is that analytical continuations directly gives the retarded, real time Green's function

$$G^R(\omega) = \mathcal{G}(i\omega_n \to \omega + i\epsilon). \tag{2.45}$$

Using a new, imaginary time interaction representation, where operators follow the free Hamiltonian we define

$$\Psi_{M,0}(\mathbf{r},\tau) = \exp(H_0\tau)\Psi(\mathbf{r})\exp(-H_0\tau), \tag{2.46}$$

which leads to

$$\mathbf{\Psi}_{M,0}(\mathbf{r},\tau) = \sum_\alpha \mathbf{F}_\alpha(\mathbf{r})a_\alpha(\tau) = \sum_\alpha \mathbf{F}_\alpha(\mathbf{r})a_\alpha e^{-\xi_\alpha\tau}, \tag{2.47}$$

$$\bar{\mathbf{\Psi}}_{M,0}(\mathbf{r},\tau) = \sum_\alpha \mathbf{F}^H_\alpha(\mathbf{r})a^\dagger_\alpha e^{\xi_\alpha\tau}, \tag{2.48}$$

$$\xi_\alpha = \varepsilon_\alpha - \mu, \tag{2.49}$$

and rewrite everything in terms of expectation values

$$\langle\hat{A}\rangle_0 = \mathrm{Tr}\left(e^{\beta(\Omega_0-\mathcal{H}_0)}\right). \tag{2.50}$$

We will further use

$$\langle a^\dagger_\alpha a_\beta\rangle_0 = \delta_{\alpha\beta}\begin{cases} n_F(\xi_\alpha), & \text{fermionic} \\ n_B(\xi_\alpha), & \text{bosonic} \end{cases}, \tag{2.51}$$

and define a Fourier transform to imaginary frequencies $i\omega_n$

$$\mathcal{G}(i\omega_n) = \int_0^\beta \mathrm{d}\tau e^{i\omega_n\tau}\mathcal{G}(\tau), \tag{2.52}$$

$$\mathcal{G}(\tau) = \frac{1}{\beta}\sum_n e^{-i\omega_n\tau}\mathcal{G}(i\omega_n), \tag{2.53}$$

where the discrete frequencies are

$$\omega_n = \begin{cases} \frac{2n\pi}{\beta}, & \text{bosons}, \\ \frac{(2n+1)\pi}{\beta}, & \text{fermions}. \end{cases} \tag{2.54}$$

Then we can express the Matsubara Green's function of free particles with the Hamiltonian

$$\breve{H}_0 = \sum_\alpha \xi_\alpha a^\dagger_\alpha a_\alpha \tag{2.55}$$

as

$$\mathcal{G}^{(0)}_{ij}(\mathbf{r}_1,\mathbf{r}_2;i\omega_n) = \sum_\alpha \frac{F_{\alpha,i}F^*_{\alpha,j}}{i\omega_n - \xi_\alpha} \tag{2.56}$$

for both fermions and bosons.

Monolayer graphene

We consider the non-interacting many-body Hamiltonian introduced in Eq. (1.1), which leads to the single particle Hamiltonian (1.3). From this it is clear, that the Green's function is actually a 2×2 matrix in sublattice space. In all situations we consider, we can restrict ourselves to one valley $\xi = +$. As shown in Sec. 1.1 we then obtain the eigenenergies and states (1.8) for vanishing magnetic field and thus the Matsubara Green's function

$$\mathcal{G}^{(0)}(\mathbf{r}_1;\mathbf{r}_2;i\omega) = \sum_{s,\mathbf{k}} \frac{\mathbf{F}_{s,\mathbf{k}}(\mathbf{r}_1)\mathbf{F}^H_{s,\mathbf{k}}(\mathbf{r}_2)}{i\omega - \varepsilon_{s,\mathbf{k}}} = \sum_{s,\mathbf{k}} \mathbf{F}_{s,\mathbf{k}}(\mathbf{r}_1)\mathbf{F}^H_{s,\mathbf{k}}(\mathbf{r}_2)\mathcal{G}^{(0)}_{s,\mathbf{k}}(i\omega). \tag{2.57}$$

For finite magnetic field we use (1.10) and obtain

$$\mathcal{G}^{(0)}(\mathbf{r}_1;\mathbf{r}_2;i\omega) = \sum_{n,k_y} \frac{\mathbf{F}_{n,k_y}(\mathbf{r}_1)\mathbf{F}^H_{n,k_y}(\mathbf{r}_2)}{i\omega - \varepsilon_{n,k_y}} = \sum_{n,k_y} \mathbf{F}_{n,k_y}(\mathbf{r}_1)\mathbf{F}^H_{n,k_y}(\mathbf{r}_2)\mathcal{G}^{(0)}_{n,k_y}(i\omega) \tag{2.58}$$

instead.

2.2.3 Interacting systems

The very fundament of the diagrammatic approach is the Gell-Mann and Low theorem, which relates the ground state $|\phi_0\rangle$ of the interacting theory to that of the non-interacting one $|0\rangle$. It states that

$$\begin{aligned} iG_{i,j}(\mathbf{r}_1,t_1;\mathbf{r}_2,t_2) &= \left\langle \phi_0 | \mathcal{T}\hat{\Psi}_i(\mathbf{r}_1,t_1)\hat{\Psi}^\dagger_j(\mathbf{r}_2,t_2)|\phi_0\right\rangle \\ &= \langle 0|\hat{\mathcal{S}}|0\rangle^{-1} \left\langle 0 \left| \mathcal{T}\left[\exp\left(-i\int_{-\infty}^{\infty} \mathrm{d}t' \hat{U}_I(t')\right)\hat{\Psi}_{i,I}(\mathbf{r}_1,t_1)\hat{\Psi}^\dagger_{j,I}(\mathbf{r}_2,t_2)\right]\right| 0\right\rangle . \end{aligned} \tag{2.59}$$

The field operators are given by

$$\hat{\mathbf{\Psi}}_I(\mathbf{r},t) = \sum_\alpha \mathbf{F}_\alpha(\mathbf{r})\hat{a}_\alpha e^{-i\varepsilon_\alpha t}, \quad \hat{\mathbf{\Psi}}^\dagger_I(\mathbf{r},t) = \sum_\alpha \mathbf{F}^H_\alpha(\mathbf{r})\hat{a}^\dagger_\alpha e^{+i\varepsilon_\alpha t}, \tag{2.60}$$

i.e. they are the same as in the non-interacting theory. The interaction Hamiltonian we consider is diagonal in sublattice space

$$\hat{U}_I(t) = \frac{1}{2}\int \mathrm{d}t'\delta(t-t')\int \mathrm{d}^2r\mathrm{d}^2r' \hat{\mathbf{\Psi}}^\dagger_I(\mathbf{r},t)\hat{\mathbf{\Psi}}^\dagger_I(\mathbf{r}',t')\check{V}(\mathbf{r}-\mathbf{r}')\hat{\mathbf{\Psi}}_I(\mathbf{r}',t')\hat{\mathbf{\Psi}}_I(\mathbf{r},t). \tag{2.61}$$

When expanding the exponential in Eq. (2.59) for a small parameter, we see, that we get non-interacting expectation values of combinations of several field operators, which can be rewritten by means of the Wick theorem. It turns out, that the factor $\langle 0|\hat{\mathcal{S}}|0\rangle^{-1}$ exactly cancels all non connected diagrams, so we only need to consider the connected ones. The corresponding expression for the Matsubara Green's function is

$$\mathcal{G}_{ij}(\mathbf{r}_1,\tau_1;\mathbf{r}_2,\tau_2) = -\frac{1}{\langle\mathcal{S}\rangle_0}\left\langle \mathcal{T}_\tau \mathcal{S}\Psi_{M,0,i}(\mathbf{r}_1,\tau_1)\bar{\Psi}_{M,0,j}(\mathbf{r}_2,\tau_2)\right\rangle_0, \tag{2.62}$$

$$\hat{\mathcal{S}} = \mathcal{T}_\tau \exp\left(-\int_0^\beta \mathrm{d}\tau \hat{U}_0(\tau)\right), \tag{2.63}$$

for an interaction Hamiltonian

$$\hat{U}_0(\tau) = \frac{1}{2}\int \mathrm{d}\tau' \delta(\tau-\tau') \int \mathrm{d}^2 r \mathrm{d}^2 r' \bar{\mathbf{\Psi}}_{M,0}(\mathbf{r},\tau)\bar{\mathbf{\Psi}}_{M,0}(\mathbf{r}',\tau')\check{V}(\mathbf{r}-\mathbf{r}')\mathbf{\Psi}_{M,0}(\mathbf{r}',\tau')\mathbf{\Psi}_{M,0}(\mathbf{r},\tau), \tag{2.64}$$

where the denominator again exactly cancels all non-connected diagrams.

2.2.4 Disordered systems

The existence of random impurities inside the mesoscopic samples plays an important role. Generally, the presence of a potential can be included via

$$\begin{aligned} iG_{i,j}(\mathbf{r}_1,t_1;\mathbf{r}_2,t_2) &= \left\langle \phi_0 | \mathcal{T}\hat{\Psi}_i(\mathbf{r}_1,t_1)\hat{\Psi}_j^\dagger(\mathbf{r}_2,t_2)|\phi_0\right\rangle \\ &= \langle 0|\hat{\mathcal{S}}|0\rangle^{-1}\left\langle 0\left|\mathcal{T}\left[\exp\left(-i\int_{-\infty}^{\infty}\mathrm{d}t'\hat{U}_I(t')\right)\hat{\Psi}_{i,I}(\mathbf{r}_1,t_1)\hat{\Psi}_{j,I}^\dagger(\mathbf{r}_2,t_2)\right]\right|0\right\rangle. \end{aligned} \tag{2.65}$$

$$\begin{aligned} \hat{U}_I(t) &= \int \mathrm{d}^2 r \hat{\mathbf{\Psi}}_I^\dagger(\mathbf{r},t)\check{V}(\mathbf{r})\hat{\mathbf{\Psi}}_I(\mathbf{r},t) \\ &= \sum_{\alpha\beta}\underbrace{\int \mathrm{d}^2 r \mathbf{F}_\alpha^H(\mathbf{r})\check{V}(\mathbf{r})\mathbf{F}_\beta(\mathbf{r})}_{V_{\alpha\beta}}\hat{a}_\alpha^\dagger(t)\hat{a}_\beta(t). \end{aligned} \tag{2.66}$$

Since these impurities are randomly distributed, only the disorder averaged value of quantities can be observed. We note disorder averaging by

$$\langle f(\mathbf{r}_i)\rangle = \frac{1}{V}\int \mathrm{d}^2 r_i f(\mathbf{r}_i). \tag{2.67}$$

We consider scattering off of a random short range potential without spin or valley mixing, i.e.

$$\check{V}(\mathbf{r}) = V(\mathbf{r})\check{\mathbb{1}} = u_0\sum_i \delta(\mathbf{r}-\mathbf{r}_i)\begin{pmatrix}1 & 0\\ 0 & 1\end{pmatrix}, \tag{2.68}$$

$$\langle V(\mathbf{r})V(\mathbf{r}')\rangle = \kappa\delta(\mathbf{r}-\mathbf{r}'), \tag{2.69}$$

where $\kappa = u_0^2 c_{\mathrm{imp}}$ When expanding the exponential under the assumption, that u_0 is small, we come across disorder averages of the form

$$\begin{aligned} &\left\langle \int \mathrm{d}^2 r \hat{\mathbf{\Psi}}_I^\dagger(\mathbf{r},t)\check{V}(\mathbf{r})\hat{\mathbf{\Psi}}_I(\mathbf{r},t)\right\rangle = \int \mathrm{d}^2 r \sum_j \hat{\Psi}_j^\dagger(\mathbf{r},t)\hat{\Psi}_j(\mathbf{r},t)\frac{u_0}{V}\sum_i \int \mathrm{d}^2 r_i \delta(\mathbf{r}-\mathbf{r}_i) \\ &= c_{\mathrm{imp}}u_0\int \mathrm{d}^2 r\sum_j \hat{\Psi}_j^\dagger(\mathbf{r},t)\hat{\Psi}_j(\mathbf{r},t), \end{aligned} \tag{2.70}$$

which simply amount to a shift of the total energy which we thus set to zero. Importantly we note, that translational invariance is restored after disorder averaging. We will restrict ourselves to the self consistent Born approximation, which can be represented by the following Dyson series for the disorder averaged Green's function $\langle G_{\alpha\beta}(\varepsilon)\rangle$ represented by a thick propagator, the free Green's function $G_{\alpha\beta}^{(0)}$ represented by a thin propagator and the self energy, represented as a blob

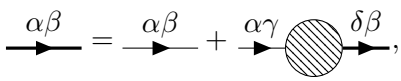

(2.71)

where the self energy in self consistent Born approximation is given by

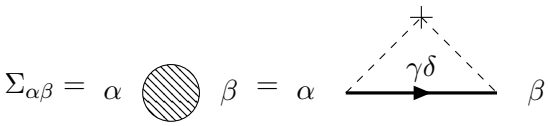

(2.72)

and disorder averaging is represented by

$$= \langle V_{\alpha\beta} V_{\gamma\delta} \rangle. \tag{2.73}$$

Here external indices are to be understood as belonging to the end of the Green's function, that would attach there. This is equivalent to the following expressions

$$\langle G_{\alpha\beta}(\varepsilon) \rangle = \delta_{\alpha\beta} G^{(0)}_{\alpha}(\varepsilon) + G^{(0)}_{\alpha} \sum_{\delta} \Sigma_{\alpha\delta} \langle G_{\delta\beta}(\varepsilon) \rangle, \tag{2.74}$$

$$G^{(0)}_{\alpha\beta}(\varepsilon) = \delta_{\alpha\beta} G^{(0)}_{\alpha}(\varepsilon), \tag{2.75}$$

$$\Sigma_{\alpha\beta} = \sum_{\gamma,\delta} \langle V_{\alpha\gamma} V_{\delta\beta} \rangle \langle G_{\gamma\delta}(\varepsilon) \rangle, \tag{2.76}$$

where Greek indices label the eigenstates of the free Hamiltonian.

2.2.5 Kubo formula for conductivity

The conductivity σ of a system is defined as the linear response of the current to an external electric field $\mathbf{E}$

$$j_a(\mathbf{r}, \varepsilon) = \int \mathrm{d}^2 r' \sigma_{ab}(\mathbf{r}, \mathbf{r}'; \varepsilon) E_b(\mathbf{r}', \varepsilon), \tag{2.77}$$

where $a, b = x, y$ label the real space coordinate. This can be found by means of the Kubo formula of linear response. We consider a perturbation of the form

$$\hat{H} = \hat{H}_0 + \hat{A} F(t), \tag{2.78}$$

where F is a generalized force coupling to an operator $\hat{A}$. Then one finds, that the change to an observable $\hat{B}$ to linear order is given by

$$\delta B(t) = \int \mathrm{d}t' \mathcal{D}^R_{BA}(t, t') F(t'), \tag{2.79}$$

$$D^R_{BA}(t, t') = -i\Theta(t - t') \langle \phi_0 | \left[\hat{B}(t), \hat{A}(t') \right] | \phi_0 \rangle, \tag{2.80}$$

where $[A, B]$ is the commutator and the index R marks the retarded nature of this generalized Green's function.

Let us start with the case of monolayer graphene. Then, the bare problem has the Hamiltonian

$$H_0 = \int \mathrm{d}^2 r \hat{\mathbf{\Psi}}^\dagger(r) \frac{v_g}{\hbar} \xi \begin{pmatrix} 0 & \hat{\pi}^\dagger \\ \hat{\pi} & 0 \end{pmatrix} \hat{\mathbf{\Psi}}(r). \tag{2.81}$$

An external field is again introduced by replacing $\mathbf{p} \to \mathbf{p} - e\mathbf{A}/c = \mathbf{p}^{\mathrm{kin}}$, in which case we find the new Hamiltonian

$$\begin{aligned} H &= \int \mathrm{d}^2 r \hat{\mathbf{\Psi}}^\dagger(r) \frac{v_g}{\hbar} \xi \begin{pmatrix} 0 & \xi(-i\hbar\partial_x - \frac{e}{c}A_x) - i(-i\hbar\partial_y - \frac{e}{c}A_y) \\ \xi(-i\hbar\partial_x - \frac{e}{c}A_x) + i(-i\hbar\partial_y - \frac{e}{c}A_y) & 0 \end{pmatrix} \hat{\mathbf{\Psi}}(r) \\ &= H_0 + \int \mathrm{d}^2 r \frac{v_g}{\hbar} \frac{-e}{c} \left(A_x \hat{\mathbf{\Psi}}^\dagger(r) \sigma_x \hat{\mathbf{\Psi}}(r) - A_y \xi \hat{\mathbf{\Psi}}^\dagger(r) \sigma_y \hat{\mathbf{\Psi}}(r) \right) \\ &= H_0 - \frac{1}{c} \int \mathrm{d}^2 r \mathbf{j}(\mathbf{r}) \mathbf{A}(\mathbf{r}), \end{aligned} \tag{2.82}$$

$$j_{x/y}(\mathbf{r}) = e\mathbf{\Psi}^\dagger(\mathbf{r}) v_{x/y} \mathbf{\Psi}(\mathbf{r}), \quad v_{x/y} = \frac{v_g}{\hbar} \sigma_{x/y}, \tag{2.83}$$

where the vector $\sigma_{x/y}$ is one of the first two Pauli matrices σ_x and σ_y. Then we find from the Kubo formula

$$\delta j_a(\mathbf{r}, t) = \frac{i}{c} \int_{-\infty}^{t} \mathrm{d}t' \int \mathrm{d}^2 r' \langle \phi_0 | [j_a(\mathbf{r}, t), j_b(\mathbf{r}', t')] | \phi_0 \rangle A_b(\mathbf{r}', t'). \tag{2.84}$$

With the gauge $\mathbf{E} = -1/c\partial_t \mathbf{A}$ we can perform a Fourier transform and find

$$\sigma_{ab}(\mathbf{r}, \mathbf{r}'; \omega) = \frac{-1}{i\omega} D^R_{jj;ab}(\mathbf{r}, \mathbf{r}'; \omega) = \frac{1}{i\omega} \left\{ i \int_0^\infty \mathrm{d}t e^{i\omega t} \langle \phi_0 | [j_a(\mathbf{r}, t), j_b(\mathbf{r}', 0)] | \phi_0 \rangle \right\rangle \tag{2.85}$$

with the retarded current-current correlator

$$D^R_{jj;ab}(\mathbf{r}, t; \mathbf{r}' t') = -i\Theta(t - t') \langle \phi_0 | \left[j_a(\mathbf{r}, t), j_b(\mathbf{r}', t') \right] | \phi_0 \rangle. \tag{2.86}$$

Making use of analytical continuation we instead practically calculate

$$\mathcal{D}_{jj;ab}(\mathbf{r}, \tau; \mathbf{r}', \tau') = -\langle \mathcal{T}_\tau j_a(\mathbf{r}, \tau) j_b(\mathbf{r}', \tau') \rangle. \tag{2.87}$$

The diagrammatic series can most easily be developed by first taking a look at the non-interacting result

$$\begin{aligned} \mathcal{D}^{(0)}_{jj;ab}(\mathbf{r}, \tau; \mathbf{r}', \tau') &= -\langle \mathcal{T}_\tau j_a(\mathbf{r}, \tau) j_b(\mathbf{r}', \tau') \rangle_0 \\ &= -e^2 v_{a,ij} v_{b,kl} \langle \mathcal{T}_\tau \bar{\Psi}_i(\mathbf{r}, \tau) \Psi_j(\mathbf{r}, \tau) \bar{\Psi}_k(\mathbf{r}', \tau') \Psi_l(\mathbf{r}', \tau') \rangle_0 \\ &= +e^2 v_{a,ij} v_{b,kl} \mathcal{G}_{jk}(\mathbf{r}, \tau; \mathbf{r}', \tau') \mathcal{G}_{li}(\mathbf{r}', \tau'; \mathbf{r}, \tau), \end{aligned} \tag{2.88}$$

$$\mathcal{D}^{(0)}_{jj;ab}(\mathbf{r}, \mathbf{r}'; \omega_m) = e^2 \frac{1}{\beta} \sum_{\varepsilon_n} \mathrm{Tr} \left(v_a \mathcal{G}^{(0)}(\mathbf{r}, \mathbf{r}'; \varepsilon_n + \omega_m) v_b \mathcal{G}^{(0)}(\mathbf{r}', \mathbf{r}; \varepsilon_n) \right), \tag{2.89}$$

where the trace runs over sublattice indices. Interaction or disorder effects are included by substituting $\mathcal{G}^{(0)}$ by the full $\mathcal{G}$ and by replacing one velocity vertex v_b by a vertex operator Γ_b, i.e.

$$\mathcal{D}_{jj;ab}(\mathbf{r}, \mathbf{r}'; \omega_m) = e^2 \frac{1}{\beta} \sum_{\varepsilon_n} \mathrm{Tr} \left(v_a \mathcal{G}(\mathbf{r}, \mathbf{r}'; \varepsilon_n + \omega_m) \Gamma_b(\varepsilon_n + \omega_m, \varepsilon_n) \mathcal{G}(\mathbf{r}', \mathbf{r}; \varepsilon_n) \right). \tag{2.90}$$

The Matsubara sum can be performed under the assumption, that Γ_b is analytical everywhere, except for the two branch cuts of the product of Green's functions. Then we can consider

$$\begin{aligned} S(i\omega_m) &= \frac{1}{\beta}\sum_{i\varepsilon_n} f(i\varepsilon_n + i\omega_m, i\varepsilon_n) = -\int_{\mathcal{C}} \frac{\mathrm{d}z}{2\pi i} n_F(z) f(z+i\omega_m, z) \\ &= \int_{-\infty}^{\infty} \frac{\mathrm{d}\epsilon}{-2\pi i} \Big[n_F(\epsilon) \Big(f(\epsilon + i\omega_m, \epsilon + i0) - f(\epsilon + i\omega_m, \epsilon - i0) \Big) \\ &\quad + n_F(\epsilon - i\omega_m) \Big(f(\epsilon + i0, \epsilon - i\omega_m) - f(\epsilon - i0, \epsilon - i\omega_m) \Big) \Big]. \end{aligned} \tag{2.91}$$

After analytical continuation we find

$$\begin{aligned} S^R(\omega) &= S(i\omega_m \to \omega + i0) \\ &= \int_{-\infty}^{\infty} \frac{\mathrm{d}\epsilon}{-2\pi i} n_F(\epsilon) \Big(f(z+\omega+i0, \epsilon+i0) - f(z+\omega+i0, \epsilon-i0) \\ &\quad + f(\epsilon+i0, \epsilon-\omega-i0) - f(\epsilon-i0, \epsilon-\omega-i0) \Big). \end{aligned} \tag{2.92}$$

Applying this to the conductivity we find

$$\begin{aligned} \sigma_{ab}(\mathbf{r}, \mathbf{r}'; \omega) = \frac{-1}{i\omega} \frac{e^2}{-i} \int_{-\infty}^{\infty} \frac{\mathrm{d}\epsilon}{2\pi} n_F(\epsilon) \Big\{ &\mathrm{Tr} \Big(v_a G^R(\mathbf{r}, \mathbf{r}'; \epsilon+\omega) \Gamma_b(\epsilon+\omega, \epsilon) \Big[G^R(\mathbf{r}', \mathbf{r}; \epsilon) - G^A(\mathbf{r}', \mathbf{r}; \epsilon) \Big] \Big) \\ + &\mathrm{Tr} \Big(v_a \Big[G^R(\mathbf{r}, \mathbf{r}'; \epsilon) - G^A(\mathbf{r}, \mathbf{r}'; \epsilon) \Big] \Gamma_b(\epsilon, \epsilon-\omega) G^A(\mathbf{r}', \mathbf{r}; \epsilon-\omega) \Big) \Big\}. \end{aligned} \tag{2.93}$$

To find the static conductivity we only need the integral up to linear order in ω. For this we shift the integration in the second part, expand to linear order in ω and then get

$$\begin{aligned} \sigma_{ab}(\mathbf{r}, \mathbf{r}'; \omega) \approx \frac{-e^2}{\omega} \int_{-\infty}^{\infty} \frac{\mathrm{d}\epsilon}{2\pi} \Big\{ &n_F(\epsilon) \mathrm{Tr} \Big(v_a G^R(\mathbf{r}, \mathbf{r}'; \epsilon) \Gamma_b(\epsilon, \epsilon) \Big[G^R(\mathbf{r}', \mathbf{r}; \epsilon) - G^A(\mathbf{r}', \mathbf{r}; \epsilon) \Big] \Big) \\ + &\Big(n_F(\epsilon) + \omega n_F'(\epsilon) \Big) \mathrm{Tr} \Big(v_a \Big[G^R(\mathbf{r}, \mathbf{r}'; \epsilon) - G^A(\mathbf{r}, \mathbf{r}'; \epsilon) \Big] \Gamma_b(\epsilon, \epsilon) G^A(\mathbf{r}', \mathbf{r}; \epsilon) \Big) \Big\}. \end{aligned} \tag{2.94}$$

What is measured is usually the real part of the conductivity. Using $\mathrm{Re}\, G^R = \mathrm{Re}\, G^A$, $\mathrm{Im}\, G^R = -\mathrm{Im}\, G^A$ we then find

$$\mathrm{Re}\, \sigma_{ab}(\mathbf{r}, \mathbf{r}'; \omega) \approx -e^2 \int_{-\infty}^{\infty} \frac{\mathrm{d}\epsilon}{2\pi} n_F'(\epsilon) \mathrm{Tr} \Big(v_a \Big[G^R(\mathbf{r}, \mathbf{r}'; \epsilon) - G^A(\mathbf{r}, \mathbf{r}'; \epsilon) \Big] \Gamma_b(\epsilon, \epsilon) G^A(\mathbf{r}', \mathbf{r}; \epsilon) \Big). \tag{2.95}$$

For the sake of clarity, let us restrict ourselves to $a = b = x$. In this case v_x is real and we assume, that Γ_x stays real as well. The we finally find the expression

$$\mathrm{Re}\, \sigma_{xx}(\mathbf{r}, \mathbf{r}', 0) = \frac{e^2}{\pi} \int_{-\infty}^{\infty} \mathrm{d}\epsilon \left(-\frac{\mathrm{d}n_F(\epsilon)}{\mathrm{d}\epsilon} \right) \sigma_{xx}(\mathbf{r}, \mathbf{r}'; \epsilon), \tag{2.96}$$

$$\sigma_{xx}(\mathbf{r}, \mathbf{r}'; \epsilon) = \mathrm{Tr} \Big(v_x\, \mathrm{Im}\, G^R(\mathbf{r}, \mathbf{r}'; \epsilon) \Gamma_x(\epsilon, \epsilon)\, \mathrm{Im}\, G^R(\mathbf{r}', \mathbf{r}; \epsilon) \Big), \tag{2.97}$$

which can be re expressed in the eigenbasis as

$$\sigma_{xx}(\mathbf{r},\mathbf{r}';\epsilon) = \sum_{\alpha\beta} v^x_{\beta\alpha}(\mathbf{r}) \operatorname{Im} G^R_\alpha(\epsilon)\Gamma^x_{\alpha\beta}(\mathbf{r}')(\epsilon,\epsilon) \operatorname{Im} G^R_\beta(\epsilon), \tag{2.98}$$

$$v^x_{\beta\alpha}(\mathbf{r}) = \mathbf{F}^H_\beta(\mathbf{r}) v_x \mathbf{F}_\alpha(\mathbf{r}). \tag{2.99}$$

After performing the disorder averaging, which is denoted by angled brackets, translational invariance is restored, i.e. $\langle\sigma_{ab}(\mathbf{r},\mathbf{r}')\rangle = \langle\sigma_{ab}(\mathbf{r}-\mathbf{r}')\rangle$. We will assume, that σ means the disorder averaged conductivity from here on. Usually we are interested in the response to a homogeneous electric field, i.e.

$$\sigma_{xx}(\mathbf{q}=0;0) = \int \mathrm{d}^2(r-r')\frac{e^2}{\pi}\int_{-\infty}^{\infty}\mathrm{d}\epsilon\left(-\frac{\mathrm{d}n_F(\epsilon)}{\mathrm{d}\epsilon}\right)\sigma_{xx}(\mathbf{r}-\mathbf{r}';\epsilon). \tag{2.100}$$

Since translational invariance is restored in the end, but the only terms that depend on the coordinate are the vertices, we can Fourier transform once:

$$\sigma_{xx}(\mathbf{r},\mathbf{r}') = f(\mathbf{r})g(\mathbf{r}') = \int \frac{(\mathrm{d}^2q)(\mathrm{d}^2p)}{(2\pi)^4} e^{i\mathbf{qr}} e^{i\mathbf{pr}'} f(q)g(p). \tag{2.101}$$

Because the result may only depend on $\mathbf{r}-\mathbf{r}'$ this requires $\mathbf{p}=-\mathbf{q}$ and thus we especially find

$$\sigma_{xx}(\mathbf{q}=0;\epsilon) = \left\langle \sum_{\alpha\beta} v^x_{\beta\alpha}(\mathbf{q}=0) \operatorname{Im} G^R_\alpha(\epsilon)\Gamma^x_{\alpha\beta}(\mathbf{q}=0)(\epsilon,\epsilon) \operatorname{Im} G^R_\beta(\epsilon)\right\rangle, \tag{2.102}$$

$$v^x_{\beta\alpha}(\mathbf{q}=0) = \int \mathrm{d}^2 r \mathbf{F}^H_\beta(\mathbf{r}) v_x \mathbf{F}^(_\alpha\mathbf{r}) = v^x_{\beta\alpha}. \tag{2.103}$$

This can be visualized as follows. The bare conductivity would look like

$\sigma_{xx} =$ 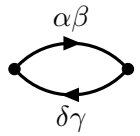

, (2.104)

where we use the bare velocity operator $v^x_{\delta\alpha}$ and the Green's functions obtained from the self consistent Born approximation. However, the Ward identity requires, that in order not to violate the continuity equation, we also have to include the corresponding graphs in the vertex, which we call Γ_x. This can be represented in the following way

$\sigma_{xx} =$ 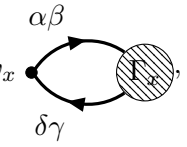

, (2.105)

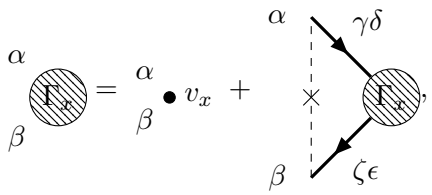

, (2.106)

i.e. vertex required due to the Ward identity is visually found, by inserting a bare velocity in the middle of the Green's function of the corresponding self energy.

Short range disorder in monolayer Graphene without magnetic field

Let us start by calculating the disorder induced conductivity in monolayer graphene without interaction effects and without a magnetic field. Since the chosen disorder is diagonal in the valley index, we can restrict ourselves to one valley and multiply by a factor of two in the very end. This is discussed in Ref. [56] under the label of "long-range scatterers". In this case eigenstates are labeled by $\alpha = (s, \mathbf{k})$ and we set $\xi = 1$. The first step is to calculate the disorder averaged Green's function in the self consistent Born approximation.

$$\langle G_{\alpha\beta}(\varepsilon)\rangle = \delta_{\alpha\beta} G^{(0)}_{\alpha}(\varepsilon) + G^{(0)}_{\alpha} \sum_{\delta} \Sigma_{\alpha\delta} \langle G_{\delta\beta}(\varepsilon)\rangle, \tag{2.107}$$

$$G^{(0)}_{\alpha\beta}(\varepsilon) = \delta_{\alpha\beta} G^{(0)}_{\alpha}(\varepsilon), \tag{2.108}$$

$$\Sigma_{\alpha\beta} = \sum_{\gamma,\delta} \langle V_{\alpha\gamma} V_{\delta\beta}\rangle \langle G_{\gamma\delta}(\varepsilon)\rangle, \tag{2.109}$$

where Greek indices label the eigenstates of the free Hamiltonian. First we recognize, that the most simple building block is the term

$$\Sigma^{(0)}_{\alpha\beta} = \sum_{\gamma,\delta} \langle V_{\alpha\gamma} V_{\delta\beta}\rangle G^{(0)}_{\gamma\delta}(\varepsilon) = \sum_{\gamma} \langle V_{\alpha\gamma} V_{\gamma\beta}\rangle G^{(0)}_{\gamma}(\varepsilon) = \quad \alpha$$

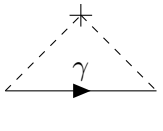

$$\beta\ . \tag{2.110}$$

The disorder averaged term is given by

$$\begin{aligned}\langle V_{\alpha\gamma} V_{\delta\beta}\rangle &= u_0^2 c_{\mathrm{imp}} \int \mathrm{d}^2 r \left(\mathbf{F}^H_{\alpha}(\mathbf{r})\mathbf{F}_{\gamma}(\mathbf{r})\right)\left(\mathbf{F}^H_{\delta}(\mathbf{r})\mathbf{F}_{\beta}(\mathbf{r})\right) \\ &= u_0^2 c_{\mathrm{imp}} \frac{4\pi^2}{4}\left(1 + s_\alpha s_\gamma e^{i(\theta_\alpha - \theta_\gamma)}\right)\left(1 + s_\beta s_\delta e^{i(\theta_\beta - \theta_\delta)}\right)\delta(\mathbf{k}_\gamma - \mathbf{k}_\alpha + \mathbf{k}_\beta - \mathbf{k}_\delta).\end{aligned} \tag{2.111}$$

Thus for $\delta = \gamma$ we immediately find $\mathbf{k}_\alpha = \mathbf{k}_\beta$ and thus $\theta_\alpha = \theta_\beta$. Moreover the sum over γ in the self energy includes and integral over θ_γ and thus only terms with $s_\alpha = s_\beta$ survive and we find $\Sigma^{(0)}_{\alpha\beta} = \delta_{\alpha\beta}\Sigma^{(0)}$ and inductively we also find

$$\Sigma_{\alpha\beta}(\varepsilon) = \delta_{\alpha\beta}\Sigma(\varepsilon) \tag{2.112}$$

$$\langle G_{\alpha\beta}(\varepsilon)\rangle = \frac{\delta_{\alpha\beta} G^{(0)}_{\alpha}(\varepsilon)}{1 - G^{(0)}_{\alpha}(\varepsilon)\Sigma(\varepsilon)} = \delta_{\alpha\beta} G_{\alpha}(\varepsilon), \quad G_{\alpha}(\varepsilon) = \frac{1}{\varepsilon - \varepsilon_\alpha - \Sigma(\varepsilon)}, \tag{2.113}$$

$$\Sigma(\varepsilon) = u_0^2 c_{\mathrm{imp}} \frac{1}{4}\sum_{\alpha} G_{\alpha}(\varepsilon) = \frac{u_0^2 c_{\mathrm{imp}}}{2\pi}(\varepsilon - \Sigma(\varepsilon)) \int \frac{k\mathrm{d}k}{(\varepsilon - \Sigma(\varepsilon))^2 - \hbar^2 v_g^2 k^2}. \tag{2.114}$$

In fact we only care for the imaginary part of the retarded self energy, since the real one will simply shift the origin of the energy. We define the real and the imaginary part of the self energy by

$$\Sigma(\epsilon \pm i0) = \Delta \mp i\Gamma \tag{2.115}$$

and then find here

$$\Gamma_0 = \frac{u_0^2 c_{\mathrm{imp}}}{4\hbar^2 v_g^2}|\varepsilon|. \tag{2.116}$$

The bare velocity operator has the matrix elements

$$v^x_{\alpha\beta} = v_g(2\pi)^2\delta(\mathbf{k}_\alpha - \mathbf{k}_\beta)\frac{1}{2}\left(s_\alpha e^{i\theta_\alpha} + s_\beta e^{-i\theta_\alpha}\right). \tag{2.117}$$

In order to find the conductivity we first realize, that

$$\begin{aligned}\sigma_{xx}(\mathbf{q}=0;\epsilon) &= \left\langle \sum_{\alpha\beta} v^x_{\beta\alpha}(\mathbf{q}=0)\,\mathrm{Im}\,G^R_\alpha(\epsilon)\Gamma^x_{\alpha\beta}(\mathbf{q}=0)(\epsilon,\epsilon)\,\mathrm{Im}\,G^R_\beta(\epsilon)\right\rangle \\ &= \frac{1}{2}\,\mathrm{Re}\left[I(\epsilon+i0,\epsilon-i0) - I(\epsilon+i0,\epsilon+i0)\right], \qquad (2.118)\\ I(\epsilon,\omega) &= \frac{e^2\hbar}{\pi}\sum_{\alpha\beta}\left\langle v^x_{\beta\alpha}G_\alpha(\epsilon)v^x_{\alpha\beta}G_\beta(\omega)\right\rangle, \qquad (2.119)\end{aligned}$$

since $\mathrm{Re}\,G^R = \mathrm{Re}\,G^A$ and $\mathrm{Im}\,G^R = -\,\mathrm{Im}\,G^A$. Then the bare diagram for $I(\epsilon,\omega)$ is represented by

$$I^{(0)}(\epsilon,\omega) = \quad v_x$$

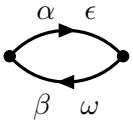

$$v_x\ , \tag{2.120}$$

and evaluates to

$$\begin{aligned}I^{(0)}(\epsilon,\omega) &= \frac{e^2\hbar}{\pi}\times 2\sum_{\alpha\beta} v^x_{\beta\alpha}\langle G_\alpha(\epsilon)\rangle v^x_{\alpha\beta}\langle G_\beta(\omega)\rangle \\ &= \frac{e^2\hbar}{\pi}v_g^2\frac{1}{(2\pi)^2}\sum_{s,t}\int k\mathrm{d}k\mathrm{d}\varphi\frac{1}{4}\left(2+2st\cos(2\phi)\right)\frac{1}{\epsilon - s\hbar v_g k - \Sigma(\epsilon)}\times\frac{1}{\omega - s\hbar v_g k - \Sigma(\omega)} \\ &= \frac{e^2}{\pi^2\hbar}\phi(\epsilon,\omega), \qquad (2.121)\\ \phi(\epsilon,\omega) &= 4\pi v_g^2\hbar^2\int\frac{\mathrm{d}^2k}{(2\pi)^2}\frac{\epsilon-\Sigma(\epsilon)}{[\epsilon-\Sigma(\epsilon)]^2 - \hbar^2v_g^2k^2}\times\frac{\omega-\Sigma(\omega)}{[\omega-\Sigma(\omega)]^2-\hbar^2v_g^2k^2}, \qquad (2.122)\end{aligned}$$

where the factor of two is due to valley degeneracy. When including disorder lines connecting the two Green's functions, we observe, that due to the momentum conservation of the velocity operator and the disorder scattering lines, another power of $\phi(\epsilon,\omega)$ enters at every order and recursively we find the full solution

$$I(\epsilon,\omega) = \frac{e^2}{\pi^2\hbar}\frac{\phi(\epsilon,\omega)}{1-\frac{u_0^2c_{\mathrm{imp}}}{4\pi v_g^2}\phi(\epsilon,\omega)}. \tag{2.123}$$

Evaluating this expression at $\epsilon \pm i0$ and using the definition (2.115), we find

$$\begin{aligned}\sigma_{xx}(\epsilon) &= \frac{e^2}{2\pi^2\hbar}\frac{S(\epsilon)+1}{(1+\frac{u_0^2c_{\mathrm{imp}}}{4\pi v_g^2})(1-\frac{u_0^2c_{\mathrm{imp}}}{4\pi v_g^2}S(\epsilon))}, \qquad (2.124)\\ S(\epsilon) &= \left(\frac{\epsilon-\Delta}{\Gamma}+\frac{\Gamma}{\epsilon-\Delta}\right)\arctan\left(\frac{\epsilon-\Delta}{\Gamma}\right). \qquad (2.125)\end{aligned}$$

In the Boltzmann limit $\Delta = 0$ and $|\epsilon| \gg \Gamma_0$ one obtains

$$\sigma(\epsilon) = \frac{2\hbar v_g^2 e^2}{\pi u_0^2 n_{\text{imp}}}, \tag{2.126}$$

which is exactly the Drude result obtained in Eq. (2.31).

One should note, that this result is only valid far away from the Dirac point. At the Dirac point, the density of states in disorder graphene saturates and one finds logarithmic corrections of the form

$$\sigma(\epsilon) \approx \frac{2\hbar v_g^2 e^2}{\pi n_{\text{imp}} u_0^2} \left[1 - 2\frac{n_{\text{imp}} u_0^2}{2\pi\hbar^2 v_g^2} \log\left(\frac{D}{|\epsilon|}\right)\right], \tag{2.127}$$

where D is the high-energy cut-off [57].

Short range disorder in monolayer Graphene with magnetic field

The calculation for finite perpendicular field follows along the same lines, but shows a few peculiarities. Starting again with the first order self energy

$$\Sigma^{(0)}_{\alpha\beta} = \sum_{\gamma,\delta} \langle V_{\alpha\gamma} V_{\delta\beta}\rangle G^{(0)}_{\gamma\delta}(\varepsilon) = \sum_{\gamma} \langle V_{\alpha\gamma} V_{\gamma\beta}\rangle G^{(0)}_{\gamma}(\varepsilon) = \quad \alpha$$

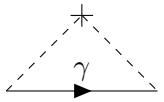

$$\beta\ . \tag{2.128}$$

we this time have

$$\langle V_{\alpha\beta} V_{\gamma\delta}\rangle = u_0^2 c_{\text{imp}} 2\pi\delta(k_y^\alpha - k_y^\beta + k_y^\gamma - k_y^\delta) \int \mathrm{d}x \left(\mathbf{f}^\dagger_\alpha(x)\mathbf{f}_\beta(x)\right)\left(\mathbf{f}^\dagger_\gamma(x)\mathbf{f}_\delta(x)\right), \tag{2.129}$$

$$\mathbf{f}_{k_y,n}(x) = C_n \begin{pmatrix} \text{sign}(n) h_{|n|-1} \\ h_{|n|} \end{pmatrix}, \tag{2.130}$$

and thus

$$\Sigma^{(0)}_{\alpha\beta} = \sum_{\gamma} G^{(0)}_{\gamma}(\varepsilon)\langle V_{\alpha\gamma} V_{\gamma\beta}\rangle G^{(0)}_{\gamma}(\varepsilon) = u_0^2 c_{\text{imp}} 2\pi \sum_{\gamma} \delta(k_y^\alpha - k_y^\beta) \int \mathrm{d}x \left(\mathbf{f}^\dagger_\alpha(x)\mathbf{f}_\gamma(x)\right)\left(\mathbf{f}^\dagger_\gamma(x)\mathbf{f}_\beta(x)\right). \tag{2.131}$$

Due to the fact, that the eigenenergies that enter G_γ do not depend on k_y^γ, this integral only concerns the f_γ combinations. Once multiplied out, these lead either to terms $h_{|n_\gamma|}h_{|n_\gamma|}$ or $h_{|n_\gamma|}h_{|n_\gamma|-1}$. Under the k_y^γ integral only the first ones survive and we find

$$\begin{aligned}\Sigma^{(0)}_{\alpha\beta} = {} & u_0^2 c_{\text{imp}} 2\pi \sum_{n_\gamma} \delta(k_y^\alpha - k_y^\beta) G_\gamma(\epsilon) \\ & \times \int \mathrm{d}x C_{n_\alpha} C_{n_\beta} C^2_{n_\gamma} \left(-\frac{1}{l^2}\right) \left(\text{sign}(n_\alpha)\text{sign}^2(n_\gamma)\text{sign}(n_\beta) h_{|n_\alpha|-1}h_{|n_\beta|-1} + h_{|n_\alpha|}h_{|n_\beta|}\right),\end{aligned} \tag{2.132}$$

then the x integral requires $n_\alpha = \pm n_\beta$, i.e. the self energy is not diagonal in the Landau levels. Recursively one sees, that this is true for the self energy at every order. Thus we may write

$$\Sigma_{\alpha\beta}(\varepsilon) = \delta_{\alpha\beta}\Sigma^d(\varepsilon) + \delta_{\alpha,-\beta}\Sigma^o(\varepsilon), \tag{2.133}$$

where $\pm\alpha = (\pm n, k_y)$. This means, that from the Dyson formula we also find

$$\langle G_{\alpha\beta}(\varepsilon)\rangle = \delta_{\alpha\beta} G^d_n(\varepsilon) + \delta_{\alpha,-\beta} G^o_n(\varepsilon), \tag{2.134}$$

since all other elements lead to homogeneous linear equations, which have the trivial solution. The we find from the definition of the self energy

$$\Sigma_{\alpha\beta} = \sum_\gamma \left(\langle V_{\alpha\gamma} V_{\gamma\beta}\rangle G^d_{n_\gamma} + \langle V_{\alpha\gamma} V_{-\gamma\beta}\rangle G^o_{n_\gamma} \right) = \delta_{\alpha\beta}\Sigma^d(\varepsilon) + \delta_{\alpha,-\beta}\Sigma^o(\varepsilon), \tag{2.135}$$

$$\Sigma^d(\varepsilon) = \sum_\gamma \left(\langle V_{\alpha\gamma} V_{\gamma\alpha}\rangle G^d_{n_\gamma} + \langle V_{\alpha\gamma} V_{-\gamma\alpha}\rangle G^o_{n_\gamma} \right), \tag{2.136}$$

$$\Sigma^o(\varepsilon) = \sum_\gamma \left(\langle V_{\alpha\gamma} V_{\gamma,-\alpha}\rangle G^d_{n_\gamma} + \langle V_{\alpha\gamma} V_{-\gamma,-\alpha}\rangle G^o_{n_\gamma} \right). \tag{2.137}$$

Performing the integral over k_y^γ we encounter terms of the form

$$\begin{aligned} \int \frac{\mathrm{d}k}{2\pi} \langle V_{nq,mk} V_{\pm mk,\pm nq}\rangle &= u_0^2 c_{\mathrm{imp}} \frac{1}{2\pi} C_n^2 C_m^2 \left(\frac{1}{l^2}\right) \Big\{ \mathrm{sign}(n)\mathrm{sign}(\pm n)\mathrm{sign}(m)\mathrm{sign}(\pm m) + 1 \Big\} \qquad (2.138) \\ &= \begin{cases} \frac{u_0^2 c_{\mathrm{imp}}}{4\pi l^2}, & \langle V_{nq,mk} V_{+mk,+nq}\rangle \quad \text{or} \quad \langle V_{nq,mk} V_{-mk,-nq}\rangle \quad \text{or} \quad m = 0, \\ 0, & \left(\langle V_{nq,mk} V_{+mk,-nq}\rangle \quad \text{or} \quad \langle V_{nq,mk} V_{-mk,+nq}\rangle \right) \quad \text{and} \quad m \neq 0 \end{cases}. \end{aligned}$$

The sum in the curly brackets vanishes exactly, if we chose one minus sign. Thus in the terms $\langle V_{\alpha\gamma} V_{\gamma,-\alpha}\rangle$ and $\langle V_{-\alpha\gamma} V_{\gamma\alpha}\rangle$ only the $n_\gamma = 0$ terms survive and we find

$$\Sigma^d(\varepsilon) = \frac{u_0^2 c_{\mathrm{imp}}}{4\pi l^2} \left[\left(\sum_{n_\gamma} G^d_{n_\gamma}(\varepsilon) \right) + G^o_0(\varepsilon) \right], \tag{2.139}$$

$$\Sigma^o(\varepsilon) = \frac{u_0^2 c_{\mathrm{imp}}}{4\pi l^2} \left[\left(\sum_{n_\gamma} G^o_{n_\gamma}(\varepsilon) \right) + G^d_0(\varepsilon) \right]. \tag{2.140}$$

On the other hand we find from the Dyson equation, when carefully keeping track of the $\pm n$ in $\alpha = (n, k_y)$

$$G^d_n = G^{(0)}_\alpha + G^{(0)}_\alpha \left(\Sigma^d G^d_n + \Sigma^o G^o_{-n} \right), \tag{2.141}$$

$$G^o_n = G^{(0)}_\alpha \left(\Sigma^d G^0_n + \Sigma^o G^d_{-n} \right). \tag{2.142}$$

When combining these equations with the corresponding ones for $-n$ we find with $\varepsilon_n = -\varepsilon_{-n}$

$$G^+_n = G^d_n + G^o_n = \frac{\varepsilon + \varepsilon_n - \Sigma^-}{(\varepsilon - \Sigma^+)(\varepsilon - \Sigma^-) - \varepsilon_n^2}, \tag{2.143}$$

$$G^-_n = G^d_n - G^o_n = \frac{\varepsilon + \varepsilon_n - \Sigma^+}{(\varepsilon - \Sigma^+)(\varepsilon - \Sigma^-) - \varepsilon_n^2}, \tag{2.144}$$

where we have also introduced

$$\Sigma^+ = \Sigma^d + \Sigma^o, \quad \Sigma^- = \Sigma^d - \Sigma^o. \tag{2.145}$$

Combining these result we then also find

$$\Sigma^+ = \frac{u_0^2 c_{\rm imp}}{2\pi l^2} \sum_{n=0}^{N_c} \frac{\varepsilon - \Sigma^-}{(\varepsilon - \Sigma^+)(\varepsilon - \Sigma^-) - \varepsilon_n^2}, \tag{2.146}$$

$$\Sigma^- = \frac{u_0^2 c_{\rm imp}}{2\pi l^2} \sum_{n=1}^{N_c} \frac{\varepsilon - \Sigma^+}{(\varepsilon - \Sigma^+)(\varepsilon - \Sigma^-) - \varepsilon_n^2}. \tag{2.147}$$

When calculating the conductivity we first find the velocity matrix element

$$v^x_{nk,mq} = \frac{v_g}{\hbar} C_n C_m \delta_{k,q} \left(\text{sign}(n)\delta_{|n|-1,|m|} + \text{sign}(m)\delta_{|m|-1,|n|} \right), \tag{2.148}$$

and then follow exactly along the same lines as in the case without magnetic field. In this case we find the bare diagram for $I(\epsilon, \omega)$ is represented by

$$I^{(0)}(\epsilon,\omega) = \quad v_x \quad \begin{matrix} \alpha\beta \quad \epsilon \\ \delta\gamma \quad \omega \end{matrix} \quad v_x \ , \tag{2.149}$$

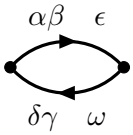

and evaluates to

$$\begin{aligned} I^{(0)}(\epsilon,\omega) &= \frac{e^2\hbar}{\pi} \times 2 \sum_{\alpha\beta\gamma\delta} v^x_{\delta\alpha} \langle G_{\alpha\beta}(\epsilon)\rangle v^x_{\beta\gamma} \langle G_{\gamma\delta}(\omega)\rangle \\ &= \frac{e^2}{\pi^2\hbar}\phi(\epsilon,\omega), \end{aligned} \tag{2.150}$$

$$\phi(\epsilon,\omega) = \frac{1}{2}\left(\hbar\Omega\right)^2 \sum_{n=0}^{\infty} g_n^+(\epsilon) g_{n+1}^-(\omega), \tag{2.151}$$

$$g_n^\pm(\epsilon) = \frac{1}{2}\left(G_n^\pm(\epsilon) + G_{-n}^\pm(\epsilon) \right), \tag{2.152}$$

where the factor of two is due to valley degeneracy. When including the full vertex corrections one obtains the final result

$$\sigma_{xx}(\varepsilon) = \frac{e^2}{\pi^2\hbar}\frac{1}{2}\,\text{Re}\left[\frac{\phi(\varepsilon + i0, \varepsilon - i0)}{1 - \frac{c_{\rm imp}u_0^2}{4\pi\hbar^2 v_g^2}\phi(\varepsilon + i0, \varepsilon - i0)} - \frac{\phi(\varepsilon + i0, \varepsilon + i0)}{1 - \frac{c_{\rm imp}u_0^2}{4\pi\hbar^2 v_g^2}\phi(\varepsilon + i0, \varepsilon + i0)} \right]. \tag{2.153}$$

Following Ref. [58] one can rewrite this result. In the limit of large energies $\varepsilon \gg \hbar v_g/l$ the expressions (2.147) are identical and we find a diagonal self energy

$$\Sigma \approx \frac{u_0^2 c_{\rm imp}}{2\pi l^2} \sum_{n=0}^{N_c} \frac{\varepsilon - \Sigma}{(\varepsilon - \Sigma)^2 - \varepsilon_n^2}, \tag{2.154}$$

which fulfills $\Sigma(\varepsilon) = \Delta(\varepsilon) \pm i\Gamma(\varepsilon)$. It turns out, that the properties of the system strongly depend on the relation of the energy $x = \frac{\varepsilon_*^2}{\varepsilon^2}$, where $\varepsilon_* = \hbar\omega_c\sqrt{\gamma}$ and $\gamma = 2\hbar^2 v_g^2/(n_{\text{imp}} u_0^2)$. We can find analytical results for $\log N_c \ll \gamma$ in the two limits $\varepsilon \gg \varepsilon_*$ ("classical") and $\varepsilon \ll \varepsilon_*$ ("quantum"). To this end we define the parameter

$$z(\varepsilon) = \frac{\Gamma(\varepsilon)}{\Gamma_0(\varepsilon)} = \frac{\nu(\varepsilon)}{\nu_0(\varepsilon)}, \tag{2.155}$$

where $\Gamma_0(\varepsilon) = \hbar/2\tau_q(\varepsilon)$ is given by the quantum scattering time $\tau_q(\varepsilon)$ in zero magnetic field written down in Eq. (2.116) and obtain

$$\Delta = \begin{cases} 2\Gamma_0 e^{-\pi/x} \sin\left(\frac{2\pi\varepsilon^2}{\hbar^2\Omega^2}\right), & \varepsilon \gg \varepsilon_*, \\ \sum_n \vartheta\left(\frac{\varepsilon-\varepsilon_n}{\Gamma_n}\right)\frac{\varepsilon}{2}, & \varepsilon \ll \varepsilon_* \end{cases} \tag{2.156}$$

$$z \approx \begin{cases} 1 + 2ae^{-\pi/x}, & \varepsilon \gg \varepsilon_*, \\ \sqrt{\frac{2x}{\pi}} \sum_n \vartheta\left(\frac{\varepsilon-\varepsilon_n}{\Gamma_n}\right)\sqrt{1-\left(\frac{\varepsilon-\varepsilon_n}{\Gamma_n}\right)^2}, & \varepsilon \ll \varepsilon_*, \end{cases} \tag{2.157}$$

$$a = \cos\left(\frac{2\pi\varepsilon^2}{\hbar^2\Omega^2}\right), \quad \vartheta(y) = \begin{cases} 1, & |y| < 1, \\ 0, & |y| > 1, \end{cases} \tag{2.158}$$

$$\Gamma_n = \Gamma(\varepsilon_n) = \hbar\sqrt{\frac{2\hbar\Omega^2}{\varepsilon\pi\tau_q(\varepsilon_n)}}. \tag{2.159}$$

This shows, why the limit $\epsilon \gg \varepsilon_*$ is known as the classical limit: the density of states is only slightly modified compared to it's zero magnetic field value. Landau levels are sufficiently smeared by impurity scattering to not lead to any quantization in the conductivity. In the opposite limit $\epsilon \ll \varepsilon_*$ the are very clearly separated and the system behaves very differently. Using the parameter z, one can rewrite the conductivity (2.153) in a form similar to the Drude formula result in Eq. (2.27)

$$\sigma_{xx}(\varepsilon) = \sigma_0 \frac{z(\varepsilon)^2}{z(\varepsilon)^2 + \left(\omega_c(\varepsilon)\tau_{\text{tr}}(\varepsilon)\right)}. \tag{2.160}$$

This again shows, that in the limit $\varepsilon \gg \varepsilon_*$, where $z \approx 1$ we are in the quasi-classical regime, where the Drude result is applicable.

2.2.6 Summary

Perturbation theory is one of the most successful methods in quantum field theory and is for example used to calculate the values of coupling constants in the standard model of particle physics to extremely high precision. It is also the best controlled analytical method in describing condensed matter phenomena, that include a small parameter.

In this section, we have given an introduction into the perturbative treatment of interactions and disorder in the Green's function formalism. We have derived the Kubo formula for linear response conductivity, which can be represented by the diagram shown in Eq. (2.2.5). If we apply this to monolayer graphene without a magnetic field, we obtain the result (2.126) which is exactly the Drude result obtained before in Eq. (2.31). For a finite perpendicular magnetic field one obtains (2.160) ,

which in general gives corrections to the Boltzmann equation result (2.29). The result for σ_{xx} will be used in Chapter 5 to describe the magnetoresistance of a graphene Corbino disk. It turns out, that for the relatively small magnetic fields considered there, the perturbative result (2.160) simplifies to the solution obtained from the Boltzmann calculation (2.29).

2.3 Landauer theory

In this section we discuss the behavior of systems, that have system sizes between the elastic mean free path ℓ_0 (average distance between impurity scattering events) and ℓ_{in} (average distance between electron-electron scattering events). This range can typically be reached in a temperature range between 50 mK and 4 K. In this range, electron-electron interaction can be largely disregarded. Moreover electron will scatter off of impurities more often than from device interfaces, so exact geometric details of the sample are also less relevant. In this regime, the sample can be seen as an effective barrier between the leads, which are well described by scattering states expressed through plane waves. The sample then determines the relationship between the different states (channels) in the two (or more) leads, similarly to a barrier potential in the Schrödinger equation. To this end, one introduces the scattering matrix (S-matrix), which connects the scattering states in the different leads. In this formalism the number of leads is actually not limited. Instead, one assumes, that in each lead α, the scattering state can be written as

$$\psi_\alpha(\mathbf{r}) = \sum_n a^+_{\alpha,n}\phi^+_{\alpha,n}(\mathbf{r}) + a^-_{\alpha,n}\phi^-_{\alpha,n}(\mathbf{r}), \tag{2.161}$$

where superscript $+$ and $-$ mark incoming (into the scattering region) and outgoing states respectively and $n = 1, ..., N$ labels the number of channels in the lead. The amplitudes of incoming and outgoing states can be grouped into vectors $\mathbf{c}_{\text{in}} = \{a^+_{\alpha,n}\}$ and $\mathbf{c}_{\text{out}} = \{a^-_{\alpha,n}\}$. The S-matrix $\mathcal{S}$ is then defined by

$$\mathbf{c}_{\text{out}} = \mathcal{S}\mathbf{c}_{\text{in}}. \tag{2.162}$$

Due to current conservation, the S-matrix is unitary. For time-reversal symmetric problems it is more over symmetric. When considering a subset of two leads $\alpha = i, j$ only, the S-matrix has a block structure of the form

$$\mathbf{c}_{\text{out}} = \begin{pmatrix} \begin{pmatrix} a^-_{i,1} \\ \dots \\ a^-_{i,N} \end{pmatrix} \\ \begin{pmatrix} a^-_{j,1} \\ \dots \\ a^-_{j,N} \end{pmatrix} \end{pmatrix} = \begin{pmatrix} r & t' \\ t & r' \end{pmatrix} \begin{pmatrix} \begin{pmatrix} a^+_{i,1} \\ \dots \\ a^+_{i,N} \end{pmatrix} \\ \begin{pmatrix} a^+_{j,1} \\ \dots \\ a^+_{j,N} \end{pmatrix} \end{pmatrix} = \mathcal{S}\mathbf{c}_{\text{in}}. \tag{2.163}$$

The (two-terminal) Landauer-Büttiker conductance is given by

$$G = D\frac{e^2}{h}\int \mathrm{d}E \left(-\frac{\partial n_F(E)}{\partial E}\right) \mathrm{Tr}(t^\dagger t), \tag{2.164}$$

where D is a degeneracy factor (i.e. $D = 2$ for spin degenerate systems). It can be derived from the Kubo formula of conductance, as shown in Appendix B.1.

2.3.1 Summary

The Landauer-Büttiker formula has a very intuitive interpretation, which is that at low temperatures, every open channel (i.e. every mode with a lower band-edge smaller than the chemical potential) contributes exactly one conductance quantum e^2/h times its transmission to the overall conductance of the device. This result will be used in Sec. 3.1 to describe the conductance of a general quantum point contact and in Chapter 4 to describe the non-interacting part of the conductance of a bilayer graphene quantum point contact. In Chapter 4 it will furthermore be used, to phenomenologically describe an additional, interaction induced, feature in the conductance, which is discussed in Sec. 3.1.2.

2.4 Hydrodynamics in graphene

Until now we have worked in a regime, where disorder and electron-electron interaction effects were weak and could be treated perturbatively. However, for graphene this is not always the case. While modern fabrication techniques allow for extremely clean systems, with very little disorder one should take a closer look at the dimensionless parameter $\alpha = e^2/(4\pi\epsilon\hbar v_F)$ which describes the ratio between typical potential and kinetic energy. For low temperatures $k_B T \ll \mu$, electrons in graphene can be described by long-lived quasi particles and form a conventional, two dimensional Fermi liquid. For the opposite case $k_B T \gg \mu$ one needs a more sophisticated treatment. While a first order renormalization group treatment as in [59–61] renders Coulomb interactions marginally irrelevant, since they vanish logarithmically for low temperatures, the bare value at high energies, which is not renormalized, is actually not a small number but can be of the order of $\alpha_0 \approx 1$. For this reason, the effective coupling constants at temperatures of around 100K are still not negligible and in this range electrons in graphene form a relatively strongly interacting Dirac fluid [62]. The description of such strongly-correlated systems is one of the major unsolved questions in condensed matter physics. The natural choice for the description of interacting thermalizing systems is hydrodynamics [63], in which one describes the behavior of conserved quantities on long length scales. However graphene has a peculiarity. The energy current

$$\mathbf{j}_E = \int \frac{(\mathrm{d}^2 k)}{(2\pi)^2} \varepsilon_k \mathbf{v}_k f(\mathbf{k}, \mathbf{r}) = \int \frac{(\mathrm{d}^2 k)}{(2\pi)^2} v_g k v_g \frac{\mathbf{k}}{k} f(\mathbf{k}, \mathbf{r}) \tag{2.165}$$

is proportional to the momentum, so electron-electron interaction alone cannot relax the system into the steady state, but finite disorder is required [64] to do so. There are in general different ways of deriving sets of hydrodynamic equations, which are outlined in the review articles [62, 64].

2.4.1 Kinetic theory in graphene

Following Ref. [65] we reproduce here, how hydrodynamic equations can be directly obtained from the Boltzmann equation. While this is clearly applicable in doped graphene, universality of the hydrodynamic approach makes it reasonable to also apply this formalism at the Dirac point. The starting point is the already mentioned Boltzmann equation

$$\mathcal{L} f = \mathrm{St}_{ee}[f] + \mathrm{St}_R[f] - \frac{f - \langle f \rangle_\varphi}{\tau_{\mathrm{dis}}}, \tag{2.166}$$

$$\mathcal{L} = \partial_t + \mathbf{v}\nabla_{\mathbf{r}} - \left(e\mathbf{E} + \frac{e}{c}\mathbf{v} \times \mathbf{B} \right) \cdot \nabla_{\mathbf{k}}, \tag{2.167}$$

where the charge of an electron is denoted by $e < 0$ and $f_{\lambda \mathbf{k}}$ is the distribution function, which we already discussed in Sec. 2.1. Especially close to the Dirac point it is important to include both bands $\lambda = \pm 1$. Since processes like Auger scattering or recombination do not conserve the values of electrons in the to bands separately. Compared to our earlier treatment, disorder scattering is still treated within a relaxation time approximation with

$$\langle f \rangle_\varphi = \int_{-\pi}^{\pi} \frac{\mathrm{d}\varphi}{2\pi} f_{\lambda \mathbf{k}}. \tag{2.168}$$

However, as already discussed, electron-electron interaction is important in this regime, so we also include the corresponding collision integral $\mathrm{St}_{ee}[f]$ and moreover $\mathrm{St}_R[f]$ which exactly describes the

aforementioned electron-hole recombination processes. Since graphene is a two band system, one has to be a bit careful when defining macroscopic quantities, since a completely filled lower band formally hosts and infinite number of particles. The dispersion is given by

$$\epsilon_{\lambda,\mathbf{k}} = \lambda v_g k, \tag{2.169}$$

while the velocity and momentum can be expressed via

$$\mathbf{v}_{\lambda,\mathbf{k}} = \lambda v_g \frac{\mathbf{k}}{k}, \quad \mathbf{k} = \frac{\lambda k}{v_g}\mathbf{v}_{\lambda,\mathbf{k}}. \tag{2.170}$$

Then the number of low energy excitations in the upper band is given by

$$n_+ = N \int \frac{\mathrm{d}^2 k}{(2\pi)^2} f_{+,\mathbf{k}}, \tag{2.171}$$

while for the lower band we find

$$n_- = N \int \frac{\mathrm{d}^2 k}{(2\pi)^2} \left(1 - f_{-,\mathbf{k}}\right) \tag{2.172}$$

where the distribution function $f_{\lambda,\mathbf{k}}$ includes the spectrum $\epsilon_{-,\mathbf{k}}$ and the chemical potential μ_λ and $N = 4$ describes the spin and valley degeneracy. The total charge density is then

$$n = n_+ - n_-, \tag{2.173}$$

while

$$n_I = n_+ + n_- \tag{2.174}$$

describes the imbalance or total quasiparticle density. Similarly we define the currents

$$\mathbf{j}_+ = N \int \frac{\mathrm{d}^2 k}{(2\pi)^2} \mathbf{v}_{+,\mathbf{k}} f_{+,\mathbf{k}}, \quad \mathbf{j}_- = N \int \frac{\mathrm{d}^2 k}{(2\pi)^2} \mathbf{v}_{-,\mathbf{k}} \left(1 - f_{-,\mathbf{k}}\right) \tag{2.175}$$

leading to the charged current $\mathbf{j} = \mathbf{j}_+ - \mathbf{j}_-$ and the imbalance current $\mathbf{j}_I = \mathbf{j}_+ + \mathbf{j}_-$.

Then we integrate both sides of the Boltzmann equation with different weights over all momenta and sum over all bands. Without any additional weights, we obtain the standard continuity equation

$$\partial_t n + \nabla_{\mathbf{r}} \cdot \mathbf{j} = 0. \tag{2.176}$$

Similarly one finds for the weight λ

$$\partial_t n_I + \nabla_{\mathbf{r}} \cdot \mathbf{j}_I = -\frac{n_I - n_I^{(0)}}{\tau_R} \tag{2.177}$$

within a relaxation time approximation for relaxation processes. The equilibrium imbalance density is described by $n_I^{(0)}$. This term exactly describes, that the densities for each band are not conserved individually. When using the weight $\epsilon_{\lambda\mathbf{k}}$ we find the continuity equation for the energy current $\mathbf{j}_E$

$$\partial_t n_E + \nabla_{\mathbf{r}} \cdot \mathbf{j}_E = e\mathbf{E} \cdot \mathbf{j}, \tag{2.178}$$

$$n_E = N \int \frac{\mathrm{d}^2 k}{(2\pi)^2} \left[\epsilon_{+,\mathbf{k}} f_{+,\mathbf{k}} + \epsilon_{-,\mathbf{k}} (f_{-,\mathbf{k}} - 1)\right], \tag{2.179}$$

$$\mathbf{j}_E = N \sum_\lambda \int \frac{\mathrm{d}^2 k}{(2\pi)^2} \epsilon_{\lambda\mathbf{k}} \mathbf{v}_{\lambda\mathbf{k}} f_{\lambda\mathbf{k}} \tag{2.180}$$

and finally we find the continuity equation of momentum current for the weight $\mathbf{k}$

$$\partial j^{\alpha}_{\mathbf{k}} + \nabla^{\beta}_{\mathbf{k}} \Pi^{\alpha\beta}_{E} - enE^{\alpha} - \frac{e}{c} \left(\mathbf{j} \times \mathbf{B}\right)^{\alpha} = -\frac{j^{\alpha}_{\mathbf{k}}}{\tau_{\mathrm{dis}}}, \tag{2.181}$$

$$\mathbf{j}_{\mathbf{k}} = N \sum_{\lambda} \int \frac{\mathrm{d}^2 k}{(2\pi)^2} \mathbf{k}_{\lambda\mathbf{k}} f_{\lambda\mathbf{k}} = \frac{\mathbf{j}_E}{v_g^2}, \tag{2.182}$$

$$\Pi^{\alpha\beta}_{E} = N \sum_{\lambda} \int \frac{\mathrm{d}^2 k}{(2\pi)^2} k^{\alpha} v^{\beta}_{\lambda\mathbf{k}} f_{\lambda\mathbf{k}}, \tag{2.183}$$

where $\Pi^{\alpha\beta}_{E}$ is the stress-energy tensor. Thus we have found 4 continuity equations (2.176), (2.177),(2.178) and (2.181).

As already mentioned, the combination of relatively strong disorder and the presence of disorder scattering establishes a local equilibrium, which leads to the distribution function

$$f^{(0)}_{\lambda\mathbf{k}}(\mathbf{r}) = \frac{1}{1 + e^{\frac{\epsilon_{\lambda\mathbf{k}} - \mu_{\lambda}(\mathbf{r}) - \mathbf{u}(\mathbf{r})\cdot\mathbf{k}}{T(\mathbf{r})}}} \tag{2.184}$$

for ideal hydrodynamics. Using this specific distribution function in the definitions above, we find several important relation. First of all, the charge and imbalance current are given by

$$\mathbf{j} = n\mathbf{u}, \quad \mathbf{j}_I = n_I \mathbf{u}, \tag{2.185}$$

where the densities are functions of the temperature T, the chemical potentials and the absolute value of $\mathbf{u}$. Similarly we find

$$\mathbf{j}_E = \frac{3n_E}{2 + u^2/v_g^2} \mathbf{u}, \tag{2.186}$$

where n_E is again a function of the temperature T, the chemical potentials and the absolute value of $\mathbf{u}$. When introducing the thermodynamical pressure

$$P = TN \frac{\mathrm{d}^2 k}{(2\pi)^2} \log\left[1 + e^{\mu_+ - \epsilon_{+,\mathbf{k}} + \mathbf{u}\cdot\mathbf{k}/T}\right] + TN \frac{\mathrm{d}^2 k}{(2\pi)^2} \log\left[1 + e^{\epsilon_{-,\mathbf{k}} - \mu_- - \mathbf{u}\cdot\mathbf{k}/T}\right] \tag{2.187}$$

and using the standard relation $W = n_E + P$ for the enthalpy W we can re-express

$$W = n_E + P = \frac{3n_E}{2 + u^2/v_g^2}, \tag{2.188}$$

$$\mathbf{j}_E = W\mathbf{u}, \quad \Pi^{\alpha\beta}_{E} = P\delta_{\alpha\beta} + \frac{W}{v_g^2} u_{\alpha} u_{\beta}. \tag{2.189}$$

This means, that we can re express the continuity equations with this new quantities. Then we find a generalization of the Euler equation

$$W(\partial_t + \mathbf{u}\cdot\nabla)\mathbf{u} + v_g^2 \nabla P + \mathbf{u}\partial_t P + e(\mathbf{E}\cdot\mathbf{j})\mathbf{u} = v_g^2 en\mathbf{E} + v_g^2 \frac{e}{c} \mathbf{j} \times \mathbf{B} - \frac{W\mathbf{u}}{\tau_{\mathrm{dis}}}. \tag{2.190}$$

On top of this we can introduce the entropy density s of the system by

$$s = -N \sum_{\lambda} \int \frac{\mathrm{d}^2 k}{(2\pi)^2} \left[f_{\lambda\mathbf{k}} \log f_{\lambda\mathbf{k}} + (1 - f_{\lambda\mathbf{k}}) \log(1 - f_{\lambda\mathbf{k}})\right] \tag{2.191}$$

and find the final equation

$$\partial_t s + \nabla_{\mathbf{r}} \cdot (s\mathbf{u}) = \frac{\mathbf{u} \cdot \mathbf{j}_{\mathbf{k}}}{T\tau_{\mathrm{dis}}} \tag{2.192}$$

for the entropy current $s\mathbf{u}$ describing thermal transport. The combined equations (2.176),(2.177), (2.190) and (2.192) describe the system if the assumption of local equilibrium is exactly fulfilled. However there are also dissipative processes, which lead to irreversible transfer of charge or momentum.

2.4.1.1 Dissipative corrections

These dissipative corrections are usually obtained within linear response, by linearizing the collision integral in small deviations $\delta f = f - f^{(0)}$ from local equilibrium. To this end, one writes

$$\delta f_{\lambda\mathbf{k}} = -T\frac{\partial f^{(0)}_{\lambda\mathbf{k}}}{\partial \epsilon_{\lambda\mathbf{k}}} h_{\lambda\mathbf{k}} = f^{(0)}_{\lambda\mathbf{k}} \left(1 - f^{(0)}_{\lambda\mathbf{k}}\right) h_{\lambda\mathbf{k}} \tag{2.193}$$

and the linearized collision integral can be written as

$$\begin{aligned} \mathrm{St}_{ee}[f] &\approx N \sum_{1,2,3,4} W_{12,34} f^{(0)}_1 f^{(0)}_2 \left[1 - f^{(0)}_3\right] \left[1 - f^{(0)}_4\right] \left(h_3 + h_4 - h_1 - h_2\right), \\ \sum_1 &= \sum_{\lambda_1} \int \frac{\mathrm{d}^2 k_1}{(2\pi)^2}, \end{aligned} \tag{2.194}$$

where the transition probability can be found from the Fermi Golden Rule

$$W_{12,34} = (2\pi)^3 |U|^2 \delta(\epsilon_1 + \epsilon_2 - \epsilon_3 - \epsilon_4) \delta(\mathbf{k}_1 + \mathbf{k}_2 - \mathbf{k}_3 - \mathbf{k}_4) \tag{2.195}$$

and U is the dynamically screened Coulomb interaction. This already reveals the collinear scattering singularity in graphene, since for electrons and holes, that move nearly along the same direction, energy and momentum conservation are equivalent and the collision integral would vanish, leading to a very fast decay of these modes. This is cured for three choices of h, namely

$$h \propto \mathbf{k}, \mathbf{v}, \lambda\mathbf{v}, \tag{2.196}$$

which are longer lived. Up to second rank tensors, we then find the following combinations, that can be used to describe $h_{\lambda\mathbf{k}}$

$$h_{\lambda\mathbf{k}} = \frac{\mathbf{v}_{\lambda\mathbf{k}}}{v_g} \sum_1^3 \phi_i \mathbf{h}^{(i)} + \frac{v^\alpha_{\lambda\mathbf{k}} v^\beta_{\lambda\mathbf{k}}}{v_g^2} \sum_1^3 \phi_i h^{(i)}_{\alpha\beta}, \tag{2.197}$$

with the coefficients $\mathbf{h}^{(i)}$ and $h^{(i)}_{\alpha\beta}$ and the three modes are expressed by

$$\phi_1 = 0, \quad \phi_2 = \lambda, \quad \phi_3 = \epsilon_{\lambda\mathbf{k}}/T. \tag{2.198}$$

After applying constraints due to momentum conservation $\mathbf{h}^{(3)} = 0$ and conservation of number and energy $\mathrm{Tr} h^{(i)}_{\alpha\beta} = 0$ the corresponding macroscopic currents

$$\delta\mathbf{j} = N \sum_\lambda \int \frac{\mathrm{d}^2 k}{(2\pi)^2} \mathbf{v}_{\lambda\mathbf{k}} \delta f_{\lambda\mathbf{k}}, \quad \delta\mathbf{j}_I = N \sum_\lambda \lambda \int \frac{\mathrm{d}^2 k}{(2\pi)^2} \mathbf{v}_{\lambda\mathbf{k}} \delta f_{\lambda\mathbf{k}}, \quad \delta\mathbf{j}_E = 0, \tag{2.199}$$

can be related to the coefficients $\mathbf{h}^{(i)}$ as

$$\begin{pmatrix}\delta\mathbf{j}\\ \delta\mathbf{j}_I\end{pmatrix} = \frac{v_g T}{2}\hat{M}_h \begin{pmatrix}\mathbf{h}^{(1)}\\ \mathbf{h}^{(2)}\end{pmatrix}, \qquad \hat{M}_h = \begin{pmatrix}\frac{\partial n}{\partial\mu} & \frac{\partial n_I}{\partial\mu}\\ \frac{\partial n_I}{\partial\mu} & \frac{\partial n}{\partial\mu}\end{pmatrix}. \tag{2.200}$$

In an analogous manner, the tensor coefficients can be connected to tensor quantities like the stress tensor.

Now, one may essentially redo the original idea, of integrating over the Boltzmann equation with different weights, but include the non-equilibrium corrections when evaluating the collision integral. For the ideal quantities on the non collision integral side, the conservation equations derived in the ideal limit are still valid and thus one may find after a lengthy calculation

$$\hat{M}_n \begin{pmatrix} e\mathbf{E} - T\nabla\frac{\mu}{T} + \frac{e}{c}\mathbf{u}\times\mathbf{B}\\ T\nabla\frac{\mu_I}{T}\end{pmatrix} = -\frac{1}{v_g^2}\left[\frac{\partial n}{\partial\mu}\hat{T}_m\hat{M}_h^{-1} + \frac{1}{\tau_{\text{dis}}}\hat{1}\right]\begin{pmatrix}\delta\mathbf{j}\\ \delta\mathbf{j}_I\end{pmatrix} - \frac{\omega_B}{v_g^2}\frac{\partial n}{\partial\mu}\hat{\mathfrak{M}}_K\hat{M}_h^{-1}\mathbf{e}_B\times\begin{pmatrix}\delta\mathbf{j}\\ \delta\mathbf{j}_I\end{pmatrix}, \tag{2.201}$$

with the following matrices

$$\hat{M}_n = \begin{pmatrix}\frac{2n^2}{3n_E} - \frac{1}{2}\frac{\partial n}{\partial\mu} & -\frac{2nn_I}{3n_E} + \frac{1}{2}\frac{\partial n_I}{\partial\mu}\\ \frac{2nn_I}{3n_E} - \frac{1}{2}\frac{\partial n_I}{\partial\mu} & -\frac{2n_I^2}{3n_E} + \frac{1}{2}\frac{\partial n}{\partial\mu}\end{pmatrix}, \quad \hat{T}_m = \begin{pmatrix}\tau_{11}^{-1} & \tau_{12}^{-1}\\ \tau_{12}^{-1} & \tau_{22}^{-1}\end{pmatrix} \tag{2.202}$$

and for $\mu_\pm = \mu$ or $\mu_I = 0$

$$\hat{\mathfrak{M}}_K = \begin{pmatrix}\tanh\frac{\mu}{2T} & 1\\ 1 & \tanh\frac{\mu}{2T}\end{pmatrix}. \tag{2.203}$$

The scattering rates in matrix $\hat{T}_m$ stem from the integrated collision integral and are given by

$$\mathcal{I}_i^{ee}\left[\delta f\right] = N^2\sum_{1,1',2,2'}\mathbf{v}_2\phi_{i,2}W_{12,1'2'}f_1^{(0)}f_2^{(0)}\left[1-f_{1'}^{(0)}\right]\left[1-f_{2'}^{(0)}\right]\Big[h_{1'}+h_{2'}-h_1-h_2\Big]. \tag{2.204}$$

which can be brought to the form

$$\begin{pmatrix}\mathcal{I}_1^{ee}\\ \mathcal{I}_2^{ee}\end{pmatrix} = -\frac{1}{2}v_g T\frac{\partial n}{\partial\mu}\begin{pmatrix}\tau_{11}^{-1} & \tau_{12}^{-1}\\ \tau_{12}^{-1} & \tau_{22}^{-1}\end{pmatrix}\begin{pmatrix}\mathbf{h}^{(1)}\\ \mathbf{h}^{(2)}\end{pmatrix} = -\frac{\partial n}{\partial\mu}\begin{pmatrix}\tau_{11}^{-1} & \tau_{12}^{-1}\\ \tau_{12}^{-1} & \tau_{22}^{-1}\end{pmatrix}\hat{M}_h^{-1}\begin{pmatrix}\delta\mathbf{j}\\ \delta\mathbf{j}_I\end{pmatrix}. \tag{2.205}$$

The explicit definitions of τ_{ij} are given in Ref. [65].

Since the energy current is proportional to the momentum, only finite disorder leads to a relaxation. This is however already taken into account, by allowing for finite τ_{dis} at the level of the Navier-Stokes equation obtained from momentum conservation. The tensor components of Eq. (2.197) lead to dissipative corrections of the stress tensor, which lead to corrections of the Navier-Stokes equation, which finally takes the form

$$\mathcal{W}(\partial_t + \mathbf{u}\cdot\nabla)\mathbf{u} + v_g^2\nabla P + \mathbf{u}\partial_t P + e(\mathbf{E}\cdot\mathbf{j})\mathbf{u} = v_g^2\left[\eta\Delta\mathbf{u} - \eta_H\Delta\mathbf{u}\times\mathbf{e}_B + en\mathbf{E} + \frac{e}{c}\mathbf{j}\times\mathbf{B}\right] - \frac{\mathbf{j}_E}{\tau_{\text{dis}}}. \tag{2.206}$$

Here η and η_H are the shear and Hall viscosity respectively, which are known from the dissipative corrections and the current densities are

$$\mathbf{j} = n\mathbf{u} + \delta\mathbf{j}, \quad \mathbf{j}_I = n_I\mathbf{u} + \delta\mathbf{j}_I, \quad \mathbf{j}_E = n_E\mathbf{u}. \tag{2.207}$$

The enthalpy $\mathcal{W}$ always fulfills $\mathcal{W} = n_E + P$ with the pressure P and the energy density n_E. The generalized Navier-Stokes equation (2.206), supplemented with the continuity equations for current and imbalance current

$$\partial_t n_I + \nabla\cdot\mathbf{j}_I = -\frac{n_I - n_{I,0}}{\tau_R}, \tag{2.208}$$

$$\partial_t n + \nabla\cdot\mathbf{j} = 0, \tag{2.209}$$

and the thermal transport equation

$$T\left[\frac{\partial s}{\partial t} + \nabla_{\mathbf{r}}\cdot\left(s\mathbf{u} - \delta\mathbf{j}\frac{\mu}{T} - \delta\mathbf{j}_I\frac{\mu_I}{T}\right)\right] = \delta\mathbf{j}\cdot\left[e\mathbf{E} + \frac{e}{c}\mathbf{u}\times\mathbf{B} - T\nabla\frac{\mu}{T}\right] - T\delta\mathbf{j}_I\cdot\nabla\frac{\mu_I}{T}$$
$$+ \frac{\eta}{2}\left(\nabla_\alpha u_\beta + \nabla_\beta u_\alpha - \delta_{\alpha\beta}\nabla\cdot\mathbf{u}\right)^2 - \frac{n_E - n_{E,0}}{\tau_{RE}} + \mu_I\frac{n_I - n_{I,0}}{\tau_R} + \frac{\mathcal{W}\mathbf{u}^2}{v_g^2\tau_{\mathrm{dis}}}, \tag{2.210}$$

forms a set of four hydrodynamic equations. In most cases the hydrodynamic equations are solved within linear response. In Chapter 6 we will show, how this hydrodynamic approach can be applied to the problem of a graphene Corbino disc at elevated temperatures and charge neutrality, where the charge current is carried by the dissipative mode alone.

2.4.2 Summary

At sufficiently high temperatures and in sufficiently clean samples, electron-electron interactions sets the smallest length scale in monolayer graphene and electrons are strongly correlated. The resulting collective behavior can no longer be described by perturbative methods discussed in Sec. 2.2, since the coupling parameter is not small. In this Section, the concept of electron hydrodynamic was introduced, which solves this dilemma by introducing a set of effective equations, that follow from the Boltzmann equation introduced in Sec. 2.1 and model these collective modes as a classical fluid. We will apply this description in Chapter 6 to a graphene Corbino disk at elevated temperatures.

2.5 Summary and conclusions

Transport in mesoscopic systems strongly depends on the hierarchy of length scales set by the system size and internal processes, like electron-electron interaction or disorder. In this chapter, we have discussed different methods of transport theory. In semi-classical systems, the Boltzmann equation approach discussed in Sec. 2.1 leads to reliable results, like the Drude-like magneto conductivities in graphene (2.29) and (2.30). A more careful approach of including disorder or interaction effects, that also allows for the treatment of quantizing magnetic fields, which are clearly not classical, is the Green's function approach discussed in Sec. 2.2, which leads to the corrected result of the magneto conductivity (2.160). The results obtained in this Sections will be applied in Chapter 5 to describe the magnetoresistance of a graphene Corbino disk in small perpendicular magnetic field. This device geometry is introduced in Sec. 3.2.

Perturbation theory for interacting systems as discussed in Sec. 2.2.3 will also be applied to describe the free energy in bilayer graphene in Sec. 3.1.2.3. There we will make explicit use of the spin and valley degree of freedom discussed in Sec. 1.2. The resulting free energy, which is effectively quadratic in all subband densities, is the foundation for the phenomenological model of the point seven anomaly introduced in Sec. 3.1.2 and applied in Chapter 4 to a bilayer graphene quantum point contact.

If there are no quantizing fields and interaction effects are small, one can derive the Landauer-Büttiker formula (2.164) discussed in Sec. 2.3 from the Kubo-conductivity (2.97), which describes the two terminal resistance in terms of the scattering matrix. This result will be used in Chapter 4 to describe the conductance of a bilayer graphene quantum point contact, which is introduced in Sec. 3.1.

Finally we discussed in Sec. 2.4, that the Boltzmann equation can be used to derive a set of hydrodynamic-like continuity equations for graphene, which describes the collective behavior of the electron fluid if interactions are indeed not very weak. This concept is applied to the already mentioned graphene Corbino disk at elevated temperatures in Chapter 6.

3 Chapter 3
Special devices and geometries

In this chapter we introduce the special devices that are considered in the main part, Chapters 4, 5 and 6. We start by discussing quantum point contacts, and two important effects, that are often observed in this device: Fabry-Pérot oscillations and the 0.7 *anomaly in Section 3.1. We show, that simple arguments based on the grand canonical potential of a four band system can build the foundation of a phenomenological model in Sec. 3.1.2.3. Finally, we discuss the special effect of a Corbino geometry on the magnetoresistance in graphene in Sec. 3.2. While the methods introduced in Chapter 2 can be used independent of the exact device geometry, some specific ones are especially interesting. The first one discussed in this chapter is the quantum point contact (QPC) 3.1, which shows, that electrons in a two-dimensional material can be confined to a single dimension, leading to a quantization of conductance. While this behavior is already seen without any interaction effects, an additional conductance feature, called* 0.7 *anomaly observed in QPCs shows, that interaction effects do indeed play a role and are strongest at low densities and dimensionality. This is investigated in Chapter 4. The second considered device is the Corbino disk, discussed in Sec. 3.2, which, due to its polar symmetry, leads to special behavior in magnetic field and is further investigated in Chapters 5 and 6.*

3.1 Quantum point contacts

Dimensionality is often an interesting aspect of quantum systems that can have strong implications for transport properties. As already discussed in Chapter 1, both monolayer and bilayer graphene are materials, that host a two-dimensional electron gas. Historically, two dimensional electron gases were usually realized by GaAs-AlGaAs heterostructures.

It is possible, to confine the electrons even further, by making them have to pass a very small bottleneck in this two dimensional landscape. This is called a quantum point contact (QPC), and the first experiments, where this confinement was of electrostatic nature were reported in Ref. [66, 67]. A schematic setup of a QPC device realized in dual gated bilayer graphene (BLG) is shown in Fig. 3.1. According to Bloch's theorem, electrons inside the periodic potential of a lattice can be represented by Bloch waves and form periodic energy bands of finite width. In most low energy situations, only one of these bands (a partially filled conduction band) contributes to the transport properties. In situations, where electron-electron interaction is weak, Coulomb interaction only leads to a small change in their effective mass, but they still behave very similar to non-interacting electrons. Then we can apply the result of the Landauer-Büttiker formula (B.42) derived in Sec. 2.3, where we just need to find the transmission coefficients of the corresponding single electron problem.

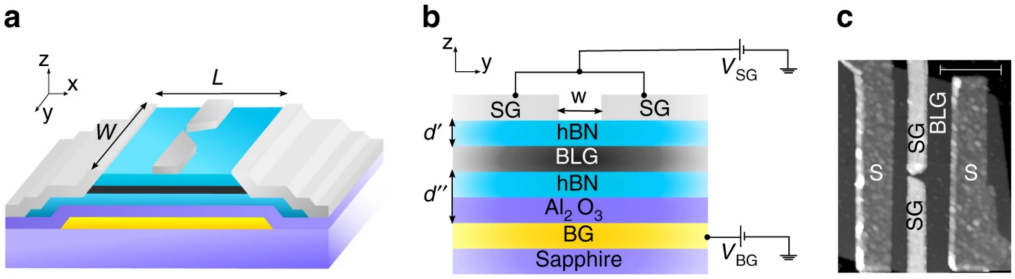

Figure 3.1: (a) Schematic illustration of a setup with a electrostatically formed QPC in BLG. (b) Cross-section of the setup along the dashed line in left panel. The QPC is tunable by the split gates (SG) and back gate (BG) (c) Atomic force microscopy image of the device
Adapted figure with permission from R. Kraft, J. Mohrmann, R. Du, et al. , Nat Commun, **9**, 1722 (2018). `https://www.nature.com/articles/s41467-018-04153-4`, licensed under CC BY 4.0

The presence of a confining potential along one of the directions clearly leads to the presence of size-quantized energy bands. A scenario, where these can be obtained analytically while still staying close to the experimental realization, where one applies perpendicular electric fields, that open a band gap in certain regions and thus confine in a very smooth manner, is the saddle point potential discussed in Ref. [68]. One assumes, that the local, confining potential can be modeled by

$$V(x,y) = V_0 - \frac{1}{2}m\omega_x^2 x^2 + \frac{1}{2}m\omega_y^2 y^2, \tag{3.1}$$

where we confine the electrons along the y direction. Due to electrostatic effects, this will also induce a potential along the x direction, in which transport is still possible. The full Hamiltonian is then

$$\left[\frac{-\hbar^2}{2m}\left(\partial_x^2 + \partial_y^2\right) + V(x,y)\right]\psi(x,y) = E\psi(x,y), \tag{3.2}$$

which is clearly separable into $\psi(x,y) = \phi(x)\chi(y)$. Along the y direction we find a quantum harmonic oscillator

$$\left[\frac{-\hbar^2}{2m}\partial_y^2 + \frac{1}{2}m\omega_y^2 y^2\right]\chi(y) = E_{y,n}\chi(y) \tag{3.3}$$

with the eigenenergies $E_{y,n} = \hbar\omega_y(n+1/2)$, which leads to the new problem

$$\left(-\frac{\hbar^2}{2m}\partial_x^2 + V_0 + E_{y,n} - \frac{1}{2}m\omega_x^2 x^2\right)\phi(x) = E\phi(x). \tag{3.4}$$

Thus we have formed bands with lower band edges determined by $V_0 + E_{y,n}$. Each of these bands forms a lead mode and for each of them, electrons are still subject to a one dimensional harmonic potential, through which they have to get transmitted. By solving this one dimensional problem, we find the transmission eigenvalues, that go into the Landauer-Büttiker formula Eq. (2.164). For the

given harmonic potential, these transmission eigenvalues are

$$T_n = \frac{1}{1+\exp(-\pi\varepsilon_n)}, \tag{3.5}$$

$$\varepsilon_n = \frac{2\left[E - \hbar\omega_y\left(n+\frac{1}{2}\right) - V_0\right]}{\hbar\omega_x}, \tag{3.6}$$

from which one obtains the total Landauer-Büttiker conductance

$$G = D\frac{e^2}{h}\int \mathrm{d}E\left(-\frac{\partial n_F(E)}{\partial E}\right)\sum_n T_n, \tag{3.7}$$

where in most situations $D = 2$ due to spin degeneracy. This means, that we find a conductance trace, that has clear steps at multiples of $D \times \frac{e^2}{h}$. Every time the chemical potential reaches the lower band edge of a new lead mode, we start a new step. The width and shape of the steps is determined both by the details of the constriction, and also by the temperature. The lower the temperature, the sharper the conductance steps appear.

3.1.1 Zeeman effect

If one applies a strictly in-plane magnetic field to a spin-degenerate two dimensional sample, the different spin projections couple with opposite sign to the magnetic field due to the Zeeman effect. This can be modeled with the Hamiltonian

$$\check{H} = \frac{\Delta E_z}{2}\check{\sigma}_z, \tag{3.8}$$

$$\Delta E_z = g\mu_B B, \tag{3.9}$$

where $\check{\sigma}_z$ is a Pauli matrix acting on spin space. As long as there is no spin-orbit coupling present, this simply leads to a splitting of the spin degenerate energy levels E_0 as

$$E_\sigma = E_0 + \frac{\sigma}{2}g\mu_B B, \tag{3.10}$$

where $\sigma = \pm 1$ labels the two spin species, μ_B is the Bohr magneton and g is called the Landé g-factor. For electrons in a vacuum, one finds $g = 2$, but interaction effects can renormalize this value [69].

If one now applies such a in-plane magnetic field to a QPC, spin degeneracy is lifted, so we should use $D = 1$. Moreover, the transmission values T_n are shifted by adding $\pm\Delta E_Z/2$, which can be seen as effectively shifting the height of the barrier, the different spin projections see, and thus to some extend as a spin filter. This means, that we reproduce Eq. (3.7) exactly for $B = 0$, but for high B we instead find steps at $1 \times \frac{e^2}{h}$ compared to the spin-degenerate $2 \times \frac{e^2}{h}$ as seen in Fig. 3.2. These additional steps appear for $\Delta E_Z > k_B T$, i.e. as soon the splitting can be resolved at the chosen temperatures. Any modification of the single particle energy bands can only lift degeneracies or influence the shape of the steps, but it can not lead to any additional features at other values.

3.1.2 The *0.7* anomaly

This is very different, if one takes into account interaction effects. A rather special phenomenon, where interaction effects are likely involved, is commonly known as the 0.7 conductance anomaly. It appears

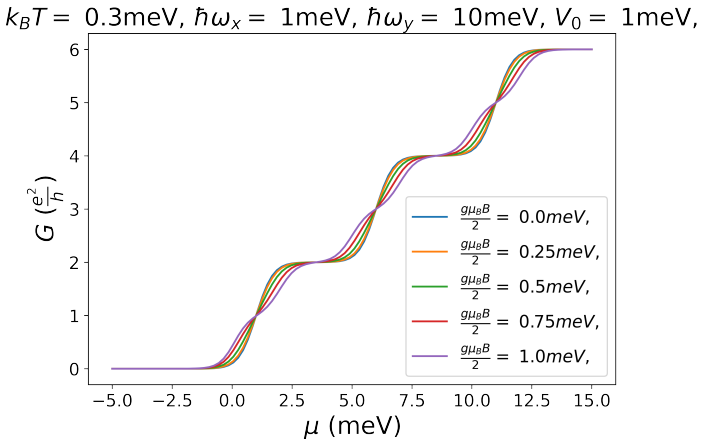

Figure 3.2: Conductance obtained from the Landauer-Büttiker formula with a saddle point potential from Eq. (3.7) for different in-plane magnetic field values.

as an additional shoulder in the quantized conductance of QPCs below the lowest plateau, usually close to the value

$$G \approx 0.7 \times 2\,\frac{e^2}{h}.$$

in spin degenerate systems. In the already mentioned GaAs QPCs it was first observed in Ref. [15], but it can be stated, that there is still no commonly accepted theory capable of explaining all features of this phenomenon. However, there are several microscopic theories that can explain some features of the phenomenon. These theories are based on several different physical mechanisms driven by electron-electron correlations. Under discussion are variants of the Kondo effect [70–75], Wigner crystallization [76–78], and other interaction-based mechanisms [79–85].

Specifically, several studies investigate the interplay between the QPC barrier and electron-electron interaction effects perturbatively. Why this interplay might be important for this phenomenon can be understood on a very simplistic level. If one considers local interaction, only the Hartree type processes involving electrons with opposite spin contributes, since the other one would be canceled by the Fock contribution. This repulsive interaction would effectively block the channel for one spin species for a certain amount of time, leading to a lower transmission ad thus lower conductance. Since this would not just lift any degeneracy of the system, it could lead to additional features in the conductance trace at values apart of multiples of $\frac{e^2}{h}$. The fact, that this additional feature is usually only observed below the very first conductance plateau, and not at higher values can be understood by taking into account, that interaction effects are enhanced at low densities, so would be strongest in the lowest size quantized subband.

There are several features of this anomaly, that a full theory should capture. First of all, it appears close to the value $0.7 \times 2\frac{e^2}{h}$ in spin degenerate samples, but the exact value does depend on the details of the device [15, 86, 87]. Very peculiarly, this shoulder shows a thermal activation behavior [87]. It is still visible at temperatures, where the normal quantized conductance steps are already too smeared to be experimentally resolved. This is shown in Fig. 3.3(d) taken from Ref. [73]. Interestingly, it strongly depends on an applied in-plane magnetic field. Starting from the value around $0.7 \times 2\frac{e^2}{h}$ it smoothly and continuously lowers into the value of the lowest Zeeman split band at $0.5 \times 2\frac{e^2}{h}$ [15, 86, 87]. This is shown in Fig. 3.3(a) taken from Ref. [73], where one sees it appear in the lowest conductance step

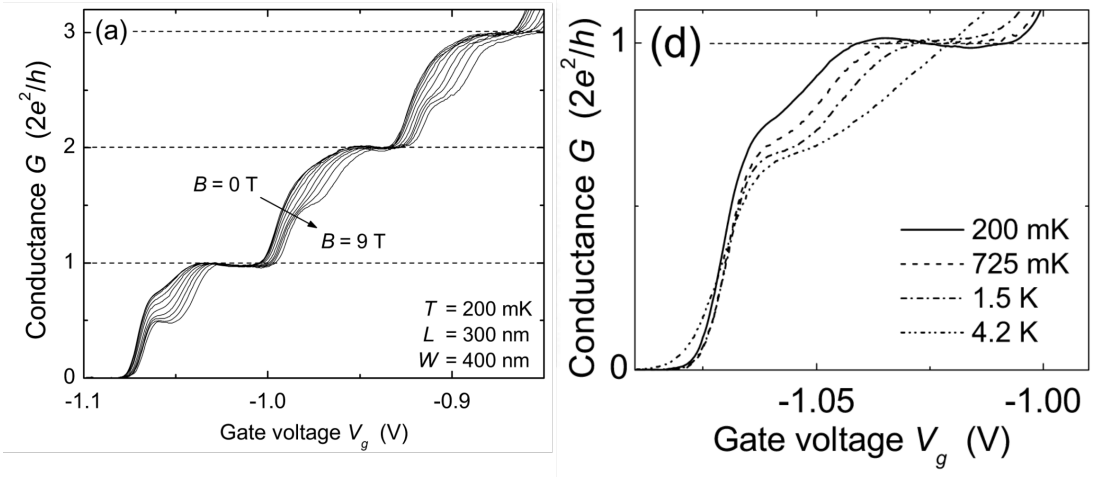

Figure 3.3: (a)The differentiated differential conductance G as a function of the voltage V_g controlling the gates that form the QPC in a GaAs/AlGaAs heterostructure measured at 200 mK with in-plane magnetic fields between 0 and 9 T. The 0.7 shoulder is present only in the lowest conductance step and visible at vanishing magnetic field. For finite magnetic field it continuously transitions into the Zeeman split level. (d) Temperature dependence of the conductance feature in the lowest conductance plateau at vanishing magnetic field for different temperatures between 200 mK and 4.2 K. The features becomes stronger for higher temperatures, while the shape of the regular conductance step is continuously smoothened.
Reprinted figures with permission from E. J. Koop, A. I. Lerescu, J. Liu, B. J. van Wees, D. Reuter, A. D. Wieck and C. H. van der Wal , Journal of Superconductivity and Novel Magnetism volume **20**, 433-441 (2007). `https://link.springer.com/article/10.1007/s10948-007-0289-5`, licensed under CC BY-NC 2.0

and continuously transition into the lowest Zeeman split level. For even higher magnetic fields, one can observe so called 0.7 analogues [88], which appear, when two subbands of opposite spin cross. This is the reason, why theories involving all sorts of spin polarization were taken into account. Finally, if one takes a look at the non-linear conductance at finite source-drain bias voltages, one observes a peak around zero source-drain bias, which is known as the zero-bias peak [83, 87].

3.1.2.1 Microscopic theories

As already mentioned, the 0.7 anomaly in the QPC conductance curve is seen as an additional shoulder below the lowest plateau sitting at around $0.7 \times 2\,e^2/h$ [15] for systems without degeneracies other than spin-degeneracy. It has been subject of intense experimental studies in GaAs/AlGaAs heterostructures for both electrons [15, 71, 75, 83, 85–96], and holes [97–103]; signatures of the 0.7 anomaly have also been observed in Si/SiGe heterostructures [104].

This phenomenon is beyond the single-particle picture [9, 105], and it is commonly linked to spin [15, 86]. In addition, it appears to be thermally activated and therefore not a ground-state property [87]. Moreover, experiments show that the details of the confinement potential seems to play a crucial role in the strength and exact position of this conductance feature [95, 96]. Theoretically, various explanations have been suggested to capture the physical origin of the 0.7 anomaly. These include dynamical spin polarization or spin gap models due to electron-electron interaction [20, 87, 89, 103,

106, 107],the Kondo effect [70–72, 102, 108–111], Wigner crystallization [112–114], or charge density waves [77]. To our knowledge, no comprehensive study of the interaction-induced 0.7 anomaly in systems where both spin and valley degrees of freedom are degenerate has been reported so far.

We here summarize two possible explanations for its appearance.

3.1.2.2 Interplay of interaction effects and constriction

In Refs. [83, 84, 115] it is argued, that the only ingredients for a full microscopic model are an on-site potential and a Hubbard-like onsite density-density interaction of opposite spins. Further they restrict the situation to a one-dimensional model, describing only the lowest quasi-one-dimensional mode that passes the constriction, as the anomaly is only seen below the first plateau using the discretised Hamiltonian

$$\mathcal{H} = \sum_{i,\sigma} \left[E_{i\sigma} \hat{n}_{i\sigma} - t_i \left(\hat{c}^\dagger_{i+1,\sigma} \hat{c}_{i\sigma} + \text{h.c.} \right) \right] + \sum_i U_i \hat{n}_{i\uparrow} \hat{n}_{i\downarrow}, \tag{3.11}$$

where $\hat{n}_{i\sigma} = \hat{c}^\dagger_{i,\sigma} \hat{c}_{i\sigma}$ is the number of electrons on site i with spin projection σ, $E_{i\sigma} = E_i - \sigma \Delta E_z/2$ is the potential energy in an in-plane magnetic field, U_i the local interaction and t_i the next neighbor hopping parameter. First of all it should be pointed out, that, as long as spin is the only quantum degree of freedom, in a local interaction the Hartree and Fock term for parallel spins exactly cancel, so it makes sense to consider an effective Hubbard interaction.

Reference [83] discusses the static situation assuming a parabolic barrier top and shows, that the local density of states, which in semi-classical terms is related to the inverse velocity, has a strong maximum a bit above the band minimum, before the channel is completely open. This reflects, that electrons with this energy are the slowest. Since a large density-of-states also amplifies interaction effects, these electrons also interact the strongest. These interaction effects change the effective barrier height, in a naive calculation it would be changed by Hartree typer terms of the self-energy, which increase the barrier height proportional to the density in exactly this band, which is thus pinned to the chemical potential. Thus their transmission and conductance is reduced. Using a functional renormalization group approach, they are able to find the mentioned zero bias peak in their model, although the 0.7 anomaly itself is not reproduced very clearly. Notably, the do not find a static spin polarization, that is often invoked in explanations and they also don't see any signs of a quasi-localized state at the top of the barrier, that is needed for Kondo-based explanation.

This point is further investigated in Ref. [84], where the model introduced in Ref. [83] is extended to a general barrier shape including a quantum dot, where one would expect a Kondo effect. They observe, that for low energies, the behavior derived from the Kondo effect and the general miscroscopic model are indeed very similar, but for higher energies they are different. Considering different barrier-top potentials, they also argue, that the exact value of the 0.7 anomaly should indeed depend on the details of the constriction.

Finally, in Ref. [115] the dynamical behavior of such a model is investigated. They conclude, that, while there is no static spin polarization in this model, there is indeed a slowly fluctuating spin structure, which, as long as electrons traverse the constriction fast enough, will have similar effects as a static spin polarization, thus giving those theories an effective validity.

This numerical analysis should be compared to Ref. [80], where a similar situation is investigated using kinetic equations, but the considered interaction does not conserve momentum. There it is argued, that elastic scattering inside the constriction only leads to a weak renormalization of the effective potential, but it is the inelastic processes, that lead to the 0.7 anomaly.

As to a purely perturbative treatment including the full Coulomb interaction, Ref. [81] could show, that several effects like the general expected temperature dependence can be explained by combining non-equilibrium perturbation theory with a WKB description of the states involved in the scattering off the barrier, but the gate-voltage dependence at elevated temperatures, where the shoulder-like feature could be seen, is in fact inaccessible in this approach.

3.1.2.3 Free energy with interaction effects

Alternatively one could take a look at the perturbative interaction effects on the free energy. A similar treatment was performed in [116, 117] to find instabilities in transition metal dichalcogenides, which like graphene or bilayer graphene posses two valleys, but additionally possesses strong intrinsic spin-orbit coupling. The general idea is to find corrections to the free energy $\mathcal{F}$, that lead to a non-trivial groundstate, where bands can have individual chemical potentials that differ from the Fermi energy of the non-interacting system and thus also different densities. The two valleys $\xi = \pm$ are positioned at the $\pm\mathbf{q}_0$ in k space, which is a large momentum. Then one can construct three matrix elements of the Coulomb interaction

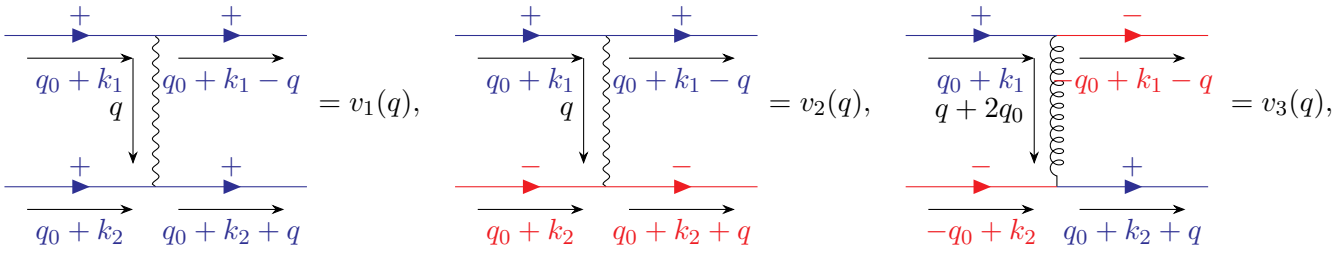

(3.12)

where the spin σ is conserved at each vertex. The first two matrix elements $v_1(q)$ and $v_2(q)$ denote intra-valley scattering. The transferred momentum is very small and we can approximate it by it's value at $q = 0$, which is kept finite by screening. In case $v_3(q)$ the momentum transfer is on the order of the valley separation and thus very large, thus we can fix it by it's value at $q = 2q_0$ and introduce

$$V = v_1(q) = v_2(q) \approx V_{\text{Coulomb}}(q = 0), \tag{3.13}$$

$$U = v_3(q) \approx V_{\text{Coulomb}}(q = 2q_0). \tag{3.14}$$

Corrections to the free grand canonical potential per unit area Ω_0 are then given by

$$\Omega - \Omega_0 = \frac{i}{T} \log\langle 0|\mathcal{S}|0\rangle = \sum \text{ connected vacuum diagrams}, \tag{3.15}$$

where

$$\mathcal{S}(t, t_0) = \mathcal{T} \exp\left\{-i \int_{t_0}^{t} \mathrm{d}t_1 \hat{U}_I(t_1)\right\} \tag{3.16}$$

is the time evolution operator of the system with the interaction operator U_I in interaction representation.

The free grand canonical potential can be found from the Green's function. Assuming, that the index a labels any kind of additional degree of freedom (spin, valley, etc), a general non-interacting

Green's function in Matsubara formalism will look like

$$G_a(i\omega, \mathbf{k}) = \frac{1}{i\omega - \varepsilon_a(\mathbf{k}) + \mu_a}. \tag{3.17}$$

One then looks at the expression

$$\Omega_0 = T \sum_\omega \sum_a \int \frac{\mathrm{d}^d k}{(2\pi)^d} \tag{3.18}$$

and performs the Matsubara summation

$$\begin{aligned}
&T \sum_\omega \log\left(i\omega - \xi + \mu\right) \exp(i\omega\tau) \\
&= \int_{-\infty}^{\infty} \frac{\mathrm{d}\varepsilon}{2\pi i} \Big\{ \log(\varepsilon + i\delta - \xi + \mu) - \log(\varepsilon - i\delta - \xi + \mu) \Big\} n_F(\varepsilon) \exp(\varepsilon\tau) \\
&= -\frac{1}{\beta} \int_{-\infty}^{\infty} \frac{\mathrm{d}\varepsilon}{2\pi i} \Big\{ \log(\varepsilon + i\delta - \xi + \mu) - \log(\varepsilon - i\delta - \xi + \mu) \Big\} \exp(\varepsilon\tau) \partial_\varepsilon \log\Big(1 + \exp(-\beta\varepsilon)\Big) \\
&= \frac{1}{2\pi\beta} \int_{-\infty}^{\infty} \mathrm{d}\varepsilon \left\{ \frac{1}{\varepsilon + i\delta - \xi + \mu} - \frac{1}{\varepsilon - i\delta - \xi + \mu} \right\} \log\Big(1 + \exp(-\beta\varepsilon)\Big) \\
&= \frac{-1}{\beta} \int_{-\infty}^{\infty} \mathrm{d}\varepsilon \delta(\varepsilon - \xi + \mu) \log\Big(1 + \exp(-\beta\varepsilon)\Big) \\
&= -\frac{1}{\beta} \log\Big(1 + \exp\Big(-\beta(\xi - \mu)\Big)\Big),
\end{aligned} \tag{3.19}$$

where we used partial integration and $\frac{1}{x \pm i\delta} = \mathcal{P}\left(\frac{1}{x}\right) - i\pi\delta(x)$. Thus we find

$$\Omega_0 = T \sum_\omega \sum_a \int \frac{\mathrm{d}^d k}{(2\pi)^d} \log\left(\frac{1}{i\omega - \varepsilon_a(k) + \mu_a}\right) = -T \int \frac{\mathrm{d}^d k}{(2\pi)^d} \sum_a \log\left(1 + \exp\left(\frac{\mu_a - \varepsilon_a(k)}{k_B T}\right)\right). \tag{3.20}$$

which is indeed the definition of the grand canonical potential per unit area. Since we are usually interested in the low temperature regime, i.e. large $\beta = 1/(T)$, the exponential is very small and we can rewrite the logarithm as a series around 1:

$$\log(1 + x) = -\sum_{n=1}^{\infty} \frac{(-x)^n}{n} \tag{3.21}$$

Thus we get

$$\Omega_0 = T \sum_a \sum_{n=1}^{\infty} \frac{(-1)^n}{n} \int \frac{\mathrm{d}^d k}{(2\pi)^d} e^{-n\beta(\varepsilon_a(k) - \mu_a)}. \tag{3.22}$$

From this we can especially extract the free density $n_\alpha^{(0)}$

$$n_a^{(0)} = -\frac{\partial \Omega_0}{\partial \mu_a} = \int \frac{\mathrm{d}^d k}{(2\pi)^d} \frac{1}{1 + \exp\Big(\beta(\varepsilon_a(k) - \mu_a)\Big)} \tag{3.23}$$

as expected.
Making the spin (σ) and valley (ξ) degree of freedom explicit, i.e. $a = \omega\xi$, the first order corrections are given by the bubble diagrams involving one interaction line. They fall into three subsets. Fock-like corrections exist for both U and V, but do not mix different spins and are shown in Eq. 3.25

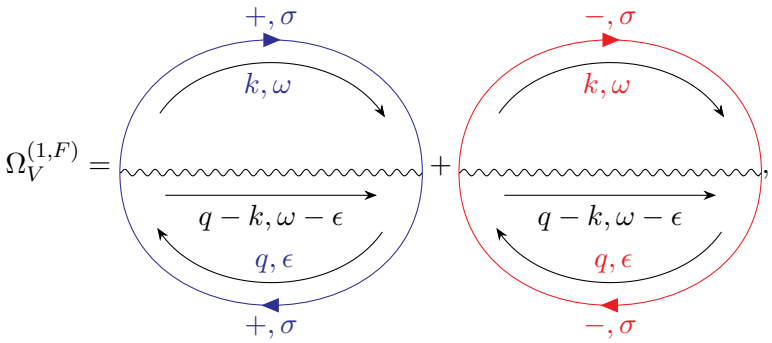

(3.24)

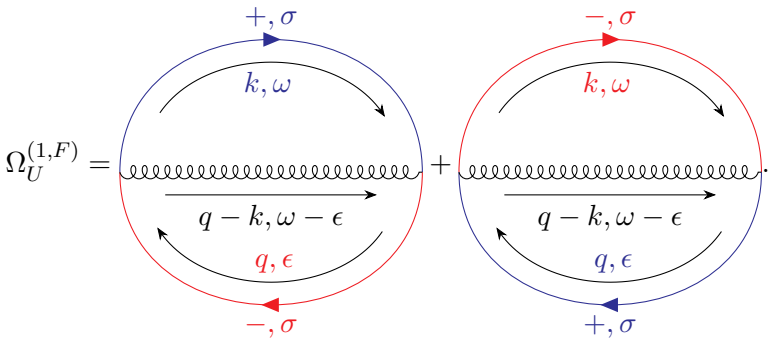

(3.25)

Hartree like terms only exist for zero momentum transfer i.e. V, but can mix different spins.

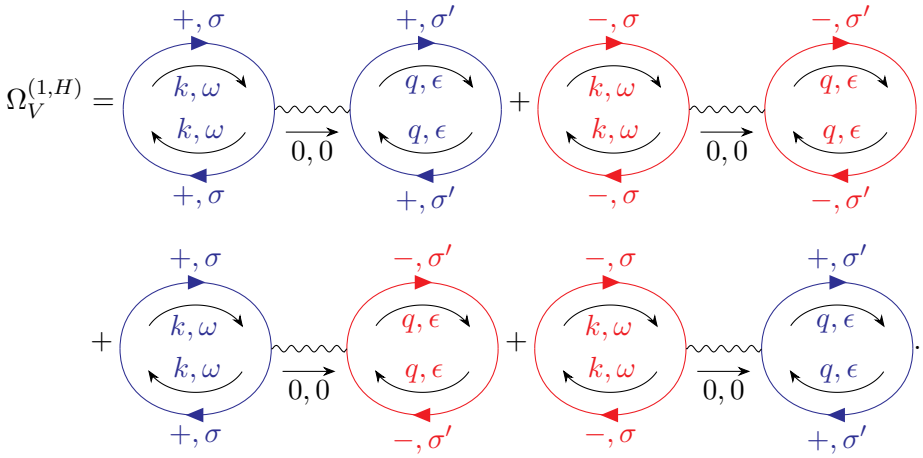

(3.26)

The first line of Eq. 3.25 is for example given by

$$\Omega_V^{(1,F)} = \sum_\sigma T^2 \sum_{\omega,\epsilon} \int \frac{\mathrm{d}^d k \mathrm{d}^d q}{(2\pi)^{2d}} V \left[G_{+,\sigma}(i\omega, \mathbf{k}) G_{+,\sigma}(i\epsilon, \mathbf{q}) + G_{-,\sigma}(i\omega, \mathbf{k}) G_{-,\sigma}(i\epsilon, \mathbf{q}) \right]$$
$$= V \sum_\sigma \sum_\xi \left(\left[T \sum_\omega \int \frac{\mathrm{d}^d k}{(2\pi)^d} G_{\xi,\sigma}(i\omega, \mathbf{k}) \right]^2 \right), \tag{3.27}$$

The second line is

$$\Omega_U^{(1,F)} = \sum_\sigma T^2 \sum_{\omega,\epsilon} \int \frac{\mathrm{d}^d k \mathrm{d}^d q}{(2\pi)^{2d}} U \left[G_{+,\sigma}(i\omega, \mathbf{k}) G_{-,\sigma}(i\epsilon, \mathbf{q}) + G_{-,\sigma}(i\omega, \mathbf{k}) G_{+,\sigma}(i\epsilon, \mathbf{q}) \right]$$
$$= U \sum_\sigma \sum_\xi \left(\left[T \sum_\omega \int \frac{\mathrm{d}^d k}{(2\pi)^d} G_{\xi,\sigma}(i\omega, \mathbf{k}) \right] \left[T \sum_\omega \int \frac{\mathrm{d}^d k}{(2\pi)^d} G_{-\xi,\sigma}(i\omega, \mathbf{k}) \right] \right), \tag{3.28}$$

while the Hartree terms are

$$\Omega_V^{(1,H)} = -V \sum_{\sigma,\sigma'} \sum_{\xi,\xi'} \left[T \sum_\omega \int \frac{\mathrm{d}^d k}{(2\pi)^d} G_{\xi,\sigma}(i\omega, \mathbf{k}) \right] \left[T \sum_\omega \int \frac{\mathrm{d}^d k}{(2\pi)^d} G_{\xi',\sigma'}(i\omega, \mathbf{k}) \right] \tag{3.29}$$

The full correction is thus given by

$$\Omega^{(1)} = \Omega_V^{(1,F)} + \Omega_U^{(1,F)} + \Omega_V^{(1,H)}$$
$$= U \sum_\sigma \sum_\xi \left(\left[T \sum_\omega \int \frac{\mathrm{d}^d k}{(2\pi)^d} G_{\xi,\sigma}(i\omega, \mathbf{k}) \right] \left[T \sum_\omega \int \frac{\mathrm{d}^d k}{(2\pi)^d} G_{-\xi,\sigma}(i\omega, \mathbf{k}) \right] \right)$$
$$- V \left(\sum_{\sigma,\sigma'} \sum_{\xi,\xi'} - \sum_{\sigma=\sigma'} \sum_{\xi=\xi'} \right) \left[T \sum_\omega \int \frac{\mathrm{d}^d k}{(2\pi)^d} G_{\xi,\sigma}(i\omega, \mathbf{k}) \right] \left[T \sum_\omega \int \frac{\mathrm{d}^d k}{(2\pi)^d} G_{\xi',\sigma'}(i\omega, \mathbf{k}) \right]. \tag{3.30}$$

In any case we just need to calculate

$$T \sum_\omega \int \frac{\mathrm{d}^d k}{(2\pi)^d} G_{\xi,\sigma}(i\omega, \mathbf{k}) = \int \frac{\mathrm{d}^d k}{(2\pi)^d} n_F \left(\varepsilon_{\xi\sigma}(k) - \mu_{\xi\sigma} \right) = n_{\xi\sigma}^{(0)}, \tag{3.31}$$

which will depend on the band structure. The grandcanoncical potential can to first order be written as

$$\Omega = \Omega_0 + U \sum_\sigma \sum_\xi \left(\left[n_{\xi,\sigma}^{(0)} \right] \left[n_{-\xi,\sigma}^{(0)} \right] \right) - V \left(\sum_{\sigma,\sigma'} \sum_{\xi,\xi'} - \sum_{\sigma=\sigma'} \sum_{\xi=\xi'} \right) \left[n_{\xi,\sigma}^{(0)} \right] \left[n_{\xi',\sigma'}^{(0)} \right], \tag{3.32}$$

$$n_{\xi\sigma}^{(0)} = -\frac{\partial \Omega_0}{\partial \mu_{\xi\sigma}}. \tag{3.33}$$

In the end, we are looking for the free energy, which is given by

$$F = \Omega + \sum_a \mu_a n_a = \Omega - \sum_a \mu_a \frac{\partial \Omega}{\partial \mu_a} \tag{3.34}$$

and look for solutions, which fulfill the condition, that $n = \sum_a n_a = const.$ by introducing a Laplace multiplier and thus minimizing

$$\bar{F} = F - \mu n, \tag{3.35}$$

where at higher orders, we find corrections to n. In general we can perform an expansion up to second order, which would look like

$$\bar{F} = \sum_{\sigma,\xi} c_a^{(1)} n_a + \sum_{\sigma,\xi} c_a^{(2)} n_a^2 + \sum_{a \neq b} \gamma_{ab} n_a n_b - \mu n, \tag{3.36}$$

which is exactly the generalized phenomenological free energy, that is minimized in Ref. [20] to find the pinning of the overall chemical potential μ to minority subbands that leads to the 0.7 anomaly. The coefficients can be related to microscopic parameters of the band structure by calculating F to at least first order and then performing the expansion in powers of n_a. This relationship is beyond the scope of this work. Since the tuning of the band structure by external gates in bilayer graphene is quite intricate, one should not expect to be able to find the correct coefficients from a simple microscopic consideration, but for the very simple case considered in Refs. [116, 117] a similar instability is indeed found analytically.

3.1.3 Fabry-Pérot oscillations

While the quantized conductance in QPCs is due to the one-dimensional nature of the modes traversing the constriction, the device as a whole is still two-dimensional. This part of its nature shows up in a feature called Fabry-Pérot oscillations. This feature is the electron-wave equivalent to Fabry-Pérot oscillations in classical wave-optics, where light of a well defined frequency bounces inside an optical resonator, defined by two partially reflective surfaces. A wave of a fixed wavelength hits the surface with a certain angle, getting partially reflected and transmitted with a certain different angle. The transmitted wave hits the second interface, where it again gets partially reflected and transmitted. In summary, waves that leave the interferometer have thus traveled over different lengths until reaching that point. If the difference in times of flight is a multiple of the wavelength, we have positive interference and the amplitude will be noticeable increased. The same happens to electronic wavefunctions in the two dimensional regions of a QPC. For a given density, determined by the gates used to tune the sample, we find even waves with a fixed Fermi-wavevector k_F originating from one of the leads. In the QPC region, away from a very small point in space, the split-gates effectively form a barrier to a thin region of different density, from which electrons either get reflected or transmitted. The angle of transmission ensures conservation of energy, while the momentum-component perpendicular to the barrier is kept constant. The same happens at the other interface between the QPC barrier and the two dimensional region and also to some extend at the interface between BLG and the leads. Simplistically, the transmission coefficient accounting for the Fabry-Pérot resonance can be described by

$$\mathcal{T} = \frac{1}{1 + F \sin^2\left[Lk\cos(\theta)\right]}, \tag{3.37}$$

where F is the finesse and θ is the angle of incidence of the electron wave and L the distance between the plates. At very low temperatures, the contribution of the resonance to the conductance is given by

$$G = \frac{e^2}{h} \frac{1}{1 + F \sin^2\left(Lk_F\right)}. \tag{3.38}$$

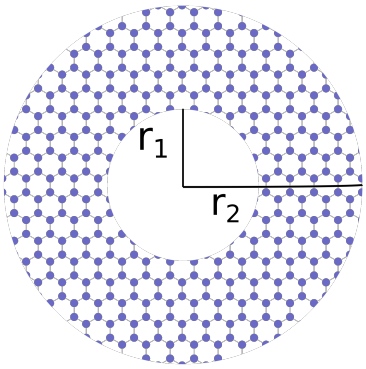

Figure 3.4: A Corbino disk consists of a circular slap of graphene with radius r_2, which has a hole of radius r_1 in the middle. We will assume, that a constant current I is transmitted from a source in the origin, an voltage is measured between electrodes placed at the inner and outer radius. The honeycomb lattice is not shown true to size. Effects related to the exact edge termination are not relevant at the considered scales.

In a realistic situation, the gate configuration changes both the Fermi momenta in the two dimensional region and underneath the splitgates and the effective length L due to electrostatic effects. For this reason it is quite difficult, to exactly predict the gate dependence of Fabry-Pérot oscillations. A quite thorough study of Fabry-Pérot interferences in BLG can be found in Ref. [118].

3.1.4 Summary

Quantum point contacts are a very important building block of nano-technology and explicitly show the quantum nature of electrons. In Sec. 3.1 we discussed, how one can explain the observed quantization of conductance by means of the Landauer theory introduced in Sec. 2.3. The difference between most two dimensional electron gases, which only possess a spin degree of freedom to bilayer graphene, as discussed in Sec. 1.2, is the additional valley degree of freedom, which leads to an additional factor of two and thus conductance steps of $4\frac{e^2}{h}$. Such a bilayer graphene quantum point contact is investigated in Chapter 4, where these steps are exactly found experimentally. Moreover, there we also find a version of the 0.7 anomaly discussed in Sec. 3.1.2 and explain it with a phenomenological model, that combines the ideas of Sec. 3.1.2.2, i.e. a slowly oscillating spin-polarization, with the free energy calculation presented in Sec. 3.1.2.3. We will also observe Fabry-Pérot oscillations as discussed in Sec. 3.1.3.

3.2 Corbino geometry

A geometric setup, that is of particular interest for transport measurements is the Corbino geometry, which is shown in Fig. 3.4. In all situations we will restrict ourselves to perpendicular magnetic fields. In this case, the setup is rotationally invariant and all quantities can only depend on the radial coordinate r, choosing polar coordinates $\mathbf{r} = (r, \vartheta)$. In a situation, where current I is fixed and charge

conserved, we find for every radius r

$$\begin{aligned} I &= \int \mathrm{d}\mathbf{A} \cdot \mathbf{j} = \int (r\mathrm{d}\varphi)\mathbf{e}_r \cdot \mathbf{j} \\ &= 2\pi r j_r. \end{aligned} \tag{3.39}$$

Due to charge conservation this holds for any radius r and thus

$$j_r(r) = \frac{I}{2\pi r}. \tag{3.40}$$

In polar coordinates we further have $\mathbf{E} = E_r \mathbf{e}_r$ and thus

$$j_r = \sigma_{rr} E_r, \quad j_\vartheta = \sigma_{\vartheta r} E_r. \tag{3.41}$$

Using the symmetry properties of the conductivity we found in the last chapter and a constant conductivity we thus find

$$\sigma_{rr} = \sigma_{xx}, \tag{3.42}$$

$$E_r = \frac{I}{2\pi\sigma_{xx} r}, \quad R = \frac{U}{I} = \frac{1}{2\pi\sigma_{xx}} \log\left(\frac{r_2}{r_1}\right), \tag{3.43}$$

i.e. the magnetoresistance $R(B)$ is determined solely by σ_{xx} and thus we find a quadratic magnetoresistance already in this simple model.

$$R(B) = \frac{1}{2\pi} \log\left(\frac{r_2}{r_1}\right) \frac{d}{e^2 v_g^2} \frac{1 + (\omega_c(\mu)^2 \tau_\mu^2)}{\tau_\mu \nu(\mu)}. \tag{3.44}$$

This is in contrast to the Hall Bar setup, where magnetoresistance is determined by

$$\rho_{xx} = \frac{-\sigma_{xx}}{\sigma_{xx}^2 + \sigma_{xy}^2} = \frac{-1}{\sigma_{xx}(1 + (\omega_c(\mu)^2 \tau_\mu^2))} = \frac{d}{e^2 v_g^2} \frac{1}{\tau_\mu \nu(\mu)} \tag{3.45}$$

and is actually independent of the magnetic field in this approximations.

3.2.1 Summary

The Corbino geometry is special, since even with a perpendicular magnetic field, it preserves radial symmetry and quantities can only depend on the radial coordinate r. As such, a Corbino disk somewhat resembles an infinitely wide strip geometry. The magnetoresistance in a Corbino disk is especially simple, since it only depends on the longitudinal conductivity σ_{xx}. We will consider a monolayer graphene Corbino disks in Chapter 5 in a perpendicular magnetic field and at low temperatures. Depending on the strength of the perpendicular magnetic field, one can then either use the semi-classical result (2.29) in low magnetic fields or the perturbative result (2.160) for quantizing magnetic fields. The large field limit has to be used, if Landau levels are clearly separated. If they are sufficiently smeared by disorder, the semi-classical limit is sufficient. Since the dependence on the magnetic field is rather simple (quadratic), one may use the density dependence, which is different for scattering off short range scatterers or charged particles, to characterize these types of disorder and extract the true bulk mobility, which is usually disguised by the large contact resistance in these clean samples.

In Chapter 6 a similar system is considered at elevated temperatures without a magnetic field. In this case, one makes use of the hydrodynamic equations discussed in Sec. 2.4 and the practical description of the problem in polar coordinates. In principle, one can also include small perpendicular magnetic fields in this setup and again observe the magnetoresistance, but it turns out, that we observe non-trivial behavior already without such a field.

3.3 Summary and conclusions

In this chapter we have discussed the two device geometries, that are studied in the main part of this thesis. The first one is a quantum point contact in bilayer graphene (Sec. 1.2) in an in-plane magnetic field, discussed in Sec. 3.1. By quantizing the momentum and thus the energy of the bands along one more direction, one obtains a quantized energy spectrum, where the chemical potential determines, how many of these bands are filled. Each of these filled bands contribute a conductance quantum $2 \times \frac{e^2}{h}$ to the overall device conductance for a system with spin degeneracy. In an in-plane magnetic field, spin degeneracy is lifted and each spin projections sees a different effective barrier, leading to quantized steps of $1 \times \frac{e^2}{h}$ in the conductance.

If one takes a look at the experimentally obtained curves at slightly elevated temperature (a few mK), an additional shoulder below the first plateau appears in zero magnetic field, close to the value of $0.7 \times 2 \times \frac{e^2}{h}$ in spin degenerate systems. This feature smoothly transitions into the $1\frac{e^2}{h}$ plateau for larger in-plane magnetic fields and shows a curious temperature activation behavior. Several theories were proposed and discussed in Sec. 3.1.2.1 to explain this feature, but a final answer has not yet been found.

Additionally, the fact that electrons don't get transmitted with unit probability through the constriction leads to effects similar to those in a Fabry-Pérot interferometer in optics, leading to small oscillations on top of the conductance curves discussed in Sec. 3.1.3. All of this will be applied to experimental data obtained in a bilayer graphene quantum point contact in Chapter 4

Then, we introduced the second considered device, a Corbino disk in monolayer graphene in Sec. 3.2, which is of special interest, since it has a particularly easy magnetoresistance determined solely by the longitudinal conductivity due to its rotational symmetry. This system is considered in the disorder dominated regime in Chapter 5, where depending on the strength of the magnetic field compared to disorder, one can describe the longitudinal conductivity either by the semi-classical result (2.29) or the perturbative result (2.160), if Landau levels are clearly separated.

Secondly, we consider the same monolayer graphene Corbino disk in Chapter 6 without a magnetic field at elevated temperatures. There electron-electron interaction starts to dominate and one can use the hydrodynamic description discussed in Sec. 2.4 to describe the system. Already at zero magnetic field, we obtain interesting effects related to the finite viscosity, due to electron-electron interaction.

Chapter 4

4 Interaction effects in a bilayer graphene quantum point contact

Mesoscopic transport in the ballistic regime is usually described quite well without taking interaction effects into account. In the case of a quantum point contact investigated in this chapter, one may apply the Landauer-Büttiker formula Eq. (2.164) *to find the quantized conductance as discussed in Sec. 3.1. The only special effect of the used material, bilayer graphene, is then the additional valley degeneracy. However, there are certain cases in which interaction effects are indeed visible.*

A very prominent and still largely unresolved example is the 0.7 *conductance anomaly in quantum point contacts (QPCs), which manifests as an additional shoulder at around* $0.7 \times 2\frac{e^2}{h}$ *within the first conductance step. The special temperature and magnetic field dependence of this feature have inspired several competing microscopic explanations and a lot of experiments have been conducted to test these. An overview on different microscopic explanations was already given in Sec. 3.1.2.1 and a closer look at a very fundamental explanation was given in Sec. 3.1.2.2.*

Bilayer graphene (BLG) quantum point contacts are a very interesting platform to study interaction effects like the 0.7 anomaly or the renormalization of the Landé g-factor, due to its additional valley degree of freedom, as discussed in Sec. 1.2. Moreover, the easy gate tunability of the density of states and thus electron-electron interaction strength is a feature that is not accessible in most other systems. While in most materials, the gates, which are needed to tune the spectrum, can lead to a strong suppression of electron-electron interaction due to screening, it was demonstrated that this gate screening is only able to strongly suppress electron-electron interaction in mono- and bilayer graphene, when they are closer than a few nm, which is experimentally inaccessible [119]. For this reasons one can indeed expect to see and be able to tune electron-electron interaction effects in BLG QPCs.

The reason to specifically consider a QPC setup is the additional amplification of interaction effects in lower dimensions and at low densities. While previous studies have investigated BLG QPCs in parallel magnetic field (Ref. [120] and Ref. [52]), the chosen setups, where the QPC constriction was very wide compared to the experiment presented here, did not allow for the observation of interaction effects that is possible here. Although the conductance data at the lower temperature of 20 *mK presented here shows both an additional conductance shoulder and Fabry-Pérot oscillations on top of the quantized conductance curves, the data at higher temperature* 4 *K does not show any Fabry-Pérot references anymore and the conductance steps are clearly smoothened. However, the additional shoulder still survives, showcasing the well reported thermal activation behavior of the* 0.7 *anomaly. A phenomenological model is used to show, how a* 0.7 *anomaly could manifest in a BLG QPC and how the*

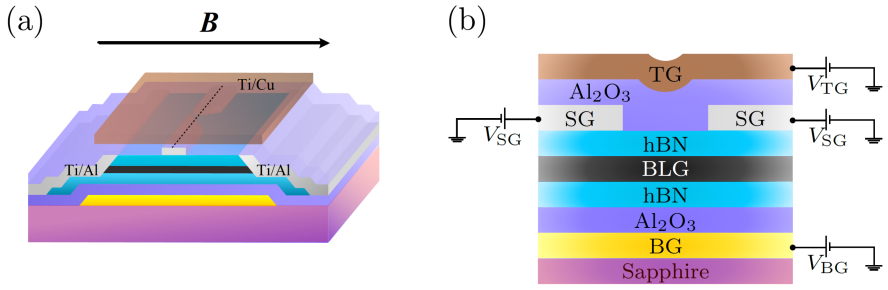

Figure 4.1: (a) Schematic illustration of the setup with the QPC formed in BLG subject to the in-plane magnetic field B. In experiment, the magnetic field B is oriented in plane with an angle of approximately 45° with regard to the black dashed line. (b) Cross-section of the setup along the dashed line in left panel. The QPC is tunable by the split gates (SG), back gate (BG), and top gate (TG).
Reprinted figure with permission from Vanessa Gall, Rainer Kraft, Igor V. Gornyi, and Romain Danneau, Phys. Rev. Research, **4**, 023142 (2022). `https://journals.aps.org/prresearch/abstract/10.1103/PhysRevResearch.4.023142`, licensed under CC BY 4.0

behavior with in-plane magnetic field can be used to distinguish them in an experiment. Finally, this is applied to an experimental setup.

In this Chapter we try to answer the question which role effects due to electron-electron interaction play for the conductance of a bilayer graphene quantum point contact and how they are different from single valley materials. The answer we find is, that interaction effects visibly change the conductance curves by introducing the additional 0.7 ***shoulder, which in bilayer graphene, as in other two dimensional electron gases, can be modeled by an effective spin splitting, while valley remains degenerate.***

The content of this chapter is published in [19] and is based on joint theory- experimental work with Romain Danneau and Rainer Kraft from KIT.

Reprinted excerpts with permission from Vanessa Gall, Rainer Kraft, Igor V. Gornyi, and Romain Danneau, Phys. Rev. Research, 4, 023142 (2022). `https://journals.aps.org/prresearch/abstract/10.1103/PhysRevResearch.4.023142`, *licensed under CC BY 4.0*

4.1 Introduction

Exploiting the quantum degrees of freedom of charge carriers offers a potential route for designing new types of quantum electronic devices. While most studied systems involve the electron's spin degree of freedom aiming at spintronic applications [121, 122], more recently the additional valley isospin in a variety of materials has attracted a growing interest for use in valleytronics [123]. However, irrespective of the system of choice, the implementation of spin- or valley-based functionalities into electronic devices requires a full control of the quantum state itself. A quantum point contact that confines charge carriers into one dimension [124], is one of the basic building blocks for efficient injection, control, and read-out measures.

Recently, a similar system of an electrostatically-induced quantum point contact (QPC) in bilayer graphene (BLG) [49, 52, 125–131], *i. e.*, a system with four-fold spin and valley degeneracy, where the constriction is realized by local band gap engineering with a displacement field perpendicular to the

BLG plane was investigated in [21]. There, confinement with well-resolved conductance quantization in steps of $4\,e^2/h$ down to the lowest one-dimensional (1D) subband, as well as a peculiar valley subband splitting and merging of K and K' valleys from two non-adjacent subbands in an out-of-plane magnetic field (see also Ref. [128]) was observed.

Here, we investigate the same system in an in-plane magnetic field. In this context, we became aware of the publication [129] that reported on conductance measurements in a similar setup and found certain features additional to the expected conductance quantization. These features were attributed [129] to the substrate-induced Kane-Mele spin-orbit coupling [132] below the lowest plateau. Since the reported values of the spin-orbit coupling in monolayer graphene is of the order of $40\,\mu$eV [133] (corresponding to temperatures of the order of 0.5 K) and there is no clear mechanism that would lead to an enhancement of spin-orbit coupling by hexagonal boron nitride (hBN), we expect another mechanism behind such features. Here, we explore alternative possibilities for the explanation of the appearance of additional features in the conductance.

A very natural guess is that the lifting of degeneracy is due to interaction effects. While renormalization-group studies show that the Coulomb interaction in clean graphene becomes marginally irrelevant [134], BLG behaves more like a typical two-dimensional (2D) electron gas. Non-perturbative approaches to the effects of long-range interactions show that graphene may feature interaction-induced instabilities. These effects are expected to be particularly important in very clean samples, at very low densities, and in high magnetic fields. Proposed theories include superconducting instabilities [134–137], (anti-)ferromagnetic instabilities [47, 138, 139], excitonic instabilities [140–142], and whole lot of others [143–149]. For a summary or comparison see, e.g., Refs. [6, 150–155].

One rather notorious phenomenon, where interaction effects show up in transport measurements is the 0.7 anomaly discussed in Sec. 3.1.2, which we believe to have identified in this experiment. Since interaction effects are enhanced at low densities, such type of effects would be strongest in the lowest quantization subband.

In this chapter, we study the conductance of a BLG QPC for in-plane magnetic field orientation. We start with presenting the experimental results (Sec. 4.2), which were obtained in the same sample as in Ref. [21], but in another cool down for changing the sample orientation within the magnet. In particular, we demonstrate the importance of interaction effects in the lowest size-quantized subbands by measuring the renormalized Landé g-factor governing the Zeeman splitting of the subbands. This motivates us to employ the picture based on the interaction-induced spontaneous polarization of spin or valley degrees of freedom to describe the shoulder-like features in the conductance. After a short reminder on the band structure of BLG and, especially, the influence of external gating on the gap and the densities (Sec. 4.3), we discuss the conductance of the BLG QPC. In Sec. 4.4 we detail an extension of a phenomenological model for the 0.7 anomaly proposed in Ref. [20] to BLG. Within this framework, we investigate all possible scenarios in order to find the one most likely to be present in this experiment. We do not explicitly consider any microscopic model of the anomaly, but, instead, assume that some sort of interaction-induced spin and/or valley splitting is present at zero magnetic field and investigate the consequences of possible types of splitting on the conductance in increasing magnetic field. In fact, the assumed polarization does not need to be static, it just needs to fluctuate slowly compared to the traveling time through the constriction, which according to Ref. [115] is indeed fulfilled. By comparing the experimental results with these scenarios (Sec. 4.6), we conclude that this sample shows spontaneous spin polarization but no valley splitting. Our findings are summarized in Sec. 4.7.

4.2 Experimental results

4.2.1 Fabrication and characterization

The experiment that motivates this chapter was conducted on the same BLG device already presented in Ref. [21] but with an in-plane magnetic field, see Fig. 4.1. The chosen gate configurations is $V_{\mathrm{BG}} = 10$ V (back-gate voltage) and $V_{\mathrm{SG}} = -12$ V (split-gate voltage). The device consists of a hBN-BLG-hBN heterostructure, which is edge contacted with Ti/Al electrodes. The thickness of the top and bottom hBN layers of the sandwich are 38 nm and 35 nm, respectively. The sandwich is placed onto a pre-patterned back gate, which is designed on a sapphire substrate that is, in turn, covered by an additional layer of the dielectric Al_2O_3. The magnetic field was applied in the plane of the BLG layer. The measurements were performed under the same experimental condition as in Ref. [21], but in a different cool down, with the magnetic field oriented in the plane of the BLG (at approximately 45° from the current direction).

The QPC in BLG is engineered electrostatically by means of the split gate placed on top of the device and the whole sample is covered in an extra layer of Al_2O_3 with 30 nm thickness before adding the overall top gate made from Ti/Cu. The measurements were performed at either 20mK or 4K in a ^{3}He/^{4}He dilution refrigerator BF-LD250 from BlueFors. A two-terminal configuration was used employing the standard low-frequency ($\approx$ 13Hz) lock-in technique, with an AC-excitation ranging from 1 to 20μV. For further details of the characterization of the sample the reader is referred to the Supplemental Material in Ref. [21]. Figure 8 of the Supplemental Material in Ref. [21] also shows the finite-bias measurements used to extract the gate-coupling parameter.

To the best of our knowledge, there are two reports by other groups that have investigated similar setups, namely Ref. [120] and Ref. [52]. While both these papers also studied transport through a BLG QPC, the confinement conditions there were different from those in this setup. This difference might be crucial for observation interaction effects, including the 0.7 anomaly. Specifically, in the present work, the QPC is formed by split gates of a physical width $w \approx 65$ nm. Because of the additional layers of Al_2O_3, the distances between the channel and the global back and top gate are 55 nm and 68 nm, respectively. In Ref. [120], the physical width of the split gates is 120 nm, while the distance to the back gate and split gate is not specified. Since Ref. [120] did specify that the BLG is encapsulated in hBN, the distance to the back gate and the split gate is likely of the order of 30 nm, with an additional 35 nm of Al_2O_3 between split gates and local top gate. Similarly, Ref. [52] stated a width of 250 nm, a distance of 25 nm to the back gate (and, probably, a similar one to the split gates), and additionally 25 nm of Al_2O_3 between split gates and a local top gate. This means, that channel considered here is a lot narrower, confinement a lot stronger, and, thus, the density of states way larger, which enhances all interaction effects.

Moreover, interaction effects in Refs. [52, 120] should be more strongly suppressed by the top and bottom gate, which are closer than the typical distance of interacting electrons within the constriction. It is worth noting that Ref. [119] stated that gates need to be closer than a few nanometer, to fully suppress electron-electron interaction in graphene and BLG. At this point, it should be mentioned that, depending on the exact shape of the constriction, the 0.7 shoulder can appear at different conductance values (for example, at 0.5 e^2/h [83, 84]), which would fit with the alleged spin-orbit gap of Ref. [52].

The global back gate that covers also parts of the leads in this device leads to a smoother coupling in the QPC region, while also modifying the band structure and gap in the non-QPC regions. As has been shown, for example, in Refs. [83, 84], both the presence and shape of the 0.7 anomaly depend rather strongly on the exact constriction profile, so that a smoother constriction region might be necessary

for its appearance. This also applies to the larger parameter space explored by varying the split gate and back gate not only along the direction of zero displacement field. Lastly, we want to point out that most of the results reported here are based on the three lowest size quantized levels, which are not even resolved in Ref. [120], while Ref. [52] does not reach full pinch-off.

4.2.2 Conductance

We start by investigating the dependence of the conductance on the magnetic field and top-gate voltage. Figures 4.2(a)-(d) show the experimental data at temperature 20 mK. In Fig. 4.2(d), the conductance is shown as a function of the top-gate voltage V_{TG} for two different values of in-plane magnetic fields $B_{\parallel}$. The black curve corresponds to $B_{\parallel} = 0.2$ T and the light-blue one to $B_{\parallel} = 6$ T as marked in Fig. 4.2(a). The light-blue curve highlights the appearance of additional half-step conductance plateaus in high in-plane magnetic fields. The black curves contains a shoulder marked by the arrow, which we will attribute to the 0.7 conductance anomaly. We note that the valley degeneracy is apparently not affected by the application of the in-plane magnetic field, and the Zeeman spin-split subbands remain degenerate in the two valleys K and K'. Since the aluminum leads are superconducting at 20 mK, a finite magnetic field is needed to kill this effect and curves below 0.2 T show influence of the superconducting leads, cf. additional plots presented in Sec. 4.6.5.

Cubic spline fits of the conductance for all measured values of magnetic field between 0.2 T and 6 T are shown in Fig. 4.2(b) and Fig. 4.2(c) for temperatures 20 mK and 4 K, respectively. Curves in both figures are shifted vertically for clarity and colored according to their first derivative. For both temperatures, there are two regions of steep incline (orange-red) for high magnetic field, corresponding to the chemical potential crossing through the spin-split bands. The splitting is both sharper and higher for the lower temperature, and plateaus are flatter there as well. The lower spin-subband stays roughly at the same value of V_{TG}.

Figure 4.2(a) shows a grayscale map of the differentiated differential conductance dG/dV_{TG} as a function of top gate voltage V_{TG} and in-plane magnetic field $B_{\parallel}$ for $T = 20$ mK. Transitions across 1D subband edges appear as dark lines, while conductance plateaus are visible as light regions in between. One clearly sees the four well-resolved conductance plateaus. These are separated by the three regions corresponding to the 1D subbands, which are split roughly symmetrically with the applied in-plane field for higher bands. This corresponds to the evolution from the spin-degenerate into spin-split energy levels. The lifting of the spin degeneracy occurs for the lowest three subbands, where the confinement and interactions are the strongest.

Figure 4.2(e) shows the same data as 4.2(a), but as a function of $B_{\parallel}$ and G. The bright horizontal lines at multiples of $4e^2/h$ correspond to the spin- and valley-degenerate conductance quantization plateaus for zero magnetic field, the additional half-integer multiples for higher magnetic fields correspond to the spin-split plateaus due to the Zeeman effect.

4.2.3 Extra features of the conductance

Additionally, we note the presence of a shoulder-like feature below the lowest conductance plateau at about $G = 2.5\,e^2/h$, similar to the 0.7 structure described in many other materials [105], which develops into the lowest spin-split subband at $G = 2\,e^2/h$. This feature is well visible in the black curves in Figs. 4.2(a) and 4.2(d). Since flatter parts of the conductance correspond to brighter color in Figs. 4.2(c) and 4.2(f), it corresponds to a bright region in between the zeroth and first plateau, i.e., within the darker region to the left of $V_{\mathrm{TG}} = -12$ V, making it look like a spin splitting of the 1D

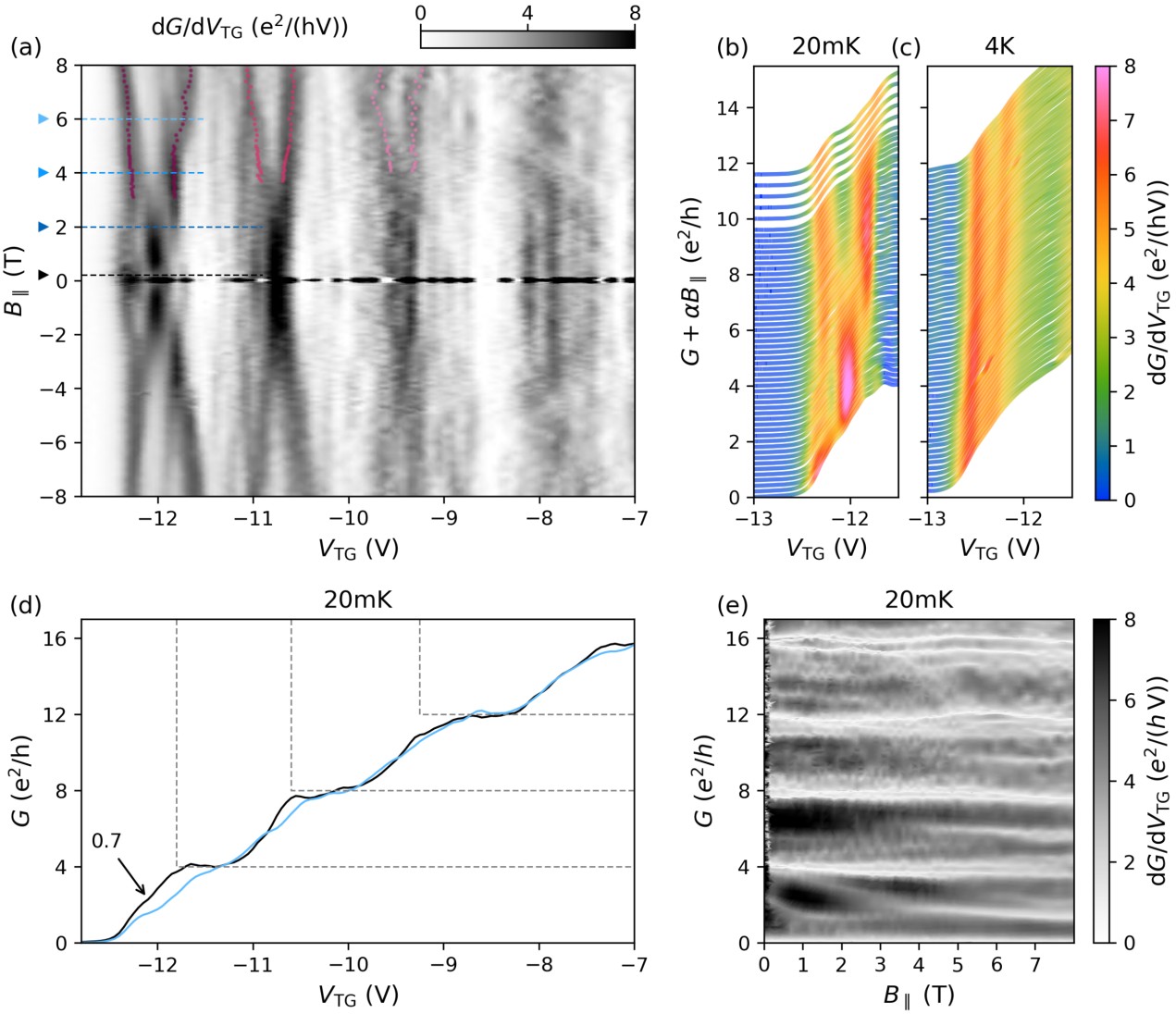

Figure 4.2: Measured conductance of the QPC in BLG for $V_{\mathrm{BG}} = 10$ V and $V_{\mathrm{SG}} = -12$ V. (a): Differentiated differential conductance as a function of the top-gate voltage V_{TG} and in-plane magnetic field B for temperature 20 mK. Plateaus of the conductance corresponds to bright regions, steps correspond to dark region. The map scale is cut at $0\,e^2/hV$ and $8\,e^2/hV$ to bring out the details. The black dashed line corresponds to $B = 0.2$ T, the lines of blue tones to $2, 4, 6$ T. The dots of different shades of pink mark the development of the spin subbands used to extract the Zeeman splitting and the effective Landé g-factors. (b) and (c): Cubic spline fit of the differential conductance G as a function of the V_{TG} in elevating B for 20 mK and 4 K, respectively. The curves are shifted vertically with $\alpha = 2e^2/h$T and colored according to their first derivative. (d): Differential conductance G as a function of V_{TG} at 20 mK for $B = 0.2$ T (black curve) and $B = 6$ T (light blue). The arrow marks the additional shoulder, which we identify as a 0.7 anomaly. (e): Differentiated differential conductance as a function of B and conductance G for 20 mK. Plateaus of the conductance correspond to bright regions, slopes correspond to dark regions.

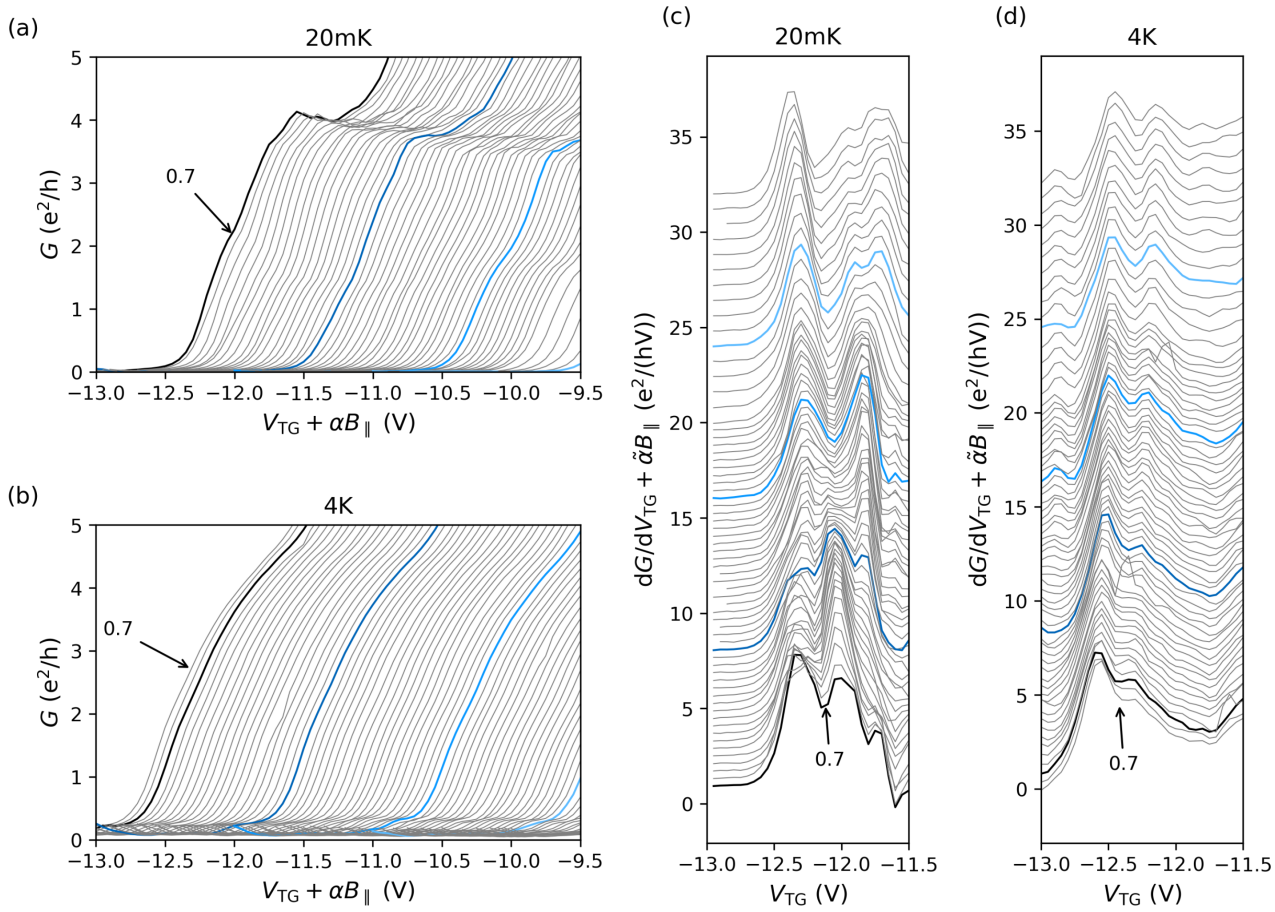

Figure 4.3: (a) and (b): Zoom-in view for the lowest plateau of the differential conductance G at 20 mK and 4 K, respectively, as a function of V_{TG} with horizontal shifts for different values of magnetic field, $\alpha = 0.5$ V/T. (c) and (d): Differentiated differential conductance as a function of V_{TG} for 20 mK and 4 K respectively. Curves for different magnetic field values are shifted vertically with $\tilde{\alpha} = 4\mathrm{e}^2/(\mathrm{hVT})$. In all panels, the colored curves correspond to the magnetic field values introduced in Fig. 4.2(a).
Reprinted figure with permission from Vanessa Gall, Rainer Kraft, Igor V. Gornyi, and Romain Danneau, Phys. Rev. Research, **4**, 023142 (2022). `https://journals.aps.org/prresearch/abstract/10.1103/PhysRevResearch.4.023142`, licensed under CC BY 4.0

subbands at zero magnetic field.

This additional feature is also visible in Fig. 4.3, which shows cadence plots of the conductance at 20 mK and 4 K in Fig. 4.3(a) and (b), respectively, and of the derivative of the conductance at 20 mK and 4 K in Fig. 4.3(c) and (d), respectively. In all cases, only the lowest band is shown. The cadence plots for a larger range of conductance variation are shown in Sec. 4.6.5. The colored curves correspond to the values of magnetic field marked in Figure 4.2(a). In the black curves in both Figure 4.3(a) and (b) the is an additional shoulder at around $2.5e^2/h$, which develops into the spin split plateau for higher magnetic fields. In the cadence plots of the conductance Figure 4.3(c) and (d) this shoulder corresponds to an additional peak. which clearly develops into the spin split peak for 4 K whereas this transition is somewhat obscured by yet another feature at 20 mK. We identify this obscuring feature as part of a larger oscillation pattern discussed later. Similar plots are shown in Ref. [73] for GaAs, where the observed behavior was attributed to the 0.7 structure.

The extra feature cannot be an effect caused by the finite magnetic field needed to kill superconductivity, since it is not located on the imaginary line extending the Zeeman splitting down to small magnetic fields. Instead, a finite magnetic field is needed to bring this feature down to the spin-split value. Moreover, this feature is seen already at zero magnetic field in Figs. 4.2(c) and 4.3(b) and (d) at higher temperature, where the contacts are not superconducting. At stronger magnetic fields, $B_\parallel \gtrsim 4\,\mathrm{T}$, this feature merges with the shoulder that, at the lowest magnetic fields, splits off the lowest main conductance quantization plateau at $G = 4\,e^2/h$ and goes down to form a plateau slightly below $G = 2\,e^2/h$. This behavior is clearly observed as the evolution of the red region above $V_{\mathrm{TG}} \approx -12\,\mathrm{V}$ in Fig. 4.2(b). The merging of the two shoulders is also evident in Fig. 4.2(a) as an intersection of the two bright regions at $B_\parallel \approx 4\,\mathrm{T}$ and $V_{\mathrm{TG}} \approx -12\,\mathrm{V}$.

Finally, there are additional oscillations in the conductance (of which the obscuring feature in Fig. 4.3(c) is one), which are most visible close to conductance plateaus in Figs. 4.2 (d). These appear as vertical lines in Fig. 4.2(a) and are less visible for the higher temperature in Fig. 4.3(b). Most notably, a maximum of such an oscillation is seen to go straight through one of the spin-split bands of the lowest 1D subband in Fig. 4.2(a) and (b) and Fig. 4.3(c), starting at around −12V and 0T in the lowest plateau, crossing one spin subband at around 3T, and ending up in the $0.5\,e^2/h$ plateau for higher magnetic field. Similar oscillations appear at other voltages in a regular fashion.

4.2.4 Effective Landé *g*-factor

From the spin splitting of the 1D subbands marked in pink in Fig. 4.2(a) we extract the Zeeman energy splitting ΔE_Z by converting the top-gate voltage V_{TG} into energy, using the splitting rate of the energy levels in source-drain bias measurements [21], as described in Ref. [156–159]. The confinement in this cooldown, $V_{\mathrm{BG}} = 10$ V and $V_{\mathrm{SG}} = -12$ V, does not exactly correspond to the setup in the source-drain measurement, where $V_{\mathrm{SG}} = -11.6$ V. We observed a good agreement between the two measurements in Ref. [21], which had a bigger difference in the confining potentials. Most importantly, the extracted gate coupling is the same for all nine visible subbands. Thus, we expect this value to be a very good fit here as well and use

$$E = \alpha_{\mathrm{TG}}\, e \left(V_{\mathrm{TG}} - V_{\mathrm{TG}}^{(0)} \right), \quad \alpha_{\mathrm{TG}} = 3.8 \times 10^{-3}.$$

The obtained value of ΔE_Z for each of the three lowest subbands is plotted in Fig. 4.4(a) as a function of magnetic field, revealing linearly increasing Zeeman energy splittings. Remarkably, in case of the $N = 0$ subband, the Zeeman splitting shows a linear behavior only for $B_\parallel \gtrsim 5$ T, whereas at smaller fields an almost constant splitting is observed.

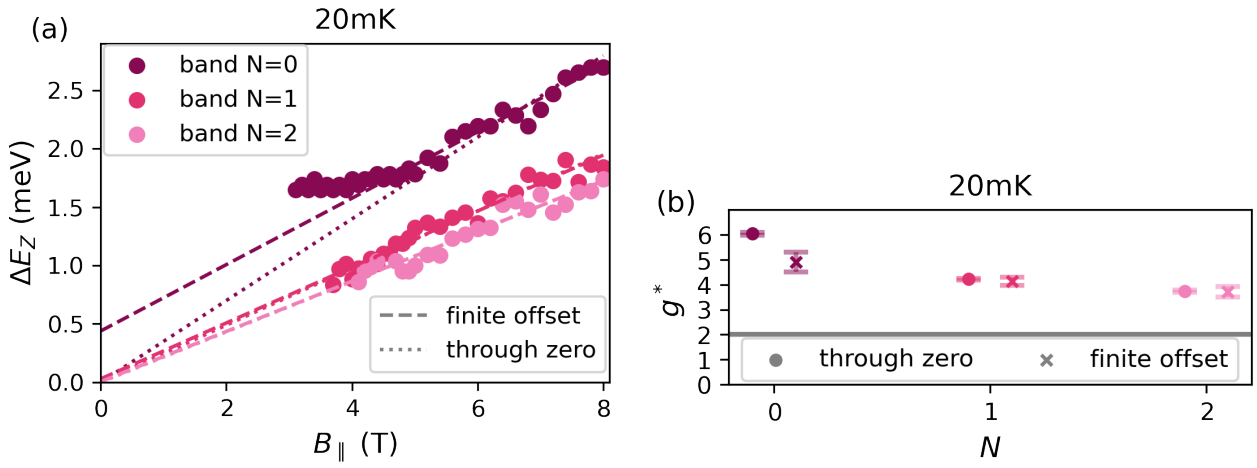

Figure 4.4: (a) Zeeman energy splitting ΔE_Z as a function of magnetic field B for various 1D subbands. Dashed lines show best linear fits of high-field data points, dotted ones are linear fits going through zero at zero magnetic field. (b) Extracted effective Landé g-factors $|g^*|$ for the three quantization subbands [solid dots of the colors corresponding to legend in panel (a)], obtained for the in-plane magnetic field. The gray line indicates the value bare 2D g-factor $g = 2$ for BLG. The error bars mark the 1σ intervals from the two performed fits shown in panel (a). The dotted points correspond to the dotted lines above, the crosses to the dashed lines. All parameters are given in Table 4.1.
Reprinted figure with permission from Vanessa Gall, Rainer Kraft, Igor V. Gornyi, and Romain Danneau, Phys. Rev. Research, **4**, 023142 (2022). `https://journals.aps.org/prresearch/abstract/10.1103/PhysRevResearch.4.023142`, licensed under CC BY 4.0

This saturation effect can be linked to the observed additional shoulder in the conductance curves in Figs. 4.2(b) and 4.2(c) at not too strong magnetic fields. The plateau in the Zeeman splitting corresponds to the magnetic fields below 4 T in Fig. 4.2(a), where the bright region to the left of $V_{\mathrm{TG}} = -12\,\mathrm{V}$ disappears. One can either fit the dependence of ΔE_Z on the magnetic field requiring a vanishing splitting extrapolated to zero B or not (using then the best linear fit at high magnetic field). In the latter case, a finite intercept at $\Delta E_Z \approx 1.7\,\mathrm{meV}$ is observed for $N = 0$ subband at $B_\parallel = 0$, unlike the cases $N = 1$ and $N = 2$, which extrapolate to close to zero energy splitting. This suggests that a spontaneous spin splitting occurs for the $N = 0$ subband, where the effects of the interaction and confinement are expected to be the most prominent. Fitting with a finite intercept, as was done, e.g., in Ref. [73], establishes a bound on zero-field splitting without interaction effects. One should note that this splitting is fully obscured by the much larger, interaction-induced 0.7 anomaly that produces a much larger value of the zero-B splitting.

From the slopes of the Zeeman splitting in Fig. 4.4(a), we find the (independent of the magnetic field) values of effective Landé g-factors $|g_N^*|$ for each of the subbands, shown in Fig. 4.4(b), see Table 4.1. These values are obtained by taking the linear fit to the splitting with and without a finite intercept. For both fits we use the 1σ intervals to obtain error bars. The obtained $|g_N^*|$ values are increasingly enhanced for lower subbands compared to the bare 2D g-factor $g = 2$, with a maximum enhancement by a factor of about 2–3 for $N = 0$. This observation also supports the idea of an enhanced role of interaction effects for the $N = 0$ subband. Independent of the exact value of the gate coupling, this

subband	0	1	2
g^* (no offset)	6.04(6)	4.22(4)	3.73(4)
g^* (finite offset)	4.91(40)	4.14(17)	3.72(22)
offset in meV	0.438(154)	0.0288(546)	0.00506(755)

Table 4.1: Parameters extracted from the fit of the splitting in magnetic field. The uncertainty corresponds to the uncertainty of the fit, i.e., a 1σ interval.

enhancement only relies on a gate coupling that is the same for the three subbands. This enhancement is seen both for a fit with finite intercept or without. Since the reported Kane-Mele spin-orbit gap of $0.04 - 0.08$ meV is in between the finite and the vanishing intercept, it would also not change the resulting enhancement of the Landé g-factor by more than a few percent.

4.3 Theoretical model

The quantization of conductance in a QPC is a well-known experimental proof of the possibility of confining charge carriers and it clearly shows their quantum nature [67] and was already discussed in Sec. 3.1. What makes BLG an interesting platform for such measurements, is its additional valley degree of freedom and the high electrostatic tunability of its band gap [125, 160], as introduced in Sec. 1.2. In this Section, we discuss the effects of the applied gate voltages on the band structure and, thus, on the observed conductance within the essentially non-interacting model (interaction here is taken into account only through the self-consistent screening of the gate potentials).

4.3.1 Effective Hamiltonian and dispersion of BLG

We describe the low-energy properties of BLG relevant for the transport measurements in the QPC geometry by the effective two-band Hamiltonian, see Ref. [44]. The details of this approximation are given in Appendix A.2 and the result was already presented in Sec. 1.2. The two-band matrix Hamiltonian, acting in the space of the pseudospin degree of freedom (Pauli matrices $\hat{\sigma}$) combined with the Zeeman interaction in the spin space (Pauli matrices $\hat{s}$), has the form

$$\hat{H} = \left(\hat{H}_0 + \hat{H}_M\right) \otimes \hat{s}_0 + \frac{1}{2}\Delta E_Z \hat{\sigma}_0 \otimes \hat{s}_z, \tag{4.1}$$

$$\hat{H}_0 = -\frac{1}{2m}\begin{pmatrix} 0 & (\pi^\dagger)^2 \\ \pi^2 & 0 \end{pmatrix} - \frac{U}{2}\begin{pmatrix} 1 & 0 \\ 0 & -1 \end{pmatrix}, \tag{4.2}$$

$$\hat{H}_M = \frac{Uv^2}{\gamma_1^2}\begin{pmatrix} \pi^\dagger\pi & 0 \\ 0 & -\pi\pi^\dagger \end{pmatrix}. \tag{4.3}$$

Here, $\pi = \xi p_x + i p_y$ is the kinetic momentum, with $\xi = \pm$ referring to the $K_\pm$ valley. Here, we disregard possible spin-orbit coupling, which is a small effect at the energy scales of the experiment and not capable of explaining the zero-field splitting or the magnetic field behavior we observe, as seen by the obtained zero-field splitting of Fig. 4.4(a). We will return to this issue again below.

In what follows, we disregard the Mexican-hat term $\hat{H}_M$ that develops for finite layer asymmetry U as discussed in Ref. [7]. We also neglect the skew interlayer hopping, which leads to trigonal warping [7, 46]. The effect of these subtle features of the BLG spectrum on the conductance of a QPC in in-plane

magnetic field will be discussed elsewhere. Here, we adopt the simplest model that, as we demonstrate below, is capable of describing the salient features of the conductance.

Clearly, we have to distinguish the two spatial regions in the physical sample. Away from the split gates there is no confinement and electrons feel an approximately constant top-gate and back-gate voltage. Close to the split gate, the shape of the confinement leads to a non-trivial, spatially dependent effective top-gate voltage.

The dispersion of the spin $\sigma =\uparrow,\downarrow$ band for the low-energy Hamiltonian (4.1) without the Mexican-hat feature (4.3) is given by

$$E_\sigma = \pm\sqrt{\frac{U^2}{4} + \frac{\hbar^4 k^4}{4m^2}} + \frac{\sigma}{2}\Delta E_Z. \tag{4.4}$$

This corresponds to a 2D density for spin projection σ:

$$n_\sigma^{\mathrm{2D}}(\mu) = 2\frac{m}{8\pi\hbar^2}\sqrt{4\left(\mu - \frac{\sigma}{2}\Delta E_Z\right)^2 - U^2}, \tag{4.5}$$

where the factor of 2 accounts for the valley degree of freedom and the chemical potential μ is measured with respect to the middle of the asymmetry gap. For a small Zeeman splitting, $\Delta E_Z \ll \sqrt{4\mu^2 - U^2}$, one can use the expansion

$$n_\sigma^{\mathrm{2D}}(\mu) \approx \frac{m}{4\pi\hbar^2}\left(\sqrt{4\mu^2 - U^2} - \frac{2\sigma\mu\Delta E_Z}{\sqrt{4\mu^2 - U^2}}\right). \tag{4.6}$$

This expansion tells us that the effect of the Zeeman splitting on the density is enhanced when the chemical potential is close to the gap. The total density $n^{2D} = \sum_{\sigma=\pm} n_\sigma^{\mathrm{2D}}$ is, to first order in ΔE_Z, independent of magnetic field, and we get for the chemical potential in weak fields:

$$\begin{aligned}\mu(n^{\mathrm{2D}}) = &\frac{\sqrt{m^2U^2 + 4\pi^2(n^{\mathrm{2D}})^2\hbar^4}}{2m} \\ &- \frac{m^3U^2(\Delta E_Z)^2}{16\pi^2(n^{\mathrm{2D}})^2\hbar^4\sqrt{m^2U^2 + 4\pi^2(n^{\mathrm{2D}})^2\hbar^4}}.\end{aligned} \tag{4.7}$$

4.3.2 Controlling BLG with gates

In the 2D regions away from the QPC, the effect of a constant back-gate and top-gate voltage is described by the self-consistent gap equation [7, 8]. The total density $n = n_\uparrow + n_\downarrow$ is electrostatically determined by the gates and given by

$$n = \frac{\varepsilon_0\varepsilon_{\mathrm{BG}}V_{\mathrm{BG}}}{eL_{\mathrm{BG}}} + \frac{\varepsilon_0\varepsilon_{\mathrm{TG}}V_{\mathrm{TG}}}{eL_{\mathrm{TG}}}. \tag{4.8}$$

Here, ε_0 is the vacuum permittivity, L_{BG} (L_{TG}) is the distance from the BLG plane to the back gate (top gate), and $\varepsilon_{\mathrm{BG}}$, $\varepsilon_{\mathrm{TG}}$ are the relative dielectric constants of the material between BLG and the back gate and top gate, respectively. In the absence of screening, the interlayer asymmetry factor U is given by

$$U_{\mathrm{ext}} = \frac{ec_0}{2\varepsilon_r}\left(\frac{\varepsilon_{\mathrm{BG}}}{L_{\mathrm{BG}}}V_{\mathrm{BG}} - \frac{\varepsilon_{\mathrm{TG}}}{L_{\mathrm{TG}}}V_{\mathrm{TG}}\right), \tag{4.9}$$

where c_0 is the distance between the two BLG planes and ε_r is the relative permittivity between these sheets.

Since the two layers of BLG screen the effect of the closer gate for the other BLG plane depending on their density and thus the felt voltage, the actual asymmetry as a function of the density is given by the self-consistent equation [7]

$$\begin{aligned} U(n) &= \frac{U_{\text{ext}}}{1 - \frac{\Lambda}{2}\ln\left(\frac{|n|}{2n_\perp} + \frac{1}{2}\sqrt{\frac{n^2}{n_\perp^2} + \frac{U^2}{4\gamma_1^2}}\right)} \\ &\approx U_{\text{ext}}\left[1 - \frac{\Lambda}{2}\ln\left(\frac{|n|}{n_\perp}\right)\right]^{-1}, \end{aligned} \tag{4.10}$$

$$n_\perp = \frac{\gamma_1^2}{\pi\hbar^2 v^2}, \qquad \Lambda = \frac{c_0 e^2 n_\perp}{2\gamma_1 \varepsilon_0 \varepsilon_r}. \tag{4.11}$$

Thus, changing the top-gate voltage tunes the density n according to Eq. (4.8), which, in turn, influences the asymmetry factor U according to Eq. (4.10) and hence the dispersion (4.4) and the chemical potential according to Eq. (4.7). This chemical potential remains constant over the whole sample, including the QPC constriction, where the density is no longer given by Eq. (4.5):

$$\mu(V_{\text{BG}}, V_{\text{TG}}) \simeq \sqrt{\left(\frac{U_{\text{ext}}}{2 - \Lambda\ln\frac{|n^{2\text{D}}|}{n_\perp}}\right)^2 + \left(\frac{\pi\hbar^2 n^{2\text{D}}}{m}\right)^2}. \tag{4.12}$$

Here, the chemical potential depends on V_{BG} and V_{TG} through the corresponding dependence of the 2D density, Eq. (4.8), and the dependence of U_{ext}, Eq. (4.9).

In the experiment, the combination of back-gate and split-gate voltages is used to open a gap U under the constricted region and tune the chemical potential inside this gap, as shown in Ref. [21], and thus form the QPC, see Fig. 4.5. The overall top gate is used to tune into the low-density regime, where the observation of conductance quantization is possible [21]. Importantly, for fixed back-gate and split-gate voltages, like in the experimental setup, the top-gate voltage tunes the electronic density in the sample linearly [7].

As proposed in Ref. [68], we model the QPC by projecting the 2D problem onto a one-dimensional one, as discussed in Sec. 3.1 for a normal Schrödinger equations and in Sec. 4.3.4 for the case of BLG. The quantization of conductance is already visible in the simplest approximation of hard-wall boundary conditions, as we will show now. In the case of a channel of width W, the dispersion relation for the longitudinal wavevector k resulting from Eq. (4.1) takes the form [21]

$$E_{N,\sigma}(k) = \pm\sqrt{\frac{U^2}{4} + \frac{\hbar^4}{4m^2}q_N^4(k)} + \frac{\sigma}{2}\Delta E_Z, \tag{4.13}$$

$$q_N^2(k) = k^2 + \left(\frac{N\pi}{W}\right)^2, \tag{4.14}$$

where $N = 0, 1, 2\ldots$ labels the size-quantized bands. While the case $N = 0$, strictly speaking, requires a different choice of boundary condition, we still chose to investigate the effect of the resulting k^4 dispersion, which one would also get in the 2D setup. It will turn out, that the choice of any non-linear

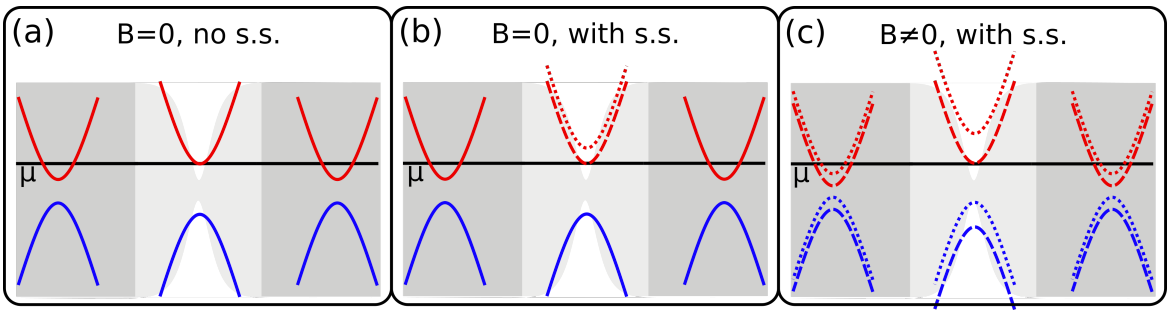

Figure 4.5: (a) and (b): Band structure in the 2D regions (dark gray) and inside the constriction (light gray) for zero magnetic field, with and without spontaneous splitting (s.s.), respectively. Here, the spontaneous splitting is between spin subbands shown as dashed or dotted lines. Since it requires the proximity of the chemical potential, there is no s.s. in the valence band. Because of the split-gate stray fields, the asymmetry gap inside the constriction is larger. Energies are measured with respect to the middle of the gap in the 2D region. (c): The magnetic field introduces a spin splitting of the bands with respect to the $B = 0$ band bottom, which leaves the middle of the gap at the same value. The splitting inside the constriction is larger, since the Landé g-factor is enhanced. As observed experimentally, the Zeeman splitting inside the constriction is not symmetric. To the lowest order in a weak magnetic field, the chemical potential for a fixed total 2D density is independent of magnetic field, see Eq. (4.6).
Reprinted figure with permission from Vanessa Gall, Rainer Kraft, Igor V. Gornyi, and Romain Danneau, Phys. Rev. Research, **4**, 023142 (2022). `https://journals.aps.org/prresearch/abstract/10.1103/PhysRevResearch.4.023142`, licensed under CC BY 4.0

dispersion does not have qualitative consequences for the 0.7 effect. Note that U in Eq. (4.13) differs from the 2D expression (4.10), since the screening in a 1D channel differs from that in the unconfined regions of BLG. We also note that the channel width is affected in a non-trivial way by V_{BG} and V_{TG}.

The lowest band is, to leading order, quartic in the momentum, so that the zero-temperature density resulting from Eq. (4.13) is given by

$$n_\sigma^{\mathrm{1D}}(\mu) = \frac{2\sqrt{2m}}{\pi\hbar}\left[(\mu - \sigma\Delta E_Z/2)^2 - U^2\right]^{1/4}, \tag{4.15}$$

as opposed to the square-root dependence of the 2D density (4.5). The total density in the constriction is again determined electrostatically by the gates, but the stray fields of the split gates make the evaluation of the dependence of the density on the gate voltages harder. Since the split-gate voltage is applied additionally in the constricted region, the gap there is larger and the density inside the QPC is lower than away from the barrier (Fig. 4.5), enabling the observation of the very lowest size-quantized bands.

4.3.3 Screening and electron-electron correlations

Electrons in the device are subject to Coulomb interaction, which is screened by the electrons themselves, by the metallic gates, and by the dielectric material. Let us first discuss the screening effect of the gates. There are three relevant length scales in the system. The first one is the physical distance between the split gate fingers is $w \approx 65$ nm and the electrostatically induced channel is smaller than that. The width of the split-gate fingers is of the order of $L \approx 300$ nm, so that we can distinguish two ranges of length scales relevant to electrostatic screening in this device.

On scales smaller or of the order of w, the system is truly 2D, only for larger distances it crosses over to 1D. Another relevant scale is the distance to the back gate and top gate, which are both of the order of $d \approx 55$ nm. Here, we also take into account the dielectric screening by further assuming, for simplicity, that the insulating layers in between have the same dielectric constant ϵ_r (the vacuum dielectric constant is denoted below by ϵ_0). The bare, only dielectrically screened Coulomb interaction is given by its Fourier component at wave vector $\mathbf{q}$ (different in 1D and 2D cases):

$$V(q) = \begin{cases} \dfrac{e^2}{2\epsilon_0\epsilon_r}\dfrac{1}{q}, & \text{2D}, \\ \dfrac{e^2}{2\pi\epsilon_0\epsilon_r}\ln\dfrac{1}{qw}, & \text{1D}. \end{cases} \tag{4.16}$$

The gate-screened interaction can be found by summing up the infinite series of mirror charges. For this one starts by placing a single charge e in the BLG layer at $z = 0$, as shown in Fig. 4.6 (a). Since the potential exactly in the backgate plane at $z = -L_B$ has to vanish, we can model this by placing an opposite charge $-e$ at position $z = -2L_B$ as shown in 4.6 (b). However, the potential also has to vanish at the topgate position $z = L_T$, which we achieve by putting a charge $-e$ at $z = 2L_T$ and a charge e at $z = 2L_T + 2L_B$ as shown in Fig. 4.6 (c). For two planes, this amount to an infinite series

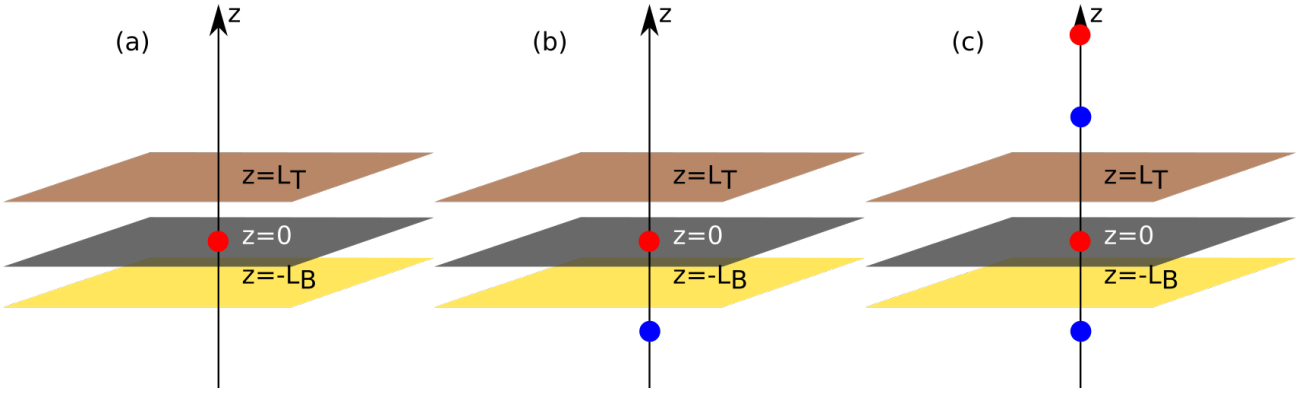

Figure 4.6: (a),(b) and (c): Side view of the BLG plane at $z = 0$ with the top and bottom gates. (a) We want to find the screened potential due to a charge e (red) being placed in the BLG plane. (b) According to the method of image charges, for the lower conducting plane, the backgate, this is equivalent to placing an opposite charge $-e$ (blue) at $z = -2L_B$. (c) In order to also put the topgate plane to zero field, we need to place two additional charges. Since now the backgate plane is not field free, this procedure has to be repeated ad infinitum.

of image charges one needs to place, which has to be summed up. In the 2D case, this leads to

$$V(q) = \frac{e^2}{2\epsilon_0\epsilon_r} \sum_{k=-\infty}^{\infty} \left(\frac{e^{-2l|k|q}}{q} - \frac{e^{-2|l'-kl|q}}{q} \right) \tag{4.17}$$

$$= \frac{e^2}{2\epsilon_0\epsilon_r} \frac{2}{q} \frac{\sinh\left(ql - ql'\right) \sinh\left(ql'\right)}{\sinh\left(ql\right)} \tag{4.18}$$

$$= \frac{e^2}{2\epsilon_0\epsilon_r} \frac{\tanh(qd)}{q}, \tag{4.19}$$

where $l = L_{\mathrm{TG}} + L_{\mathrm{BG}}$, $l' = L_{\mathrm{BG}}$ and in the last line we assumed $L_{\mathrm{TG}} = L_{\mathrm{BG}} = d$. This means that screening strongly alters the interaction if $qd \ll 1$. But in the 2D case we require $r < w$, i.e., $q > 1/w$, and thus $qd \gtrsim d/w \gtrsim 1$, so that the interactions are not strongly altered by the screening of the gates.

A closer look, including the screening effects on the interaction for monolayer graphene based on the perturbative treatment explained in Sec. 2.2.3, is discussed in Ref. [119] and reveals, that gates need to be closer than a few nanometer to really alter the interaction, which is not experimentally accessible and certainly not the case here. There, it has also been stressed that for BLG distances need to be even closer. In the 1D case the presence of the gates is relevant only on scales $x > d$ and $q < 1/d$. In this case, we get a constant interaction strength, which is in agreement with our phenomenological model.

One effect of electron-electron interaction is an enhancement of both the Landé g-factor and spin-orbit coupling, as discussed in Refs. [161–163]. By introducing the Fermi-liquid constants F_0, F_1 we can express the Landé g-factor enhancement as $\tilde{g} = g/(1-|F_0|)$. Spin-orbit coupling has an additional linear momentum dependence, which means that $|F_1|$ enters instead of $|F_0|$. Since $|F_0| > |F_1|$, this means that the g-factor will always be more strongly enhanced than the spin-orbit coupling. The enhancement is largest for large density of states, so that a strong confinement further enhances this effect.

4.3.4 Projection procedure

In the experiment, one electrostatically induces a constriction in the shape of a QPC, as introduced in Sec. 3.1. While the full self-consistent treatment of this electrostatic problem is very involved, the main features can be described by the inclusion of a local potential in the corresponding Schrödinger equation, thus neglecting the coupling between the Schrödinger and the Poisson equations. The obtained energy spectrum would extend dispersion (4.13) and thus also the density (4.15).

In Sec. 3.1 it was already shown, how one can perform a projection procedure to an effectively one-dimensional problem with an effective potential for each mode in a usual two-dimensional electron gas. In the present case of BLG it is easier to include the constriction by means of boundary conditions than a real local potential. The Hamiltonian (4.1) acts as

$$\hat{H}\begin{pmatrix}\psi_{A1\uparrow}\\ \psi_{A1\downarrow}\\ \psi_{B2\uparrow}\\ \psi_{B2\downarrow}\end{pmatrix} = E\begin{pmatrix}\psi_{A1\uparrow}\\ \psi_{A1\downarrow}\\ \psi_{B2\uparrow}\\ \psi_{B2\downarrow}\end{pmatrix} \tag{4.20}$$

on the four-component wave-function in the spin and sublattice space. These four coupled second-order equations can be decoupled into a fourth-order one and we get for the first two components:

$$\begin{aligned}&\left[\left(\frac{U}{2} - U\frac{v^2}{\gamma_1^2}\pi^\dagger\pi\right)^2 + \frac{(\pi^\dagger\pi)^2}{(2m)^2}\right]\psi_{A1\sigma}\\ &= \left(E - \sigma\frac{\Delta E_Z}{2}\right)^2\psi_{A1\sigma}.\end{aligned} \tag{4.21}$$

Here, we have used that, without a magnetic field, the momentum operators commute.

We expand the wave-function $\psi_{A1\sigma}$ in transverse modes $\chi_{nx\sigma}(y)$ as

$$\psi_{A1\sigma}(x,y) = \sum_n \phi_{n\sigma}(x)\chi_{nx\sigma}(y), \tag{4.22}$$

which leads to a new differential equation, where the x and y component are still coupled. We already assume, that $\chi_{nx\sigma}(y) \propto \sin(k_{nx\sigma}y)[\cos(k_{nx\sigma}y)]$ if the solution is antisymmetric [symmetric] when describing the QPC by imposing hard-wall boundary conditions along the y direction. The width of the channel $W(x)$ depends smoothly on x and we get standing waves with wavevector

$$k_n(x) = \frac{n\pi}{W(x)}.$$

We decouple the components by neglecting all x derivatives of $\chi_{nx\sigma}(y)$, which leads to the effective 1D equation:

$$\begin{aligned}&\left[\left(\frac{U}{2} + \hbar^2 U\frac{v^2}{\gamma_1^2}[\partial_x^2 - k_n^2(x)]\right)^2 + \frac{\hbar^4[\partial_x^2 - k_n^2(x)]^2}{(2m)^2}\right]\phi_{n\sigma}(x)\\ &= (E - \sigma\frac{\Delta E_Z}{2})^2\phi_{n\sigma}(x),\end{aligned} \tag{4.23}$$

where the constriction $W(x)$ acts as an effective 1D potential $E_n(x) = \frac{\hbar^2 n^2 \pi^2}{2mW(x)^2}$. At low energies, only the lowest transverse mode contributes and we can approximate the full solution as $\psi_{A1\sigma} = \phi_{1\sigma}(x)\chi_{1x\sigma}(y)$. Choosing, for example, $W(x) = \cosh\Big(x/L\Big)$ we get a very realistic 1D potential containing terms of the form $1/\cosh\Big(x/L\Big)^2$.

4.3.5 Conductance quantization

We describe the conductance of the system by means of the Landauer-Büttiker formula introduced in Sec. 2.3,

$$G = \frac{e^2}{h} \sum_{\sigma,\xi} \int_{-\infty}^{\infty} \mathrm{d}\epsilon \mathcal{T}_{\sigma,\xi}(\epsilon) \Big[-f'(\epsilon - \mu)\Big], \tag{4.24}$$

where $\mathcal{T}_{\sigma,\xi}(\epsilon)$ is the transmission of a subband with spin σ and valley ξ and $f'(x)$ is the derivative of the Fermi function $f(x) = [1 + \exp\Big(x/k_B T\Big)]^{-1}$. Assuming an idealized step-function transmission coefficient, where a band contributes to G as soon as it is starting to get filled, the Landauer-Büttiker conductance is given by

$$G(T,B) = 2\frac{e^2}{h} \sum_{N,\sigma} f\left(E_N^0 + \frac{1}{2}\sigma g^* \mu_B B - \mu\right), \tag{4.25}$$

where the factor of 2 accounts for the valley degeneracy,

$$E_N^0 = \sqrt{\frac{U^2}{4} + \left(\frac{\hbar^2}{2m}\right)^2 \left(\frac{N\pi}{W}\right)^4} \tag{4.26}$$

is the lower band edge of band N at zero magnetic field, and the Zeeman interaction is written explicitly.

Every time the chemical potential crosses another lower band edge at finite magnetic field, the conductance makes a step of $\Delta G = 2\,e^2/h$ and, for zero magnetic field, a step of $\Delta G = 4\,e^2/h$. Each step has the shape of the Fermi function. The steps are separated by conductance plateaus, thus giving rise to a staircase structure seen in Fig 4.2 and Fig 4.3. This is the conventional conductance quantization for a QPC, with an appropriate degeneracy of the bands. In contrast to the case of an out-of-plane magnetic field [21, 46], the in-plane magnetic field does not couple to the valley degree of freedom. As discussed in Ref. [53], the direct effect on the band structure is also negligible at experimentally accessible magnetic fields. Therefore, at arbitrary fields, the steps of non-interacting conductance have a factor of two corresponding to the two valleys of BLG.

4.4 The *0.7* anomaly in BLG QPC

In contrast to the conductance quantization, the shoulder-like feature appearing in the conductance cannot be explained by the non-interacting theory presented in Sec. 4.3. In this section, we explore the possibility of explaining this special feature in the context of the interaction-induced 0.7 conductance anomaly. As already discussed above, several microscopic theories were used to describe the 0.7 anomaly, but there is none that is universally accepted. An overview on these microscopic theories is found in Sec. 3.1.2.1. Thus we chose a phenomenological description, which extends the model of

Ref. [20] to four bands and the BLG band structure from Sec. 1.2. This approach can be microscopically justified as it is in principle the combination of two aspects. The first ingredient is an effective, low density approximation of the full, interacting free energy discussed in Sec. 3.1.2.3, which, as shown in Refs. [116, 117] can indeed have, in their case magnetic, instabilities. The second ingredient is the observation discussed in Ref. [115] and Sec. 3.1.2.2, that a slowly oscillating spin structure does indeed result from the combination of local interaction and constriction potential. Thus, we assume that there is effectively a spin and/or valley polarization, which does not have to be static, but can fluctuate slowly compared to the typical traveling time through the constriction. For simplicity we nevertheless describe the model for a static situation. The "classic" 0.7 effect is only seen in the lowest conductance step, Fig. 4.2, so that below we restrict our consideration to the lowest size-quantized band shown in Fig. 4.3.

4.4.1 Phenomenological model

Following the general idea of [20], we again use the Landauer-Büttiker formula (4.24) for the conductance, here for the quantized band $N = 0$ from Eq. (4.13). The 0.7 effect requires a finite temperature. Assuming that the energy scale for the variation of the transmission probability is smaller than that of the thermal distribution function, we approximate the former as a step function. A spin-valley subband contributes to the conductance as soon as the chemical potential reaches its lower band edge $\epsilon^0_{\sigma,\xi}$ within the temperature window.

In this section, we develop a phenomenological model to describe how interaction effects may influence these lower band edges beyond the self-consistent screening. There are two ways in which these can differ from the non-interacting single-particle ones. The first one is the spontaneous polarization mentioned above, which is assumed to be arbitrary in the space of spin and valleys. Already when the chemical potential is way below any of the relevant subbands, these subbands may be spontaneously split to different values of energy. The arrangement of these values, which are acquired for very low chemical potential and zero magnetic field, is referred to as the initial subband configuration. All subbands that are above the lowest subband are called minority bands; those that are characterized by the lowest band edge are majority bands.

The second effect is the dependence of the subbands on the chemical potential when it is close to the band edge. A particular type of this dependence—pinning of the band edge to the chemical potential—gives rise to additional plateaus in the conductance. It is this interaction-induced dependence of the lower band edge of minority bands on the chemical potential that our phenomenological model describes for any assumed initial configuration. We then consider the corresponding evolution of the conductance with increasing in-plane magnetic field, and, by comparing the resulting behavior with the experimentally observed one (Sec. 4.2), infer the initial splitting configuration.

The general consequence of the pinning of a band edge to the chemical potential can be seen by considering only one band with lower band edge $\epsilon^0_{\sigma,\xi}(\mu)$, which depends on the chemical potential according to the following equation

$$\epsilon^0_{\sigma,\xi}(\mu) = \begin{cases} \mu_{\sigma,\xi}, & \mu < \mu_{\sigma,\xi} \\ \mu - (\mu - \mu_{\sigma,\xi})^\alpha, & \mu > \mu_{\sigma,\xi} \end{cases}, \tag{4.27}$$

where $\alpha > 1$ has do be deduced from the specific dispersion. The pinning here is represented by the second line $\mu > \mu_{\sigma,\xi}$, which states, that the lower band edge does not stay at the previous constant value $\mu_{\sigma,\xi}$ but moves up with the chemical potential μ. This behavior of the lower band edge is shown

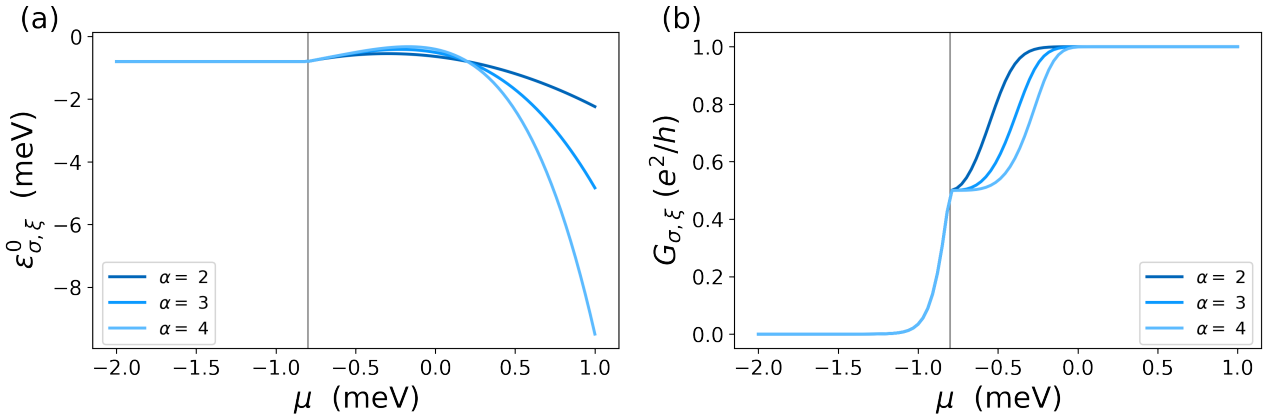

Figure 4.7: (a) Lower band edge $\epsilon^0_{\sigma,\xi}$ of a single subband as a function of the chemical potential μ for different α at $T = 0.7$ K and $\mu_{\sigma,\xi} = -0.8$ meV (gray line) according to Eq. (4.27) (b) Corresponding conductance according to Eq. (4.28). There is an additional, shoulder-like feature, close to the value of $0.5\frac{e^2}{h}$.

in Fig. 4.7 (a). The lower band edge stays at the constant value $\mu_{\sigma,\xi}$, until it is reached by the chemical potential, at which point it depends on the difference between the chemical potential and its initial position with a parameter α. Over a certain range of chemical potential it moves up with μ, which is exactly what we describe as a pinning here. If one plugs this lower band edge into the Landauer-Büttiker conductance with a step function transmission one would obtain the conductance

$$G_{\sigma,\xi}(\mu) = \frac{e^2}{h} f(\epsilon^0_{\sigma,\xi}(\mu) - \mu) \tag{4.28}$$

for this single band, which is depicted in Fig. 4.7 (b). As soon as the chemical potential reaches the initial position of the lower band edge, an additional feature, similar to a shoulder, appears close to the value of $0.5\frac{e^2}{h}$. The general idea is, that exactly this could happen for every considered subband. The reason why it happens, depends on the microscopic model one trusts. The energy, at which the lowest band bottom is reached is close to the energy at the top of the effective one-dimensional QPC barrier. This barrier is affected by interactions. In a very naive Hartree-Fock approximation only the Hartree-type self-energy with the opposite spin species would survive and effectively change the height of the barrier proportional to the electronic density in exactly this opposite spin subband. If we look at the effective potential seen by the spin σ subband, this means that by increasing the chemical potential and thus the density in the $-\sigma$ band, the barrier height for the σ species increases, which counteracts the increase of the density in the σ band and thus leads to exactly this type of pinning of the chemical potential to the lower band edge for the σ subband [115].

4.4.1.1 General four-band model

For a system with four degrees of freedom, like BLG, we label the subbands by their spin and valley index, i.e., $\epsilon^0_{\sigma,\xi}$. Moreover, we assume that the lower band edges of minority bands start to depend on the chemical potential once it reaches a certain value $\mu_{\sigma,\xi}$, i.e., $\epsilon^0_{\sigma,\xi} = \epsilon^0_{\sigma,\xi}(\mu)$.

All possible initial spontaneously polarized configurations of the band edges are shown in Fig. 4.8(a). For the analysis of the dependence of the band edges on μ, we look at the local spin-valley energy-

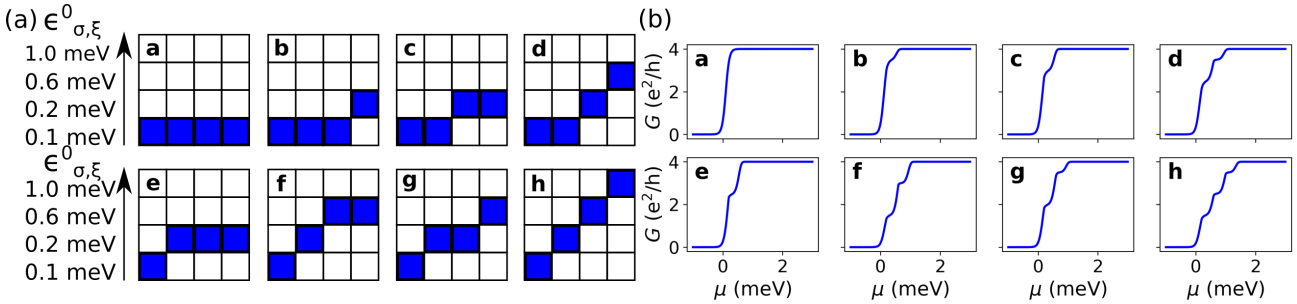

Figure 4.8: (a) Subfigures **a** to **h** show every possible initial subband structure. The x axis labels spin and valley degree of freedom and the y axis shows the position of the lower band edges in energy space with the values used for all plots. The assignment of spin σ and valley ξ to the x axis is not unique, yet. In **a** there is no initial splitting, all lower band edges are equivalent. In case **b**, three bands are fixed and there is one minority band. Whether the single minority band is spin up/down or valley K/K' can only be distinguished once we include a magnetic field. In **c** to **d** and **e** to **h** there are two and three split subbands, respectively. (b) Exemplary conductance for the initial configuration shown in (a) for zero magnetic field. The parameters are chosen to suppress the plateaus at multiples of $1\,e^2/h$, where the majority band is filled and minority bands are not yet populated. The majority bands are fixed at 0.1 meV, the next levels correspond to $\epsilon_1^0 = 0.2\,\text{meV}$, $\epsilon_2^0 = 0.6\,\text{meV}$, $\epsilon_3^0 = 1\,\text{meV}$. The temperature is $T = 0.7\,\text{K}$ and $C = 6\,\text{meV}^{-3}$ for all minority bands [see Eq. (4.36)].
Reprinted figure with permission from Vanessa Gall, Rainer Kraft, Igor V. Gornyi, and Romain Danneau, Phys. Rev. Research, **4**, 023142 (2022). `https://journals.aps.org/prresearch/abstract/10.1103/PhysRevResearch.4.023142`, licensed under CC BY 4.0

density functional in the form

$$\mathcal{F} = \mathcal{E}[\{n_{\sigma,\xi}\}] - \mu \sum_{\sigma,\xi} n_{\sigma,\xi}. \tag{4.29}$$

Here, $\mathcal{F}$ is the free energy of the system and $\mathcal{E}$ is its internal energy. A diagrammatic approach to obtaining such a free energy and a corresponding analysis of possible instabilities in models with multiple species of quasiparticles is discussed, e.g., in Refs. [116, 117].

The lowest bands in Fig. 4.8 are majority bands with a fixed lower band edge and we decompose their density into $n = n_0 + \delta n$. All changes with the chemical potential are included in δn. For minority bands, we do not make this decomposition, but assume that $n = 0$ for $\mu < \mu_{\sigma,\xi}$. We approximate the free energy functional $\mathcal{F}$ as bilinear in all partial majority density contributions δn and minority densities n, i.e.

$$\mathcal{F} = \sum_{i=\sigma,\xi} \left[(\alpha_i - \mu) n_i + \frac{\beta_i}{2} n_i^2 \; + \sum_{j=\sigma',\xi'} \gamma n_i n_j \right], \tag{4.30}$$

where $\alpha_{\sigma,\xi}$, $\beta_{\sigma,\xi}$, and γ are phenomenological constants to be determined experimentally and $n_{\sigma,\xi}$ is understood as $\delta n_{\sigma,\xi}$ for majority bands. The minimum of the energy functional is achieved when

$$\frac{\partial \mathcal{F}}{\partial n_{\sigma,\xi}} = \alpha_{\sigma,\xi} - \mu + \beta_{\sigma,\xi} n_{\sigma,\xi} + \gamma \sum_{\sigma',\xi'} n_{\sigma',\xi'} = 0, \tag{4.31}$$

which leads to solutions of the form

$$n_{\sigma,\xi} \propto (\mu - \mu_{\sigma,\xi}) \tag{4.32}$$

for minority bands, where $\mu_{\sigma,\xi}$ is the critical chemical potential of the minority subband that depends on the parameters of the free energy Eq. (4.30).

4.4.1.2 Application to BLG

At this point, we have to specify the band structure in order to get access to the single-particle densities entering the energy functional (4.30). For this purpose, we use the results of Sec. 4.3.2 and Sec. 1.2 for the non-interacting 1D dispersion in the BLG QPC, and modify them to include the interaction effects at the phenomenological level.

Without a magnetic field, we consider a quartic dispersion relation of the form

$$\epsilon_{\sigma,\xi}(k) = a k^4 + \epsilon^0_{\sigma,\xi}(\mu), \tag{4.33}$$

where a is a constant. This form of the effective—modified by interactions—form of single-particle energies in BLG QPC is based on the fourth-order expansion of dispersion relation (4.13) for $N = 0$, namely

$$E_{N=0,\sigma}(k) \approx \left(\frac{\hbar^2}{2m} \right)^2 \frac{k^4}{U} + \frac{U}{2}. \tag{4.34}$$

As shown above, the gap magnitude U depends on the chemical potential through the self-consistent electrostatic screening. Specifically, $U = U(n)$, according to Eq. (4.10) with additional effects of the

split gates, and $n = n(\mu)$ according to Eq. (4.15). The chemical potential is set by the 2D density according to Eq. (4.5) and Eq. (4.8). Within the lowest band, these dependencies are very smooth and do not lead to any additional features. The main role in our consideration is played by the interaction-induced bandgap that determines the band edge $\epsilon^0_{\sigma,\xi}(\mu)$. For this reason, we neglect all electrostatic contributions [effectively fixing $U = U(\mu_{\sigma,\xi})$] and introduce a new bandgap instead of $U/2$. One could just as well assume that this bandgap is applied on top of the fixed gap $U(\mu_{\sigma,\xi})/2$, since this would only lead to an overall shift and a redefinition of the origin.

For the dispersion (4.33), we get a one-dimensional density in the form

$$n_{\sigma,\xi}(\mu) = \frac{2}{\pi}\left\{\frac{1}{a}\left[\epsilon^0_{\sigma,\xi}(\mu) - \mu\right]\right\}^{1/4}. \tag{4.35}$$

By combining this with Eq. (4.32), we thus get the dependence

$$\epsilon^0_{\sigma,\xi}(\mu) = \begin{cases} \mu - C_{\sigma,\xi}(\mu - \mu_{\sigma,\xi})^4, & \mu > \mu_{\sigma,\xi} \\ \mu_{\sigma,\xi}, & \mu < \mu_{\sigma,\xi} \end{cases}. \tag{4.36}$$

where $C_{\sigma,\xi}$ is a phenomenological constant depending on the parameter a as well as the parameters of the free energy functional $\mathcal{F}$. This means that once the chemical potential reaches the lower band edge of a minority band they become pinned together over a certain energy range. For continuity reasons we require $\epsilon^0_{\sigma,\xi} = \mu_{\sigma,\xi}$, i.e., the initial configuration determines the critical chemical potentials. It is worth emphasizing that the enhanced density of states at the bottom of the almost flat (quartic in momentum) band in BLG QPC (4.33) is expected to enhance the role of interactions compared to the case of conventional parabolic bands. This should also be compared with the proposed cases noted in Eq. (4.27) and shown in Fig. 4.7, where for $\alpha = 4$ we would expect a stronger shoulder than for the conventional parabolic case, where $\alpha = 2$.

4.4.1.3 Resulting conductance

With the step-function transmission probabilities, the conductance reads:

$$G(T) = \frac{e^2}{h}\sum_{\sigma,\xi} f(\epsilon^0_{\sigma,\xi}(\mu) - \mu). \tag{4.37}$$

At this point, one should take another look at Fig. 4.8 (b), which describes what happens for a minority band. If we tune the chemical potential through all band edges, the crossing of a fixed majority band corresponds to a plateau of $1\,e^2/h$, while for every minority band we get an additional less sharp shoulder at $0.5\,e^2/h$. Any additional plateau from a majority band at $1\,e^2/h$ can be smeared by temperature. If we have several minority band edges at different initial energies, the distance between the bands compared to the temperature determines whether lower minority bands already contribute fully or not, cf. Ref. [20].

The conductance corresponding to the initial splitting configurations from Fig. 4.8(a) is shown in Fig. 4.8(b). The values of the additional shoulders are summarized in Table 4.2. In experimental conductance curves in Fig. 4.2(d), there is one additional shoulder at around $2.5\,e^2/h$ and another one around $3.5\,e^2/h$ for zero magnetic field. Thus we can rule out case **a**, because it does not have any additional shoulder and cases **f**, **g**, and **h**, which have a too low first shoulder from the very beginning. Only cases **b**, **c**,**d** and **e** from Fig. 4.8 are relevant here.

case	conductance shoulders in units of e^2/h
a	none
b	3.5
c	3
d	2.5 and 3.5
e	2.5
f	1.5 and 3
g	2 and 3.5
h	1.5 and 2.5 and 3.5

Table 4.2: Values of conductance shoulders for initial configurations shown in Fig. 4.8

case	spin configurations
a	$(\uparrow\uparrow\downarrow\downarrow)$
b	$(\uparrow\uparrow\downarrow)\downarrow$, $(\uparrow\downarrow\downarrow)\uparrow$
c	$\uparrow\uparrow\downarrow\downarrow$, $(\uparrow\downarrow)(\downarrow\uparrow)$, $\downarrow\downarrow\uparrow\uparrow$
d	$\uparrow\uparrow\downarrow\downarrow$, $(\uparrow\downarrow)\downarrow\uparrow$, $(\uparrow\downarrow)\uparrow\downarrow$, $\downarrow\downarrow\uparrow\uparrow$
e	$\downarrow(\downarrow\uparrow\uparrow)$, $\uparrow(\uparrow\downarrow\downarrow)$
f	$\uparrow\uparrow\downarrow\downarrow$, $\downarrow\uparrow(\uparrow\downarrow)$, $\uparrow\downarrow(\uparrow\downarrow)$, $\downarrow\downarrow\uparrow\uparrow$
g	$\uparrow\downarrow\downarrow\uparrow$, $\downarrow\uparrow\uparrow\downarrow$, $\downarrow(\uparrow\downarrow)\uparrow$, $\uparrow(\uparrow\downarrow)\downarrow$
h	$\uparrow\uparrow\downarrow\downarrow$, $\uparrow\downarrow\downarrow\uparrow$, $\uparrow\downarrow\uparrow\downarrow$, $\downarrow\downarrow\uparrow\uparrow$, $\downarrow\uparrow\uparrow\downarrow$, $\downarrow\uparrow\downarrow\uparrow$

Table 4.3: Different spin configurations for the arrangements shown in Fig. 4.8; brackets "(...)" denote all possible permutations. The order corresponds to the subband ordering shown in Fig. 4.8. For each permutation we can assign the valley indices in four different ways, which does not lead to different behavior in this model and is thus not distinguishable. For example, the last arrangement in case g corresponds to the eight valley-resolved cases: $\uparrow(\uparrow\downarrow)\downarrow = \{\uparrow_1\uparrow_2\downarrow_1\downarrow_2, \uparrow_1\uparrow_2\downarrow_2\downarrow_1, \uparrow_2\uparrow_1\downarrow_1\downarrow_2, \uparrow_2\uparrow_1\downarrow_2\downarrow_1, \uparrow_1\downarrow_1\uparrow_2\downarrow_2, \uparrow_1\downarrow_2\uparrow_2\downarrow_1, \uparrow_2\downarrow_1\uparrow_1\downarrow_2, \uparrow_2\downarrow_2\uparrow_1\downarrow_1\}$, where the index $1, 2$ corresponds to the K, K' valley, respectively.

4.4.2 Behavior of conductance in magnetic field

In order to distinguish between the cases of spin, valley or spin-valley splitting, we consider the behavior of the conductance in parallel magnetic field B. This is incorporated by the following replacement

$$\epsilon^0_{\uparrow,\xi} \to \epsilon^0_{\uparrow,\xi} - \frac{1}{2} g\mu_B |B|, \tag{4.38}$$

$$\epsilon^0_{\downarrow,\xi} \to \epsilon^0_{\downarrow,\xi} + \frac{1}{2} g\mu_B |B|. \tag{4.39}$$

There are in total 6 possibilities of assigning 2×2 spins to four subbands. Since one cannot distinguish different valley indices this way, after this assigning, the spins are still four-fold degenerate in their valley index. We only know that each valley has two opposite spins. The permutation of spins within subbands with the same lower band edge does not change the outcome. From this we get in total 26 different arrangements with distinct development with magnetic field for the eight initial cases shown in Fig. 4.8. These are shown in Table 4.3.

The magnetic field behavior of the relevant cases **b**, **c**, **d**, **e** is shown in Fig. 4.9 in analogy to Fig. 4.3(a). Here one should note, that the initial spontaneous splitting is a spontaneous symmetry breaking and if the magnetic field is tuned adiabatically, it will always favor the initial splitting in the direction of the magnetic field. Behavior like case **c2**, where the initial spontaneous splitting is opposite to the Zeeman splitting will only be observed if the magnetic field is switched on very fast.

A comparison of the experimental data and theoretical ones for symmetric splitting Eqs. (4.38) and (4.39) and a phenomenological asymmetric one, where we use

$$\epsilon^0_{\uparrow,\xi} \to \epsilon^0_{\uparrow,\xi} - g\mu_B |B|, \tag{4.40}$$

$$\epsilon^0_{\downarrow,\xi} \to \epsilon^0_{\downarrow,\xi}, \tag{4.41}$$

assuming that the spin up band is energetically higher is shown in Fig. 4.10. From this we see that an asymmetric splitting, Eqs. (4.40) and (4.41), yields a better agreement with the experimental observations in this particular case, that will turn out to be the most relevant one. However, owing to the special dependence of minority bands on the chemical potential, this asymmetric replacement rule may lead to unphysical half-integer plateaus in high magnetic fields for some initial configurations. Therefore, we have used the symmetrical splitting introduced in Eqs. (4.38) and (4.39) to produce Fig. 4.9.

4.5 Possible additional features

Several phenomena, that could in principle play a role in the experiment, were not yet discussed. In this section we discuss the effects they would have on the conductance curves and why we think, it is safe to ignore them based on the used experimental data.

4.5.1 Effect of spin orbit coupling

The effective two-band Hamiltonian as derived in Appendix A.2 is given by

$$\mathcal{H}_2 = h_0 + h_U + h_3 + h_{\mathrm{AB}} + h_4 + h_{\Delta'} + h_Z + h_{\mathrm{so}}, \tag{4.42}$$

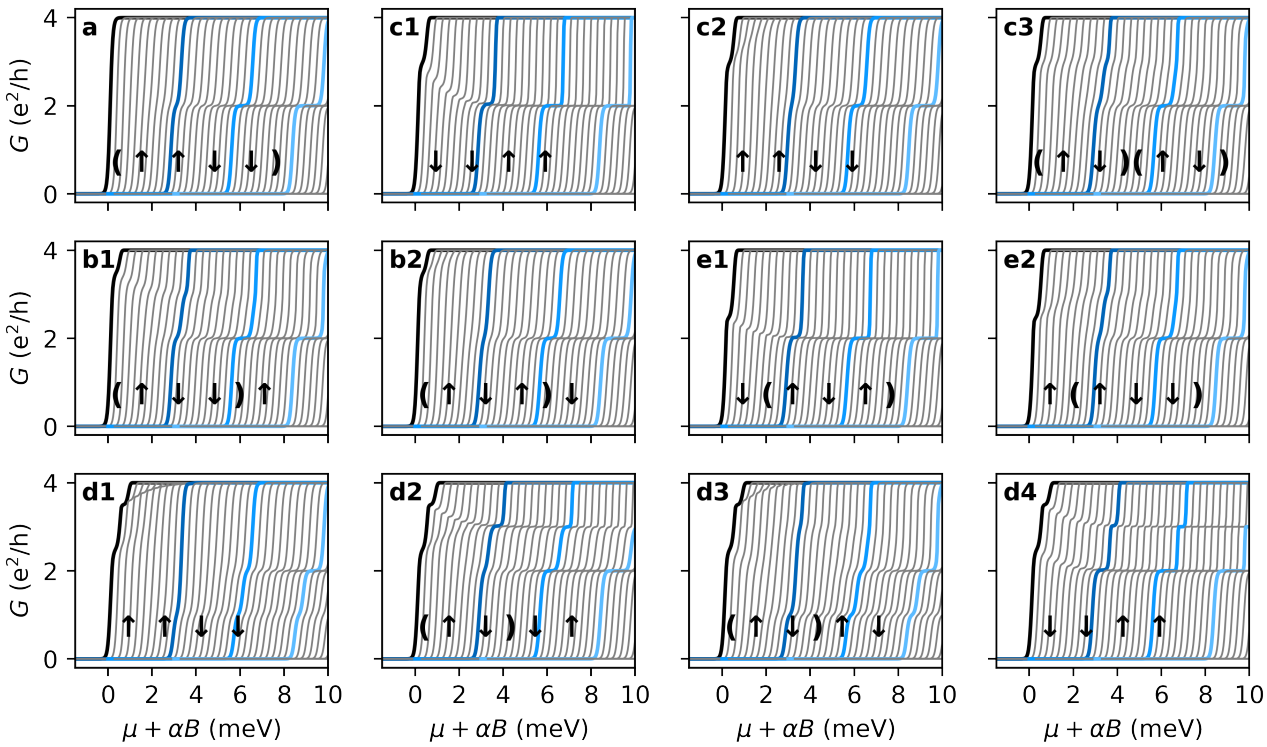

Figure 4.9: Behavior of the four different initial splitting cases **a**, **b**, **c** and **e** from Fig. 4.8 in an in-plane magnetic field. Conductance curves for magnetic fields between 0T and 8T are shown with a horizontal shift parametrized by $\alpha = 1.5\text{meV/T}$. The thick black curve corresponding to $B = 0\,\text{T}$ is non-shifted. The blue lines correspond to $2\,\text{T}$, $4\,\text{T}$ and and $6\,\text{T}$, as in Fig. 4.3. Without any initial splitting, there is no continuous development of a shoulder in **a**, the additional plateau appears, as soon as it can be resolved. The particular assignment of spin to the subbands is irrelevant: all six possibilities are indistinguishable. In case **c**, three different scenarios are possible. Each case happens for all four possible valley assignments. For cases **b** and **e**, there are two distinguishable spin configurations; for case **d** four. Same parameters as in Fig. 4.8; according to the measured Landé g-factor, g=4 was chosen.
Reprinted figure with permission from Vanessa Gall, Rainer Kraft, Igor V. Gornyi, and Romain Danneau, Phys. Rev. Research, **4**, 023142 (2022). `https://journals.aps.org/prresearch/abstract/10.1103/PhysRevResearch.4.023142`, licensed under CC BY 4.0

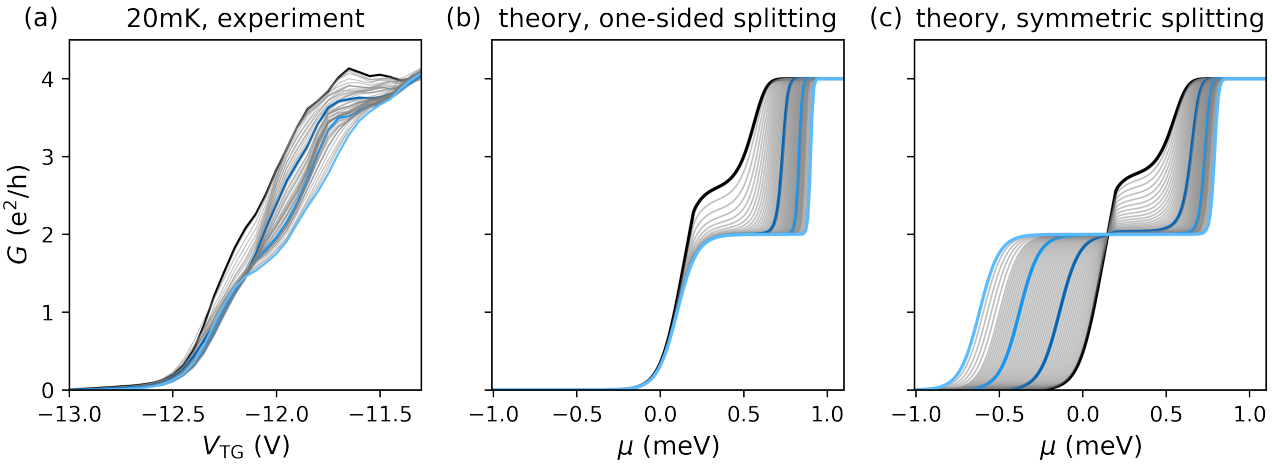

Figure 4.10: Zoom into the evolution of the lowest conductance step with increasing magnetic fields (without shifts). The colored curves correspond to those marked in Fig. 4.2a. (a): Experimental data for 20 mK. Curves for higher magnetic fields show lower conductance at a fixed value of the top-gate voltage. (b): Theoretical curve for case **c1** in Fig. 4.9 with the non-symmetric splitting (sp.) introduced in Eqs. (4.40) and (4.41). Same parameters as in Fig. 4.8; according to the measured Landé g-factor, g=4 was chosen. The behavior of (a) is qualitatively replicated. (c): Same as in (b), but with a symmetric Zeeman splitting introduced in Eqs. (4.38) and (4.39). There is a fixed(crossing) point clearly absent in the experimental data. As is apparent by comparing the distance of the blue plateaus in chemical-potential space in (b) and (c) a symmetric splitting enhances the g-factor even more.
Reprinted figure with permission from Vanessa Gall, Rainer Kraft, Igor V. Gornyi, and Romain Danneau, Phys. Rev. Research, **4**, 023142 (2022). `https://journals.aps.org/prresearch/abstract/10.1103/PhysRevResearch.4.023142`, licensed under CC BY 4.0

where

$$h_0 = -\frac{v^2}{\gamma_1}\begin{pmatrix} 0 & (\pi^\dagger)^2 \\ \pi^2 & 0 \end{pmatrix} \otimes \hat{s}_0, \tag{4.43}$$

$$h_U = -\frac{U}{2}\left[\begin{pmatrix} 1 & 0 \\ 0 & -1 \end{pmatrix} - \frac{v^2}{\gamma_1^2}\begin{pmatrix} \pi^\dagger\pi & 0 \\ 0 & -\pi\pi^\dagger \end{pmatrix}\right] \otimes \hat{s}_0, \tag{4.44}$$

$$h_3 = v_3\begin{pmatrix} 0 & \pi \\ \pi^\dagger & 0 \end{pmatrix} \otimes \hat{s}_0, \tag{4.45}$$

$$h_{\mathrm{AB}} = \frac{\delta_{AB}}{2}\begin{pmatrix} 1 & 0 \\ 0 & -1 \end{pmatrix} \otimes \hat{s}_0, \tag{4.46}$$

$$h_{\Delta'} = 2\Delta'\frac{v^2}{\gamma_1^2}\begin{pmatrix} \pi^\dagger\pi & 0 \\ 0 & \pi\pi^\dagger \end{pmatrix} \otimes \hat{s}_0, \tag{4.47}$$

$$h_4 = 2v_4\frac{v^2}{\gamma_1^2}\begin{pmatrix} \pi^\dagger\pi & 0 \\ 0 & \pi\pi^\dagger \end{pmatrix} \otimes \hat{s}_0, \tag{4.48}$$

$$h_Z = \frac{\Delta E_Z}{2}\begin{pmatrix} 1 & 0 \\ 0 & 1 \end{pmatrix} \otimes \hat{s}_z, \tag{4.49}$$

$$h_{\mathrm{so}} = \xi\begin{pmatrix} \lambda_1+\lambda_2+\lambda_u & 0 \\ 0 & -\lambda_1-\lambda_2-\lambda_d \end{pmatrix} \otimes \hat{s}_z. \tag{4.50}$$

Before, we restrict ourselves to the terms h_0, h_U, and h_Z. This is exactly equation (4.1) and (4.3). For all calculations, we furthermore neglect the second term of h_U that describes the Mexican-hat feature of the spectrum. The only terms capable of lifting spin degeneracy are h_Z and the spin-orbit term

$$\xi\begin{pmatrix} \lambda_u & 0 \\ 0 & -\lambda_d \end{pmatrix} \otimes \hat{s}_z \tag{4.51}$$

for asymmetry between the layers $\lambda_u \neq \lambda_d$, which can be caused by the lack of mirror symmetry of the whole stack [164]. Because of the valley index ξ in this expression, the splitting is opposite in the two valleys, so that there is no net spin splitting due to spin-orbit interaction at all. If such a term is present in the Hamiltonian, it would lead to full spin-valley splitting in an applied magnetic field, i.e., four steps of $1\,e^2/h$. This is, however, not seen in the experiment. This type of effect of spin-orbit coupling on the first conductance plateau in in-plane magnetic fields for the parameters specified in Ref. [52] is shown in Fig. 4.11.

4.5.2 Effect of tilted magnetic field

We have investigated the effect of a perpendicular magnetic field on the quantized conductance in the same device in Ref. [21]. Large out-of-plane magnetic fields lead to a valley splitting, similar to the Zeeman spin splitting, with characteristic braiding behavior. Since we see neither a lifting of the valley degree of freedom, which would lead to a full resolution of conductance steps of $1\,e^2/h$ for large magnetic fields, nor any hint at a non-linear splitting, we can exclude a large out-of-plane component of the magnetic field. The presence of an appreciable out-of-plane component of the magnetic field would also show up in a curving of the Fabry-Pérot oscillations, which is also not observed here.

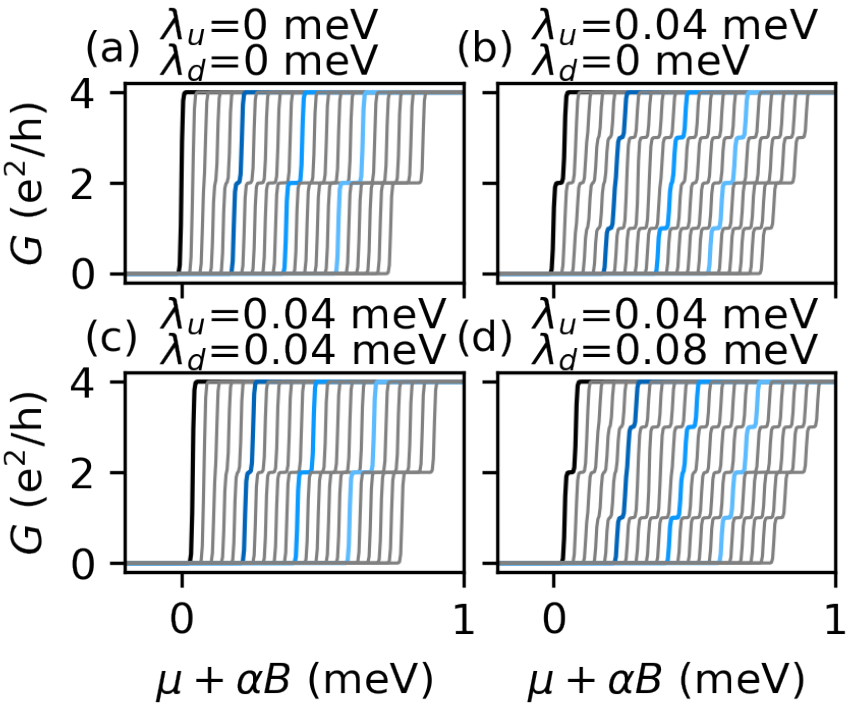

Figure 4.11: Influence of a finite Kane-Mele spin-orbit coupling on the first conductance plateau in in-plane magnetic field, including the effect of layer-asymmetry encoded in $\lambda_u \neq \lambda_d$ for $U = 0$. In all plots we chose $g = 2$ and $\alpha = 0.1$ meV/T, thus the rightmost curve corresponds to $B = 8$ T and the temperature is 20 mK. (a) No spin-orbit coupling, there is no splitting at zero magnetic field. (b) and (d) Different spin-orbit couplings in the two layers, finite splitting at zero magnetic field, full lifting of spin and valley degeneracy at higher magnetic field. (c) Same spin-orbit coupling in both layer, no splitting at zero magnetic field. For finite U we always obtain results as in (d). The splitting is no spin splitting but a spin-valley splitting.
Reprinted figure with permission from Vanessa Gall, Rainer Kraft, Igor V. Gornyi, and Romain Danneau, Phys. Rev. Research, **4**, 023142 (2022). `https://journals.aps.org/prresearch/abstract/10.1103/PhysRevResearch.4.023142`, licensed under CC BY 4.0

For small out-of-plane components the valley splitting is roughly linear [46] and can be easily included into our model by adding a term $\tau g_v B$ to the energy spectrum, where $\tau = \pm 1$ corresponds to the valleys K and K', respectively, and g_v contains both the angular dependence on the tilt angle and the magnetic moment due to the non-trivial Berry curvature. The expected effect of the tilt on the conductance traces is shown in Fig. 4.12. We see that a very small tilt does not lead to any noticeable difference, while a bigger one leads to a full lifting of all degeneracies at strong magnetic fields. This is in contrast to quantum dots in BLG, see, e.g., Ref. [165], where all four single-particle energies can be extracted at all values of magnetic field due to their additional charging energies and one can construct an effective g-factor by combining spin and valley splitting in a specific way, that would get enhanced over the bare spin Landé g-factor for one combination, while reducing it for the other combination. Since we do not observe a valley splitting, this effect would exactly average out in our case.

4.6 Application to the experiment

Let us now compare the results of our phenomenological model with the experimental results reported in Sec. 4.2. Many, but not all, features in Fig. 4.2, e.g., conventional conductance quantization, can be explained without considering interaction effects. Other features, e.g., additional shoulders in the conductance curves and behavior of the g-factor, are compatible with the phenomenological model presented in Sec. 4.4.

4.6.1 Conductance plateaus

Every time the chemical potential, tuned by the top gate voltage, reaches a new lower band edge, the conductance makes a step of $1\,e^2/h$ per spin and valley. For zero magnetic field, the plateaus are at multiples of $4\,e^2/h$, which can be clearly seen in the cadence plots in Fig. 4.3. This is in contrast to Ref. [130], where the valley splitting was observed in a similar setup with changing the split-gate voltage, but at much higher back-gate voltage. The Zeeman coupling of the spin to the in-plane magnetic field leads to appearance of steps at multiples of $2\,e^2/h$ for higher magnetic field. The additional plateaus become visible when the Zeeman-split bands have a spacing that can be experimentally resolved, which occurs in this case above 2 T.

4.6.2 Effective *g*-factor

The Zeeman splitting in the first three subbands shown in Fig. 4.4(a) for 20mK is very close to linear at sufficiently high magnetic fields. For the lowest subband, a nearly constant splitting is observed up to nearly 4T. The extracted g-factors show a strong enhancement compared to the bare value of $g = 2$ for BLG. We attribute this enhancement to the strong confinement and interaction effects, similar to those discussed in Ref. [69].

These effects are strongest for the lowest subbands because of lower densities in the almost flat (quartic) band, which is consistent with the increase of the enhancement with lowering the band index. This effect should only be present for electrons going through the constriction. Electrons that bounce back and stay in the 2D region are at too high densities for the interaction-induced enhancement to be visible. This effect combined with the peculiar low-field behavior of the lowest subband strongly hints at the importance of interaction effects in this experiment.

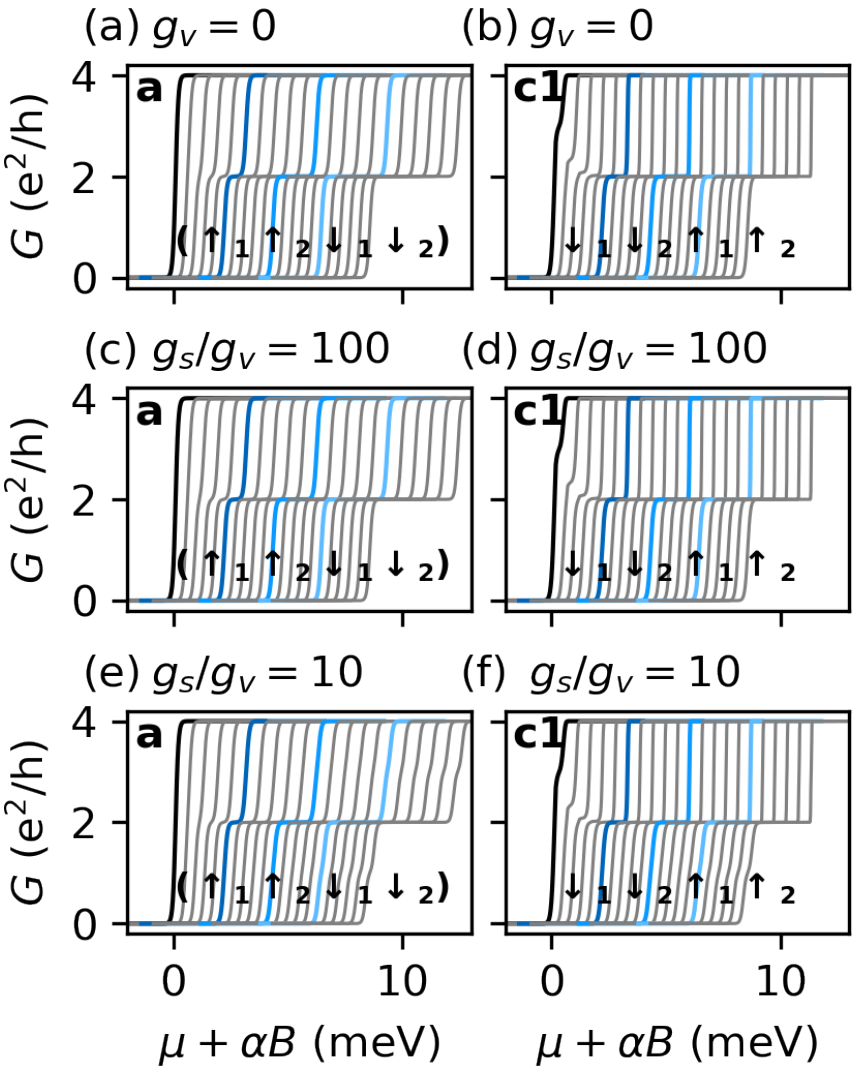

Figure 4.12: Influence of finite tilt angle on the conductance traces for the cases **a** and **c1**. In all plots, we chose $g_s = 4$ and $\alpha = 1.3$ meV/T, thus the rightmost curve corresponds to $B = 8$ T and the temperature is 20 mK. The configurations corresponding those in Fig. 4.8 are marked inside the panels; the index 1,2 corresponds to the K, K' valley respectively. Panels (a) and (b): No finite tilt and thus no valley splitting. Panels (c) and (d): Finite tilt angle resulting in $g_v = 0.04$. No change compared to g_v=0 is visible. Panels (e) and (f): Finite tilt angle resulting in $g_v = 0.4$. At a certain magnetic field this would lead to the appearance of additional conductance steps at $1\,e^2/h$ and $3\,e^2/h$, which are not observed in this experiment.
Reprinted figure with permission from Vanessa Gall, Rainer Kraft, Igor V. Gornyi, and Romain Danneau, Phys. Rev. Research, **4**, 023142 (2022). `https://journals.aps.org/prresearch/abstract/10.1103/PhysRevResearch.4.023142`, licensed under CC BY 4.0

4.6.3 The *0.7* anomaly

There are two additional features below the conventional conductance quantization step at $G = 4\,e^2/h$, which thus only involve the lowest quantized subband. The first one starts at around $3\,e^2/h$ at zero magnetic field, and the second one at around $2.5\,e^2/h$.

One might try to identify both these features with case **d** in Fig. 4.8, where there are two additional shoulders at zero magnetic field. However, considering the conductance behavior in magnetic field shown in Fig. 4.9, one sees that when these two additional shoulder move down with magnetic field, as in case **d4**, the additional plateau at $3\,e^2/h$ persists for higher magnetic fields. We do not see such a plateau in the experimental data. The feature starting around $2.5\,e^2/h$ in Fig. 4.3(a) moving down into the $2\,e^2/h$ plateau is visible in Fig. 4.2(a) as a splitting of the spin-valley subbands at vanishing magnetic field, which makes it a strong contender for the 0.7 effect. It also leads to the non-linear behaviour of the Zeeman splitting in the first subband in Fig. 4.4.

Since we have ruled out case **d**, only the cases **b**, **c** and **e** in Table 4.2 are still possible. Upon comparing the magnetic field behavior with Fig. 4.9, we conclude that we are in either case **c1** or **e1**. While one might not be convinced by the value of the theoretical shoulder of case **c**, that is $3\,e^2/h$ compared to the experimental one at $2.5\,e^2/h$, which is exactly the value in case **e**, as shown in Fig. 4.8, this would require the spin-up state of one valley split to the same energy as the non-spin split bands of the other valley, which implies an accidental fine-tuning. Instead, if only one valley was spin split, cases **d**, **f** and **g** would be way more probable, but these were already ruled out. Thus, we identify the experimentally observed behavior as case **c1**, which assumes an initial spin splitting, but no valley splitting.

It is also clear that, in contrast to [52], we do not see any crossing of Zeeman-split bands. A shoulder similar to the one observed here but at $2\,e^2/h$ was attributed to the substrate-enhanced Kane-Mele spin-orbit coupling in Ref. [52]. We note that such effects of the weak spin-orbit coupling can be observed only at very low temperatures, but we still see a similar effect at 4K. Finally, the proposed Kane-Mele spin-orbit splitting would lead to opposite spin splitting in the two valleys, so that there is no net spin splitting, as detailed in Sec 4.5.1. However, the observed Zeeman splitting at low magnetic fields suggests the presence of spontaneous net spin splitting in the case considered here, while the enhancement of the effective g-factor points towards rather strong interaction effects. We thus identify this feature in the conductance as an interaction-induced 0.7 anomaly. As mentioned in Ref. [84], the exact value of the shoulder may depend on the exact QPC geometry, so that it may also appear very close to the value of $0.5 \times 4\,e^2/h$.

4.6.4 Fabry-Pérot resonances

We identify the upper feature in the lowest subband conductance at low magnetic field, corresponding to an additional peak in the low-temperature plot in Fig. 4.3(c) at around $-11.8\,\mathrm{V}$ that goes vertically through the right spin-split band, as a Fabry-Pérot resonance [41, 118, 166–170]. In Fig. 4.2(e), this additional feature is seen as a faint bright curve moving down from the $4\,e^2/h$ plateau (at weak fields) and merging with the 0.7-feature to from the spin-split $2\,e^2/h$ plateau at magnetic field around $4\,\mathrm{T}$. Note that at this same value of magnetic field, the Zeeman splitting of the lowest subband starts growing linearly with magnetic field, see Fig. 4.4(a). With increasing temperature, this feature disappears, in contrast to the 0.7 anomaly, see Fig. 4.3(d).

The Fabry-Pérot resonances in this geometry emerge from interferences of electronic waves in the 2D region, which are back-scattered from the interface with the contact on one hand, and the barrier

created by the split gates, see Ref. [21] and Sec. 3.1.3. In a parallel magnetic field, there are two Fermi-wavevectors, one for each spin, so that the minima and maxima of these oscillations disperse with the magnetic field. Since Fabry-Pérot resonances correspond to electrons bouncing back and forth between the contacts and the split gate, these electrons are inherently two-dimensional and are not affected by the enhancement of the g-factor in the QPC region. A closer look reveals additional Fabry-Pérot peaks at other values of the top-gate voltage, which do not move to different plateaus in the considered range of magnetic fields. In the experiment (Fig. 4.2), the 0.7 shoulder in the conductance of the lowest subband merged at magnetic field of about 4 T merges with an additional conductance feature, which was identified with the Fabry-Pérot resonances in the main text. Here, we present additional details supporting this identification. The transmission coefficient accounting for the Fabry-Pérot resonance can be described by

$$\mathcal{T} = \frac{1}{1 + F \sin^2\left[Lk\cos(\theta)\right]}, \tag{4.52}$$

where F is the finesse and θ is the angle of incidence of the electron wave. At very low temperatures, the contribution of the resonance to the conductance is given by

$$G = \frac{e^2}{h}\frac{1}{1 + F \sin^2\left(Lk_F\right)}. \tag{4.53}$$

One should note that, according to Ref. [171], the Zeeman splitting in BLG is around 1.1 meV for 10T. Using the conversion formula for top-gate voltages to energies from the Supplemental Materials of [21] for the same device at slightly different voltages, the distance between $V_{\mathrm{TG}} = -12\,\mathrm{V}$ and $V_{\mathrm{TG}} = -8\,\mathrm{V}$ corresponds to the band splitting of 15.2 meV. Moreover, the density in the 2D region is not as low as in the constriction, since the split gates do not cover this region. Therefore, the total spin polarization of these 2D bands cannot be achieved and, since we only observe faint oscillations on top of the plateaus, the finesse F is small. As a result, this dependence of the conductance on the magnetic field is not experimentally resolved. These Fabry-Pérot oscillations are clearly visible in the differentiated differential conductance in Fig. 4.13, where they appear as small oscillations over the full top-gate and magnetic field range.

An experimental example of the dependence of this conductance contribution on V_{TG} and magnetic field is shown in Fig. 4.14(a) for the case of vanishing back-gate and split-gate voltage and a theoretical plot based on Eq. (4.53) in Fig. 4.14(b). The Fabry-Pérot resonances are seen for all magnetic field values and over the whole top-gate voltage range. These peaks, in contrast to the Zeeman-split subbands, only weakly depend on magnetic field, since the Zeeman splitting in the 2D bulk is smaller than in the QPC region.

While the plots in Fig. 4.14 agree qualitatively, there are two points to keep in mind. The theoretical plot was obtained using no residual density, which is certainly not the case in the experiment, and does not account for the peculiarity of the screening in the experimental setup in the presence of the split gates. Even if the split-gate voltage is zero, the split gates affect the electrostatics of the setup by locally screening the top gate and developing mirror charges for carriers in this region. In addition, the dielectric layer in the split-gate region is noticeably thinner. This introduces inhomogeneity in the middle of the sample, and the length scale corresponding to the distance between the leads and the split gates naturally appears.

In order to fully reproduce the experimentally observed pattern one would need a full electrostatic simulation. One very apparent difference is the fact that the period stays nearly constant in the

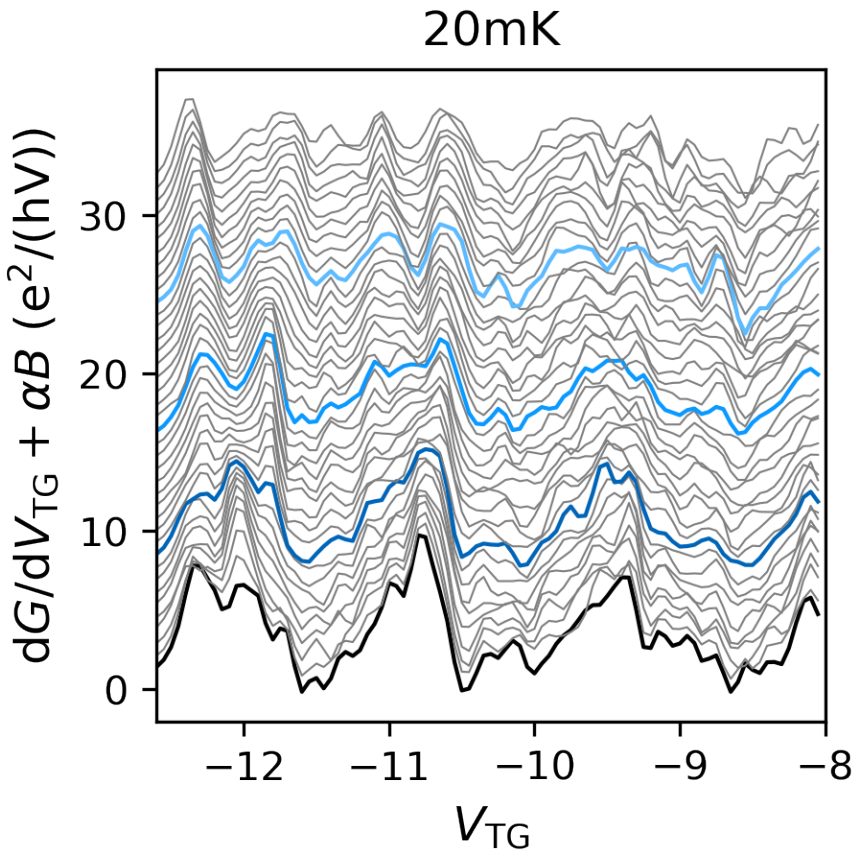

Figure 4.13: Differentiated differential conductance at 20 mK for different magnetic fields with a vertical shift with $\alpha = 4e^2/(hVT)$. Only magnetic fields with magnitudes of multiples of 0.2 T are shown for clarity. The blue curves correspond to the magnetic field values given in Fig. 4.2(a). For all magnetic field values and over the full plotted voltage range repetitive behavior corresponding to Fabry-Pérot oscillations is visible.
Reprinted figure with permission from Vanessa Gall, Rainer Kraft, Igor V. Gornyi, and Romain Danneau, Phys. Rev. Research, **4**, 023142 (2022). `https://journals.aps.org/prresearch/abstract/10.1103/PhysRevResearch.4.023142`, licensed under CC BY 4.0

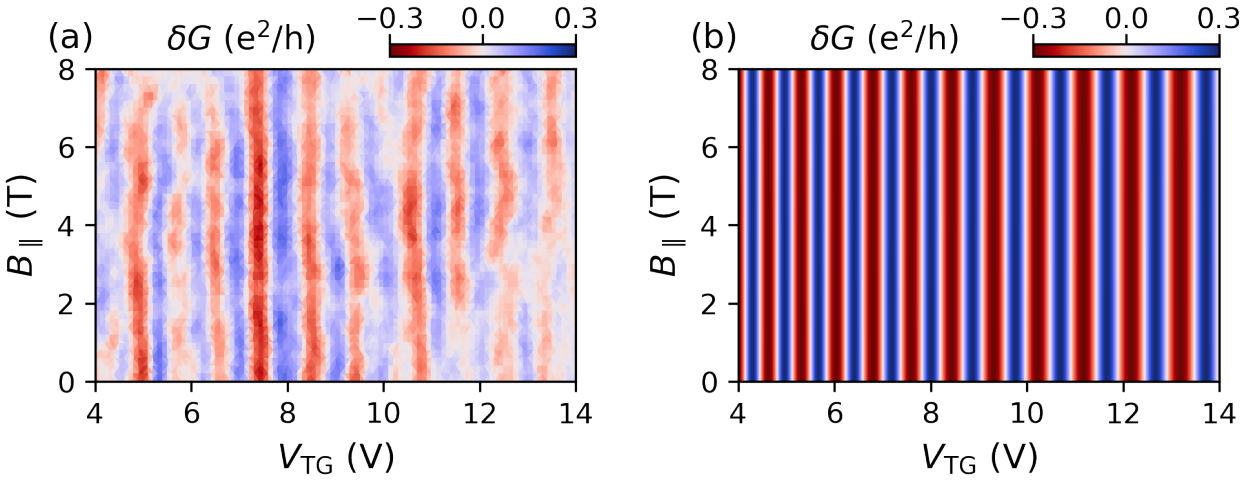

Figure 4.14: (a) Oscillations of conductance $\delta G = G - \bar{G}$for $V_{\mathrm{BG}} = V_{\mathrm{SG}} = 0$. The smooth background conductance $\bar{G}$ is obtained by means of a Savitzky-Golay Filter of the measured data. (b) Fabry-Pérot oscillations given by Eq. (4.53) in a magnetic field. The Fermi vectors in magnetic field were obtained by calculating the gap from Eq. (4.10) and the chemical potential, Eq. (4.7), for the given voltage and $n = c(V - V_0)$. The value $c = 0.8 \times 3.9 \times 10^{15}$ was determined in Quantum Hall measurements and $V_0 = -1.2$ V is the position of the Dirac point for $V_{\mathrm{BG}} = V_{\mathrm{SG}} = 0$. The chosen length $L = 230\,\mathrm{nm}$ corresponds to the distance between the leads and the split-gate fingers. The maxima and minima of oscillations stay nearly parallel over a large range of magnetic field. Reprinted figure with permission from Vanessa Gall, Rainer Kraft, Igor V. Gornyi, and Romain Danneau, Phys. Rev. Research, **4**, 023142 (2022). `https://journals.aps.org/prresearch/abstract/10.1103/PhysRevResearch.4.023142`, licensed under CC BY 4.0

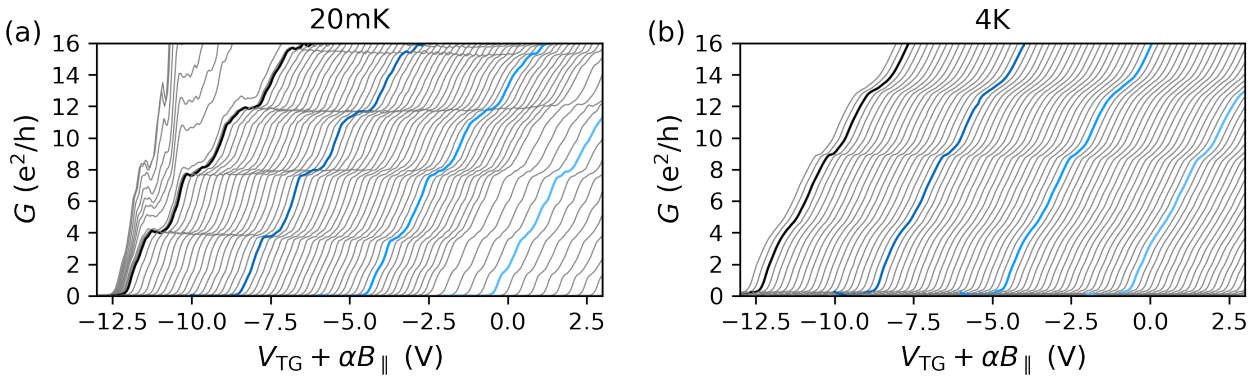

Figure 4.15: (a) and (b): Differential conductance G as a function of the top gate voltage V_{TG} for different values of magnetic field B and for 20 mK and 4 K, respectively. The curves are shifted with $\alpha = 2\mathrm{V/T}$. Figures 4.3(a) and 4.3(d) are a zoom into the lowest plateau shown here.
Reprinted figure with permission from Vanessa Gall, Rainer Kraft, Igor V. Gornyi, and Romain Danneau, Phys. Rev. Research, **4**, 023142 (2022). `https://journals.aps.org/prresearch/abstract/10.1103/PhysRevResearch.4.023142`, licensed under CC BY 4.0

experiment but not in the theory. While we did take into account the influence of the top-gate voltage on the density and the gap, the voltage also changes the boundary condition at the contacts and close to the split-gate fingers. Moreover we neglected any present residual density, which might change the position within the spectrum and thus the top-gate dependence. Finally, the presence of the split gates will naturally induce a breaking of translational symmetry, as the side boundaries do, which were not taken into account. For additional Fabry-Pérot interference data in the same sample, the reader is referred to the Supplemental Material of Ref. [21]. A more thorough study of Fabry-Pérot interferences in BLG can be found in Ref. [118].

4.6.5 Additional plots

The 0.7 anomaly discussed before is only visible in the lowest conductance plateau. The other discussed features, including the Fabry-Pérot resonances, are visible in other plateaus as well. In this Section, we show cadence plots of the measured conductance for larger ranges of conductances and top-gate voltages, than in Figs. 4.3(a) and 4.3(b). Figures 4.15(a) and 4.15(b) show the differential conductance as a function of the applied top-gate voltage with horizontal shift linear in the applied in-plane magnetic field. The additional 0.7-shoulder is seen in the lowest step for both temperatures. The main difference between the two temperatures is the smoother and flatter behavior for higher temperatures. Moreover, there are two additional features that are only visible in the 20 mK case, Fig. 4.15(a). For magnetic fields below 0.2T, the aluminum leads are still superconducting, so that the conductance is affected by superconducting fluctuations. Additionally, one sees Fabry-Pérot resonances, which are most clear on top of plateaus.

Since the aluminum leads are superconducting at 20 mK, a finite magnetic field is needed to kill this effect and curves below 0.2T show a higher conductance than the quantized values. This should be contrasted with the data shown in Fig. 4.3(b) for 4K, where there are no superconducting effects even at vanishing magnetic field. The superconducting proximity effect for the QPC in BLG is out of scope of the present discussion; the analysis of conductance curves affected by superconducting fluctuations

is an interesting task from both the experimental and theoretical points of view (for a related analysis of the supercurrent in this geometry, see Ref. [49]).

Since it is well known that the 0.7 anomaly is very sensitive to the exact shape of the constriction, we include data of the same sample in a different cool down at $T = 20$ mK and with a perpendicular magnetic field of 20 mT. The back-gate voltage is again $V_{\mathrm{BG}} = 10$ V and the split-gate voltage ranges between -12 V and -11.5 V. Figure 4.16 shows a cubic spline fit of the obtained conductance data in a form similar to Fig. 4.2 (b) and (c) but the vertical shifts correspond to different split-gate voltages, starting at $V_{\mathrm{SG}} = -12$ V for the lowest curve and ending with $V_{\mathrm{SG}} = -11.5$ V as a function of V_{TG}. The curves are colored according to their derivative. The thick solid lines mark the onset of the conductance plateaus, showing their dependence on the exact confinement condition, i.e., the split-gate voltage. The lowest curve corresponds to the same split-gate and back-gate configuration as the data in the main text, where we have identified the 0.7 anomaly by its magnetic field dependence, see Fig. 4.2 (b) and (e).

In this cooldown, we see a similar feature, marked by the arrow. When following the split-gate dependence of this feature (black dotted line), one observes that it stays parallel to the onset of the lowest plateau, which verifies that it is a feature of the QPC modes. Additionally, we again see Fabry-Pérot oscillation on top of the $4\,e^2/h$ and $8\,e^2/h$ plateaus (black dashed lines). Since they are generated by the lead modes, they show a different dispersion with the split-gate voltage. They always appear at the same electronic 2D density, which is only slightly tuned by the split-gate voltage. The onset of the conductance steps (and the 0.7 anomaly) is much more strongly dependent on the exact gate configuration, which makes the two effects clearly distinct.

4.7 Discussion

We have studied an electrostatically defined QPC (Sec. 3.1) in BLG (Sec. 1.2) which shows a zero field quantized conductance in steps of $4\,e^2/h$ owing to the spin and valley degeneracy, which is perfectly described by the Landauer-Büttiker formula derived in Sec. 2.3. In an in-plane magnetic field, as discussed in Sec. 3.1.1, a splitting of the first three subbands at 20 mK is observed that results from the Zeeman spin splitting, while the valley degeneracy is not affected. Additionally, a 0.7-like structure is located below the lowest size-quantized energy level which develops into the lowest spin split subband at $2\,e^2/h$. This additional feature is also observed in the 4K data, where only the splitting of the lowest band is clearly resolved. On top of the quantized conductance we observe Fabry-Pérot resonances, which were introduced in Sec. 3.1.3. Because of the higher densities in the 2D region and the relatively small bare Zeeman splitting in BLG, these stay at fixed top gate values with increasing magnetic field.

From the Zeeman energy splitting, the effective 1D g-factors in an in-plane magnetic field are found to be increasingly enhanced for lower subbands compared to the bare 2D Landé g-factor $g = 2$ in BLG. Moreover, the fact that the linear fitting of the Zeeman energy splitting for $N = 0$ does not extrapolate to zero at $B = 0$ further indicates the spontaneous spin polarization of the lowest subband. The behavior of the Zeeman spitting is a clear sign of the importance of interaction effects and confinement in this experiment. Based on this, we also attribute the observed shoulder below the lowest subband to the 0.7 anomaly stemming from the interaction-induced lifting of the band degeneracy.

We employ a phenomenological model, combining the slowly oscillating spin structure discussed in Sec. 3.1.2.2 with the free energy discussed in Sec. 3.1.2.3, to qualitatively describe the behavior of this feature in the applied in-plane magnetic field. In this model we assume, that each spin-valley subband

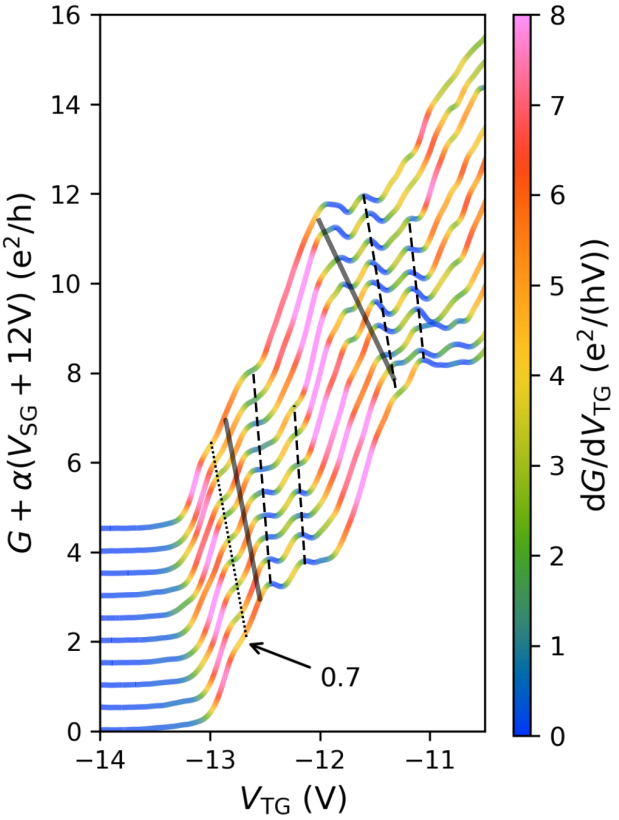

Figure 4.16: Cubic spline fit of the differential conductance G of the same sample in a different cooldown for $V_{BG} = 10$ V and a perpendicular magnetic field of 20 mT as a function of the V_{TG} in elevating V_{SG} for 20 mK. The curves are shifted vertically with $\alpha = 10e^2/h$V and colored according to their first derivative. The onset of the conductance plateau (black solid lines serving as guides for the eye) shows a clear dependence on the exact gate configuration. The black dotted line shows the dispersion of a feature, that we identify as a 0.7 shoulder, with a dispersion parallel to the onset of the plateau, in agreement with its quasi-1D nature. Fabry-Pérot oscillations are marked by black dashed lines and show a different (weaker) split-gate voltage dependence, since they are generated by the 2D lead modes.
Reprinted figure with permission from Vanessa Gall, Rainer Kraft, Igor V. Gornyi, and Romain Danneau, Phys. Rev. Research, **4**, 023142 (2022). `https://journals.aps.org/prresearch/abstract/10.1103/PhysRevResearch.4.023142`, licensed under CC BY 4.0

can be spontaneously split by the electron-electron correlations. By comparing the development of resulting features in a magnetic field, Fig. 4.9, with the experimental conductance curves in Fig. 4.3, we conclude, that the observed behavior can be explained by the assumption of an effective spontaneous spin splitting, while the valley degree of freedom is not affected. This is in a full agreement with the picture of spontaneous spin polarization inferred from the measured Zeeman splitting.

The experimental findings, explained by phenomenological calculations and combined with the results of Ref. [21] for out-of-plane magnetic field, establish the exquisite tunability of spin and valley degree of freedom by the application of gates or external magnetic fields. Furthermore, these results also demonstrate relevance of electron-electron correlations in BLG QPC geometry, as well as a possibility to control the effective strength of interactions by means of electrostatic spatial confinement by a combination of external gates.

Our results concerning the position of additional shoulders in the quantized conductance are also relevant for other materials. Generally, if a material has multiple valleys and spin, an asymmetry between these degrees of freedom is visible already at the level of possible interactions, as shown in the diagrams (3.12). While the normal Coulomb interaction may change the valley, it does not flip the spin. For this reason we would expect, that materials without strong spin-orbit coupling will show a 0.7 anomaly, that is consistent with a phenomenological model with spontaneous spin splitting, while other degrees of freedom remain degenerate. It is only the shape of the shoulder, that depends on the exact dispersion relation. For flatter band bottoms a stronger shoulder should be observed.

In materials with strong Kane-Mele type spin orbit coupling like transition metal dichalcogenide this is more involved. The spin up and down bands will be split exactly the opposite direction in opposite valleys, which leads to a non-interacting conductance similar to the one depicted in Fig. 4.11 (d). A behavior as in Fig. 4.11 (c) is only obtained for bilayer graphene with $U = 0$. This leads to a true plateau at zero magnetic field and a full lifting of all degeneracies in large magnetic field. Interaction effects would lead to an additional shoulder around $0.7 \times 4\frac{e^2}{h}$ like in case **c3** in Fig. 4.9. So one could expect to see both a shoulder at $0.5 \times 4\frac{e^2}{h}$ and at $0.7 \times 4\frac{e^2}{h}$.

4.8 Summary and conclusions

In summary, we have found that the zero field conductance in a bilayer graphene quantum point contact is quantized in steps of height $4\frac{e^2}{h}$, while the step height is $2\frac{e^2}{h}$, once the in-plane magnetic field is high enough. This transition is not continuous but appears as soon as the Zeeman splitting is resolved at the given temperature. In the higher temperature case, the steps are smoother and the Fabry-Pérot oscillations visible at the lower temperature disappear. These oscillations do not disperse with the magnetic field in the considered regime.

Additionally we find a shoulder below the first plateau at both temperatures, that continuously moves into the lowest Zeeman split plateau at higher magnetic field. This behavior can be explained as a 0.7 anomaly by assuming an effective spontaneous spin splitting, while valley remains degenerate. The effective Landé g-factor is enhanced for the lowest three size-quantized subbands. We interpret both of these phenomena as interaction induced, since screening by the gates does not have a very significant effect at the considered distances for mono- and bilayer graphene.

In conclusion, we can state, that the main features of the conductance curves in a bilayer graphene quantum point contact can be explained by employing a non-interacting Landauer-Büttiker approach, similarly to the one presented in Sec. 3.1, except with an additional valley degeneracy. However, on top of this, electron-electron interaction indeed has a visible influence on the conductance curves. The

first interaction induced feature is the additional shoulder beneath the first plateau which can, again similar to a single valley material, be explained by an effective instability in the spin channel, while valley remains degenerate. The second interaction induced feature is the enhancement of the Landé g-factor in the three lowest subbands, which is strongest for the lowest subband due to the large density of states enhanced by the strong confinement.

Our phenomenological model can be extended to materials with additional degrees of freedom or strong spin orbit coupling. **Generally, if Coulomb interaction is the only relevant interaction in the system and without interaction we have $N_s \times N_v$ degenerate spin and valley degree of freedom, the symmetry between spin and valley degree of freedom is naturally broken by the absence of spin-flipping processes. Then we expect a spontaneous spin instead of valley splitting and one additional interaction induced shoulder at $0.7 \times N_s \times N_v \frac{e^2}{h}$. This shoulder is expected to be stronger for flatter dispersions.** If spin orbit coupling is strong and of the Kane-Mele type, we would expect an additional plateau at $0.5 \times N_s \times N_v \frac{e^2}{h}$, which should be stronger than the interaction induced shoulder at $0.7 \times N_s \times N_v \frac{e^2}{h}$ and additional plateaus at high magnetic field.

Additionally, an enhancement of the effective Landé g-factor due to interactions can also be expected in quantum wires. While the 0.7 anomaly requires a rather strong local potential, the effective Landé g-factor is always enhanced at small density, large density of states and reduced dimensionality and so should be observable in the absence of a 0.7 anomaly.

Interaction effects in bilayer graphene are expected to play a similar role as in other, conventional two-dimensional electron gases. This is different in monolayer graphene, especially close to the Dirac point. While effects due to electron-electron interaction have a visible effect on the conductance curves in this chapter, they turn out to be negligible in Chapter 5, where we specifically consider the influence of electron-electron interaction on the magnetoresistance in a monolayer graphene Corbino disk at low temperatures and finite densities in Sec. 5.3.5. In contrast, they dominate in the same monolayer graphene Corbino disk at elevated temperatures and charge neutrality in Chapter 6, where electronic correlation allow for a hydrodynamic treatment, as introduced in Sec. 2.4.

Chapter 5

5 Disorder dominated transport in a graphene Corbino disk

In this chapter we discuss the magnetoresistance in a graphene Corbino disk (introduced in Sec. 3.2) at low temperatures, where transport is dominated by disorder. If the magnetic field is high enough, this can be described by the method introduced in Sec. 2.2.5, which already takes the special band structure of graphene, discussed in Sec. 1.1, into account. If disorder is strong enough to smear the clear separation of Landau levels, a semi-classical approach based on the Boltzmann equation in Sec. 2.1.1 is sufficient.

In contrast to the quantum point contact in bilayer graphene discussed in Chapter 4, the system considered here has a physical size of the order of μm*, which is larger than the typical mean-free path even in a very clean system, so that the clear quantum nature of the electronic liquid will only appear, if magnetic fields are large enough to fit a whole Landau orbit inside the system. Moreover, it will turn out, that in this device electron-electron interaction does not lead to any clearly visible effects.*

This should also be contrasted to Chapter 6, where the same setup is investigated at elevated temperatures in the hydrodynamic regime. However, as we will point out, as long as the semi-classical Boltzmann equations are applicable, one can find a similar set of quasi-hydrodynamic equations in the disorder dominated regime, which is however not based on the assumption of a local equilibrium.

In a Hall-bar geometry both transverse and longitudinal bulk conductivities, $\sigma_{xy}(B)$ *and* $\sigma_{xx}(B)$*, respectively enter the magnetoresistance and* $R(B)$ *becomes independent of the magnetic field* B*, as can be seen from Eqs.* (2.29) *and* (2.30)*. In the corresponding Corbino setting, that was introduced in Sec. 3.2, the magnetoresistivity is determined solely by* $\rho_{xx}(B) \stackrel{def}{=} 1/\sigma_{xx}(B)$*, which, again using* (2.29)*, leads to pure* B^2 *behavior.*

The gate dependence of the coefficient reveals information about the scattering mechanisms in the sample, allowing for a characterization of the role of scattering on long-range (Coulomb impurities, ripples) and short-range disorder (adatoms, atomic defects), as well as to separate the bulk resistance from the contact resistance and thus extract the true bulk mobility. This is demonstrated by an application to the measured magnetoresistance of suspended graphene in the Corbino geometry at magnetic fields up to $B = 0.15\ T$*, where Shubnikov-de Haas oscillations are not relevant, yet.*

In this chapter we investigate the magnetoresistance of graphene in a Corbino disk geometry. While the magnetoresistance in the Hall-bar geometry is rather complicated, a semi-classical analysis in the Corbino geometry leads to a simple quadratic magnetoresistance. ***Here we introduce a mixed disorder model and demonstrate that magnetotransport can indeed be dominated by this***

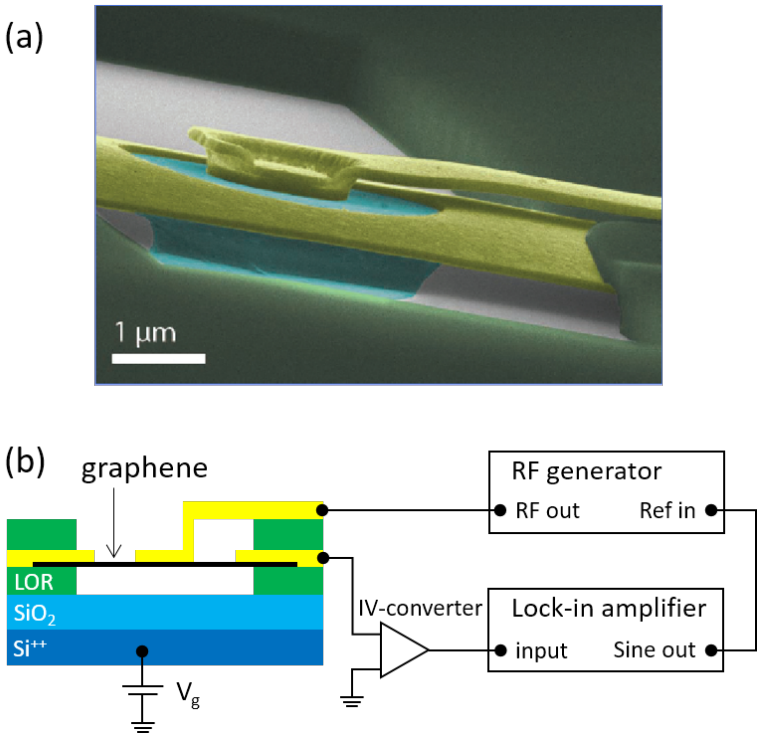

Figure 5.1: (a) Scanning electron microscope image of a suspended graphene Corbino disk (green part in the center) with 4.5 µm diameter outer Au contact and 1.8 µm diameter inner Au contact; the scale is given by the white bar. (b) Cross-sectional view of the sample and its basic two-lead measurement connections. The thicknesses of the SiO_2 and LOR layers amount to 285 nm and 500 nm, respectively.
Reprinted figure with permission from Masahiro Kamada, Vanessa Gall, Jayanta Sarkar, Manohar Kumar, Antti Laitinen, Igor Gornyi, and Pertti Hakonen, Physical Review B, **104**, 115432 (2021). Copyright 2021 by the American Physical Society. `https://journals.aps.org/prb/abstract/10.1103/PhysRevB.104.115432`

contribution and why measuring the low field magnetoresistance in the Corbino geometry is an ideal route to characterize the disorder in the sample. *For this, one considers the density dependence of the different kinds of scatterers which can be used to extract their characteristics from the gate voltage dependence of the data.*

This chapter is based on publication [12] and its supplemental material and was a joint work with the experimental group of Pertti Hakonen from Aalto University.

5.1 Introduction

Graphene exhibits properties, that make it an ideal candidate in electrical transport experiments. Electrons in monolayer graphene can show ballistic behavior over several microns, but the mean free path is usually limited by Coulomb scattering and short-range scatterers [172]. In most situations Coulomb scatterers, that are either embedded in the sustrate or cause by fabrication residue dominate the transport properties and short-range scattering is only relevant at large carrier densities. It is however possible, to mimimize the carrier scattering resulting from charged impurities and short-range defects by using freely suspended graphene flakes and current annealing [173] and thus obtain truly intrinsic properties of graphene. This strength of suspended graphene samples has been used to reveal many basic transport properties. An example is for example the suspended graphene in Corbino-ring geometry, which can be used to inverstigate the fractional quantum Hall states in graphene [174] and was introduced in Sec. 3.2.

In order to access these basic quantum transport properties, one can for example study the magnetoresistance, i.e. the dependence of the resistance on an applied magnetic field, as done in Refs. [5, 24, 25, 175, 176]. Typically, the resistance at low temperatures is governed by disorder-induced scattering, while electron-electron and electron-phonon scattering require higher temperatures to become relevant. The presence of disorder also leads to quantum effects that correct the conductance and lead to universal conductance fluctuations, which are very sensitive to applied fields. When these quantum effects can be neglected, the classical magnetoresistance predicts both a linear and a quadratic dependence [177, 178]. Here we show in the Corbino geometry, that the intrinsic behavior of suspended graphene yields a strong magnetoresistance, which can be used to characterize the sample. By fitting the gate voltage dependence of the magnetoresistance date with a model containing both short range and charged impurity scatterers, which show a different density dependence, we are able to characterize the strength of both types of disorder and extract the true bulk resistance, which, for a clean sample like this, is smaller than the contact resistance. From this bulk resistance one may then extract the true bulk mobility, which is much larger than the naively extracted value, which contains the contact resistance. We carefully take into account, that most of the data is obtained rather close to the Dirac point at very low residual densities, which is a rather unusual regime for this sort of measurement.

As already discussed in Sec. 3.2, the Corbino geometry is special, since the Hall conductivity drops out of the magnetoresistance, which is determined solely by the longitudinal conductivity $\rho_{xx}(B) \stackrel{\text{def}}{=} 1/\sigma_{xx}(B)$. Previous theoretical studies have focused on the Hall-bar geometry, where the Hall conductivity σ_{xy} enters into the magnetoresistance and thus these are not applicable for the description and analysis presented here. In a general anisotropic Corbino sample, the magnetoresistance is calculated in Ref. [179]. We will assume spatial isotropy, in which case one obtains

$$R(B) = \frac{1}{2\pi}\ \rho_{xx}(B)\ \ln\frac{r_{\text{out}}}{r_{\text{in}}}. \tag{5.1}$$

Here r_{in} and r_{out} are, respectively, the inner and outer radii of the disk. The logarithmic geometrical factor in Eq. (5.1) is obtained by the requirement of current conservation, as we demonstrate in Sec. 3.2. While the magnetoresistance in graphene in the Hall-bar geometry was found to display a complex magnetic-field dependence [58, 180–182] depending on the assumed disorder, the results obtained here show a simple, strong parabolic magnetoresistance for all considered disorder potentials and field up to 0.1 T.

This chapter is organized as follows. In Section 5.2 we present the experimental setup, that motivated and was analyzed in Ref. [183]. The most relevant data obtained is the resistance R of the device as

a function of an overall, varying backgate V_g and for low magnetic fields up to 0.15 T. In Section 5.3 we discuss the theory of disorder dominated transport in this setup, which combines the perturbative calculation from Sec. 2.2.5 with the semiclassical linear response result in Sec. 2.1.1 with the special geometry of the Corbino disk. We discuss the behavior in the presence of short-range scatterers, charged impurities and also the influence of low temperature and electron-electron interaction, paying special notice to the fact, that some data points are obtained close to the Dirac point. In Section 5.4 we show, that this theory can be used to analyze the obtained data, specifically the role of different kinds of impurities. We end this chapter with the conclusion in Sec. 5.5.

5.2 Experimental setup and sample characterisation

The data presented in this chapter was measured on a Corbino disk with inner and outer radii of 0.9 and 2.25 μm respectively pictured in Fig. 5.1(a) as a false-color scanning electron microscope picture. The disk consist of suspended graphene and has an overall back gate, with a gate capacitance of $C_g = 1.5 \times 10^{-5}$ F/m^2. There are two leads attached to the disk, which are employed in a standard voltage-biased measurement, with bias voltages in the range $1-13$ mV. The corresponding connections are shown in Fig. 5.1(b). The field-effect mobility was determined to be $\mu_{\mathrm{FE}}^{\max} \simeq 1 - 2 \times 10^5$ cm^2/Vs, which is very high. In this setup, the current passing through the Corbino disk (between inner and outer contact) was measured for two temperatures $T = 4$ K and $T = 27$ K while varying the backgate voltage V_g and a small perpendicular magnetic field $B < 0.15$ T.

The thusly obtained magnetoresistance is shown in 5.2. The measured data (dots) are shown together with a cubic spline fit. Starting with the lowest curve for both temperatures, which corresponds to the case $B = 0$ T, one observes a shift of the Dirac point (the point of highest resistance R) away from $V_g = 0$ V, which is in opposite directions for the two temperatures. At $T = 27$ K the shift amounts to $V_g^D(0) \approx 0.2$ V, which corresponds to a residual charge density of $n_0 \approx 8 \times 10^9$ cm^{-2}. Turning to the the data at finite magnetic field, the resistance increases strongly, while the Dirac point is further shifter away from zero gate voltage. Each single curve is not mirror symmetric, but shows finite electron-hole asymmetry, which is to the largest part determined through the contact resistance at the leads, where the forming *pn* interface influences electrons and holes differently [184].

In Sec. 5.4, we deduce charge carrier mobility from the measured geometric magnetoresistance. For comparison, we display in Fig. 5.3 the field-effect mobility defined by $\mu_{\mathrm{FE}} = e^{-1} d\sigma_{xx}/dn$, obtained from measurements of differential resistance $R(V_g)$ at the end of the experiments. These data measured at $T = 4\,\mathrm{K}$ indicate that, for this sample at a tiny bias voltage, the maximum mobility for holes $\mu_{\mathrm{FE}} \simeq 13\,\mathrm{m}^2/\mathrm{Vs}$ is clearly larger than that for electrons $\mu_{\mathrm{FE}} \simeq 7\,\mathrm{m}^2/\mathrm{Vs}$. However, at the employed bias voltages $1 \ldots 10\,\mathrm{mV}$, the influence of the pn interface at positive gate voltages appears to be reduced and μ_{FE} for electrons and holes becomes almost equal. This corresponds to the much weaker electron-hole asymmetry in Fig. 5.2. From this strong dependence of the field-effect mobility on the contact resistance we conclude that this is not a reliable way of characterizing the bulk mobility of the sample.

As we are going to demonstrate below, looking at the magnetoresistance as a function of temperature and density (or gate voltage) in a mixed disorder model is a very efficient tool to characterize the different types of disorder. Specifically, we are able to show a different density dependence for short-range or Coulomb scatterers, which can be used to extract the concentration of these two types of scatterers from the data. While previous studies have usually restricted themselves to only one kind of disorder, we find, that both are necessary in this general sample. Since the density of states and the

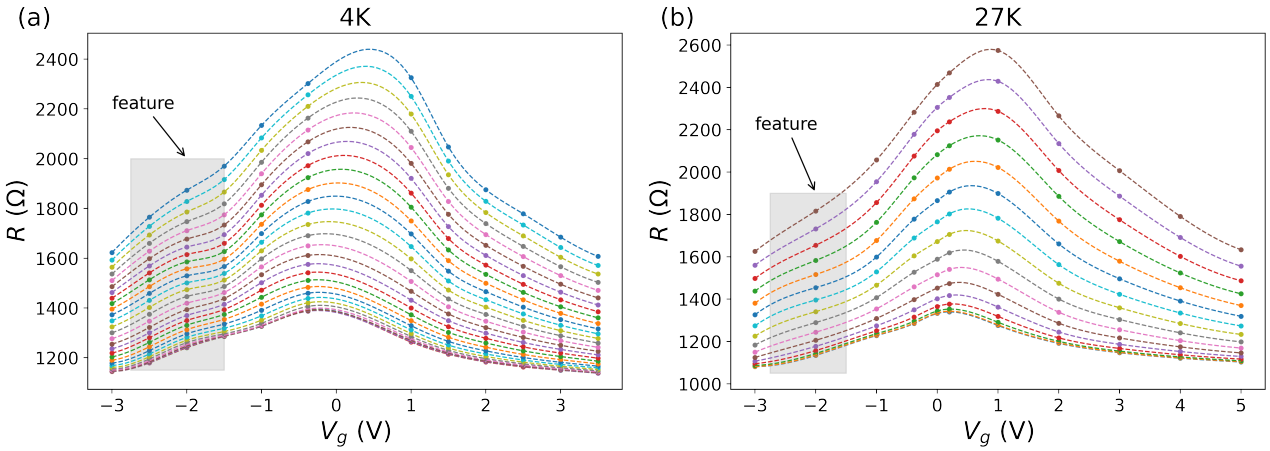

Figure 5.2: Resistance vs. V_g at various magnetic fields. (a) 4 K for magnetic fields from 0 to 0.15 T with 0.005 T step (from bottom to top); the broken curves are cubic spline interpolations to the data. (b) 27 K for magnetic fields from 0 to 0.15 T with 0.01 T step (from bottom to top); the broken curves are cubic spline interpolations. The grey area marks the region of increased resistance due to a broadened resonance level at V_g near −2 V (the feature is more pronounced at $T = 4$ K and in the middle of the magnetic field range (middle dark blue line)).
Reprinted figure with permission from Masahiro Kamada, Vanessa Gall, Jayanta Sarkar, Manohar Kumar, Antti Laitinen, Igor Gornyi, and Pertti Hakonen, Physical Review B, **104**, 115432 (2021). Copyright 2021 by the American Physical Society. `https://journals.aps.org/prb/abstract/10.1103/PhysRevB.104.115432`

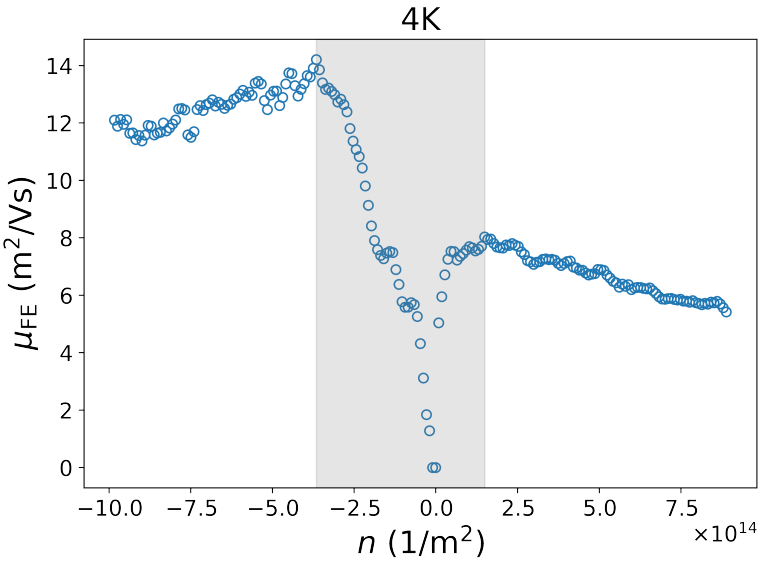

Figure 5.3: Field effect mobility μ_{FE} at $T = 4\,\mathrm{K}$ determined from the measured differential resistance dV/dI at $B = 0$. The Dirac point shift $V_g^D(0)$ has been subtracted off from the gate voltage before calculating the charge carrier density n. The dip in μ_{FE} around $n = 0$, indicated by a grey shadow, corresponds to the density range governed by disorder broadening of the Dirac point. The extend of this range is consistent with the value n_* given in Table 5.1
Reprinted figure with permission from Masahiro Kamada, Vanessa Gall, Jayanta Sarkar, Manohar Kumar, Antti Laitinen, Igor Gornyi, and Pertti Hakonen, Physical Review B, **104**, 115432 (2021). Copyright 2021 by the American Physical Society. `https://journals.aps.org/prb/abstract/10.1103/PhysRevB.104.115432`

conductance do not diverge at the Dirac point [57], looking at values close to that point gives especially valuable information. These effects observed clearer in a Corbino disk than in a Hall bar, since here one obtains a quadratic magnetoresistance already from the semi-classical Drude calculation. This also means, that interaction effects are sub-leading in the temperature range we consider, but should dominate at very low temperatures.

5.2.1 Shift of the Dirac point and additional feature

In the resistance vs. gate voltage data, Fig. 5.2, we observe a shift of the resistance maximum (associated with the position of the Dirac point) with increasing magnetic field. We attribute this shift to the dependence of the screening length on the magnetic field, which is only relevant for small densities. In this case, the total charge density induced on the membrane is less at the Dirac point at finite B, which would indicate generation of more positive charge on graphene by the screening. Thus the screening should take place by positive carriers and the impurities are negatively charged. In addition, there was a slow shift of the Dirac point position towards positive V_g over time (on the order of 0.2 V in one month). It is worth noting that the effect of magnetic field on screening is suppressed at higher densities and higher temperatures. This is in line with the stronger shift of the resistance maximum at $T = 4\,\mathrm{K}$.

In order to be able to fit the quadratic magnetoresistance, one first has to get rid of this shift of the

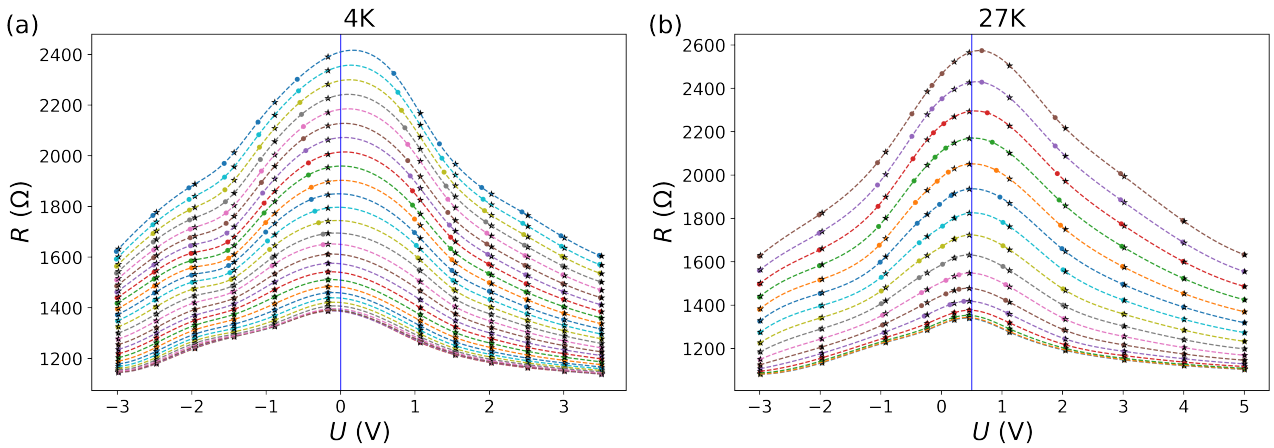

Figure 5.4: Resistance at 4 K (a) and 27 K (b), shifted according to Eq. (5.2). Colored dots are the shifted measured points and black stars show the data obtained from the spline. (a): $V_2 = 1$V and $V_1 = 0$; (b): $V_2 = 1$V and $V_1 = 0.5$V.
Reprinted figure with permission from Masahiro Kamada, Vanessa Gall, Jayanta Sarkar, Manohar Kumar, Antti Laitinen, Igor Gornyi, and Pertti Hakonen, Physical Review B, **104**, 115432 (2021). Copyright 2021 by the American Physical Society. `https://journals.aps.org/prb/abstract/10.1103/PhysRevB.104.115432`

Dirac point.

Within the picture based on the effect of magnetic field on screening, one should only shift data points close to the Dirac point, while not affecting those further away from it. Since we have data only for a discrete set of values of the gate voltage, in order to determine the gate voltage corresponding to the Dirac point, we find the maximum of the $R(V)$ curve given by a cubic spline interpolation of the measured data points. For each value of magnetic field, this maximum V_0 is shifted to the same voltage V_1. For all other data points, we adopt a phenomenological Ansatz, where, away from the Dirac point, the shift reduces exponentially, i.e., a measured point on the curve corresponding to B is shifted by

$$V \Rightarrow V - (V_0 - V_1)e^{-\frac{|V-V_0|}{V_2}}. \tag{5.2}$$

The voltage V_1 is the same for all curves and is determined by the maximum of the most symmetric curve in the unshifted case, and V_2 describes the characteristic voltage window where the effect of magnetic field on screening is seen. Since the shift for different magnetic fields will generically be different, one also has to use the spline interpolation to get access to the resistance at the same voltages for all magnetic fields. We take this voltages to be the ones on the shifted zero magnetic field curve. A result for thus shifted and unshifted data points is shown in Fig. 5.4.

Comparing Fig. 5.4 with Fig. 5.2, we see that the shifted curves are indeed more symmetric, which supports the idea of stronger shift around the neutrality point as a result of magnetic-field effect on screening. We note, however, that a homogeneous (independent of the distance to the Dirac point) shift, used for the actual fitting procedure, captures correctly the shift near the neutrality point. Since this is the main manifestation of the screening-induced shift in magnetoresistance curves (the

difference in the tails of magnetoresistance is not that important for the fitting procedure), we adopt the simplest shifting in our analysis. Note that, in all cases, the small feature close to −2V (attributed to a quasi-resonance in scattering by adsorbed local impurities) is preserved after shifting the curves.

One more peculiarity seen in the resistance curves plotted over the gate voltage is a feature close to $-2\,\mathrm{V}$, which is marked by a grey region for both temperatures shown in Fig. 5.2. The resistance around this voltage is somewhat enhanced compared to the resistance away from this voltage. There is no comparable feature at the electron side of the resistance curve and the feature is stronger for lower temperatures. We attribute this feature to a broadened resonance level associated with adsorbed local impurities. When the chemical potential is moved by the gate voltage into the vicinity of this quasi-resonance, the scattering amplitude for such impurities is enhanced, leading to shorter transport scattering time and, hence, to the increase in resistance. At the same time, the broadening of this resonance is sufficiently strong to avoid truly resonant scattering (as, e.g., in the case of vacancies); in contrast to infinitely strong impurities (vacancies), the position of the quasi-resonance is shifted away from the Dirac point. Away from the resonant energy, these impurities produce weak short-ranged disorder.

For higher temperatures, some adsorbed dirt is thermally removed form the sample, leading to a less pronounced feature. This suggests that the role of scattering off short-range disorder at higher temperatures could be decreased.

5.3 Theoretical background

In this Section we discuss the basic facts of disorder-dominated transport in graphene (for the hydrodynamic - collision-dominated - transport, higher temperatures are typically required than those in this experiment, $50\,\mathrm{K} < T < 150\,\mathrm{K}$, while phonons become important at yet higher T [34]). As already discussed in Sec. 1.1, graphene has a linear energy dispersion relation $\varepsilon_\mathrm{k} = \pm v_g \hbar k$ and thus also a linear-in-energy density of states :

$$\nu_0(\varepsilon) = \frac{N|\varepsilon|}{2\pi v_g^2 \hbar^2}, \tag{5.3}$$

where $v_g = 10^6$ m/s is the Fermi velocity, ε is the energy counted from the Dirac point, and $N = 4$ is the degeneracy due to spin and valley degrees of freedom. Due to this density of states, the charge carriers density is obtained as

$$n = N\frac{\varepsilon_F^2}{4\pi\hbar^2 v_g^2}, \tag{5.4}$$

where ε_F is the Fermi energy. Another consequence of this special dispersion relation is that the cyclotron frequency ω_c is energy-dependent [5] :

$$\omega_c(\varepsilon) = \frac{eB}{m_c(\varepsilon)} = \frac{\hbar}{m_c(\varepsilon)\ell_B^2}, \tag{5.5}$$

where B is the magnetic field and $m_c(\varepsilon) = \varepsilon/v_g^2$ is the energy dependent cyclotron mass. The magnetic length scale is set by $\ell_B = \sqrt{\hbar/eB}$.

The linear dispersion relation and the spinor nature of the wave-function also influence the scattering and relaxation rates of charge carriers. Here we consider a situation, where the major contributions to

resistance arise from short-range scattering (s) and Coulomb scattering (C) and adopt a mixed-disorder model [185] to describe the magnetoresistance. When interpreting the effect of charged scatterers, one should remember, that graphene is not perfectly flat, but has ripples [31–33], who give rise to scattering behavior similar to charged impurities [34], so that this contribution is effectively included in our treatment of Coulomb scattering and thus the obtained parameters should be interpreted accordingly.

Let us start by discussing scattering on a short-range impurity potential. We only consider not too high carrier densities for which the length scale d of random potential variations is smaller than the carriers wave-length and larger than the interatomic spacing a, i.e., $a \ll d \ll \lambda$. For this type of disorder the intervalley scattering can be disregarded, the theory presented in Sec. 2.2.5 applies and the quantum τ_q and transport $\tau_{\rm tr}$ scattering times can be estimated using Fermi's golden rule [5, 56]:

$$\tau_q^s(\varepsilon) = \frac{\hbar\gamma_s}{|\varepsilon|}\,, \quad \tau_{\rm tr}^s(\varepsilon) = 2\tau_q^s(\varepsilon)\,, \tag{5.6}$$

where

$$\gamma_s = \frac{2\hbar^2 v_g^2}{n_{\rm imp}^s U_0^2}, \tag{5.7}$$

$n_{\rm imp}^s$ is the concentration of short-range impurities, and U_0 denotes the magnitude of the impurity potential. The strength of short-range disorder can be characterized by the parameter γ_s which for short-range scattering is energy independent. The difference between $\tau_{\rm tr}$ and τ_q is caused by the weak scattering anisotropy due to the spinor nature of the wave functions.

For charged impurities, which we discuss in Sec. 5.3.2), the scattering times can be brought to similar form, but the effective parameter γ_C is in general energy dependent and a function of the Fermi energy, temperature and magnetic field. When one considers sufficiently low temperatures and magnetic fields, γ_C can be expressed as:

$$\tau_q^C(\varepsilon) = \frac{\hbar\gamma_C'(\varepsilon,\varepsilon_F)}{|\varepsilon|}\,, \quad \tau_{\rm tr}^C(\varepsilon) = 2\frac{\hbar\gamma_C(\varepsilon,\varepsilon_F)}{|\varepsilon|}\,, \tag{5.8}$$

Here $\gamma_C(\varepsilon,\varepsilon_F)$ and $\gamma_C'(\varepsilon,\varepsilon_F)$ are functions of the effective coupling (graphene "fine-structure constant") $\alpha = e^2/(\hbar v_g \epsilon_\infty)$, with ϵ_∞ the background dielectric constant, see Sec. 5.3.2. If there is no screening environment and the renormalization of velocity by Coulomb interaction is neglected, the nominal value of this constant is $\alpha_0 = 2.2$. However, both of these [5] effects reduce this value. For intermediate values of α, one may write the relation $\tau_{\rm tr}^C(\varepsilon) \approx 2\tau_q^C(\varepsilon)$, similar to Eq. (5.6), which is however no longer exact.

As discussed in Sec. 2.1.1, the conductivity in zero magnetic field in the presence of only short-range scatterers is given by the Drude formula:

$$\sigma_{xx}^D = \sigma_0 = \frac{2e^2\gamma_s}{\pi\hbar}. \tag{5.9}$$

Comparing this to the typical conductivities measured in clean graphene samples, we deduce, that γ_s should be of the order of unity if we only take into account short-ranged scatterers.

In Sec. 2.2.5 we discussed the conductivity of disordered graphene in a perpendicular magnetic field and found, that the conductivity is in essence as obtained from the semi-classical Boltzmann equation, as long as Landau levels are sufficiently broadened by disorder. This can be quantified by looking

at the product $\omega_c \tau_q^s$ which exactly describes this broadening of Landau levels. Since for short-range scatterers both ω_c and τ_q^s depend on energy [see Eqs.(5.5) and (5.6)], the parameter

$$x = \omega_c \tau_q^s = \frac{\gamma_s \hbar^2 v_g^2}{\varepsilon^2 \ell_B^2}, \tag{5.10}$$

can be either small or large, depending on the energy ε [58] and it determines the dependence of the density of states $\nu(\varepsilon)$ of disordered graphene on magnetic field. For the case of scattering on Coulomb impurities, the quantum scattering time decreases linearly with energy $\varepsilon \propto \sqrt{n}$, which means that the parameter $x = \omega_c \tau_q^C$ becomes energy independent. Since the transport scattering time $\tau_{\rm tr}$ has the same energy dependence as τ_q, the same parameter x governs the quasiclassical bending of particle trajectories in magnetic field.

The general result for the longitudinal conductivity $\sigma_{xx}(\varepsilon)$ is given by Eq. (4.13) of Ref. [56] and was discussed in Sec. 2.2.5. Introducing the relative density of states $\tilde{\nu}(\varepsilon) = \nu(\varepsilon)/\nu_0(\varepsilon)$, where $\nu_0(\varepsilon)$ is the zero-field density of states, we write the conductivity kernel (conductivity of particles at energy ε) in terms of $\tilde{\nu}(\varepsilon)$ as follows:

$$\sigma_{xx}(\varepsilon) = \sigma_0 \frac{\tilde{\nu}(\varepsilon)^2}{\tilde{\nu}(\varepsilon)^2 + [\omega_{\rm c}(\varepsilon)\tau_{\rm tr}(\varepsilon)]^2}, \tag{5.11}$$

where

$$\sigma_0 = \frac{e^2 v_g^2}{2} \tau_{\rm tr}(\varepsilon_F) \nu(\varepsilon_F) \equiv \frac{e^2 \gamma N}{2\pi\hbar}. \tag{5.12}$$

Here, we have introduced the dimensionless disorder strength γ that has a meaning of a dimensionless conductance per spin per valley and combines the effect of short range and Coulomb scatterers. For only short-range disorder, one has $\gamma = \gamma^s$. In a mixed disorder model, the total transport time is determined by

$$\frac{1}{\tau_{\rm tr}(\varepsilon)} = \frac{1}{\tau_{\rm tr}^s(\varepsilon)} + \frac{1}{\tau_{\rm tr}^C(\varepsilon)}, \tag{5.13}$$

and γ is related to the total transport scattering time, as given by Eq. (5.12).

For a finite temperature, the conductivity is given by the kernel (5.11) weighted with the derivative of the Fermi function $n_F(\varepsilon)$:

$$\sigma_{xx} = \int_{-\infty}^{\infty} {\rm d}\varepsilon \left(-\frac{\partial n_F(\varepsilon)}{\partial \varepsilon} \right) \sigma_{xx}(\varepsilon) \tag{5.14}$$

At zero temperature, the derivative of the Fermi function is a delta-distribution and the conductivity reduces to Eq. (5.11) with $\varepsilon \to \varepsilon_F$. At zero magnetic field one simply finds σ_0 from Eq. (5.12). The whole temperature dependence of the Drude conductivity is determined by the energy dependence in the kernel (5.11) when the thermal broadening of the delta-function is taken into account. At low temperatures, $k_B T \ll \varepsilon_F$, the finite-T corrections to the zero-T result are negligible, and the measured conductivity is given approximately by $\sigma_{xx} \approx \sigma_{xx}(\varepsilon_F, T = 0)$. Under these conditions, if $\tilde{\nu}_0$ is independent of the magnetic field, the conductivity in a finite magnetic field can be written in the conventional Drude form:

$$\sigma_{xx}(B) = \frac{en\mu_0}{1 + (\mu_0 B)^2}, \tag{5.15}$$

where μ_0 is the mobility at $B = 0$, i.e,

$$\mu_0 = \frac{\sigma_{xx}(B=0)}{ne}. \tag{5.16}$$

As can be seen from the calculation of $\tilde{\nu}_0(\varepsilon)$ in Refs. [57, 58], corrections to the density of states arising from the finite magnetic field can be neglected, as long as $x \ll 1$, which we will show is true over a large range of data in the present experiment.

Comparison with Eq. (5.11) shows that $\omega_c(\varepsilon)\tau_{\rm tr}(\varepsilon)/\tilde{\nu}_0(\varepsilon)$ corresponds to $\mu_0 B$. This means that the Drude conductivity is given by

$$\sigma_{xx} \approx \frac{e^2\gamma N}{2\pi\hbar}\frac{1}{1+\left(\frac{2e\gamma}{\pi\hbar n}\right)^2 B^2}, \tag{5.17}$$

which has finite temperature corrections that are detailed in the Sec. 5.3.4. There are also temperature-dependent quantum corrections to the Drude conductivity, in particular, those arising from the electron-electron interaction (EEI), as discussed in Sec. 5.3.5.

For both short-range and Coulomb impurities, Eq. (5.11) then yields a parabolic magnetoresistance in the Corbino geometry. The Drude resistivity in the Corbino geometry takes a simple form

$$\rho_{xx}(B) \stackrel{\rm def}{=} \frac{1}{\sigma_{xx}} = \frac{1}{\sigma_0}\left[1+(\mu_0 B)^2\right]. \tag{5.18}$$

According to the Mathiessen rule, the inverse mobility can be written as a sum of the contributions of different momentum-relaxing scattering processes

$$\mu_0^{-1} = \mu_C^{-1} + \mu_s^{-1}, \tag{5.19}$$

which yields in the zero-T limit:

$$\frac{1}{\mu_0} = \frac{\pi\hbar n}{2e\gamma} = \frac{\pi\hbar n}{2e}\left(\frac{1}{\gamma_s} + \frac{1}{\gamma_C(\varepsilon=\varepsilon_F,\varepsilon_F)}\right), \tag{5.20}$$

$$\gamma_C(\varepsilon=\varepsilon_F,\varepsilon_F) = \frac{n}{c(\alpha)n_{\rm imp}^C}, \tag{5.21}$$

with $c(\alpha)$ defined in Sec. 5.3.2. One sees that the contribution of Coulomb scatterers to the inverse mobility is density independent. On the other hand, the mobility governed by short-range impurities decreases with charge carrier density as $\mu_s \propto 1/n$. Thus, the density dependence of the total mobility allows one to characterize the role of short-range and Coulomb impurities in transport.

Below a certain chemical potential or the corresponding density n_*, disorder-induced broadening smears the single-particles energy and the density of states saturates. This energy scale is given by the self-consistent equation for ε:

$$\frac{\hbar}{\tau_q(\varepsilon_*)} \sim \varepsilon_* \tag{5.22}$$

For the mixed disorder model with $\gamma_s \gg 1$, we get for the corresponding density

$$n_* \sim d(\alpha) n_{\rm imp}^C, \tag{5.23}$$

where $d(\alpha)$ is given in Sec. 5.3.2. The value of n_* depends on the density of charged impurities, fine-structure constant α. We model this saturation effect by performing the replacement $n \to \sqrt{n^2 + n_*^2}$, which effectively interpolates between n at high densities and n^* at the neutrality point, in all formulas, when used for plotting or fitting. In order to keep the notation clear, we do not explicitly write down this replacement. Since this replacement is an approximate interpolation, it describes the behavior of the density of states (and other observables) at $n \sim n_*$ only qualitatively, see Sec. 5.3.3 for details. Nevertheless, this simple interpolation function allow us to confidently extract the system parameters, when the range of densities $n \gg n_*$ is included in the fit.

5.3.1 Semiclassical transport

Since Landau levels are sufficiently broadened by disorder in the experimental setup considered in this chapter, one can use the semi-classical Boltzmann equation introduced in Sec. 2.1. There are two ways to progress from there, the first one is to perform the calculations presented in Sec. 2.1.1, which directly give the Drude result of the magnetoconductivities shown in Eqs. (2.29) and (2.30). These however do not yet include any details of the geometry and thus the resistance of the whole system. This can be archived by using a relation similar to those introduced in Sec. 2.4, specifically the generalized Navier-Stokes equation (2.206). Here we argue, that a similar description also applied in the non-hydrodynamic regime presented here, following the calculation in Ref. [186]. Starting from the stationary Boltzmann equation, where we only consider disorder scattering in SI units

$$\left(\mathbf{v}\cdot\nabla_r + \frac{1}{\hbar}\mathbf{F}\cdot\nabla_k\right) f(\mathbf{r},\mathbf{k}) = S^{\mathrm{dis}}\{f\}(\mathbf{r},\mathbf{k}), \tag{5.24}$$

$$\mathbf{F} = e\mathbf{E} + e\mathbf{v}\times\mathbf{B} \tag{5.25}$$

we parametrize the difference to the equilibrium Fermi function $f_0(\epsilon_k)$ as

$$f(\mathbf{r},\mathbf{k}) = f_0(\epsilon_k) - f_0'(\epsilon_k)\mathcal{F}(\mathbf{r},\theta_k), \tag{5.26}$$

where θ_k is the polar angle of the momentum. Then we find for low energies and homogeneous magnetic field to first order in $\mathcal{F}$:

$$\mathbf{v}\cdot(\nabla_r\mathcal{F} - e\mathbf{E}) + \omega_c\partial_{\theta_k}\mathcal{F} = -\frac{\mathcal{F}-\mathcal{F}_0}{\tau}, \tag{5.27}$$

where we have used a relaxation time approximation for disorder scattering and the decomposition

$$\mathcal{F}(\mathbf{r},\theta_k) = \sum_{n=-\infty}^{\infty}\mathcal{F}_n(\mathbf{r})e^{in\theta_k}, \tag{5.28}$$

$$\mathcal{F}_n(\mathbf{r}) = \int\frac{\mathrm{d}\theta_k}{2\pi}e^{-in\theta_k}\mathcal{F}(\mathbf{r},\theta_k). \tag{5.29}$$

Making full use of this decomposition, we find a hierarchy of equations

$$\begin{aligned}&\frac{v_g}{2}\left\{\partial_x\left[\mathcal{F}_{n-1}+\mathcal{F}_{n+1}\right] - i\partial_y\left[\mathcal{F}_{n-1}-\mathcal{F}_{n+1}\right]\right\} - \frac{ev_g}{2}\left[E_x(\delta_{n,1}+\delta_{n,-1}) - iE_y(\delta_{n,1}-\delta_{n,-1})\right]\\ &+ in\omega_c\mathcal{F}_n = -\frac{1}{\tau}\left[\mathcal{F}_n - \mathcal{F}_0\delta_{n,0}\right].\end{aligned} \tag{5.30}$$

If one now introduces the macroscopic quantities

$$\begin{aligned} n(\mathbf{r}) &= \int (\mathrm{d}\mathbf{k}) f(\mathbf{r},\mathbf{k}) = \int (\mathrm{d}\mathbf{k})(f_0 - f_0' \mathcal{F}(\mathbf{r},\theta_k)) \\ &= n_0 + \nu_0(\varepsilon_F) \int \frac{\mathrm{d}\theta_k}{2\pi} \mathcal{F}(\mathbf{r},\theta_k) = n_0 + \nu_0(\varepsilon_F)\mathcal{F}_0(\mathbf{r}), \end{aligned} \tag{5.31}$$

the total current

$$\begin{aligned} \mathbf{j} &= \int (\mathrm{d}\mathbf{k}) f(\mathbf{r},\mathbf{k})\mathbf{v} = \int (\mathrm{d}\mathbf{k})(f_0 - f_0' \mathcal{F}(\mathbf{r},\theta_k)) v_g \begin{pmatrix} \cos\theta_k \\ \sin\theta_k \end{pmatrix} \\ &= v_g \nu_0(\varepsilon_F) \int \frac{\mathrm{d}\theta_k}{2\pi} \mathcal{F}(\mathbf{r},\theta_k) \begin{pmatrix} \cos\theta_k \\ \sin\theta_k \end{pmatrix} = \frac{v_g \nu_0(\varepsilon_F)}{2} \begin{pmatrix} \mathcal{F}_1(\mathbf{r}) + \mathcal{F}_{-1}(\mathbf{r}) \\ i\mathcal{F}_1(\mathbf{r}) - i\mathcal{F}_{-1}(\mathbf{r}) \end{pmatrix} \end{aligned} \tag{5.32}$$

and the stress tensor

$$\begin{aligned} \Pi(\mathbf{r}) &= \int (\mathrm{d}\mathbf{k}) \mathbf{k} \otimes \mathbf{v} f(\mathbf{r},\mathbf{k}) = \int (\mathrm{d}\mathbf{k})(f_0 - f_0' \mathcal{F}(\mathbf{r},\theta_k)) v_g k \begin{pmatrix} \cos^2\theta_k & \cos\theta_k \sin\theta_k \\ \sin\theta_k \cos\theta_k & \sin^2\theta_k \end{pmatrix} \\ &= \Pi_0 1_2 + \frac{\nu_0(\varepsilon_F)\varepsilon_F}{4} \begin{pmatrix} \mathcal{F}_2 + \mathcal{F}_{-2} + 2\mathcal{F}_0 & i(\mathcal{F}_2 - \mathcal{F}_{-2}) \\ i(\mathcal{F}_2 - \mathcal{F}_{-2}) & -(\mathcal{F}_2 + \mathcal{F}_{-2} - 2\mathcal{F}_0) \end{pmatrix}, \end{aligned} \tag{5.33}$$

that describes deformations of the Fermi surface, we can consider certain values of n in the general equation (5.30) to obtain equations connecting these quantities.

The first equation is found for $n = 0$

$$\frac{v_g}{2} \left\{ \partial_x \left[\mathcal{F}_{-1} + \mathcal{F}_1 \right] - i\partial_y \left[\mathcal{F}_{-1} - \mathcal{F}_1 \right] \right\} = 0, \tag{5.34}$$

which can be reexpressed by the macroscopic quantities as

$$\nabla \cdot \mathbf{j} = 0, \tag{5.35}$$

i.e. the current is conserved. For $n = \pm 1$ one can combine the two equations

$$\frac{v_g}{2} \left\{ \partial_x \left[\mathcal{F}_0 + \mathcal{F}_2 \right] - i\partial_y \left[\mathcal{F}_0 - \mathcal{F}_2 \right] \right\} - \frac{e v_g}{2} \left[E_x - iE_y \right] - i\omega_c \mathcal{F}_1 = -\frac{1}{\tau} \mathcal{F}_1 \tag{5.36}$$

$$\frac{v_g}{2} \left\{ \partial_x \left[\mathcal{F}_{-2} + \mathcal{F}_0 \right] - i\partial_y \left[\mathcal{F}_{-2} - \mathcal{F}_0 \right] \right\} - \frac{e v_g}{2} \left[E_x + iE_y \right] + i\omega_c \mathcal{F}_{-1} = -\frac{1}{\tau} \mathcal{F}_{-1}, \tag{5.37}$$

to form a generalized Navier-Stokes equation

$$en\mathbf{E} + e\mathbf{j} \times \mathbf{B} - \nabla\Pi = \frac{e^2 n}{\sigma_0} \mathbf{j}, \tag{5.38}$$

where we have identified σ_0 from equation (5.12) and τ as τ_{tr}. This generalized Navier-Stokes equation will be used again in Chapter 6 to describe the disorder dominated leads.

If one requires, that the series truncates at $n = \pm 2$, which leads to

$$\mathcal{F}_{\pm 2} = -\frac{v_g}{2} \frac{(\partial_x \mp i\partial_y)\mathcal{F}_{\pm 1}}{\frac{1}{\tau} \mp 2i\omega_c}, \tag{5.39}$$

we can define a disorder induced viscosity, since we find a connection between the stress tensor Π and the current $\mathbf{j}$. This gives us access to the disorder induced shear and Hall viscosties η and η_H respectively via the definition of the off diagonal part of the stress tensor

$$\Pi = P - \sigma', \tag{5.40}$$

$$\sigma' = \frac{1}{n}(\eta + i\eta_H\tau_y)) \left[(\partial_x j_x - \partial_y j_y)\tau_z + (\partial_x j_y + \partial_y j_x)\tau_x\right] \tag{5.41}$$

and we find

$$\eta = \frac{\mu^3}{\pi v_g^2 \hbar^2}\frac{\tau}{4}\frac{1}{1+4\omega_c^2\tau^2}, \quad \eta_H = \frac{\mu^3}{\pi v_g^2 \hbar^2}\frac{\omega_c\tau^2}{2}\frac{1}{1+4\omega_c^2\tau^2}. \tag{5.42}$$

Using the radial symmetry of the Corbino disk we first find from Eq. (5.35), that the total conserved current amounts to

$$I = e\int \mathrm{d}\mathbf{A}\cdot\mathbf{j} = 2\pi e r j_r \tag{5.43}$$

and thus

$$j_r = \frac{I}{2\pi e r} \tag{5.44}$$

and then subsequently

$$j_\vartheta = -\frac{\sigma_0 B}{en}\frac{I}{2\pi e r}, \tag{5.45}$$

$$E_r = \frac{I}{2\pi e r}\left(\frac{e}{\sigma_0} + \frac{\sigma_0 B^2}{en^2}\right), \tag{5.46}$$

while the gradient of the stress tensor vanishes. Thus we obtain the simple Ohm's law for the system under consideration

$$en\mathbf{E} + e\mathbf{j}\times\mathbf{B} = \frac{e^2 n}{\sigma_0}\mathbf{j}. \tag{5.47}$$

From this we obtain the voltage drop between the inner and outer radius r_{in} and r_{out} respectively as

$$\begin{aligned} U &= \int_{r_{\mathrm{in}}}^{r_{\mathrm{out}}} E_r \mathrm{d}r = \frac{I}{2\pi e}\left(\frac{e}{\sigma_0} + \frac{\sigma_0 B^2}{en^2}\right)\log\left(\frac{r_{\mathrm{out}}}{r_{\mathrm{in}}}\right) \\ &= \frac{I}{2\pi}\rho_{xx}\log\left(\frac{r_{\mathrm{out}}}{r_{\mathrm{in}}}\right), \end{aligned} \tag{5.48}$$

$$\rho_{xx} = \frac{1}{\sigma_0}\left(1 + \frac{\sigma_0^2 B^2}{e^2 n^2}\right), \tag{5.49}$$

which leads exactly to the magnetoresistance $R = U/I$ reported above. This serves to show, that also in the region of disorder dominated transport, as long as the Boltzmann equation is applicable, i.e. Landau levels are sufficiently smeared, one can find a set of equations (5.35) and (5.38) that are similar to the hydrodynamic description at elevated temperatures.

More generally, we do not need to truncate the series, if we restrict ourselves to a system with radial symmetry. After introducing polar coordinates (r, ϑ) we can rewrite the recursion formula (5.35) as

$$\frac{v_g}{2}\left\{e^{-i\vartheta}\left(\partial_r - \frac{i}{r}\partial_\vartheta\right)\mathcal{F}_{n-1} + e^{i\vartheta}\left(\partial_r + \frac{i}{r}\partial_\vartheta\right)\mathcal{F}_{n+1}\right\} - \frac{ev_g}{2}E_r\left[e^{-i\vartheta}\delta_{n,1} + e^{i\vartheta}\delta_{n,-1}\right] - in\omega_c\mathcal{F}_n$$
$$= -\frac{1}{\tau}\left[\mathcal{F}_n - \mathcal{F}_0\delta_{n,0}\right]. \tag{5.50}$$

We separate the angular and radial dependence by introducing

$$\mathcal{F}_n(r,\vartheta) = f_n(r)e^{-in\vartheta}, \tag{5.51}$$

since the only well defined angle is the one between the position vector and the momentum vector. Then we find the new expression

$$\frac{v_g}{2}\left\{\left(\partial_r - \frac{(n-1)}{r}\right)f_{n-1} + \left(\partial_r + \frac{(n+1)}{r}\right)f_{n+1}\right\} - \frac{ev_g}{2}E_r\left[e^{i(n-1)\vartheta}\delta_{n,1} + e^{i(n+1)\vartheta}\delta_{n,-1}\right] - in\omega_c f_n$$
$$= -\frac{1}{\tau}\left[f_n - f_0\delta_{n,0}e^{in\vartheta}\right]. \tag{5.52}$$

Defining n as positive we introduce

$$p_n(r) = f_n(r) + f_{-n}(r), \quad m_n(r) = f_n(r) - f_{-n}(r). \tag{5.53}$$

For $n = 0$ we then find the condition

$$\left(\partial_r + \frac{1}{r}\right)p_1 = 0 \tag{5.54}$$
$$\Rightarrow p_1(r) = \frac{c_1}{r}. \tag{5.55}$$

Taking sum and difference of the $n = \pm 1$ equations we find

$$\frac{v_g}{2}\left(\partial_r + \frac{2}{r}\right)p_2 - ev_gE_r - i\omega_c m_1 = -\frac{1}{\tau}p_1 \tag{5.56}$$
$$\frac{v_g}{2}\left(\partial_r + \frac{2}{r}\right)m_2 - i\omega_c p_1 = -\frac{1}{\tau}m_1 \tag{5.57}$$

and for $n \geq 2$ we find

$$\frac{v_g}{2}\left\{\left(\partial_r + \frac{n+1}{r}\right)p_{n+1} + \left(\partial_r - \frac{n-1}{r}\right)p_{n-1}\right\} - in\omega_c m_n = -\frac{1}{\tau}p_n \tag{5.58}$$
$$\frac{v_g}{2}\left\{\left(\partial_r + \frac{n+1}{r}\right)m_{n+1} + \left(\partial_r - \frac{n-1}{r}\right)m_{n-1}\right\} - in\omega_c p_n = -\frac{1}{\tau}m_n. \tag{5.59}$$

Generally, these equations can be solved by an Ansatz of the form

$$m_i(p_i) = \sum_{z=-\infty}^{\infty} a_z r^z \tag{5.60}$$

and comparing each power. One infinite tower of solutions is found by the Ansatz

$$p_n(r) = \frac{c_n}{r^n}, \quad m_n(r) = \frac{d_n}{r^n} \tag{5.61}$$

Then we find

$$d_1 = i\omega_c\tau c_1, \quad E_r = \frac{1}{ev_g\tau}\left(1+\omega_c^2\tau^2\right)\frac{c_1}{r}, \tag{5.62}$$

$$\begin{pmatrix} c_n \\ d_n \end{pmatrix} = \frac{(n-1)v_g\tau}{1+n^2\omega_c^2\tau^2}\begin{pmatrix} 1 & in\omega_c\tau \\ in\omega_c\tau & 1 \end{pmatrix}\begin{pmatrix} c_{n-1} \\ d_{n-1} \end{pmatrix}, \quad n \geq 2 \tag{5.63}$$

this is solved by first diagonalizing the matrix

$$\begin{pmatrix} 1 & in\omega_c\tau \\ in\omega_c\tau & 1 \end{pmatrix} = S\begin{pmatrix} 1+in\omega_c\tau & 0 \\ 0 & 1-in\omega_c\tau \end{pmatrix}S^{-1}, \tag{5.64}$$

$$S = \frac{1}{\sqrt{2}}\begin{pmatrix} 1 & -1 \\ 1 & 1 \end{pmatrix} \tag{5.65}$$

and thus we find the solution

$$\begin{pmatrix} c_n \\ d_n \end{pmatrix} = S\prod_{m=2}^{n}\frac{(m-1)v_g\tau}{1+m^2\omega_c^2\tau^2}\begin{pmatrix} 1+im\omega_c\tau & 0 \\ 0 & 1-im\omega_c\tau \end{pmatrix}S^{-1}\begin{pmatrix} c_1 \\ d_1 \end{pmatrix} \tag{5.66}$$

$$= \frac{\Gamma(n)\left(\frac{iv_g}{\omega_c}\right)^n}{2\tau v_g}\begin{pmatrix} \left(\frac{(1-i\tau\omega_c)}{\left(1+\frac{i}{\tau\omega_c}\right)_n}+\frac{(1+i\tau\omega_c)(-1)^n}{\left(1-\frac{i}{\tau\omega_c}\right)_n}\right) & \left(\frac{(1-i\tau\omega_c)}{\left(1+\frac{i}{\tau\omega_c}\right)_n}-\frac{(1+i\tau\omega_c)(-1)^n}{\left(1-\frac{i}{\tau\omega_c}\right)_n}\right) \\ \left(\frac{(1-i\tau\omega_c)}{\left(1+\frac{i}{\tau\omega_c}\right)_n}-\frac{(1+i\tau\omega_c)(-1)^n}{\left(1-\frac{i}{\tau\omega_c}\right)_n}\right) & \left(\frac{(1-i\tau\omega_c)}{\left(1+\frac{i}{\tau\omega_c}\right)_n}+\frac{(1+i\tau\omega_c)(-1)^n}{\left(1-\frac{i}{\tau\omega_c}\right)_n}\right) \end{pmatrix}\begin{pmatrix} c_1 \\ d_1 \end{pmatrix}$$

for the coefficients, where $(a)_n = \Gamma(a+n)/\Gamma(a)$ is the Pochhammer symbol and for $B = 0$ this simplifies to

$$\begin{pmatrix} c_n \\ d_n \end{pmatrix} = (v_g\tau)^{n-1}\Gamma(n)\begin{pmatrix} c_1 \\ d_1 \end{pmatrix}. \tag{5.67}$$

This type of solution generally includes the condition (5.39) without requiring a termination. From this we conclude, that in the Corbino geometry the truncation is not needed as an extra condition.

5.3.2 Charged impurities

Before, we gave the transport and quantum scattering times for short-range impurities (5.6) and Coulomb impurities (5.8). Here we show how to derive these expressions for large energies. The behavior close to the neutrality point is discussed in Sec. 5.3.3.

Very generally, the scattering rates can be written as

$$\frac{1}{\tau_i(\varepsilon)} = \frac{n_{\text{imp}}\nu(\varepsilon)}{8\hbar}\int_0^{2\pi}\mathrm{d}\theta\left|V\left(q(\theta)\right)\right|^2 \times \begin{cases} \sin^2\theta, & i = \text{tr} \\ (1+\cos\theta), & i = q \end{cases}, \tag{5.68}$$

where $\nu(\varepsilon)$ is the density of states and we express the transferred momentum as

$$q(\theta) = 2(\varepsilon/\hbar v_g)|\sin\Big(\theta/2\Big)|$$

with θ being the scattering angle. For short-range impurities, $V(q) = U_0$ and $n_{\rm imp} = n^s_{\rm imp}$; the integration over θ then leads exactly to Eq. (5.6). In the case of charged impurities, we consider the screened interaction potential in the random-phase approximation:

$$V(q) = \frac{2\pi e^2/q\epsilon_\infty}{1 + (2\pi e^2/q\epsilon_\infty)\Pi(q,0)}. \tag{5.69}$$

Here ϵ_∞ is the background dielectric constant and $\Pi(q)$ is the static polarization operator which is given by the thermodynamic density of states (μ is the chemical potential):

$$\lim_{q\to 0}\Pi(q) = \frac{\partial n}{\partial \mu}. \tag{5.70}$$

This quantity can be connected to the single-particle density of states via

$$n(\mu) = \int \mathrm{d}\varepsilon\, n_F(\varepsilon)\nu(\varepsilon) \quad \Rightarrow \quad \frac{\partial n}{\partial \mu} = \int \mathrm{d}\varepsilon \left(-\frac{\partial n_F(\varepsilon)}{\partial \varepsilon}\right)\nu(\varepsilon).$$

As mentioned before, the density of states can in general be deduced from Eq. (36) in Ref. [58]. From there we see that away from the neutrality point, the oscillatory magnetic-field dependent corrections to the compressibility are exponentially suppressed and hence not seen in the experiment. Moreover, since we are at temperatures below the chemical potential away from the neutrality point, we can use a zero T approximation and get

$$\lim_{q\to 0}\Pi(q,0) \approx \frac{2\mu}{\pi v_g^2\hbar^2} = \nu(\mu). \tag{5.71}$$

By introducing the effective interaction strength

$$\alpha = \frac{e^2}{\hbar v_g \epsilon_\infty},$$

we can bring the screened Coulomb interaction to the form

$$V(q) = \frac{2\pi e^2}{\epsilon_\infty(q+K)}, \tag{5.72}$$

$$K = \frac{2\pi e^2 N}{\epsilon_\infty}\lim_{q\to 0}\Pi(q,0) \approx 2\alpha\pi\hbar v_g\nu(\mu). \tag{5.73}$$

We get thus get for the scattering rates:

$$\frac{1}{\tau_i^C(\varepsilon)} = \frac{\pi^2}{4}\hbar^3 v_g^4\alpha^2 n^C_{\rm imp}\nu(\varepsilon)\int_0^\pi \frac{\mathrm{d}\theta}{\Big(\varepsilon\sin\frac{\theta}{2} + \alpha\nu(\mu)\pi\hbar^2 v_g^2\Big)^2}\times\begin{cases}\sin^2\theta, & i = \mathrm{tr}\\ 1+\cos\theta, & i = q\end{cases}. \tag{5.74}$$

At low temperatures, the typical energies are very close to the chemical potential and we can set $\varepsilon \to \mu$ in the transferred momentum q in the interaction matrix element:

$$\frac{1}{\tau_{\mathrm{tr}}^C(\varepsilon)} \approx \frac{\pi}{4}\alpha^2 v_g^2 \hbar n_{\mathrm{imp}}^C \varepsilon \int_0^{2\pi} \frac{\mathrm{d}\theta\, \sin^2\theta}{[\mu|\sin\Big(\theta/2\Big)| + \alpha N \mu/2]^2} = \frac{\pi}{2} v_g^2 \hbar n_{\mathrm{imp}}^C \frac{\varepsilon}{\mu^2} c(\alpha), \tag{5.75}$$

$$c(\alpha) = \alpha^2 \int_0^{\pi} \frac{\mathrm{d}\theta \sin^2\theta}{(\sin\Big(\theta/2\Big) + \alpha N/2)^2}. \tag{5.76}$$

This can be brought into the form

$$\tau_{\mathrm{tr}}^C(\varepsilon) = \frac{2\gamma^C \hbar}{\varepsilon}, \quad \gamma^C = \frac{\mu^2}{\pi v_g^2 \hbar^2 n_{\mathrm{imp}} c(\alpha)}, \tag{5.77}$$

which is exactly Eq. (5.8) for zero temperature, where $\mu = \varepsilon_F$. Using relation Eq. (5.4), this is also exactly γ_C as introduced in Eq. (5.21). Similarly, we get for the quantum scattering rate

$$\frac{1}{\tau_q^C} \approx \frac{\pi}{2}\alpha^2 v_g^2 \hbar n_{\mathrm{imp}}^C \frac{\varepsilon}{\mu^2} \int_0^{\pi} \frac{\mathrm{d}\theta\, (1+\cos\theta)}{[\sin\Big(\theta/2\Big) + \alpha N/2]^2} = \frac{\pi}{2} v_g^2 \hbar n_{\mathrm{imp}}^C \frac{\varepsilon}{\mu^2} d(\alpha), \tag{5.78}$$

$$d(\alpha) = \alpha^2 \int_0^{\pi} \frac{\mathrm{d}\theta (1+\cos\theta)}{(\sin\Big(\theta/2\Big) + \alpha N/2)^2} \tag{5.79}$$

which again is of the form

$$\tau_q^C(\varepsilon) = \frac{\gamma_C' \hbar}{\varepsilon}, \quad \gamma_C' = \frac{2\mu^2}{\pi v_g^2 \hbar^2 n_{\mathrm{imp}}^C d(\alpha)}, \tag{5.80}$$

as used in Eq. (5.8). The values of $c(\alpha)$ and $d(\alpha)$ for some realistic α are given by

$$c(\alpha) = \begin{cases} 0.14, & \alpha = 0.5 \\ 0.22, & \alpha = 1.0 \\ 0.26, & \alpha = 1.5 \\ 0.29, & \alpha = 2 \end{cases}, \qquad d(\alpha) = \begin{cases} 0.43, & \alpha = 0.5 \\ 0.55, & \alpha = 1.0 \\ 0.61, & \alpha = 1.5 \\ 0.65, & \alpha = 2 \end{cases}. \tag{5.81}$$

Thus, for intermediate α, the relation between the two scattering rates, given by $\frac{d(\alpha)}{2} \approx c(\alpha)$, is similar to that for short-range scattering. Whenever we use a specific value of α, we chose $\alpha = 1.3$, thus accounting for the renormalization of velocity, as well as for the screening by the metallic parts of the setup.

In a general setup, both short-range and Coulomb scatterers are present. Here we discuss how this mixture affects the scattering times for energies away from the Dirac point, where the density of states is not affected by disorder. We will stick with the assumption of no inter-valley scattering, diagonality in the sublattice space, and no correlations between different kinds of scattering. This corresponds to summing up the self-energies, where we would not consider mixed diagrams, and translates into a sum rule for transport times, Eq. (5.13). We will further assume that in the relevant limit, the density of states is not modified by the magnetic field, since corrections are exponentially suppressed. Then we

can use the transport times as written in Eq. (5.6) and Eq. (5.8) to write the total transport time τ_{tr} as

$$\tau_{\mathrm{tr}}(\varepsilon) = \frac{2\gamma\hbar}{|\varepsilon|}, \quad \gamma = \frac{\gamma_C\gamma_s}{\gamma_C + \gamma_s}. \tag{5.82}$$

The conductance kernel, as found from the Boltzmann equation, is then given by

$$\sigma_{xx}(\varepsilon) = \frac{e^2 v_g^2}{2} \frac{\tau_{\mathrm{tr}}(\varepsilon)\nu(\varepsilon)}{1 + \left[\omega_c(\varepsilon)\tau_{\mathrm{tr}}(\varepsilon)\right]^2} = \frac{\sigma_0}{1 + [\omega_c(\varepsilon)\tau_{\mathrm{tr}}(\varepsilon)]^2} = \frac{2e^2\gamma}{\pi\hbar} \frac{1}{1 + \left(\frac{2\gamma\hbar^2\Omega^2}{\varepsilon^2}\right)^2}, \tag{5.83}$$

where $\Omega = v_g/\ell_B$, leading to Eq. (5.17).

5.3.3 Vicinity of the Dirac point

As seen in Fig. 5.2, the resistance does not diverge at the Dirac point, as would be expected from combining the resistivity $\rho_0 = 1/\sigma_0$ from Eq. (5.12) with the effective γ from Sec. 5.3.2 using γ_C as expressed in Eq. (5.21). The reason for this is the saturation of the density of states close to the Dirac point due to disorder [5, 57]. Below a certain chemical potential μ_*, the quasiparticle pole in the Green's function is effectively absent, and all quantities should be fixed below this value. The relevant scale for this behaviour is given by Eq. (5.22). In order to determine the changes this induces and find Eq. (5.23), we discuss here how to find the relevant scale μ_* from the condition

$$\frac{\hbar}{2\tau_q(\mu_*)} = \mu_*. \tag{5.84}$$

Below μ_*, the density of states saturates, while it is not affected for larger energies, i.e.

$$\nu(\varepsilon) = \begin{cases} \nu_*, & |\varepsilon| \ll \mu_*, \\ \nu_0(\varepsilon), & |\varepsilon| \gg \mu_* \end{cases}. \tag{5.85}$$

This value enters directly into the calculation of all scattering rates Eq. (5.68) of ; it also directly determines the screening radius in the Coulomb impurity case Eq. (5.73). While it is clear, that Eq. (5.68 is only true if the density of states is not strongly broadened, the idea is to approach the crossover from the side of large energies, where this is the case. We can then calculate the Coulomb scattering rates as follows:

$$\frac{1}{\tau_{\mathrm{tr}}^C(\mu)} = \frac{\pi^2}{4}\hbar^3 v_g^4 n_{\mathrm{imp}}^C c(\alpha) \begin{cases} \dfrac{\nu_*}{\mu_*^2}, & \mu \ll \mu_* \\ \dfrac{\nu_0(\mu)}{\mu^2}, & \mu \gg \mu_* \end{cases}, \tag{5.86}$$

$$\frac{1}{\tau_q^C(\mu)} = \frac{\pi^2}{4}\hbar^3 v_g^4 n_{\mathrm{imp}}^C d(\alpha) \begin{cases} \dfrac{\nu_*}{\mu_*^2}, & \mu \ll \mu_* \\ \dfrac{\nu_0(\mu)}{\mu^2}, & \mu \gg \mu_* \end{cases}, \tag{5.87}$$

and, in a similar fashion, we get for short-range scatterers:

$$\frac{1}{\tau_{\mathrm{tr}}^{s}(\mu)} = \frac{1}{\gamma_s}\frac{\pi\hbar v_g^2}{4}\begin{cases}\nu_*, & \mu \ll \mu_* \\ \nu_0(\mu), & \mu \gg \mu_*\end{cases}, \tag{5.88}$$

$$\frac{1}{\tau_{q}^{s}(\mu)} = \frac{1}{\gamma_s}\frac{\pi\hbar v_g^2}{2}\begin{cases}\nu_*, & \mu \ll \mu_* \\ \nu_0(\mu), & \mu \gg \mu_*\end{cases}. \tag{5.89}$$

By assuming that the expression for $\mu \gg \mu_*$ is still reasonably close for $\mu \sim \mu_*$ and using both short-range and Coulomb impurities in Eq. (5.84) we find

$$\begin{aligned}\mu_* &= \sqrt{\frac{\pi}{2}v_g^2\hbar^2 d(\alpha)\frac{n_{\mathrm{imp}}^C}{2-1/\gamma_s}}, \\ n_* &= \frac{d(\alpha)n_{\mathrm{imp}}^C}{4-2/\gamma_s}.\end{aligned} \tag{5.90}$$

which leads to the approximation Eq. (5.23). This value depends on the density of charged impurities and γ_s. The effective γ can then be extracted from the definition of γ, Eq. (5.12). We see that the density of states actually drops out, only the influence of $\nu(\varepsilon)$ on the electronic density (via μ^2) is relevant. We find the required asymptotics

$$\frac{1}{\gamma} = \frac{1}{\gamma_s} + \begin{cases}\dfrac{c(\alpha)n_{\mathrm{imp}}^C}{n_*}, & n \ll n_* \\ \dfrac{c(\alpha)n_{\mathrm{imp}}^C}{n}, & n \gg n_*\end{cases}, \tag{5.91}$$

which we phenomenologically fulfill by tweaking the relation between density and chemical potential in graphene to

$$\sqrt{n^2+n_*^2} = N\frac{\mu^2}{4\pi\hbar^2 v^2}, \tag{5.92}$$

and consequently we replace n by $\sqrt{n^2+n_*^2}$ in all fits and plots, as.

Using the general conductivity formula (5.17) with the finite disorder broadening, Eq. (5.92), we get the broadened form of Eq. (5.20) and Eq. (5.21):

$$\frac{1}{\mu_0} \approx \frac{\pi\hbar}{2e}\left(\frac{\sqrt{n^2+n_*^2}}{\gamma_s} + c(\alpha)n_{\mathrm{imp}}^C\right) \tag{5.93}$$

and

$$\frac{1}{\gamma} = \frac{1}{\gamma_s} + \frac{c(\alpha)n_{\mathrm{imp}}^C}{\sqrt{n^2+n_*^2}}. \tag{5.94}$$

5.3.4 Finite-temperature effects

Before, we have restricted ourselves to the zero temperature limit of Eq. (5.14). Here we discuss finite-temperature corrections in the Drude formula, as well as effects due to electron-electron interaction (EEI) which also introduce finite-temperature corrections to Eq. (5.17 and thus Eq. (5.18). Let us consider, for the illustrative purpose, the case of only short-range potential.

The problem generally has two energy scales, the first one is the temperature k_BT, and the second one is the energy ε_m introduced by the product $\omega_c(\varepsilon)\tau_{\rm tr}(\varepsilon)$ which we write as

$$\omega_c(\varepsilon)\tau_{\rm tr}(\varepsilon) = \frac{2eB\hbar v_g^2}{\varepsilon^2} \equiv \frac{\varepsilon_m^2}{\varepsilon^2} \tag{5.95}$$

We will restrict ourselves to low temperatures $k_BT \ll \mu$ and small magnetic fields, $\varepsilon_m \ll \mu$ For finite but low temperatures and small fields, the integral of the conductance kernel Eq. (5.11) over energies can be brought into the form [58]:

$$\sigma_{xx} = \sigma_0 \int_{-\infty}^{\infty} {\rm d}\varepsilon \left(-\frac{\partial n_F(\varepsilon)}{\partial \varepsilon}\right)\left(1 - \frac{\varepsilon_m^4}{\varepsilon^4+\varepsilon_m^4}\right) = \sigma_0\left[1 - \int_{-\infty}^{\infty} {\rm d}\varepsilon \left(-\frac{\partial n_F(\varepsilon)}{\partial \varepsilon}\right)\frac{\varepsilon_m^4}{\varepsilon^4+\varepsilon_m^4}\right], \tag{5.96}$$

we used Eq. (5.6) and Eq. (5.8) for the transport scattering time. One notices that both the derivative of the Fermi function and the fraction in the second expression are peaked. The derivative of the Fermi function is peaked around $\varepsilon = \mu$ with a width given by the temperature, while the term $\varepsilon_m^4/(\varepsilon^4+\varepsilon_m^4)$ is peaked around $\varepsilon = 0$ and its width is determined by ε_m. Since we assume that both $T, \varepsilon_m \ll \mu$, these peaks are well separated, and the integral can be written as a sum of the contributions of the two peaks, i.e.,

$$\sigma_{xx} = \sigma_0 - \left(\sigma_{xx}^{(T)} + \sigma_{xx}^{(\varepsilon_m)}\right).$$

For low temperatures, the derivative of the Fermi function has a finite width of the order of T around $\varepsilon = \mu$. To incorporate finite-temperature corrections to the conductivity, we thus expand the fraction in powers of $(\varepsilon - \mu)$ and after evaluating the integral with get

$$\sigma_{xx}^{(T)} \approx \sigma_0\left[\frac{\varepsilon_m^4}{\mu^4+{\varepsilon_m}^4} - \frac{2\pi^2T^2\mu^2{\varepsilon_m}^4}{3}\frac{\left(3{\varepsilon_m}^4 - 5\mu^4\right)}{\left(\mu^4+{\varepsilon_m}^4\right)^3}\right]. \tag{5.97}$$

The first term of this expression is the only non-vanishing contribution at zero T and leads exactly to Eq. (5.17). The contribution of the second peak is found by fixing the value of the Fermi function at its value at $\varepsilon = 0$ and then evaluating the integral:

$$\sigma_{xx}^{(\varepsilon_m)} \simeq \sigma_0\varepsilon_m\frac{e^{-\mu/T}}{\sqrt{2}T}. \tag{5.98}$$

Thus the total Drude resistivity for short-range impurities is given, in the regime of low temperatures and low magnetic fields, by

$$\rho_{xx} = \frac{1}{\sigma_{xx}} \approx \frac{1}{\sigma_0}\left[1 + \frac{{\varepsilon_m}^4}{\mu^4}\left(1 + \frac{10\pi^2T^2}{3\mu^2}\right) - \frac{{\varepsilon_m}^8}{\mu^8}\frac{16\pi^2T^2}{3\mu^2} + \frac{\pi\varepsilon_m}{\sqrt{2}T}e^{-\frac{\mu}{T}}\right].$$

From this expressions we see, that the mobility μ_0 itself does not acquire finite temperature corrections, since they all require finite magnetic field. However the B dependence of the magnetoresistance does acquire additional terms (in particular, the B^4 term which is absent at $T = 0$, as well as the $\sqrt{B}$ term [58] which is, however, exponentially suppressed at low $T \ll \mu$). Furthermore, the B^2 dependence is also slightly modified by a finite temperature. Finite-T corrections would have a similar structure if one includes Coulomb impurities.

5.3.5 Effects of electron-electron interaction

The effect of electron-electron interaction (EEI) on the magnetoresistance of graphene was explored in Refs. [182, 187]. Since EEI does not influence σ_{xy}, we can directly employ their main result, which is the EEI correction to magnetoresistivity:

$$\Delta\rho_{\mathrm{EEI}} = \left[(\omega_c\tau_{\mathrm{tr}})^2 - 1\right] \frac{e^2\rho_0^2}{2\pi^2\hbar} A \ln\frac{k_B T\tau_{\mathrm{tr}}}{\hbar}, \tag{5.99}$$

where

$$A = 1 + c\left[1 - \frac{\ln\left(1+F_0^\sigma\right)}{F_0^\sigma}\right], \tag{5.100}$$

$$F_0^\sigma = -\alpha\int_0^{2\pi}\frac{\mathrm{d}\theta}{2\pi}\frac{\cos^2\theta/2}{\sin\theta/2+2\alpha}, \tag{5.101}$$

and c is the number of multiplets. Depending on the temperature, $c = 3$, 7, or 15 for very low, moderately low, and high temperatures, respectively. It describes the number of ungapped non-singlet two-particle states contributing to Hartree-type correction to the conductivity. Since each electron has a well defined spin and valley quantum number, which can both take two values, there are in total 16 possibilities for two particle states, one of which will always be a spin and valley singlet. In fact, since there may be inter- or intra-valley scattering, valley is not necessarily a good quantum number in this sense, depending of the hierarchy of the temperature, the intra-valley phase breaking time τ_*, and the inter-valley scattering time τ_{iv}.

For $k_BT < \hbar/\tau_*$, channels mixing different spins do not contribute, thus there remain $2 \times 4 = 8$ channels, of which one is a singlet, i.e., $c = 7$. If $k_BT < \hbar/\tau_{\mathrm{iv}}$, valley is not a good quantum number anymore, thus we get 4 states, of which one is a multiplet, i.e., $c = 3$. According to Ref. [182], the relation $\tau_* < \tau_{\mathrm{iv}}$ is usually fulfilled. Below we give the numerical values of the Fermi liquid constant F_0^σ for some values of α:

$$F_0^\sigma = \begin{cases} -0.18, & \alpha = 0.5 \\ -0.21, & \alpha = 1 \\ -0.22, & \alpha = 1.5 \\ -0.23, & \alpha = 2 \end{cases}. \tag{5.102}$$

While Eq. (5.101) is controlled only for small α, in suspended graphene we often reach values close to unity. However, this naive calculation already shows, that the value of F_0^σ does not depend strongly on the choice of α. Correction (5.99) does influence the mobility and it also influences the prefactor of the B^2 dependence. For low temperatures, this is a negative correction.

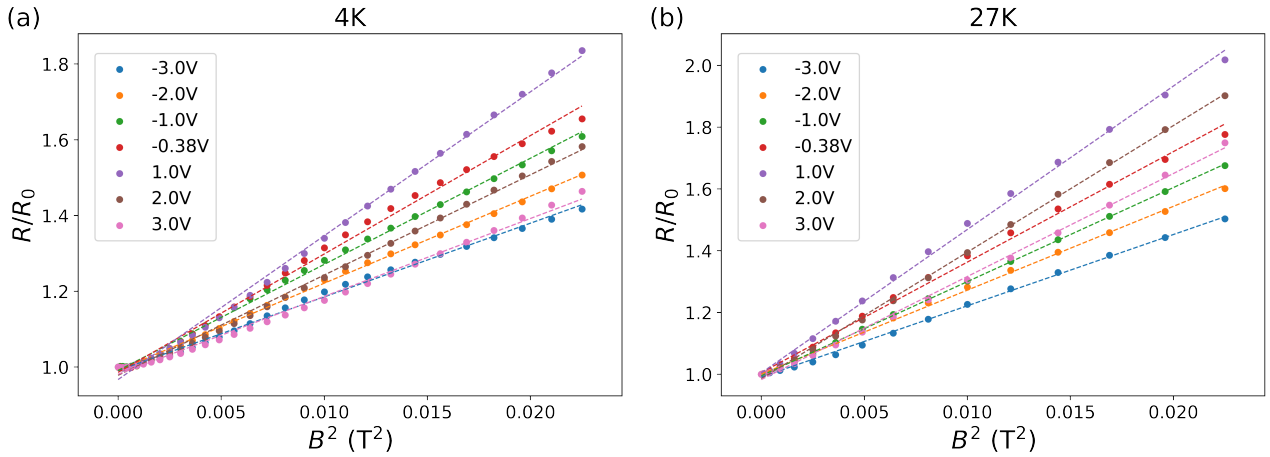

Figure 5.5: (a) Scaled resistance $R/R(0)$ vs.B^2 at $T = 4\,\mathrm{K}$ measured at various gate voltage values V_g between $-3 \cdots +3\,\mathrm{V}$ (0.8×10^9 cm$^{-2} < |n| < 3 \times 10^{10}$ cm^{-2}). The Dirac point corresponds to $V_g \simeq 1\,\mathrm{V}$, the data at which is denoted by lilac symbols in the figure. The dashed curves are guides for the eye, emphasizing an overall parabolic magnetoresistance and slight deviations from parabolicity. (b) Scaled resistance $R/R(0)$ vs. B^2 at $T = 27\,\mathrm{K}$ measured at various gate voltage values between $-3 \cdots +3\,\mathrm{V}$. The magnetoresistance at low fields grows faster at 27 K than at 4 K.

5.4 Analysis of data and results

The relative magnetoresistance

$$\Delta R(B)/R(0) = R(B)/R(0) - 1$$

of this sample at $B < 0.15$ T is illustrated in Fig. 5.5 which depicts the relative resistance $R(B)/R(0)$ as a function of B^2 measured at $T = 4\,\mathrm{K}$ (Fig. 5.5a) and at $T = 27\,\mathrm{K}$ (Fig. 5.5b). In both data sets, the magnetoresistance is found to be the strongest at the Dirac point, which is due to the strong dependence of the mobility on the inverse of the density and the weak (in the case of only short-range scattering – even absent) dependence of the effective coupling constant on density. Both data sets are influenced by the growing shift of the Dirac point ΔV_g as B increases.

The strength of the measured magnetoresistance depends only weakly on temperature up to 27 K. However, when comparing the data at 4 K and 27 K, one observes that the B^2 dependence is followed better at 27 K than at 4 K in small magnetic fields. Qualitatively, this could be a signature of increased role of electron-electron scattering [58, 182] and macroscopic inhomogeneities [178, 188, 189]. In our suspended graphene sample such inhomogeneities can be due to static ripples.

The nature of scattering does not appear to play a large role in the measured magnetoresistance. The parabolic field dependence is followed for both Coulomb and short-range impurities in the range of parameters covered: $|n| \sim 0.8 - 3 \times 10^{10}$ cm^{-2} and $T = 4 - 27\,\mathrm{K}$. In general, the B^2 dependence at small magnetic fields is more closely followed in the 27 K data. The 4 K data displays deviations

	$T = 4\,\mathrm{K}$	$T = 27\,\mathrm{K}$
γ_s	9.6	38.2
n_* [m^{-2}]	1.7×10^{14}	1.8×10^{14}
$c(\alpha)n^C_{\mathrm{imp}}$ [m^{-2}]	1.1×10^{14}	0.88×10^{14}

Table 5.1: Parameters extracted from the fit of the data. These parameters are used in all following plots.

from B^2 behavior at $B < 30$ mT, which may be a sign of coherent behavior and quantum interference effects, either regular weak localization type or Corbino-geometry related as predicted for graphene in Ref. [190]. At the largest magnetic fields around $0.1 - 0.15$ T, small deviations from B^2 dependence become obvious, in particular near the Dirac point. One can interpret this deviation as the onset of the Shubnikov - de Haas (SdH) oscillation regime in the sample [191] that corresponds to $x \sim 1$.

On top of this one has to consider the additional contribution R_{cont} to the measured resistance related to the contact effects. These contributions are the resistance of the metal-graphene contacts and the interface resistance of the contact-doped graphene region. The former contribution is a microscopic material property, which we take to be constant. The latter, discussed in Ref. [184] is of the type of the *pn*-junction resistance. This contribution to the total resistance depends on the density of charge carriers in the bulk of the sample and is the main cause for the usually observed electron-hole asymmetry in transport measurements. In low magnetic fields the cyclotron radius is larger than the geometrical length scales characterizing the contact region and, hence, the overall contact resistance should not show a pronounced magnetic-field dependence.

The parabolic magnetoresistance is associated with the bulk contribution, whereas the total resistance includes the contact resistance: $R = R_{\mathrm{bulk}} + R_{\mathrm{cont}}$, where R_{bulk} describes the disorder-induced bulk resistance and R_{cont} the contact contribution. Since R_{cont} depends on the gate voltage, the normalized magnetoresistance shown in Fig. 5.5 is not particularly convenient for extracting the density dependence of the mobility. Indeed, the value of $R(B = 0)$ in the denominator of the scaled magnetoresistance is not equal to $R_{\mathrm{bulk}}(B = 0)$ in front of the B-dependent term coming from Eq. (5.18), so that the coefficient in front of the B^2 term in the scaled magnetoresistance is not equal to μ_0^2.

To overcome this complication caused by the contact resistance, we have employed a fitting function of the form of the total resistance,

$$R(B) - R(0) = MB^2, \tag{5.103}$$

where we have a single fitting parameter M fully determined by the properties of the bulk of the sample. According to Eq. (5.18) we have $M = R_{\mathrm{bulk}}(0)\mu_0^2$, where $R_{\mathrm{bulk}}(0)$ describes bulk resistance at zero field and μ_0 is the mobility. We recall that $R_{\mathrm{bulk}}(0)$ is different from the measured $R(0)$ because the latter includes the contact contribution. There is no mechanism leading to a strong magnetic-field dependence of the contact resistance in the range of magnetic fields where no skipping orbits (or edge states) appear at the interfaces between the sample and the leads. The fact that we are able to consistently fit the observed magnetoresistance using our model in a wide range of gate voltages supports this argument.

Since magnetoresistance is related to mobility, the data can be employed to derive information on

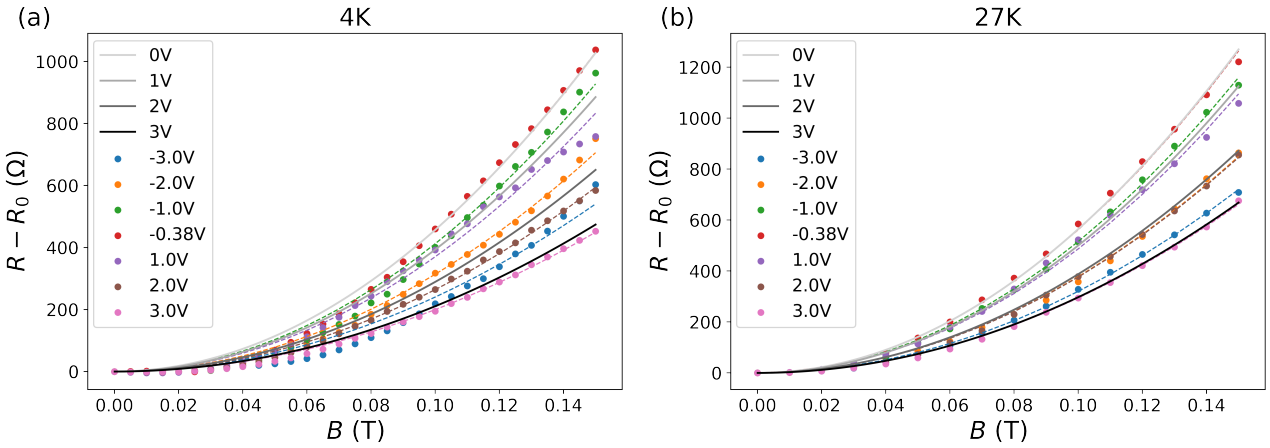

Figure 5.6: Non-normalized magnetoresistance $R(B) - R(0)$ for 4 K in (a) and 27 K in (b) for various values of U. The points are obtained after shifting the gate voltage by V_g^D. The dashed lines correspond to the fitted function Eq. (5.103) and solid lines to theoretical zero-temperature magnetoresistance, Eq. (5.18), calculated using the parameters from Table 5.1. since these parameters are obtained at finite temperature and are electron-hole averaged, the dashed and solid lines do not exactly coincide for the same values of the gate voltage.
Reprinted figure with permission from Masahiro Kamada, Vanessa Gall, Jayanta Sarkar, Manohar Kumar, Antti Laitinen, Igor Gornyi, and Pertti Hakonen, Physical Review B, **104**, 115432 (2021). Copyright 2021 by the American Physical Society. `https://journals.aps.org/prb/abstract/10.1103/PhysRevB.104.115432`

the impurity scattering in this sample from the obtained fitting parameter M which is given by

$$\begin{aligned} M = R_{\text{bulk}}(0)\mu_0^2 &= \frac{\gamma}{\pi^2\hbar n^2} \ln \frac{r_{\text{out}}}{r_{\text{in}}} \\ &= \frac{1}{\pi^2\hbar n^2} \left(\frac{1}{\gamma_s} + \frac{c(\alpha) n_{\text{imp}}^c}{n} \right)^{-1} \ln \frac{r_{\text{out}}}{r_{\text{in}}}. \end{aligned} \tag{5.104}$$

In order to include the disorder-induced saturation of the density of states, we replace n with $\sqrt{n^2 + n_*^2}$ in the fitting function, and then extract γ_s, n_*, and the effective concentration of Coulomb impurities $c(\alpha) n_{\text{imp}}^C$. We fit the obtained data over the full measured voltage range, with all the results being electron-hole averaged. The values we extract from these fits are shown in Table 5.1.

Notably, the energy corresponding to n_* is $\varepsilon_* \approx 9$ meV, which is larger than the energies corresponding to 4 K and 27 K, which are 0.3 meV and 2.3 meV, respectively, so that finite-T corrections are small, even for 27 K. Moreover the value of n_* is consistent with region corresponding to disorder broadening of the Dirac point in the field effect mobility shown in Fig. 5.3.

Let us shortly discuss how the fits are performed and how we obtain the parameters for Table 5.1. The first step is to remove the Dirac point shift as discussed in Sec. 5.2.1. In practice, we do not employ the inhomogeneous shift introduced there, but rather just shift the curves as a whole, such that the maximum is at zero voltage. From the cubic spline through the measured data points, we read off the resistance values at the original voltages and additionally all half integer ones for 27 K.

We then fit the obtained magnetoresitances $R(B) - R(0)$ over the whole measured range of B with the fit function Eq. (5.103) for all gate voltages. From the thus obtained parameter M we extract all

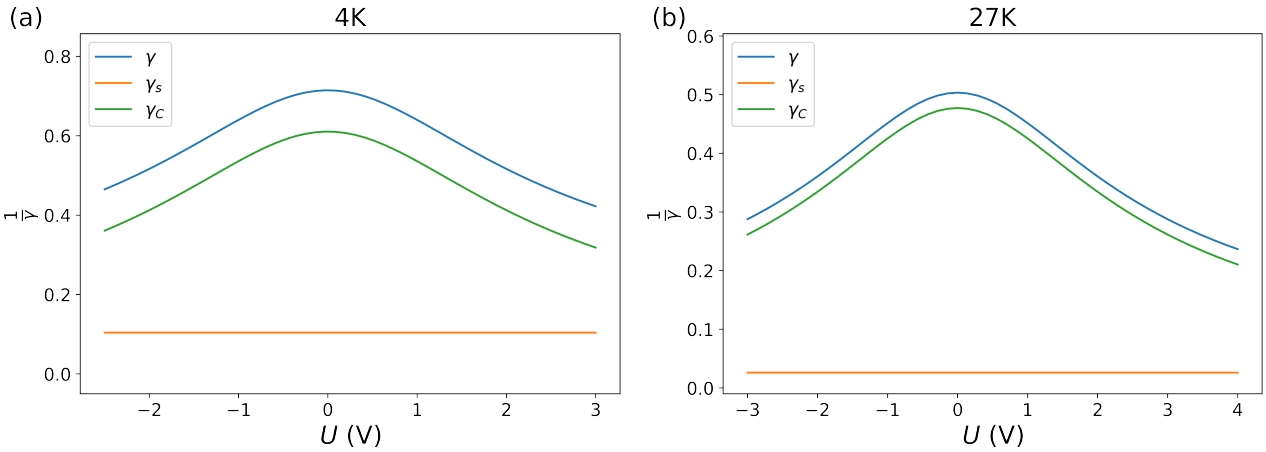

Figure 5.7: Effective disorder parameter $1/\gamma$ defined by Eq. (5.94) and its two parts $1/\gamma_C$ and $1/\gamma_s$ for $T = 4\,\mathrm{K}$ (a) and $T = 27\,\mathrm{K}$ (b). The parameter γ is smaller for 4 K, which means that disorder is stronger at lower temperatures. The parameters are given in Table 5.1.
Reprinted figure with permission from Masahiro Kamada, Vanessa Gall, Jayanta Sarkar, Manohar Kumar, Antti Laitinen, Igor Gornyi, and Pertti Hakonen, Physical Review B, **104**, 115432 (2021). Copyright 2021 by the American Physical Society. `https://journals.aps.org/prb/abstract/10.1103/PhysRevB.104.115432`

parameters of the theory according to Eq. (5.104). We fit the magnetoresistance with three parameters γ_s, $c(\alpha)n_{\mathrm{imp}}^C$, and n_*, expressing M as follows:

$$\frac{1}{M} = \pi^2\hbar\left(n^2 + n_*^2\right)\left[\frac{1}{\gamma_s} + \frac{c(\alpha)n_{\mathrm{imp}}^C}{\sqrt{n^2+n_*^2}}\right]. \tag{5.105}$$

A plot of the resulting effective disorder parameters γ for the two temperatures is shown in Fig. 5.7.

In order to summarize the effect of the two different types of impurities, in Fig. 5.8 we show the zero-field conductivity σ_0 determined by Eq. (5.12) for both our mixed disorder model and a Coulomb-impurity model. Already at experimentally accessible density ratios $n/n_{\mathrm{imp}}^C \approx 2$ we observe the sub-linear conductivity due to short-range scatterers discussed in Ref. [185].

In Fig. 5.6, we show a comparison of the shifted magnetoresistance and the corresponding fit by the theoretical curves obtained from Eq. (5.18) for various values of the gate voltage difference

$$U = V_g - V_g^D$$

relative to the gate voltage V_g^D corresponding to the Dirac point, with the fitting parameters from Table 5.1. Voltage U and density n are connected by the capacitance as $n = C_g U/e$.

With the parameters obtained from fitting the magnetoresistance curves, we get the mobility from Eq. (5.20), see Fig. 5.9, where the inverse mobility μ_0^{-1} is displayed as a function of gate voltage difference U. A clear minimum is found at the Dirac point (maximum for the mobility). The slope of the inverse mobility away from the Dirac point is determined by the strength of short-range scatterers γ_s. We observe that at $T = 27\,\mathrm{K}$, the mobility varies only very slightly as a function of the gate voltage. This indicates that the role of short-range impurities is suppressed at higher temperature. Possibly, with increasing temperature residual dirt (adsorbed atoms) is removed from the sample.

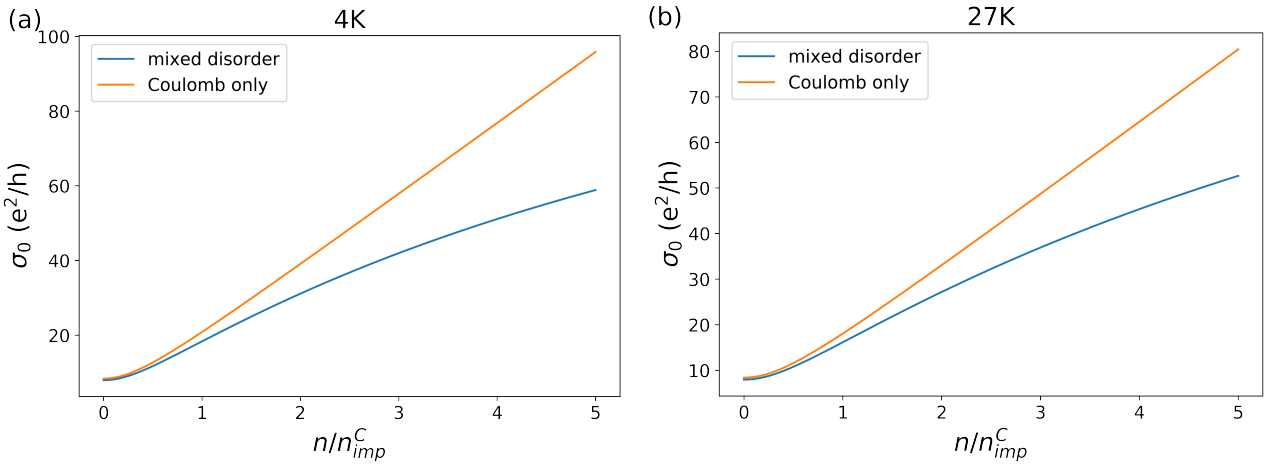

Figure 5.8: (a) Conductivity at $B = 0$T, Eq. (5.12), derived using the parameters extracted from the 4 K magnetoresistance data. (b) Zero-field conductivity derived from the 27 K data. The blue curve is the result for our mixed disorder model, the orange one for $\gamma_s = \infty$, i.e., no short-range scatterers. The parameters are given in Table 5.1, additionally we used $\alpha = 1.3$ to determine n^C_{imp}.

Reprinted figure with permission from Masahiro Kamada, Vanessa Gall, Jayanta Sarkar, Manohar Kumar, Antti Laitinen, Igor Gornyi, and Pertti Hakonen, Physical Review B, **104**, 115432 (2021). Copyright 2021 by the American Physical Society. `https://journals.aps.org/prb/abstract/10.1103/PhysRevB.104.115432`

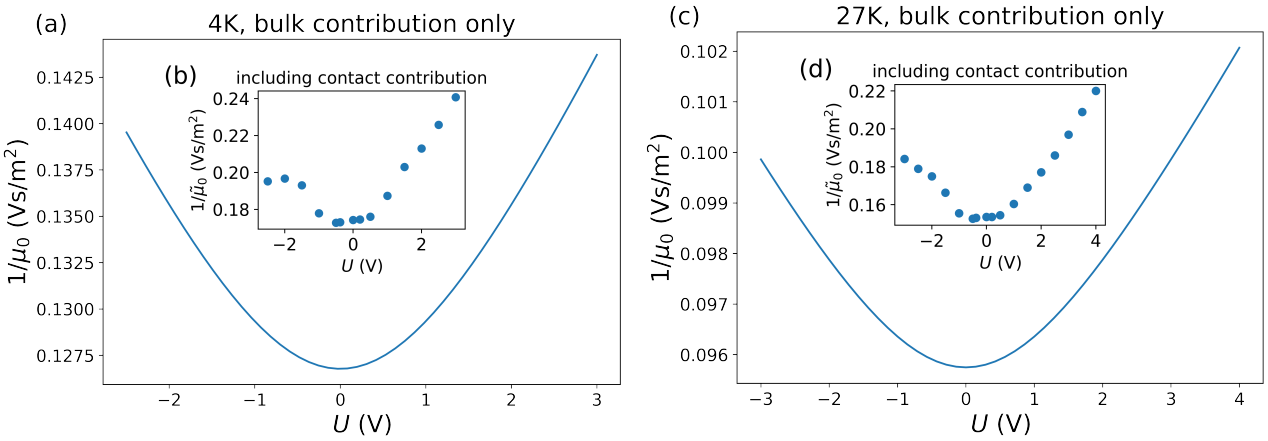

Figure 5.9: (a) Electron-hole averaged inverse mobility, Eq. (5.20), derived using the parameters extracted from the 4 K magnetoresistance data. (b) Mobility naively extracted from the scaled shifted magnetoresistance as $R(B)/R(0) = 1 + \tilde{\mu}_0^2 B^2$: this includes the contribution of the contact resistance. (c) Inverse mobility derived from the 27 K data. (d) as in (b) for 27 K. The parameters are given in Table 5.1.
Reprinted figure with permission from Masahiro Kamada, Vanessa Gall, Jayanta Sarkar, Manohar Kumar, Antti Laitinen, Igor Gornyi, and Pertti Hakonen, Physical Review B, **104**, 115432 (2021). Copyright 2021 by the American Physical Society. `https://journals.aps.org/prb/abstract/10.1103/PhysRevB.104.115432`

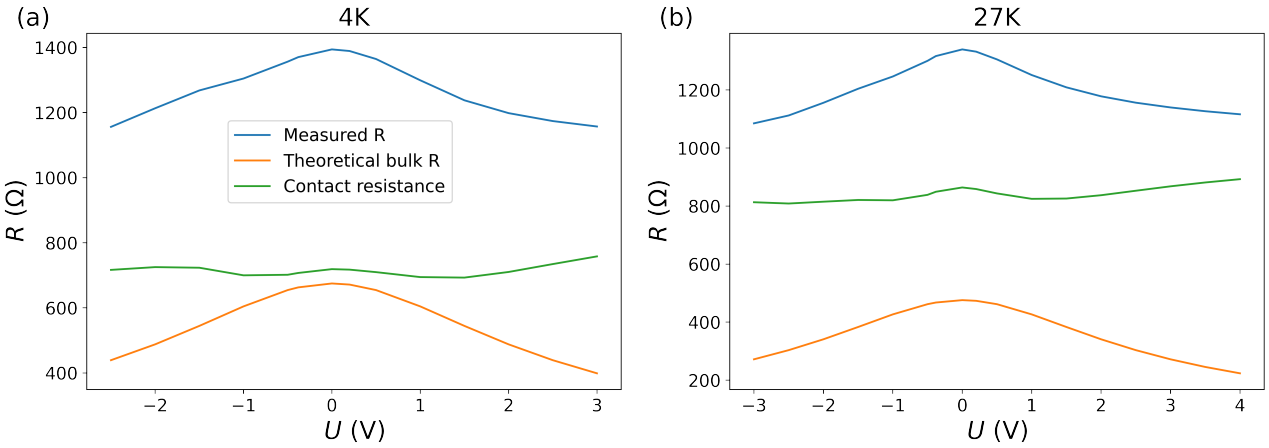

Figure 5.10: Zero-B resistance at $T = 4\,\mathrm{K}$ in (a) and $T = 27\,\mathrm{K}$ in (b). Blue curves: the measured resistance. Orange curves: the zero-T bulk resistance calculated from Eq. (5.1) with the electron-hole averaged parameters from the fit (Table 5.1). Green curves: the contact resistance which is obtained as the difference of the total measured resistance and the theoretical value of the bulk resistance. Note that the contact resistance is actually larger than the bulk contribution, as expected for high-mobility samples.
Reprinted figure with permission from Masahiro Kamada, Vanessa Gall, Jayanta Sarkar, Manohar Kumar, Antti Laitinen, Igor Gornyi, and Pertti Hakonen, Physical Review B, **104**, 115432 (2021). Copyright 2021 by the American Physical Society. `https://journals.aps.org/prb/abstract/10.1103/PhysRevB.104.115432`

For comparison, the insets in Fig. 5.9 show the mobility $\tilde{\mu}_0$ that could be naively extracted from the formula $R(B)/R(0) = 1+\tilde{\mu}_0^2 B^2$. As mentioned above, this quantity is not the genuine bulk mobility μ_0, since $\tilde{\mu}_0$ includes the effect of the contact resistance. Note that $\tilde{\mu}_0$ reveals the electron-hole asymmetry. Moreover, we rather clearly see a feature on the hole side, stemming from the feature in the resistance mentioned at $V_g = -2V$ in Fig. 5.2. Since we extract this from the shifted data, $V_g = -2V$ is mapped to different U for each magnetic field and thus this feature is not as clearly localized anymore. Mobility obtained this way is lower, since it is affected by the contact-resistance contribution.

Thus, looking at the deduced impurity scattering strengths from the obtained mobilities, the magnetoresistance data should reflect effects related to both Coulomb and short-range scatterers. Note that here the Hall mobility is slightly smaller than the field-effect mobility obtained using $R(V_g)$ which yields approximately 10^5 cm^2/Vs near Dirac point for the average mobility of electrons and holes. The value of mobility extracted from the analysis of the magnetoresistance is consistent with the field-effect mobility.

Subtracting the disorder-induced bulk resistance with the parameters obtained from the measured magnetoresistance, we get access to the overall contact resistance, which is shown in Fig. 5.10. The obtained value of the contact resistance is somewhat higher than the one reported for similar samples in the Corbino geometry, which can be related to the fact that the sample has been cooled down several times and the contact structure on top of LOR resist is not very rigid around room temperature.

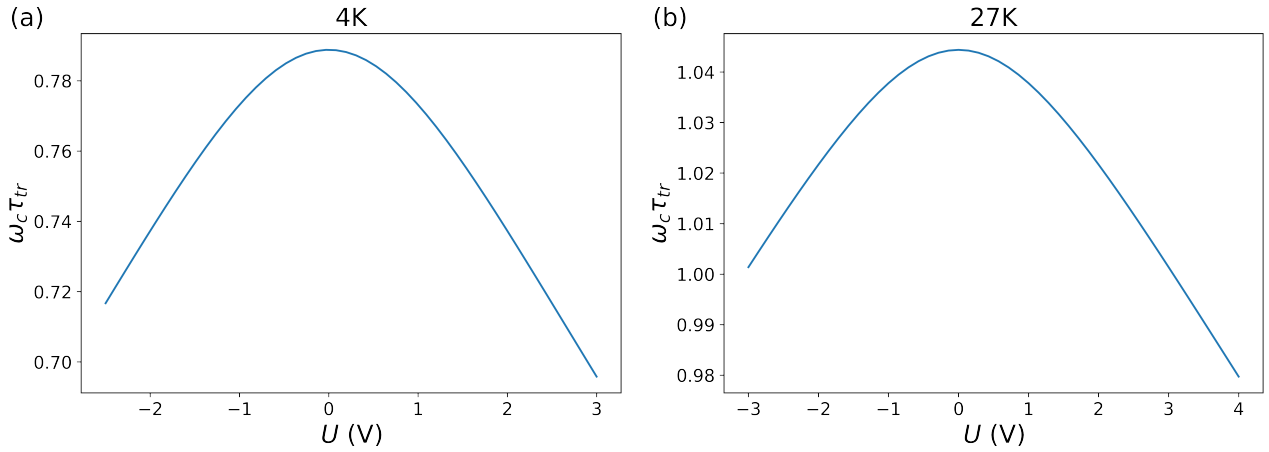

Figure 5.11: The product $\omega_c\tau_{\mathrm{tr}}$ at $B = 0.1$ T with the parameters from the fit (Table 5.1) for 4 K in (a) and 27 K in (b). The transport time is larger for the higher temperature, which is consistent with the reduction of the contribution of short-range impurities to scattering processes.
Reprinted figure with permission from Masahiro Kamada, Vanessa Gall, Jayanta Sarkar, Manohar Kumar, Antti Laitinen, Igor Gornyi, and Pertti Hakonen, Physical Review B, **104**, 115432 (2021). Copyright 2021 by the American Physical Society. `https://journals.aps.org/prb/abstract/10.1103/PhysRevB.104.115432`

5.4.1 Effects of finite temperature and electron- electron interaction in the experiment

While we argued, that finite temperature effects and electron-electron interaction apparently don't have a strong influence on the measurement, one can use the parameters obtained in Tab. 5.1 and take a look at the qualitative difference of these effects on the resulting magnetoresistance. The first quantity to look at is the product $\omega_c\tau_{\mathrm{tr}}$ for $B = 0.1$T at the two temperatures using the obtained parameters to calculate τ_{tr} including both types of disorder, which is shown in Fig. 5.11.

We see that for $B = 0.1$ T the bending of cyclotron trajectories should be already substantial. Since the quantum scattering time in graphene is smaller by about a factor of two compared to the transport scattering time, the parameter $x = \omega_c\tau_q$ is still smaller than one, and hence Landau levels overlap strong enough to not lead to any more intricate effects in the range magnetic fields $B < 0.15$ T addressed here. Next we address the effect of electron-electron interaction alone for the case of $T = 4$ K, which is shown in Fig. 5.12

By plugging the value of γ obtained from the fit of magnetoresistance in the analytical expression for zero T, Eq. (5.18), we obtain the left panel of Fig. 5.13. For comparison, in the right panel of Fig. 5.13, we show the result of numerical evaluation of Eq. (5.14) at $T = 27$ K, without the EEI correction. The EEI correction at $T = 27$ K is almost negligible, since the diffusive logarithm vanishes. Instead one would find a correction of the form

$$\Delta\rho_{EEI} \propto B^2/(T\tau_{\mathrm{tr}})^x, \tag{5.106}$$

where x depends on the nature of disorder [182, 192]. This is consistent with the result of Ref. [182] that finds a crossover to the ballistic regime at 20 K, where one should consider the higher quality of the device considered here. At the same time, the EEI produces the leading finite-T correction at

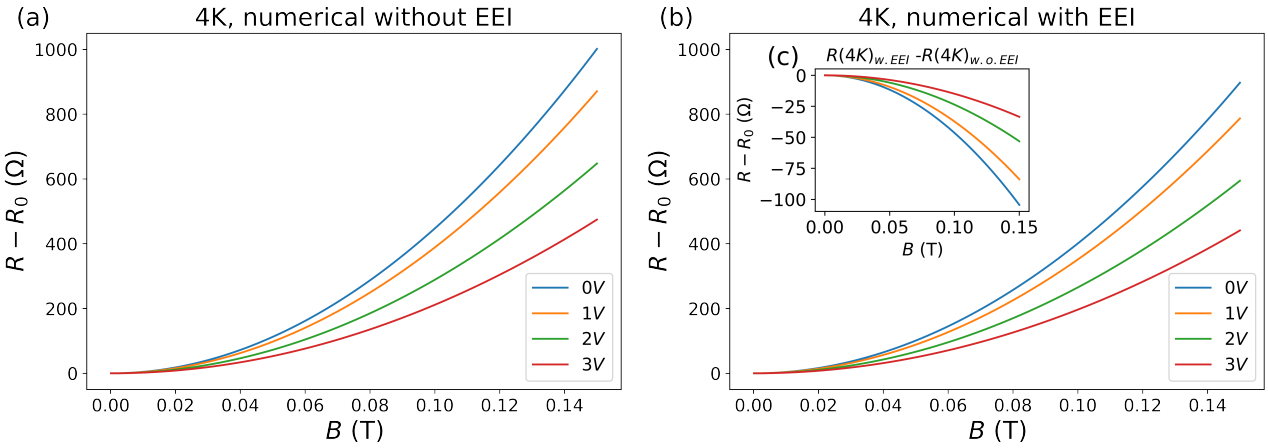

Figure 5.12: Magnetoresistance at $T = 4\,\mathrm{K}$ with parameters from the fit (Table 5.1) without the EEI correction (a) and including it (b). The EEI correction leads to a small suppression of the magnetoresistance, without changing the functional form. This negative correction is shown in inset (c). Here $\alpha = 1.3$ and $c = 3$ were chosen.
Adapted figure with permission from Masahiro Kamada, Vanessa Gall, Jayanta Sarkar, Manohar Kumar, Antti Laitinen, Igor Gornyi, and Pertti Hakonen, Physical Review B, **104**, 115432 (2021). Copyright 2021 by the American Physical Society. `https://journals.aps.org/prb/abstract/10.1103/PhysRevB.104.115432`

$T = 4\,\mathrm{K}$. Overall, we observe that the effect of finite temperature is rather weak in the considered range of parameters.

In combination, finite temperature does change the mobility and it also influences the magnetic field behaviour of the resistance, so that formula (5.18) is no longer exact and the relation (5.104) does not, strictly speaking, yield the true parameters. However, as we see from Figs. 5.12 and 5.13, these effects are rather small in the experimentally accessed range, which justifies the neglect of these effects in the main analysis of the data.

5.5 Discussion

We have investigated the geometric magnetoresistance in a suspended graphene (Sec. 1.1) Corbino disk (Sec. 3.2) at $T = 4$ K and $T = 27$ K and small magnetic fields. The main features of the measured curves are captured well by a simple zero-temperature analysis, as performed in Sec. 2.1.1. The corrections obtained for large magnetic fields calculated in Sec. 2.2.5 can be neglected here, since disorder sufficiently smears the Landau levels in the considered magnetic field range. Both short-range and charged impurities lead to the observed quadratic magnetic field dependence.

The gate dependence of the measured magnetoresistance can be used to estimate the contributions of the short-range and long-range impurity scattering to the mobility individually. Away from the Dirac point it is exclusively determined by short-range scattering, while scattering on long-range disorder (Coulomb impurities or ripples) dominates close to charge neutrality. The magnetic field dependence does not show a fundamental difference, it is quadratic in both cases.

The bulk mobility extracted from the parabolic magnetoresistance is high (of the order of 10^5

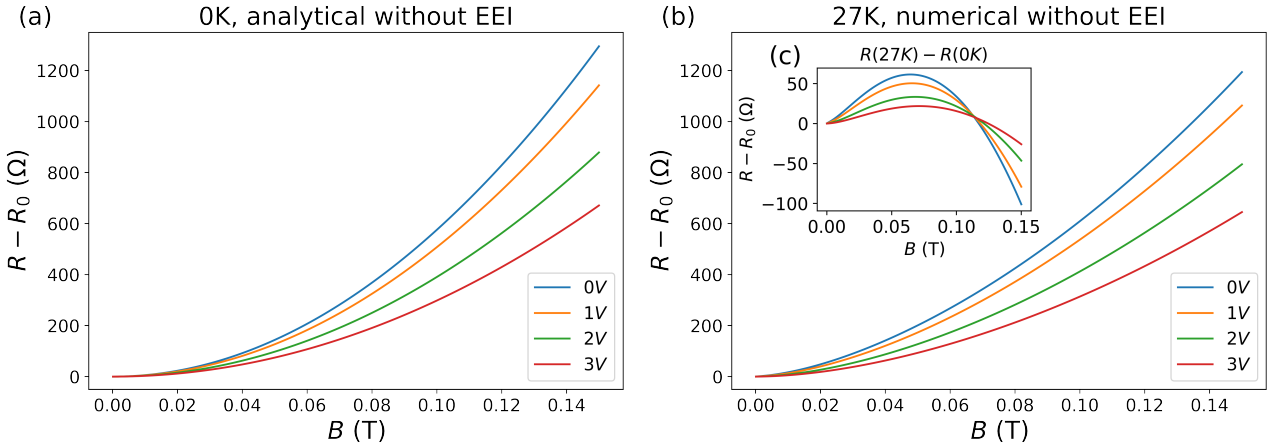

Figure 5.13: (a) Magnetoresistance obtained from the zero-temperature solution (5.18) with the parameters from the fit (Table 5.1) for $T = 27\,\mathrm{K}$. (b) Magnetoresistance obtained by using the parameters from the fit and solving Eq. (5.14) numerically. The inset (c) shows the finite temperature corrections to the magnetoresistance. Depending on the magnitude of the magnetic field this correction is either positive or negative and it also changes the functional form very slightly.
Adapted figure with permission from Masahiro Kamada, Vanessa Gall, Jayanta Sarkar, Manohar Kumar, Antti Laitinen, Igor Gornyi, and Pertti Hakonen, Physical Review B, **104**, 115432 (2021). Copyright 2021 by the American Physical Society. `https://journals.aps.org/prb/abstract/10.1103/PhysRevB.104.115432`

cm^2/Vs), which agrees with previous estimates obtained in slightly cleaner samples. Somewhat counterintuitively, the mobility is actually higher for the higher temperature considered. It is important to remember, that the total measured resistance is the sum of the bulk resistance, which is determined by the intrinsic properties of graphene, and a contact contribution, which in the case considered here, is higher than the bulk contribution, due to the high quality of the sample.

It should be emphasized, that taking into account this contact resistance is essential when analyzing the data. According to Eq. (5.104), the magnetoresistance is proportional to $R_{\text{bulk}}\mu_0^2 B^2$ where $R_{\text{bulk}} = R - R_{\text{cont}}$. If instead one uses R, one overestimates the reduction of μ_0 obtained from the magnetoresistance data as a function of gate voltage. Naively fitting the normalized data in Fig. 5.5b would lead to a reduction in μ^2 by a factor of two, while from Fig. 5.9b we obtain only $< 13\%$ reduction in μ^2. Thus, in the former case the strength of the short-range scattering would appear almost three times larger than in the correct analysis.

Thus we could show, that the magnetoresistance in the Corbino geometry in graphene is in general strongly influenced by both short range and charged impurities. Away from the Dirac point it is dominated by short-range scattering, while scattering on long-range disorder (Coulomb impurities or ripples) dominates close to charge neutrality. This is especially interesting close to the Dirac point, but should generally be taken into account. In the chosen temperature range the Drude result dominated the magnetoresistance, but for very low temperatures one should find, that electron-electron interaction leads to the leading contribution.

In the temperature range of this experiment, transport is dominated by disorder. Nevertheless we showed, that one can obtain a conservation of charge continuity equation (5.35) and a generalized Navier-Stokes equation (5.38) from the semiclassical Boltzmann equation introduced in Sec. 2.1 to describe the system. How this description has to be extended to describe hydrodynamic transport at elevated temperatures was introduced in Sec. 2.4 and what this means for the same setup is discussed in Chapter 6.

5.6 Summary and conclusions

In summary, we find that the magnetoresistance in a graphene Corbino disk in the considered magnetic field regime can be modeled by a simple mixed disorder model on a semi-classical level. Effects of finite temperature and electron-electron interaction can be neglected at the considered temperatures of 4 K and 27 K, but due to the proximity to the Dirac point, the saturation of the density of states has to be taken into account. The resulting magnetoresistance is simply quadratic, but the included short range and charged scatterers possess a different density dependence. Since this density is controlled by the external gates, we can directly use the data at different voltages to characterize the role of them separately.

In a clean sample like this, the contact resistance is large and a priori unknown. Since it depends both on the used materials and fabrication and on the relative densities of those, it will also generally have a gate voltage dependence. It should not depend on the magnetic field in the range under consideration. By analyzing the density dependence of the magnetoresistance, we can find the true bulk resistance and bulk mobility and can thus estimate the contact resistance. The thusly obtained true bulk mobility is larger, than the one naively determined, in which mobility is suppressed by the high contact resistance.

As will become important in Chapter 6, starting from the Boltzmann equation, one may derive a generalized Navier-Stokes equation with disorder induced viscosity also in this regime. In the given

setup, viscosity however drops out and one finds a simple Ohm's law instead. It is important to point out, that the validity of a generalized Navier-Stokes equation is not enough to find hydrodynamic behavior. Transport here is disorder dominated and one does not find collective behavior or a local equilibrium needed for true hydrodynamic transport.

In conclusion, magnetoresistance in graphene in the Corbino geometry is dominated by the Drude-Boltzmann result in the parameter range considered here and can be described by a mixed disorder model. A similar result can be expected in two-dimensional materials with a quadratic dispersion, although there the density dependencies will be different [193]. At 4 **K the most relevant correction is due to electron-electron interaction and leads to a diffusive logarithmic correction, which can be of the order of** 10%**. The gate voltage dependent analysis of the graphene magnetoresistance in the Corbino geometry allows one to extract parameters of different scattering mechanisms and clearly distinguish the bulk from the contact resistance. For this reason, it appears that the setup is a very powerful tool for the characterization not only of graphene samples.**

While electron-electron interaction did not play an important role in this chapter and "only" lead to additional effects on top of the non-interacting conductance curves in Chapter 4, it is the dominating process in Chapter 6, where we study the same monolayer graphene Corbino disk but at elevated temperatures.

Chapter 6

6 Hydrodynamic transport in a graphene Corbino disk

Since in Chapter 5 we already studies electronic transport in a graphene Corbino disk (Sec. 3.2) at low temperatures, where the transport is disorder dominated, the question regarding the behavior at elevated temperatures arises quite naturally. In graphene, one may reach a temperature regime where ℓ_{ee} is the shortest length scale of the problem, and thus dominated by electron-electron interaction over disorder scattering, electron-phonon coupling and interference effects with the finite sample size. As discussed in Sec. 2.4, the behavior in this regime is characterized by a collective behavior of charge carriers, which can be described by similar equations as the hydrodynamics in classical fluids.

This should be contrasted with the setup discussed in Chapter 4, where effects due to electron-electron interaction did show up in the conductance curve of a bilayer graphene quantum point contact, but could in principle still be treated on a perturbative level and only lead to additional features. In this chapter however, they completely change the behavior of the electronic liquid and thus the applicable treatment.

While this is interesting at any doping level, the behavior at charge neutrality is especially intriguing, since there, the individual number of carriers in each band is not necessarily conserved but undermined by recombination processes. Moreover, the charge current $\mathbf{j} = n\mathbf{u} + \delta\mathbf{j}$ becomes purely dissipative (i.e. only exists because of the electron-electron interaction), while the energy current $\mathbf{j}_E = W\mathbf{u}$ remains finite without these effects. Thus, the electronic transport and heat transport decouple. However, as we will show, the electronic transport is still influenced by hydrodynamics, which results in jumps of temperature and electrochemical potential at the interface between the graphene sample and leads. This transport is, however, dominated by energy relaxation as opposed to viscosity.

In this chapter we will approach the question whether hydrodynamic effects can still be seen in electronic transport measurements performed in a charge neutral graphene Corbino disk. This question can generally be answered positively, since we indeed find jumps of the electrochemical potential and the temperature at the interface, that are induced by hydrodynamics. *However, when only looking at the total resistance of such a device, the hydrodynamic effects are small. Generally, energy relaxation dominates over the role of viscosity.*

The content of this chapter is based on a preprint available at [22] and is the result of joint project with Boris N. Narozhny from KIT.

6.1 Introduction

In many materials transport properties can be described by a perturbative treatment of interaction effects, since the effective electron-electron coupling constant is small [55], like it was discussed in Sec. 2.2. This changes, if electron-electron interaction is indeed not weak, which is the case in very clean graphene samples at elevated temperatures [194–206], where one may observe signatures of collective carrier motion, which resembles the motion of a classical fluid. In this context, electron-electron interaction specifically gives rise to an electronic viscosity, which has been discussed theoretically for quite some time [207–212] but could be experimentally investigated only recently [194, 201]. The viscosity enters through the dissipative correction of the stress tensor, but only, if the flow in the sample is non-uniform. This requires special limits in common geometries, like Hall bars [213–217], but is trivially the case in the Corbino geometry, as was already shown in Sec. 3.2. For this reason, hydrodynamic flow of electrons in a Corbino geometry has been the subject of intensive research, both experimentally [218] and theoretically [219–222].

Away from charge neutrality, these systems can be described by a Navier-Stokes equation with an additional weak damping term to account for finite disorder scattering in the sample, which is indeed needed to form a local equilibrium, since energy current in graphene is proportional to the momentum, which doesn't get relaxed by electron-electron interaction alone. In this degenerate regime, charge current $\mathbf{j} = n\mathbf{u}$ and energy current $\mathbf{j}_E = \mathcal{W}\mathbf{u}$ are both carried by the hydrodynamic velocity $\mathbf{u}$ and simply proportional to each other. This changes at charge neutrality, $n(\mu = 0) = 0$, where the energy current remains finite, while the electric current is carried by the dissipative corrections $\delta\mathbf{j}$ alone. Since electron-electron interaction conserves momentum, the energy current does not obtain similar corrections. Electronic transport in this "Dirac fluid" has been subject of intensive research [201, 214–217, 223–231] leading to the general consensus, that in the absence of magnetic field, $\mathbf{B} = 0$, resistivity of neutral graphene is determined by the electron-electron interaction

$$R_0 = \frac{\pi}{2e^2 T \ln 2}\left(\frac{1}{\tau_{11}} + \frac{1}{\tau_{\mathrm{dis}}}\right) \underset{\tau_{\mathrm{dis}}\to\infty}{\longrightarrow} \frac{1}{\sigma_Q} \tag{6.1}$$

where $\tau_{11} \propto \alpha_g^{-2} T^{-1}$ describes the appropriate electron-electron collision integral introduced in Sec. 2.4.1.1 and σ_Q is the "intrinsic" or "quantum" conductivity of graphene and disorder is characterized by the mean free time τ_{dis}. This describes the uniform bulk current and is independent of the viscosity.

In the traditional Hall bar geometries, the interface with external leads is a very small region and for sufficiently long samples can be neglected. Similarly, the flow close to the outer edges will simply be parallel to these edges. This is very different in a Corbino disk, where we do not have any interfaces to the vacuum, and, unless the diameter of the disk is very large, effects related to the lead-sample interfaces can also not be neglected, but fix the boundary conditions of the leads.

The setup we consider here, is that of a Corbino disk made of graphene at charge neutrality, which is contacted by an inner circular lead of radius r_1 and an outer ring lead with inner radius r_2 to preserve rotational symmetry. The outer lead is assumed to be grounded, but both have the same doping level and temperature. In the middle of the inner lead, one attaches a current source along the third dimension, thus preserving the symmetry. The leads can in general be made of any good metal, but for the sake of completeness we will assume that they consist of highly doped graphene, in which transport is disorder dominated, as introduced in Sec. 5.3.1. The most easily measurable quantity in such a system is the resistance $R = U/I$, that we assume to be measured at a fixed current I across the whole disk between the points r_{in} and r_{out} in Fig. 6.1. The total voltage drop U between these

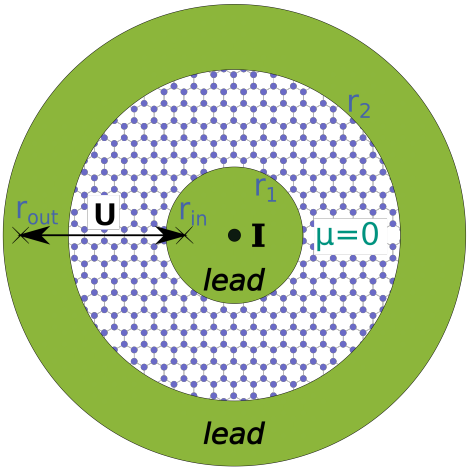

Figure 6.1: Setup considered in this chapter. A charge neutral graphene Corbino disk of inner radius r_1 and outer radius r_2 is placed between two leads (green). The current I is injected in the middle, and the voltage drop U between the points r_{in} and r_{out} is determined.

points includes the voltage drop across the graphene sample and the leads, but also across the two interfaces.

While the leads' resistance should be minimal, the contact resistance is generally important in clean systems. A very simplistic description of these interfaces, like it is done in Ref. [226], relates the jump in electrochemical potential across this interface solely to a phenomenological contact resistance due to the different work functions of the materials. On the other, as was demonstrated in Refs. [220, 232], there is an additional, specifically hydrodynamic jump, which is induced due to the mismatch of dissipation between the leads and the sample, specifically, if they are of different viscosity.

This chapter is organized as follows. We start with an overview of the general hydrodynamic equations including dissipative corrections in graphene in an external magnetic field in Sec. 6.2, and give their simplified form in polar coordinates at charge neutrality and vanishing field In Sec. 6.3.2 we introduce, how the disorder dominated leads can be described by a similar set of equations, which naturally arises from the Boltzmann equation. In the following Sec. 6.3.3, we state the boundary conditions at the interface, which can be obtained from the continuity equations and the full solution. These results are discussed in Sec. 6.3. Finally, we discuss in Sec. 6.4, how one can use the notion, that energy should not accumulate directly at the interface, to find the jump of the electrochemical potential. This chapter end with a Discussion (Sec. 6.5) and a Summary and Conclusions in Sec. 6.6.

6.2 General hydrodynamic transport in graphene

As explained in Sec. 2.4, graphene in the hydrodynamic regime, i.e. in a setup, where ℓ_{ee} is the shortest length scale of the problem, can be described by the following set of hydrodynamic equations

$$\partial_t n + \nabla \cdot \mathbf{j} = 0, \tag{6.2a}$$

which describes the exact conservation of charge

$$\partial_t n_I + \nabla\cdot\mathbf{j}_I = -\frac{n_I - n_{I,0}}{\tau_R} = -\frac{12\ln 2}{\pi^2}\frac{n_{I,0}\mu_I}{T\tau_R}, \tag{6.2b}$$

where $n_{I,0} = \pi T^2/(3v_g^2)$ is the equilibrium value of the total quasiparticle density (i.e., at $\mu_I = 0$) and τ_R is the recombination time. The individual densities in two bands are indeed not conserved, if one takes into account recombination processes, which are characterized by this timescale τ_R. There is a similar equation for the energy density

$$\partial_t n_E + \nabla\cdot\mathbf{j}_E = e\mathbf{j}\mathbf{E} - \frac{n_E - n_{E,0}}{\tau_{\mathrm{RE}}}, \tag{6.2c}$$

which is relaxed with the energy-relaxation time τ_{RE}.

The hydrodynamic velocity $\mathbf{u}$ satisfies the generalized Navier-Stokes equation

$$\mathcal{W}(\partial_t + \mathbf{u}\cdot\nabla)\mathbf{u} + v_g^2\nabla P + \mathbf{u}\partial_t P + e(\mathbf{E}\cdot\mathbf{j})\mathbf{u} = v_g^2\left[\eta\Delta\mathbf{u} + en\mathbf{E} + \frac{e}{c}\mathbf{j}\times\mathbf{B}\right] - \frac{\mathcal{W}\mathbf{u}}{\tau_{\mathrm{dis}}}, \tag{6.2d}$$

where P and η are the thermodynamic pressure and shear viscosity and $\mathbf{B}$ is a static, external magnetic field. The enthalpy density satisfies $\mathcal{W} = n_E + P$. The full hydrodynamic equations also includes the thermal transport equation (2.210), which describes the entropy s and its conjugated current. Using Eqs. (6.2a) and (6.2b) this can be brought to the simpler form

$$\begin{aligned} T\left[\frac{\partial s}{\partial t} + \nabla_{\mathbf{r}}\cdot(s\mathbf{u})\right] + \mu\partial_t n + \mu_I\partial_t n_I = \delta\mathbf{j}\cdot\left[e\mathbf{E} + \frac{e}{c}\mathbf{u}\times\mathbf{B}\right] \\ + \frac{\eta}{2}\left(\nabla_\alpha u_\beta + \nabla_\beta u_\alpha - \delta_{\alpha\beta}\nabla\cdot\mathbf{u}\right)^2 - \frac{n_E - n_{E,0}}{\tau_{RE}} + \frac{\mathcal{W}\mathbf{u}^2}{v_g^2\tau_{\mathrm{dis}}}. \end{aligned} \tag{6.2e}$$

This should be supplemented with the dissipative corrections discussed in Sec. 2.4.1.1, which describe the corrections due to electron-electron interaction explicitly.

6.3 Application to charge neutral graphene

In the present case, the graphene sample is assumed to be at charge neutrality and we further restrict ourselves to the stationary solution in linear order of the driving field, which will be the current I transmitted from the lead attached to the inner contact. Then the hydrodynamic equations in charge neutral graphene can be simplified to

$$\nabla\cdot\delta\mathbf{j} = 0, \tag{6.3a}$$

$$n_{I,0}\nabla\cdot\mathbf{u} + \nabla\cdot\delta\mathbf{j}_I = -(12\ln 2/\pi^2)n_{I,0}\mu_I/(T\tau_R), \tag{6.3b}$$

$$\nabla\delta P = \eta\Delta\mathbf{u} + (e/c)\delta\mathbf{j}\times\mathbf{B} - 3P\mathbf{u}/(v_g^2\tau_{\mathrm{dis}}), \tag{6.3c}$$

$$3P\nabla\cdot\mathbf{u} = -2\delta P/\tau_{RE}, \tag{6.3d}$$

Since the Coulomb interaction conserves momentum, there is no dissipative correction due to electron-electron interaction for the energy current $\mathbf{j}_E$ to linear order, but only $\mathbf{j} = n\mathbf{u} + \delta\mathbf{j}$ and $\mathbf{j}_I = n_I\mathbf{u} + \delta\mathbf{j}_I$, which, at charge neutrality and in linear response, are given by

$$\delta\mathbf{j} = \frac{1}{e^2\tilde{R}}\left[e\mathbf{E} + \omega_B\mathbf{e}_B\times\left(\frac{\alpha_1\delta_I\nabla\mu_I}{\tau_{\rm dis}^{-1}+\delta_I^{-1}\tau_{22}^{-1}} - \frac{2T\ln 2}{v_g^2}\mathbf{u}\right)\right], \tag{6.4a}$$

$$\delta\mathbf{j}_I = -\frac{\delta_I}{\tau_{\rm dis}^{-1}+\delta_I^{-1}\tau_{22}^{-1}}\frac{1}{e^2\tilde{R}}\times\left[\alpha_1\omega_B\mathbf{e}_B\times e\mathbf{E} + \frac{2T\ln 2}{\pi}e^2R_0\nabla\mu_I + \alpha_1\omega_B^2\frac{2T\ln 2}{v_g^2}\mathbf{u}\right],$$

where the resistivity $\tilde{R}$ is given by

$$\tilde{R} = R_0 + \alpha_1^2\delta_I\tilde{R}_B. \tag{6.4b}$$

From the integrated collision integrals due to electron-electron interaction, one obtains timescales τ_{11} and τ_{22}. These do not enter in the sense of a relaxation time approximation. They are given by [231]

$$\tau_{11(22)} = \frac{4\pi\ln 2 t_{11(22)}}{\alpha_g^2 T}, \tag{6.5}$$

$$t_{11} \approx \frac{1}{33.13}, \quad t_{11} \approx \frac{1}{5.45} \tag{6.6}$$

We further need the constants $\delta_I \approx 0.28$ and $\alpha_1 = 2.08$ and

$$R_0 = \frac{\pi}{2\ln 2}\frac{1}{e^2T}\left(\frac{1}{\tau_{11}} + \frac{1}{\tau_{\rm dis}}\right), \tag{6.7}$$

$$\tilde{R}_B = \frac{\pi}{2e^2T\ln 2}\frac{\omega_B^2}{\tau_{\rm dis}^{-1} + \delta_I^{-1}\tau_{22}^{-1}}. \tag{6.8}$$

At $B = 0$ one can find $\mathbf{u}$, $\delta\mathbf{j}$, $\mathbf{E}$, μ_I and δP rather easily. First a look at Eq. (6.3d) reveals, that the fluid remains compressible in linear response and energy relaxation $\tau_{\rm RE}$ introduces a term similar to a bulk viscosity. Next one excludes δP from Eq. (6.3c) by use of Eq. (6.3d). This leads to a second order differential equation for $\mathbf{u}$

$$\eta'\Delta\mathbf{u} = 3P\frac{\mathbf{u}}{v_g^2\tau_{\rm dis}}, \quad \eta' = \eta + \frac{3P\tau_{\rm RE}}{2}, \tag{6.9}$$

which is of the form of the standard Navier-Stokes equation, but with a renormalized viscosity. While in general $\Delta\mathbf{u} = \nabla(\nabla\cdot\mathbf{u}) - \nabla\times(\nabla\times\mathbf{u})$, the cross product term vanishes for radial symmetry and $B = 0$ and hence we can directly combine $\tau_{\rm RE}$ and the viscosity η. In radial symmetry, the general solution for the radial component has the form

$$u_r = a_1 I_1\left(\frac{r}{\ell_{\rm GE}}\right) + a_2 K_1\left(\frac{r}{\ell_{\rm GE}}\right), \quad \ell_{\rm GE}^2 = \frac{v_g^2\eta'\tau_{\rm dis}}{3P}, \tag{6.10}$$

where I_1 and K_1 are Bessel functions. Here one notices the characteristic lengthscale $\ell_{\rm GE}$. Hydrodynamic transport is usually characterized by a different characteristic lengthscale $\ell_G^2 = \frac{v_g^2\eta\tau_{\rm dis}}{3P}$, which

is known as the Gurzhi length [208]. By comparison one notices, that ℓ_{GE} corresponds to a corrected Gurzhi length that is renormalized by energy relaxation processes with τ_{RE}. The coefficients will be fixed by requiring continuity of entropy current at the interface.

The non-equilibrium quantities δP and μ_I can now be found easily. The pressure δP follows by using solution (6.10) in Eq. (6.3d) and μ_I can be found by substituting Eq. (6.4b) into Eq. (6.3b) and using solution (6.10). Their coefficients are fixed by requiring continuity of charge and imbalance current. From their combination we find δT. The details of this calculation are given in Secs. 6.3.1, 6.3.2 and 6.3.3 and the full solution is given in Sec. 6.3.4.

In order to determine the two-terminal resistance R we also need the behavior of the electrochemical potential ϕ at the interface. Traditionally, this behavior is dominated by a contact resistance, that depends on the used materials and their mismatch of chemical potential. Here, viscosity provides another channel of dissipation, that leads to a jump of ϕ at the interface discussed in Sec. 6.4.

6.3.1 Charge neutral Corbino disk at $B = 0$

Independent, of whether one applies a perpendicular magnetic field or no magnetic field, rotational symmetry will be preserved, and we may most easily solve the problem in polar coordinates (r, ϑ). Then, all quantities can only depend on the radial component r and for the case of zero magnetic field considered here, the hydrodynamic equations (6.2) can be transformed to

$$\frac{1}{r}\frac{\partial(r\delta j_r)}{\partial r} = 0, \tag{6.11a}$$

$$n_{I,0}\frac{1}{r}\frac{\partial(ru_r)}{\partial r} + \frac{1}{r}\frac{\partial(r\delta j_{Ir})}{\partial r} = -\frac{12\ln 2}{\pi^2}\frac{n_{I,0}\mu_I(r)}{T\tau_R}, \tag{6.11b}$$

$$u_\vartheta = 0, \tag{6.11c}$$

$$\frac{\partial\delta P}{\partial r} = \eta\partial_r\left(\frac{1}{r}\frac{\partial(ru_r)}{\partial r}\right) - \frac{3Pu_r}{v_g^2\tau_{\mathrm{dis}}}, \tag{6.11d}$$

$$3P\frac{1}{r}\frac{\partial(ru_r)}{\partial r} = -\frac{2\delta P(r)}{\tau_{RE}}. \tag{6.11e}$$

The electric field $\mathbf{E}$ does not enter the hydrodynamic equations at all in the case of charge neutrality, the current within the sample is carried solely by the dissipative correction $\delta\mathbf{j}$. Instead, the pressure δP enters in a very similar fashion, which corresponds to the replacement $-en\phi \to \delta P$. A similar term is also present away from charge neutrality, as mentioned for example in Refs. [232], but there it is usually either neglected (by assuming constant density n, temperature T and chemical potential μ in the sample), or argued away based on the fact, that one usually measures voltages and not pressures in these samples.

However, as we show here, it is very much not clear, how one should distribute the obtained results between the voltage part $en\phi$ and the pressure part δP away from charge neutrality, if one does allow for these variations. This also becomes clear in Ref. [220], where only the case $n = 0$ for the whole device is considered.

All angular components like u_ϑ have to vanish in the absence of a magnetic field and the dissipative corrections are

$$\delta j_r = \frac{E_r(r)}{eR_0} \tag{6.12a}$$

$$\delta j_\vartheta = 0 \tag{6.12b}$$

$$\delta j_{Ir} = -\frac{\delta_I}{\tau_{\rm dis}^{-1}+\delta_I^{-1}\tau_{22}^{-1}}\frac{2T\ln 2}{\pi}\frac{\partial \mu_I}{\partial r}, \tag{6.12c}$$

$$\delta j_{I\vartheta} = 0 \tag{6.12d}$$

At $B = 0$ the stress tensor, including a finite viscosity, which in the hydrodynamic regime is caused by electron-electron interaction, is given by

$$\Pi_E = P - \sigma, \tag{6.13}$$

$$\sigma = \eta\left[(\partial_x u_x - \partial_y u_y)\tau_z + (\partial_x u_y + \partial_y u_x)\tau_x\right], \tag{6.14}$$

$$\sigma_{rr} = -\sigma_{\vartheta\vartheta} = \eta\left(\partial_r - \frac{1}{r}\right)u_r, \quad \sigma_{r\vartheta} = \sigma_{\vartheta r} = \eta\left(\partial_r - \frac{1}{r}\right)u_\vartheta, \tag{6.15}$$

where the last line is the second one in polar coordinates. In the graphene bulk at charge neutrality, Hall viscosity η_H vanishes. Similarly Hall viscosity also vanishes for $B = 0$.

6.3.2 Description of leads

The donut shaped leads, which are attached at the inner and outer radius of the Corbino disk, are assumed to be a normal metal, in which transport is dominated by disorder scattering, with a relaxation time τ_L. For concreteness sake, we consider them to be made of graphene as well, which has however a large density and $\mu \gg T$, in which case we may restrict ourselves to one band. As is demonstrated in Ref. [186] and was discussed in Sec. 5.3.1, one can find continouity equations from the Boltzmann equation, also in the disorder dominated regime. The corresponding distribution function $f(\mathbf{r}, \mathbf{k}, t) = f_0(\varepsilon_k) - f_0'(\varepsilon_k)\mathcal{F}(\mathbf{r}, \theta_k, t)$ does however not fulfill the notion of a local equilibrium, as it would in the hydrodynamic regime. Instead, from the Fourier decomposition of $\mathcal{F}(\mathbf{r}, \theta_k, t)$ and their connection to the macroscopic quantities n_L, $\mathbf{j}$ and Π_E, we find the following set of equations

$$\partial_t n_L + \nabla \mathbf{j} = 0 \tag{6.16}$$

$$m\partial_t \mathbf{j} + \nabla \check{\Pi}_E - e n_L \mathbf{E} - \frac{e}{c}\mathbf{j}\times\mathbf{B} = -\frac{m}{\tau_L}\mathbf{j}, \tag{6.17}$$

$$\check{\Pi}_E = P - \check{\sigma}, \quad \eta_L = \frac{\mu^3 \tau_L}{4\pi v_g^2 \hbar^2}, \tag{6.18}$$

where σ has the same form as in Eq. (6.15), but with the disorder induced viscosity η_L.

In this disorder dominated regime, one can not speak of a hydrodynamic velocity $\mathbf{u}$, but one may still introduce a drift velocity $\mathbf{u}_L$, which then fulfills $\mathbf{j} = n_L \mathbf{u}_L$. The effective mass $m = \mu_L / v_g^2$ can then be used, to construct a momentum current density

$$m\mathbf{j} = \frac{3P_L}{v_g^2}\mathbf{u}_L, \tag{6.19}$$

where to lowest order in temperature we find $P_L = \frac{\mu^3}{3\pi v_g^2 \hbar^2}$ and thus in the stationary state at $B = 0$ in linear order of the current I

$$\nabla \mathbf{u}_L = 0, \tag{6.20}$$

$$\nabla \check{\Pi}_E + e n_L \nabla \phi = -\frac{3P_L}{v_g^2 \tau_L}\mathbf{u}_L. \tag{6.21}$$

Experimentally, the density n_L and the chemical potential μ are fixed by the gates. Moreover, leads are usually assumed equilibrate very fast, so that we can assume T to be fixed in the leads as well The general variation of P_L is found to be

$$\delta P_L = \left(\frac{2\pi\mu T \delta T}{3v_g^2} + \frac{\pi T^2 \delta\mu}{3v_g^2} + \frac{\mu^2 \delta\mu}{\pi v_g^2} \right) \tag{6.22}$$

and thus vanishes under the condition we consider. Since the leads are highly doped, we find $n = n_+ = n_I$, while the imbalance chemical potential μ_I vanishes.

6.3.3 Boundary conditions

The differential equations (6.11) and (6.12) should be supplemented by a suitable set of boundary conditions. One should note, that the Corbino setup is indeed a special setup in this perspective, since there are no interfaces to the vacuum, but only to the leads. As can be seen from Eq. (6.2a), charge conservation is exact and also holds in the leads. This implies

$$j_r(r_1 - \epsilon) = \delta j_r(r_1 + \epsilon), \quad \delta j_r(r_2 - \epsilon) = j_r(r_2 + \epsilon) \tag{6.23}$$

and we further find in a radially symmetric system by fixing the total current I

$$I = e \int \mathrm{d}\mathbf{A} \cdot \mathbf{j} = 2\pi e r j_r. \tag{6.24}$$

Further we assume, that none of the τs diverge at the interface and thus find, that the radial components imbalance current $j_{I,r}$ and entropy current su_r are conserved across the interface as well. For the interface r_1 this means

$$j_r(r_1 - \epsilon) = n_L u_r(r_1 - \epsilon) = \delta j_r(r_1 + \epsilon), \tag{6.25}$$
$$j_{I,r}(r_1 - \epsilon) = n_L u_r(r_1 - \epsilon) = n_{I,0} u_r(r_1 + \epsilon) + \delta j_{I,r}(r_1 + \epsilon) = \delta j_r(r_1 + \epsilon), \tag{6.26}$$
$$s_L u_r(r_1 - \epsilon) = s_B u_r(r_1 + \epsilon) \tag{6.27}$$

and similarly at the second interface

$$j_r(r_2 + \epsilon) = n_L u_r(r_2 + \epsilon) = \delta j_r(r_2 - \epsilon), \tag{6.28}$$
$$j_{I,r}(r_2 + \epsilon) = n_L u_r(r_2 + \epsilon) = n_{I,0} u_r(r_2 - \epsilon) + \delta j_{I,r}(r_2 - \epsilon) = \delta j_r(r_2 - \epsilon), \tag{6.29}$$
$$s_L u_r(r_2 + \epsilon) = s_B u_r(r_2 - \epsilon). \tag{6.30}$$

Notably, the imbalance current and the entropy current are not conserved within the sample, due to recombination processes and energy relaxation.

With these conditions, we can completely find the hydrodynamic quantities and their related counterparts in the leads.

6.3.4 Solutions

Starting with the leads, we find

$$u_{L,r} = \frac{I}{2\pi e n_L r}, \quad u_{L,\vartheta} = 0, \tag{6.31}$$

$$\sigma_{rr} = \frac{-I\eta_L}{\pi e n_L r^2}, \quad \sigma_{r\vartheta} = 0, \tag{6.32}$$

$$E_r = \frac{2P_L}{e n_L v_g^2 \tau_L} \frac{I}{2\pi e n_L r}, \tag{6.33}$$

$$\phi(r) = -\frac{I}{2\pi} \frac{2P_L}{e^2 n_L^2 v_g^2 \tau_L} \log\left(\frac{r}{r_0}\right). \tag{6.34}$$

With the found form of $u_{L,r}$ and the assumption $\delta P = 0$ we find a simple $1/r$ behavior for the electrical field E_r as well. Notably, we then indeed find a constant charge density inside the leads from the Poisson equation. While the disorder dominated viscosity η_L does not enter the electric field, the viscous stress tensor itself is not zero, which will be relevant later.

The entropy s is always defined as

$$Ts = 3P - \mu n - \mu_I n_I. \tag{6.35}$$

For $\mu \gg T$ we find

$$P_L = \frac{\pi T^2 \mu}{3v_g^2} + \frac{\mu^3}{3\pi v_g^2} = P_L^T + P_L^{T=0}, \tag{6.36}$$

$$n = \frac{\pi T^2}{3v_g^2} + \frac{\mu^2}{\pi v_g^2} \tag{6.37}$$

$$s_L T = 3P - n\mu = \frac{\pi T^2 \mu}{v_g^2} + \frac{\mu^3}{\pi v_g^2} - \frac{\pi T^2 \mu}{3v_g^2} - \frac{\mu^3}{\pi v_g^2} = \frac{2}{3}\frac{\pi T^2 \mu}{v_g^2} = 2P_L^T, \tag{6.38}$$

so we need to keep finite temperature corrections in the leads as well.

In the graphene sample, the situation is a bit more involved. Firstly, one notices, that the differential equations (6.11) and (6.12) decouple into two disjunct sets. The first one consists of equations (6.11a) and(6.12a), which has the solution

$$\delta j_r = \frac{I}{2\pi e r}, \tag{6.39}$$

$$E_r = \frac{IR_0}{2\pi r}, \quad \phi = -\frac{IR_0}{2\pi} \log\left(\frac{r}{r_0}\right). \tag{6.40}$$

The constant r_0, which is also present in the leads (and not necessarily the same) is not fixed by the boundary conditions we have imposed so far. For the entropy s we find in the sample

$$Ts = 3P = 3\frac{3T^3\zeta(3)}{\pi v_g^2}. \tag{6.41}$$

The second set of equations consists of (6.11b), (6.11d), (6.11e) and (6.12c). We immediately find, expressing δP through u_r

$$0 = \partial_r \left(\frac{1}{r} \frac{\partial (r u_r)}{\partial r} \right) - \frac{u_r}{\ell_{\mathrm{GE}}^2} \tag{6.42}$$

$$\frac{1}{\ell_{\mathrm{GE}}^2} = \left(\eta + \frac{3 P \tau_{RE}}{2} \right)^{-1} \frac{3P}{v_g^2 \tau_{\mathrm{dis}}}. \tag{6.43}$$

This shows, that for this set of equations it is usually the combination $\eta' = \left(\eta + \frac{3P\tau_{RE}}{2} \right)$ that enters, i.e. the Gurzhi length is renormalized by τ_{RE}. The other two equations can be combined to form

$$\partial_r \left(\frac{1}{r} \frac{\partial (r u_r)}{\partial r} \right) - M \partial_r \left(\frac{1}{r} \frac{\partial (r \frac{\partial \mu_I}{\partial r})}{\partial r} \right) = - \frac{M}{\ell_R^2} \frac{\partial \mu_I(r)}{\partial r} \tag{6.44}$$

$$M = \frac{2T \ln 2}{n_{I,0} \pi} \frac{\delta_I}{\tau_{\mathrm{dis}}^{-1} + \delta_I^{-1} \tau_{22}^{-1}}, \quad \ell_R^2 = \frac{\delta_I}{\tau_{\mathrm{dis}}^{-1} + \delta_I^{-1} \tau_{22}^{-1}} \frac{\pi T^2 \tau_R}{6 n_{I,0}}. \tag{6.45}$$

Thus we are left with a set of two coupled Bessel differential equations for u_r and $\partial_r \mu_I$. Defining the differential operator $\mathbb{D} = \partial_r (1/r) \partial_r r$ we can write this system as

$$\mathbb{D} \begin{pmatrix} 1 & 0 \\ 1 & -M \end{pmatrix} \begin{pmatrix} u_r \\ \frac{\partial \mu_I}{\partial r} \end{pmatrix} = \begin{pmatrix} \frac{1}{\ell_{\mathrm{GE}}^2} & 0 \\ 0 & -\frac{M}{\ell_R^2} \end{pmatrix} \begin{pmatrix} u_r \\ \frac{\partial \mu_I}{\partial r} \end{pmatrix} \Leftrightarrow \mathbb{D} \begin{pmatrix} u_r \\ \frac{\partial \mu_I}{\partial r} \end{pmatrix} = \begin{pmatrix} \frac{1}{\ell_{\mathrm{GE}}^2} & 0 \\ \frac{1}{M \ell_{\mathrm{GE}}^2} & \frac{1}{\ell_R^2} \end{pmatrix} \begin{pmatrix} u_r \\ \frac{\partial \mu_I}{\partial r} \end{pmatrix}. \tag{6.46}$$

Once we write

$$\begin{pmatrix} \frac{1}{\ell_{\mathrm{GE}}^2} & 0 \\ \frac{1}{M \ell_{\mathrm{GE}}^2} & \frac{1}{\ell_R^2} \end{pmatrix} = \hat{U}^{-1} \hat{D} \hat{U} \tag{6.47}$$

and $\hat{D}$ is diagonal with eigenvalues d_1 and d_2 (with units of inverse length squared). This coupled Bessel differential equation then has the general solution

$$u_r = M \left(1 - \frac{\ell_{\mathrm{GE}}^2}{\ell_R^2} \right) \left[f_1 I_1 \left(\frac{r}{\ell_{\mathrm{GE}}} \right) + f_2 K_1 \left(\frac{r}{\ell_{\mathrm{GE}}} \right) \right] \tag{6.48}$$

$$\frac{\partial \mu_I}{\partial r} = f_1 I_1 \left(\frac{r}{\ell_{\mathrm{GE}}} \right) + f_2 K_1 \left(\frac{r}{\ell_{\mathrm{GE}}} \right) + g_1 I_1 \left(\frac{r}{\ell_R} \right) + g_2 K_1 \left(\frac{r}{\ell_R} \right), \tag{6.49}$$

where the coefficients f_1, f_2, g_1 and g_2 still need to be fixed. From the conservation of entropy current Eq. (6.27) and (6.30) we then find f_1 and f_2 and thus

$$u_r = \frac{I s_L}{2\pi e n_L s_B} \times \left\{ \frac{I_1 \left(\frac{r}{\ell_{\mathrm{GE}}} \right) \left(r_1 K_1 \left(\frac{r_1}{\ell_{\mathrm{GE}}} \right) - r_2 K_1 \left(\frac{r_2}{\ell_{\mathrm{GE}}} \right) \right) - K_1 \left(\frac{r}{\ell_{\mathrm{GE}}} \right) \left(r_1 I_1 \left(\frac{r_1}{\ell_{\mathrm{GE}}} \right) - r_2 I_1 \left(\frac{r_2}{\ell_{\mathrm{GE}}} \right) \right)}{r_1 r_2 K_1 \left(\frac{r_1}{\ell_{\mathrm{GE}}} \right) I_1 \left(\frac{r_2}{\ell_{\mathrm{GE}}} \right) - r_1 r_2 I_1 \left(\frac{r_1}{\ell_{\mathrm{GE}}} \right) K_1 \left(\frac{r_2}{\ell_{\mathrm{GE}}} \right)} \right\}. \tag{6.50}$$

This leads to the stress tensor element

$$\sigma_{rr} = \frac{\eta I s_L}{2\pi e \ell_{\mathrm{GE}} n_L s_B} \frac{I_2\left(\frac{r}{\ell_{\mathrm{GE}}}\right)\left(r_1 K_1\left(\frac{r_1}{\ell_{\mathrm{GE}}}\right) - r_2 K_1\left(\frac{r_2}{\ell_{\mathrm{GE}}}\right)\right) + K_2\left(\frac{r}{\ell_{\mathrm{GE}}}\right)\left(r_1 I_1\left(\frac{r_1}{\ell_{\mathrm{GE}}}\right) - r_2 I_1\left(\frac{r_2}{\ell_{\mathrm{GE}}}\right)\right)}{r_1 r_2\left(K_1\left(\frac{r_1}{\ell_{\mathrm{GE}}}\right) I_1\left(\frac{r_2}{\ell_{\mathrm{GE}}}\right) - I_1\left(\frac{r_1}{\ell_{\mathrm{GE}}}\right) K_1\left(\frac{r_2}{\ell_{\mathrm{GE}}}\right)\right)}, \tag{6.51}$$

$$\sigma_{r\vartheta} = 0 \tag{6.52}$$

and

$$\delta P = -\frac{3P\tau_{\mathrm{RE}}}{2}\frac{1}{r}\frac{\partial(r u_r)}{\partial r} = -\frac{3P\tau_{\mathrm{RE}}}{2}\frac{I s_L}{2\pi e \ell_{\mathrm{GE}} n_L s_B} \times \left[\frac{K_0\left(\frac{r}{\ell_{\mathrm{GE}}}\right)\left(r_1 I_1\left(\frac{r_1}{\ell_{\mathrm{GE}}}\right) - r_2 I_1\left(\frac{r_2}{\ell_{\mathrm{GE}}}\right)\right) + I_0\left(\frac{r}{\ell_{\mathrm{GE}}}\right)\left(r_1 K_1\left(\frac{r_1}{\ell_{\mathrm{GE}}}\right) - r_2 K_1\left(\frac{r_2}{\ell_{\mathrm{GE}}}\right)\right)}{r_1 r_2 K_1\left(\frac{r_1}{\ell_{\mathrm{GE}}}\right) I_1\left(\frac{r_2}{\ell_{\mathrm{GE}}}\right) - r_1 r_2 I_1\left(\frac{r_1}{\ell_{\mathrm{GE}}}\right) K_1\left(\frac{r_2}{\ell_{\mathrm{GE}}}\right)}\right], \tag{6.53}$$

Using the conservation of the imbalance current Eqs. (6.26) and (6.29) we further find the imbalance chemical potential

$$\begin{aligned}\mu_I(r) = \frac{I s_L \ell_R}{2\pi e M n_L r_1 r_2 s_B (\ell_{\mathrm{GE}}^2 - \ell_R^2)} \Bigg[&\frac{K_0\left(\frac{r}{\ell_R}\right)\left(r_1 I_1\left(\frac{r_1}{\ell_R}\right) - r_2 I_1\left(\frac{r_2}{\ell_R}\right)\right)\left(\ell_{\mathrm{GE}}^2 + (\ell_R^2 - \ell_{\mathrm{GE}}^2)\frac{n_L}{n_{I,0}}\frac{s_B}{s_L}\right)}{K_1\left(\frac{r_1}{\ell_R}\right) I_1\left(\frac{r_2}{\ell_R}\right) - I_1\left(\frac{r_1}{\ell_R}\right) K_1\left(\frac{r_2}{\ell_R}\right)} \\ &+ \frac{I_0\left(\frac{r}{\ell_R}\right)\left(r_1 K_1\left(\frac{r_1}{\ell_R}\right) - r_2 K_1\left(\frac{r_2}{\ell_R}\right)\right)\left(\ell_{\mathrm{GE}}^2 + (\ell_R^2 - \ell_{\mathrm{GE}}^2)\frac{n_L}{n_{I,0}}\frac{s_B}{s_L}\right)}{K_1\left(\frac{r_1}{\ell_R}\right) I_1\left(\frac{r_2}{\ell_R}\right) - I_1\left(\frac{r_1}{\ell_R}\right) K_1\left(\frac{r_2}{\ell_R}\right)} \\ &+ \frac{\ell_{\mathrm{GE}}\ell_R K_0\left(\frac{r}{\ell_{\mathrm{GE}}}\right)\left(r_2 I_1\left(\frac{r_2}{\ell_{\mathrm{GE}}}\right) - r_1 I_1\left(\frac{r_1}{\ell_{\mathrm{GE}}}\right)\right)}{K_1\left(\frac{r_1}{\ell_{\mathrm{GE}}}\right) I_1\left(\frac{r_2}{\ell_{\mathrm{GE}}}\right) - I_1\left(\frac{r_1}{\ell_{\mathrm{GE}}}\right) K_1\left(\frac{r_2}{\ell_{\mathrm{GE}}}\right)} + \frac{\ell_{\mathrm{GE}}\ell_R I_0\left(\frac{r}{\ell_{\mathrm{GE}}}\right)\left(r_2 K_1\left(\frac{r_2}{\ell_{\mathrm{GE}}}\right) - r_1 K_1\left(\frac{r_1}{\ell_{\mathrm{GE}}}\right)\right)}{K_1\left(\frac{r_1}{\ell_{\mathrm{GE}}}\right) I_1\left(\frac{r_2}{\ell_{\mathrm{GE}}}\right) - I_1\left(\frac{r_1}{\ell_{\mathrm{GE}}}\right) K_1\left(\frac{r_2}{\ell_{\mathrm{GE}}}\right)} \Bigg]\end{aligned} \tag{6.54}$$

and the dissipative correction to the imbalance current

$$\begin{aligned}\delta j_{Ir}(r) = \frac{I n_{I,0} s_L}{2\pi e n_L r_1 r_2 s_B \left(\ell_{\mathrm{GE}}^2 - \ell_R^2\right)} \Bigg[&\frac{K_1\left(\frac{r}{\ell_R}\right)\left(r_1 I_1\left(\frac{r_1}{\ell_R}\right) - r_2 I_1\left(\frac{r_2}{\ell_R}\right)\right)\left(\ell_{\mathrm{GE}}^2 + (\ell_R^2 - \ell_{\mathrm{GE}}^2)\frac{n_L}{n_{I,0}}\frac{s_B}{s_L}\right)}{K_1\left(\frac{r_1}{\ell_R}\right) I_1\left(\frac{r_2}{\ell_R}\right) - I_1\left(\frac{r_1}{\ell_R}\right) K_1\left(\frac{r_2}{\ell_R}\right)} \\ &- \frac{I_1\left(\frac{r}{\ell_R}\right)\left(r_1 K_1\left(\frac{r_1}{\ell_R}\right) - r_2 K_1\left(\frac{r_2}{\ell_R}\right)\right)\left(\ell_{\mathrm{GE}}^2 + (\ell_R^2 - \ell_{\mathrm{GE}}^2)\frac{n_L}{n_{I,0}}\frac{s_B}{s_L}\right)}{K_1\left(\frac{r_1}{\ell_R}\right) I_1\left(\frac{r_2}{\ell_R}\right) - I_1\left(\frac{r_1}{\ell_R}\right) K_1\left(\frac{r_2}{\ell_R}\right)} \\ &+ \frac{\ell_R^2 K_1\left(\frac{r}{\ell_{\mathrm{GE}}}\right)\left(r_1 I_1\left(\frac{r_1}{\ell_{\mathrm{GE}}}\right) - r_2 I_1\left(\frac{r_2}{\ell_{\mathrm{GE}}}\right)\right)}{K_1\left(\frac{r_1}{\ell_{\mathrm{GE}}}\right) I_1\left(\frac{r_2}{\ell_{\mathrm{GE}}}\right) - I_1\left(\frac{r_1}{\ell_{\mathrm{GE}}}\right) K_1\left(\frac{r_2}{\ell_{\mathrm{GE}}}\right)} + \frac{\ell_R^2 I_1\left(\frac{r}{\ell_{\mathrm{GE}}}\right)\left(r_2 K_1\left(\frac{r_2}{\ell_{\mathrm{GE}}}\right) - r_1 K_1\left(\frac{r_1}{\ell_{\mathrm{GE}}}\right)\right)}{K_1\left(\frac{r_1}{\ell_{\mathrm{GE}}}\right) I_1\left(\frac{r_2}{\ell_{\mathrm{GE}}}\right) - I_1\left(\frac{r_1}{\ell_{\mathrm{GE}}}\right) K_1\left(\frac{r_2}{\ell_{\mathrm{GE}}}\right)} \Bigg].\end{aligned} \tag{6.55}$$

From δP and μ_I we find δT, which amounts to

$$\delta T = \frac{\pi v_g^2}{9T^2\zeta(3)}\delta P - \frac{\pi^2}{27\zeta(3)}\mu_I. \tag{6.56}$$

Our hydrodynamic system is not characterized by a local thermal conductivity κ, that relates the heat current

$$\mathbf{j}_Q(r) = 3P\mathbf{u} - \mu\mathbf{j} - \mu_I\mathbf{j}_I \tag{6.57}$$

and the temperature gradient $\nabla\delta T(r)$ at the same point r. Instead, we can obtain a non-local (integral) relation between $\mathbf{j}_Q(r)$ and $\nabla\delta T(r')$ characterized by a non-local kernel $\kappa(r, r')$. This follows from the fact that the equation for $\mathbf{u}(r)$ is now a second-order differential equation with a non-local Green's function. Expressing $\delta P(r)$ there in terms of $\delta T(r)$ and $\mu_I(r)$, we have a non-local relation between $\mathbf{u}(r)$, $\delta T(r')$ and $\nabla\mu_I(r')$. Substituting this $\mathbf{u}(r)$ into the definition of $\mathbf{j}_Q(r)$, we obtain a non-local thermal conductivity. As a result one can only introduce the thermal conductance for the whole setup, relating the temperature difference between the contacts with the total heat current through the system. This will be done in a subsequent publication.

6.4 Dissipation and total resistance

This still does not suffice to describe the resistance between the point r_{in} and r_{out} in the inner and outer lead respectively, since we do not know, how the potential ϕ behaves at the interface. In general the contact resistance between two materials is a manifestation of their different work functions and a mismatch of their chemical potential. We already saw, that this contribution can be large in clean samples in Chapter 5. However, there is an additional effect due to electron-electron interaction, which in the ballistic case may give rise to a "Knudsen-Poiseuille" crossover [208] and drive the electronic system to the hydrodynamic regime. This hydrodynamic flow possesses another channel for dissipation through viscosity [232]. At charge neutrality, this effect is subtle, since the electric current is decoupled from the hydrodynamic energy flow, but both are induced by the current source providing the energy dissipated not only by Ohmic effects, but also by viscosity [232] and energy relaxation processes [233] that should be taken into account in the form of an additional voltage drop.

For this, we generalize the idea proposed by Ref. [232] and take a look at the dissipation, since energy should not accumulate directly at the interface. While the ohmic resistivity alone may be small, energy is also dissipated by viscosity and energy relaxation. Since the electric field inside the sample is completely determined by R_0, this additional dissipation channels appear in form of a jump directly at the interface. Microscopically, this jump in voltage is due to an excess electric field in the Knudsen layer around the interface.

To find the magnitude of the jump, we consider the kinetic energy. The kinetic energy can be generally found from the energy density,

$$\mathcal{E} = \int \mathrm{d}V \left(n_E - n_E(\mathbf{u}=0)\right) \approx \int \mathrm{d}V \frac{6P}{v_g^2}\mathbf{u}^2 \tag{6.58}$$

where we have expanded to second order in $\mathbf{u}$ and thus the drive I. Thus the dissipation is

$$\mathcal{A} = \dot{\mathcal{E}} = 2\frac{6P}{v_g^2}\int \mathrm{dV}\mathbf{u}\partial_t\mathbf{u} = 0, \tag{6.59}$$

since we are in the steady state. This can be simplified by use of the generalized Navier-Stokes equation. At a finite density we find in the leads

$$\begin{aligned}\frac{3P_L}{v_g^2}\mathbf{u}\partial_t\mathbf{u} &= \mathbf{u}\left(-\frac{3P_L}{v_g^2}\frac{\mathbf{u}}{\tau_L} - \nabla\Pi_E + n_L e\mathbf{E}\right)\\ &= -\frac{3P_L}{v_g^2}\frac{\mathbf{u}^2}{\tau_L} - \nabla\delta P\mathbf{u} + \mathbf{u}\nabla\sigma' - e\mathbf{j}\nabla\phi.\\ &= -\frac{3P}{v_g^2}\frac{\mathbf{u}^2}{\tau_L} - \frac{\partial u_i}{\partial x_j}\sigma'_{ij} + \nabla\left(\mathbf{u}\sigma' - e\mathbf{j}\phi - \mathbf{u}\delta P\right). \end{aligned} \tag{6.60}$$

Here we recognize, that the term $en_L\mathbf{u}\mathbf{E} = e\mathbf{j}\mathbf{E}$ is exactly the Joule heating. Using the divergence theorem we can divide this into a boundary and a bulk term

$$0 = \mathcal{A} = \mathcal{A}_{\text{boundary}} - \mathcal{A}_{\text{bulk}}, \tag{6.61}$$

$$\mathcal{A}_{\text{boundary}} = 4\int \mathrm{d}\mathbf{A}\left(\mathbf{u}\sigma' - \mathbf{u}\delta P - e\mathbf{j}\phi\right), \tag{6.62}$$

$$\mathcal{A}_{\text{bulk}} = 4\int \mathrm{d}V\left(\frac{3P}{v_g^2}\frac{\mathbf{u}^2}{\tau_L} + \frac{\partial u_i}{\partial x_j}\sigma'_{ij}\right). \tag{6.63}$$

The boundary term includes the energy, that is transmitted through the interface.

Since the current density is conserved at the interface, we can immediately write down the corresponding equation in the neutral graphene sample, where the Joule heating is given by $e\delta\mathbf{j}\mathbf{E}$. Then we find

$$0 = \mathcal{A} = \mathcal{A}_{\text{boundary}} - \mathcal{A}_{\text{bulk}}, \tag{6.64}$$

$$\mathcal{A}_{\text{boundary}} = 4\int \mathrm{d}\mathbf{A}\left(\mathbf{u}\sigma' - \mathbf{u}\delta P - e\delta\mathbf{j}\phi\right), \tag{6.65}$$

$$\mathcal{A}_{\text{bulk}} = 4\int \mathrm{d}V\left(\frac{3P}{v_g^2}\frac{\mathbf{u}^2}{\tau_{\text{dis}}} + \delta\mathbf{j}e\mathbf{E} + \frac{\partial u_i}{\partial x_j}\sigma'_{ij} - \delta P(\nabla\cdot\mathbf{u})\right). \tag{6.66}$$

As stated above, under realistic experimental conditions the non-equilibrium part of the pressure at $u = 0$ on the lead side vanishes

$$\delta P = 0 \tag{6.67}$$

while we find on the side of the graphene sample

$$\delta P = \left(\frac{9T^2\delta T\zeta(3)}{\pi v_g^2} + \frac{\pi\mu_I T^2}{3v_g^2}\right) = \frac{T^2}{v_g^2}\left(\frac{9\delta T\zeta(3)}{\pi} + \frac{\pi\mu_I}{3}\right). \tag{6.68}$$

Using the hydrodynamic equations one may replace δP by $\frac{-3P_B\tau_{\text{RE}}}{2}\frac{1}{r}\frac{\partial(ru_r)}{\partial r}$, thus for finite τ_{RE} δP is completely determined and does not require any additional boundary conditions. The same goes for μ_I. Thus we know the jump of δP at the interface and the viscous part of the dissipation will only enter the difference in electrochemical potential.

We require, that without any phenomenological contact resistance, energy does not accumulate at the interface. When we include this type of resistance, we additionally include the term

$$I^2 R_c = \mathbf{I}^T \check{R} \mathbf{I}, \tag{6.69}$$

where $\mathbf{I}$ includes charge and entropy current and $\check{R}$ includes the thermoelectric coefficients of the interface.

For $B = 0$ u_ϑ and $\sigma'_{r\vartheta}$ are both zero and in the leads we have $\delta P = 0$. Thus we find the condition

$$\begin{aligned} &4\pi \left[r \left(u_r \sigma'_{rr} \right) \right]_{r_1-\epsilon} - 2I\phi(r_1 - \epsilon) = 4\pi \left[r \left(u_r \sigma'_{rr} - u_r \delta P \right) \right]_{r_1+\varepsilon} - 2I\phi(r_1 + \epsilon) - 2\mathbf{I}^T \check{R} \mathbf{I} \\ &\Leftrightarrow \phi(r_1 - \epsilon) - \phi(r_1 + \epsilon) = \frac{2\pi}{I} \left\{ \left[r \left(u_r \sigma'_{rr} \right) \right]_{r_1-\epsilon} - \left[r \left(u_r \sigma'_{rr} - u_r \delta P \right) \right]_{r_1+\varepsilon} \right\} + I R_c \end{aligned} \tag{6.70}$$

at the first interface and analogously for the second interface

$$\begin{aligned} &4\pi \left[r \left(u_r \sigma'_{rr} - \delta P u_r \right) \right]_{r_2-\epsilon} - 2I\phi(r_2 - \epsilon) = 4\pi \left[r \left(u_r \sigma'_{rr} \right) \right]_{r_2+\varepsilon} - 2I\phi(r_2 + \epsilon) - 2\mathbf{I}^T \check{R} \mathbf{I} \\ &\Leftrightarrow \phi(r_2 - \epsilon) - \phi(r_2 + \epsilon) = -\frac{2\pi}{I} \left\{ \left[r \left(u_r \sigma'_{rr} \right) \right]_{r_2+\epsilon} - \left[r \left(u_r \sigma'_{rr} - u_r \delta P \right) \right]_{r_2-\varepsilon} \right\} + I R_c. \end{aligned} \tag{6.71}$$

Using the full solution we find in the bulk this includes the expression

$$\begin{aligned} \sigma'_{rr} - \delta P &= \frac{I s_L}{2\pi e \ell_{\mathrm{GE}} n_L s_B} \\ &\times \left[\eta \frac{I_2\left(\frac{r}{\ell_{\mathrm{GE}}}\right)\left(r_1 K_1\left(\frac{r_1}{\ell_{\mathrm{GE}}}\right) - r_2 K_1\left(\frac{r_2}{\ell_{\mathrm{GE}}}\right)\right) + K_2\left(\frac{r}{\ell_{\mathrm{GE}}}\right)\left(r_1 I_1\left(\frac{r_1}{\ell_{\mathrm{GE}}}\right) - r_2 I_1\left(\frac{r_2}{\ell_{\mathrm{GE}}}\right)\right)}{r_1 r_2 \left(K_1\left(\frac{r_1}{\ell_{\mathrm{GE}}}\right) I_1\left(\frac{r_2}{\ell_{\mathrm{GE}}}\right) - I_1\left(\frac{r_1}{\ell_{\mathrm{GE}}}\right) K_1\left(\frac{r_2}{\ell_{\mathrm{GE}}}\right)\right)} \right. \\ &\left. + \frac{3P\tau_{\mathrm{RE}}}{2} \frac{K_0\left(\frac{r}{\ell_{\mathrm{GE}}}\right)\left(r_1 I_1\left(\frac{r_1}{\ell_{\mathrm{GE}}}\right) - r_2 I_1\left(\frac{r_2}{\ell_{\mathrm{GE}}}\right)\right) + I_0\left(\frac{r}{\ell_{\mathrm{GE}}}\right)\left(r_1 K_1\left(\frac{r_1}{\ell_{\mathrm{GE}}}\right) - r_2 K_1\left(\frac{r_2}{\ell_{\mathrm{GE}}}\right)\right)}{r_1 r_2 \left(K_1\left(\frac{r_1}{\ell_{\mathrm{GE}}}\right) I_1\left(\frac{r_2}{\ell_{\mathrm{GE}}}\right) - I_1\left(\frac{r_1}{\ell_{\mathrm{GE}}}\right) K_1\left(\frac{r_2}{\ell_{\mathrm{GE}}}\right)\right)} \right] \end{aligned} \tag{6.72}$$

Then we find at r_1

$$r u_r(\sigma'_{rr} - \delta P) = \frac{I^2 s_L^2 \eta \ell_{\mathrm{GE}}}{4\pi^2 e^2 n_L^2 s_B^2 \ell_G^2} \frac{\ell_{\mathrm{GE}} - r_2 K_0\left(\frac{r_1}{\ell_{\mathrm{GE}}}\right) I_1\left(\frac{r_2}{\ell_{\mathrm{GE}}}\right) - r_2 I_0\left(\frac{r_1}{\ell_{\mathrm{GE}}}\right) K_1\left(\frac{r_2}{\ell_{\mathrm{GE}}}\right)}{r_1 r_2 \left(K_1\left(\frac{r_1}{\ell_{\mathrm{GE}}}\right) I_1\left(\frac{r_2}{\ell_{\mathrm{GE}}}\right) - I_1\left(\frac{r_1}{\ell_{\mathrm{GE}}}\right) K_1\left(\frac{r_2}{\ell_{\mathrm{GE}}}\right)\right)} - \frac{\eta I^2 s_L^2}{2\pi^2 e^2 n_L^2 r_1^2 s_B^2}$$

and at r_2

$$r u_r(\sigma'_{rr} - \delta P) = -\frac{I^2 s_L^2 \eta \ell_{\mathrm{GE}}}{4\pi^2 e^2 \ell_G^2 n_L^2 s_B^2} \frac{\ell_{\mathrm{GE}} - r_1 I_1\left(\frac{r_1}{\ell_{\mathrm{GE}}}\right) K_0\left(\frac{r_2}{\ell_{\mathrm{GE}}}\right) - r_1 K_1\left(\frac{r_1}{\ell_{\mathrm{GE}}}\right) I_0\left(\frac{r_2}{\ell_{\mathrm{GE}}}\right)}{r_1 r_2 \left(K_1\left(\frac{r_1}{\ell_{\mathrm{GE}}}\right) I_1\left(\frac{r_2}{\ell_{\mathrm{GE}}}\right) - I_1\left(\frac{r_1}{\ell_{\mathrm{GE}}}\right) K_1\left(\frac{r_2}{\ell_{\mathrm{GE}}}\right)\right)} - \frac{\eta I^2 s_L^2}{2\pi^2 e^2 n_L^2 r_2^2 s_B^2}.$$

Then we find the total resistance R of the system with

$$IR = \phi(r_{\text{in}}) - \phi(r_{\text{out}}) = I(R_L + R_B + 2R_C + R_L^{\text{diss}} + R_B^{\text{diss}}), \tag{6.73}$$

$$R_L = \frac{3P_L}{2\pi e^2 n_L^2 v_g^2 \tau_L} \log\left(\frac{r_1 r_{\text{out}}}{r_{\text{in}} r_2}\right), \quad R_B = \frac{R_0}{2\pi} \log\left(\frac{r_2}{r_1}\right), \tag{6.74}$$

$$R_C = \frac{\mathbf{I}^T \check{R} \mathbf{I}}{I^2}, \tag{6.75}$$

$$R_L^{\text{diss}} = \frac{\eta_L}{\pi e^2 n_L^2} \left(\frac{1}{r_2^2} - \frac{1}{r_1^2}\right) \tag{6.76}$$

$$R_B^{\text{diss}} = \frac{\eta s_L^2}{\pi e^2 n_L^2 s_B^2} \left\{ \frac{1}{r_1^2} - \frac{1}{r_2^2} + \frac{\ell_{\text{GE}}}{2\ell_G^2} \right. \tag{6.77}$$

$$\left. \times \frac{r_2\left[K_0\left(\frac{r_1}{\ell_{\text{GE}}}\right) I_1\left(\frac{r_2}{\ell_{\text{GE}}}\right) + I_0\left(\frac{r_1}{\ell_{\text{GE}}}\right) K_1\left(\frac{r_2}{\ell_{\text{GE}}}\right)\right] + r_1\left[I_1\left(\frac{r_1}{\ell_{\text{GE}}}\right) K_0\left(\frac{r_2}{\ell_{\text{GE}}}\right) + K_1\left(\frac{r_1}{\ell_{\text{GE}}}\right) I_0\left(\frac{r_2}{\ell_{\text{GE}}}\right)\right] - 2\ell_{\text{GE}}}{r_1 r_2 \left(K_1\left(\frac{r_1}{\ell_{\text{GE}}}\right) I_1\left(\frac{r_2}{\ell_{\text{GE}}}\right) - I_1\left(\frac{r_1}{\ell_{\text{GE}}}\right) K_1\left(\frac{r_2}{\ell_{\text{GE}}}\right)\right)} \right\}.$$

This is the central result of this chapter, which we now analyze in various relevant limits.

6.5 Analysis of results

The behavior of these quantities thus depends on the hierarchy of the length scales r_1, r_2, $r_2 - r_1$, ℓ_{GE} and ℓ_R. In order to remain inside the hydrodynamic regime, these cannot take on all values. In this section, we restore all units of $\hbar$ and k_B. We will show plots, which are obtained for the following quantities. The density in the leads is given by $n_L = 5 \times 10^{14}$ m^{-2} and the equilibrium temperature in the whole device, including the leads and the sample, is fixed to $T = 100$ K. The current, that is supplied by the source is $I = 1$ μA and we assume that the effective interaction constant is screened to $\alpha = 0.2$. We further use $\tau_{\text{dis}} = 1.25 \times 10^{-12}$ s and $\tau_L = 0.189 \times 10^{-12}$ s [12], since the density is higher in the leads. This is enough, to fix all the other parameters, except for τ_{RE} and τ_R or alternatively ℓ_{GE} and ℓ_R. Since these quantities are difficult to obtain, we will show plots for three different regimes.

The times related to electron-electron interaction are given by [231]

$$\tau_{ii} = \hbar \frac{4\pi \log 2 t_{ii}}{\alpha^2 k_B T}, \tag{6.78}$$

$$t_{11} = \frac{1}{33.13}, \quad t_{22} = \frac{1}{5.45}. \tag{6.79}$$

and for the used parameters we find $\tau_{11} = 0.5 \times 10^{-12}$ s and $\tau_{22} = 3 \times 10^{-12}$ s. The viscosity is found to be

$$\eta = \frac{0.446 k_B^2 T^2}{\alpha^2 v_g^2 \hbar} \tag{6.80}$$

and amounts to $\nu = \frac{v_g^2 \eta}{3P} = 0.25$ m^2/s. From this we also find

$$R_0 = \frac{\pi \hbar^2}{2 \log 2 e^2 k_B T} \left(\frac{1}{\tau_{11}} + \frac{1}{\tau_{\text{dis}}}\right) = 1985.33\Omega \tag{6.81}$$

All other parameters are easy to find.

When describing the hydrodynamic velocity u_r and the pressure δP one can consider three different limits. If $\ell_{\mathrm{GE}} \ll r_1, r_2$, which is achieved for very small τ_{dis}, one finds

$$u_r \approx \frac{Is_L \left(\sqrt{rr_2} \sinh\left(\frac{r-r_2}{\ell_{\mathrm{GE}}}\right) - \sqrt{rr_1} \sinh\left(\frac{r-r_1}{\ell_{\mathrm{GE}}}\right)\right)}{2\pi e n_L r s_B \sqrt{r_1 r_2} \sinh\left(\frac{r_1-r_2}{\ell_{\mathrm{GE}}}\right)} \tag{6.82}$$

which means, that the velocity vanishes exponentially close to the interface and is very small in the bulk of the sample. In the opposite limit $\ell_{\mathrm{GE}} \gg r_1, r_2$ u_r shows a behavior similar to the drift velocity in the leads with logarithmic corrections

$$u_r \approx \frac{Is_L}{2\pi e n_L r s_B} + \frac{Is_L r_1^2 r_2^2 \log\left(\frac{r_1}{r_2}\right)}{4\pi e \ell_{\mathrm{GE}}^2 n_L r s_B (r_1^2 - r_2^2)} + \frac{Irs_L \left[r_1^2 \log\left(\frac{r}{r_1}\right) - r_2^2 \log\left(\frac{r}{r_2}\right)\right]}{4\pi e \ell_{\mathrm{GE}}^2 n_L s_B \left(r_1^2 - r_2^2\right)}. \tag{6.83}$$

Finally, if $r_2 - r_1 \ll r_1, r_2, \ell_{\mathrm{GE}}$ we find the same $1/r$ behavior as in the leads

$$u_r \approx \frac{Is_L}{2\pi e n_L r s_B} \tag{6.84}$$

The resulting velocity u_r and pressure δP is shown in Fig. 6.2. In the leads, the drift velocity shows a simple $1/r$ behavior, while one finds a jump due to the mismatch of entropy directly at the interface. Inside the sample, the situation depends on the relative size of ℓ_{GE}. If $\ell_{\mathrm{GE}} \ll r_1, r_2$ we indeed observe, that the velocity decreases rapidly close to the interface and exactly vanishes in the bulk of the sample. This behavior is generally only observable in rather large samples, since the quantity τ_{dis} cannot be arbitrarily small while still staying in the hydrodynamic regime. In the same situation, the pressure is constant in the bulk of the sample. In all other cases, u_r resembles a $1/r$ behavior, that is slightly modified by logarithmic corrections.

The plots for μ_I and δT are shown in Fig. 6.3. In the limit of $\ell_{\mathrm{GE}} \ll r_1, r_2$ both the imbalance chemical potential and the non-equilibrium part of the velocity δT vanish in the bulk of the sample. In this limit energy relaxation processes transfer any heating, that may develop in the sample to the substrate and out of the device. There is only a small finite effect very close to the interface. Since this is an effect of τ_R it is in principle independent of ℓ_{GE} and τ_{RE}, however we need $\ell_R < \ell_{\mathrm{GE}}$ to remain in the hydrodynamic regime. In all other scenarios, there is a finite temperature profile, which may amount to 0.5% of the equilibrium temperature.

Finally we take a look at the total resistance R of the system. In general one might place the measuring points r_{in} and r_{out} very close to the interface, in which case the bulk resistance of the leads R_L would not contribute to the total resistance R. We will further disregard the influence of the phenomenological contact resistance R_C, which only depends on the used materials and their relative chemical potential. Then one can consider again three limiting cases of the hydrodynamic, dissipative

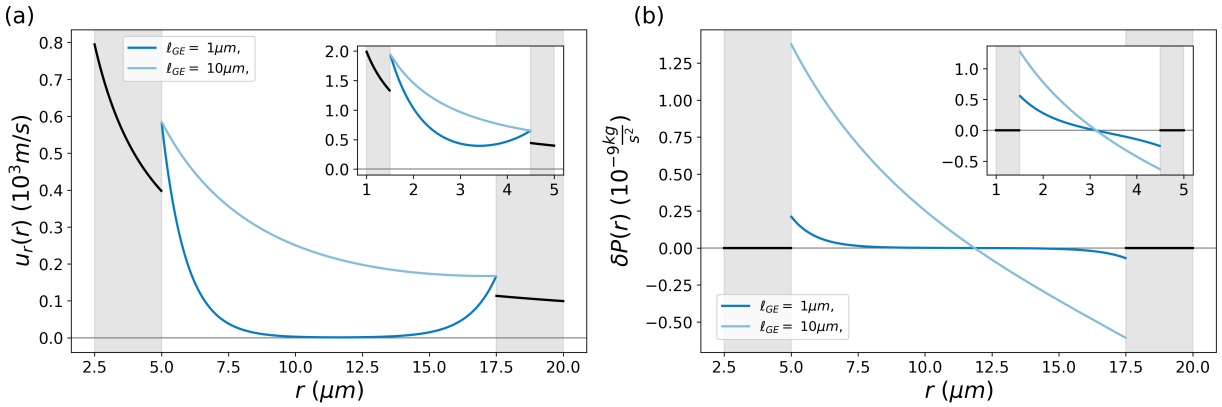

Figure 6.2: (a) Hydrodynamic velocity u_r in the graphene sample and drift velocity $u_{L,r}$ in the leads as a function of the radius r for a large (main panel) and small sample (inset). Due to the mismatch in entropy, there is a finite jump at the interface. (b) Non-equilibrium pressure δP as a function of the radius r for a large (main panel) and small sample (inset). The non-equilibrium pressure was assumed to vanish in the leads. Both: we used $\ell_{\mathrm{GE}} = 1\mu\mathrm{m}$ and $\ell_{\mathrm{GE}} = 10\mu\mathrm{m}$ which corresponds at the stated τ_{dis} to $\tau_{\mathrm{RE}} = 1.1 \times 10^{-12}$ s and $\tau_{\mathrm{RE}} = 159 \times 10^{-12}$ respectively. The gray area marks the leads.

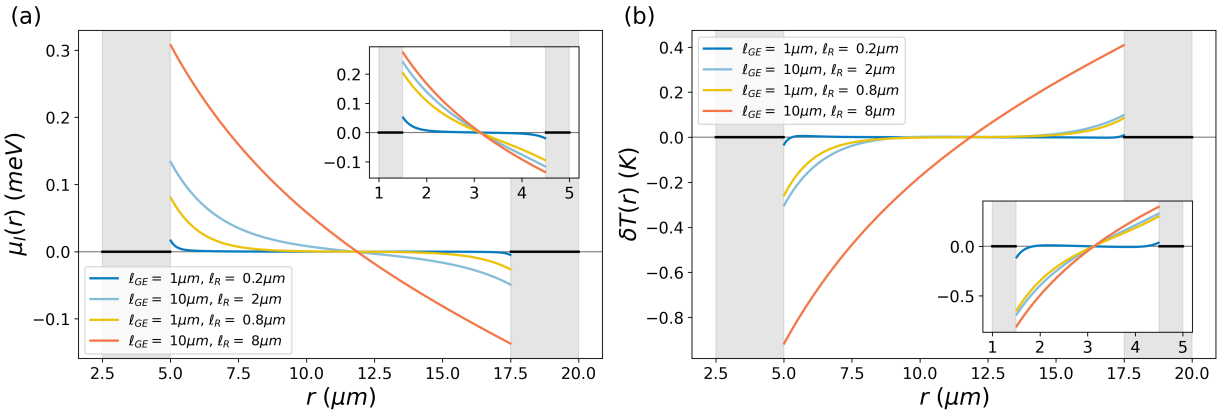

Figure 6.3: (a) Imbalance chemical potential μ_I as a function of the radius r for a large (main panel) and small sample (inset). In the leads, the imbalance chemical potential vanishes. (b) Non-equilibrium temperature δT as a function of the radius r for a large (main panel) and small sample (inset). The non-equilibrium temperature was assumed to vanish in the leads. Both: the used $\ell_{\mathrm{R}} = \{0.2,\ 0.8,\ 2,\ 8\}\,\mu\mathrm{m}$ correspond to $\tau_{\mathrm{R}} = \{0.56,\ 9,\ 56,\ 900\} \times 10^{-12}$ s respectively. The gray area marks the leads.

contribution to the resistance R_B^{diss}. The first limit is $\ell_{\text{GE}} \ll r_1, r_2$ in which case we find

$$\begin{aligned} R_B^{\text{diss}} &\approx \frac{\eta s_L^2}{\pi e^2 n_L^2 s_B^2}\left(\frac{1}{r_1^2}-\frac{1}{r_2^2}\right) \\ &\quad - \frac{s_L^2(A+\eta)\left((r_1+r_2)\cosh\left(\frac{r_1-r_2}{\ell_{\text{GE}}}\right)-2\sqrt{r_1 r_2}\right)\operatorname{csch}\left(\frac{r_1-r_2}{\ell_{\text{GE}}}\right)}{2\pi e^2 \ell_{\text{GE}} n_L^2 r_1 r_2 s_B^2} \end{aligned} \tag{6.85}$$

$$\approx \frac{\eta s_L^2}{\pi e^2 n_L^2 s_B^2}\left[\frac{1}{r_1^2}-\frac{1}{r_2^2}-\frac{\sqrt{\ell_G^2+\frac{v_g^2\tau_{\text{dis}}\tau_{\text{RE}}}{2}}}{2\ell_G^2}\left(\frac{1}{r_1}+\frac{1}{r_2}\right)\right] \tag{6.86}$$

where the second approximation requires $r_1 - r_2 \gg \ell_{\text{GE}}$. The result of Ref. [232] corresponds to neglecting the term proportional to ℓ_{GE}. The second limit is the case $\ell_{\text{GE}} \gg r_1, r_2$ and we find

$$R_B^{\text{diss}} \approx \frac{\eta s_L^2}{\pi e^2 n_L^2 s_B^2}\left(\frac{1}{r_1^2}-\frac{1}{r_2^2}+\frac{1}{2\ell_G^2}\log\left(\frac{r_2}{r_1}\right)\right), \tag{6.87}$$

which introduces a logarithmic correction of exactly the same form as the bulk resistance R_B of the sample. The final limit is $r_2 - r_1 \ll r_1, r_2, \ell_{\text{GE}}$ where we find the result

$$R_B^{\text{diss}} = \frac{s_L^2 \eta (r_2^2 - r_1^2)}{4\pi e^2 n_L^2 r_1 r_2 s_B^2 \ell_G^2}. \tag{6.88}$$

If one instead directly takes the limit $\tau_{\text{RE}} \to 0$, and additionally $\ell_G \ll r_1, r_2, r_2 - r_1$ one would obtain

$$R_B^{\text{diss}} \approx \frac{\eta s_L^2}{\pi e^2 n_L^2 s_B^2}\left[\frac{1}{r_1^2}-\frac{1}{r_2^2}-\frac{1}{2\ell_G}\left(\frac{1}{r_1}+\frac{1}{r_2}\right)\right]. \tag{6.89}$$

This is the result for the viscous correction to the resistance at charge neutrality in the setup of Ref. [220].

The plots for $\phi(r)$ and $R = R_B + R_B^{\text{diss}} + R_L^{\text{diss}}$ are shown in Fig. 6.4 (a) and (b) respectively. In the case of the potential ϕ we find a logarithmic dependence on the radial position r in both the leads and the sample, where the overall prefactor is however different. In all considered cases, the jump at the interface is in the same direction, which for the second interface is opposite to what Ref. [232] obtains. This is due to the fact, that in our case the contribution of δP is larger than the contributions due to η and η_L alone. The jump is larger, for larger ℓ_{GE}. As seen in Fig. 6.4 (b), the total measured resistance is only slightly changed. The correction shown in the inset of 6.4 (b) is nearly logarithmic for the larger ℓ_{GE}, while is saturates for the smaller ℓ_{GE}.

6.6 Summary and conclusions

In summary, we have solved the hydrodynamic equation in charge neutral graphene in linear response. To completely determine the solutions, we have imposed boundary conditions based on conservation of entropy current, charge and imbalance current directly at the interface with the highly doped graphene leads. Using these boundary conditions we see, that depending on the relative magnitude of the radii of the disk and the lengths ℓ_{GE} and ℓ_R, set by energy relaxation and recombination processes, the

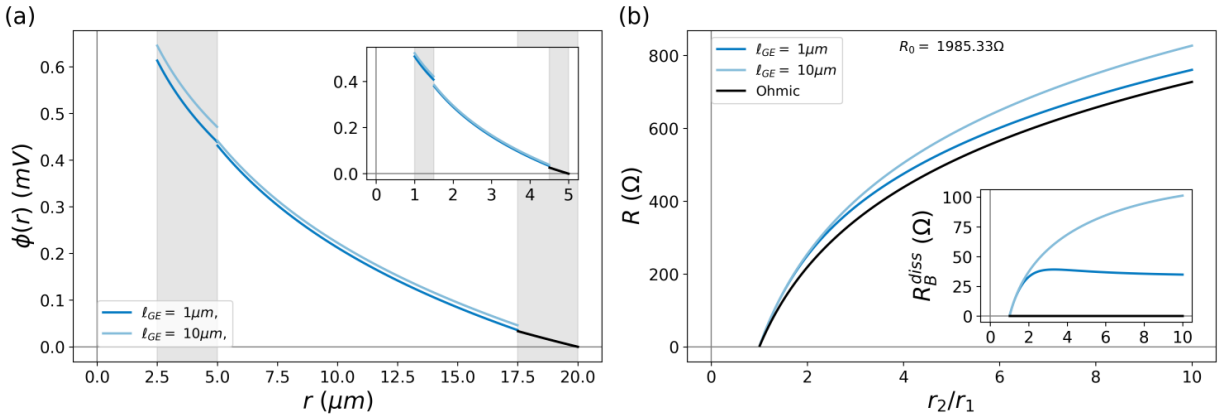

Figure 6.4: (a) Electrical potential ϕ as a function of the radius r for a large and small sample in the inset. In the leads, electrical potential behaves logarithmically. The jump at the interface is determined by the dissipation in the regions, the phenomenological contact resistance is disregarded. (b) Total resistance $R = R_B + R_B^{\text{diss}} + R_L^{\text{diss}}$ of the system as function of the effective width radius r_2/r_1 for $r_1 = 1.5\mu$m and dissipative contribution R_B^{diss} only in the inset. Both: The gray area marks the leads.

hydrodynamic velocity may stay finite in the bulk or vanish. We find a temperature profile, that shows jumps in opposite directions at the two interfaces, while in all considered scenarios the potential jumps have the same sign at both interfaces. This is a strong indicator of the relevance of energy-relaxation over viscosity in this setup.

In conclusion we find, that in charge neutral graphene, charge and energy transport decouple. While the energy current is carried by the hydrodynamic velocity $\mathbf{u}$, charge transport becomes fully dissipative. **Nevertheless, electronic transport is influenced by hydrodynamics, which leads to jumps of both the temperature and the electrochemical potential at the interface between leads and the sample, which can be measured by modern imaging techniques** (the local temperature variation can be measured using the approach of Refs. [234–236], while measurements of the local potential are at the heart of the technique proposed in Refs. [202, 237]). **In contrast to the finite density case, the fluid remains compressible in linear response, which brings the energy relaxation rate $1/\tau_{\mathbf{RE}}$ into the picture. In the regime of applicability of hydrodynamics, this energy relaxation will dominate and renormalize the effective viscosity.** The most easily measurable quantity, the resistance of the whole device, is only slightly modified by hydrodynamics and it is quite hard to extract the viscosity from such measurements, since it is masked by energy relaxation.

One can extend this analysis to different temperatures in the leads and thus study the heat transport. In this situation one should take another closer look at the used boundary conditions.

In contrast to Chapter 4 we see, that here strong electron-electron interaction can no longer be treated on a perturbative level, but completely changes the behavior of the electronic liquid and how we should describe it. Strongly correlated electrons in graphene show collective behavior and can be described similarly to a classical liquid. If one considers the same device at lower temperatures, as in Chapter 5, electron-electron interaction turns out to be completely negligible, which clearly shows, how strongly temperature affects the internal processes in graphene.

Chapter 7
7 Conclusion and outlook

7.1 Summary

In this thesis I have studied the electronic transport in graphene based devices in three different setups. Summaries of the individual situations are given in the following.

7.1.1 Interaction effects in a bilayer graphene quantum point contact

At first I considered transport in a bilayer graphene quantum point contact (BLG QPC) in Chapter 4. In this setup, the transport can be essentially described by the Landauer-Büttiker formula. I find a quantization of conductance in multiples of $4\frac{e^2}{h}$ for vanishing magnetic field and in multiples of $2\frac{e^2}{h}$ for sufficiently large, in-plane magnetic field. This is the expected behavior for weak interactions.

In fact, the experiment finds additional features in the conductance curves that indicate that interaction effects are indeed present here. While the present gates screen the Coulomb interaction, for the given distance between the gates and the BLG plane, the screening is indeed not strong enough to fundamentally alter the interaction. The first of these features is an additional shoulder in the conductance at a value close to $3\frac{e^2}{h}$ for vanishing magnetic field. For increasing in-plane magnetic field it continuously develops into the lowest Zeeman split level. The other feature is an increase of the extracted Landé g-factor for the three lowest size-quantized levels, which is strongest for the lowest subband. I interpret both of these effects as induced by electron-electron interaction.

I propose a phenomenological model to explore which interaction induced conductance features are in principle possible in BLG, considering the additional valley degree of freedom. By considering their behavior in an in-plane magnetic field and comparing it to the experimental data, I conclude that the observed feature can be interpreted along the same lines as the 0.7 anomaly in other two-dimensional electron gases, since the valleys remain degenerate. I also show that this initial splitting cannot be explained by substrate-enhanced spin-orbit coupling of the Kane-Mele type, since it would be an order of magnitude smaller than the zero field splitting I observe and should show up at higher magnetic fields as well, where I don't see any traces of it.

The enhancement of the Landé g-factor can also not be explained by a finite out-of plane component of the magnetic field, which would again show up as a full splitting of spin and valley degree of freedom for higher magnetic fields, which are not observed. The experimental data also shows Fabry-Pérot oscillations on top of the quantized conductance curves for the lower temperature of 20 mK,

which however do not disperse with magnetic field and show a different voltage dependence, making them distinguishable from the 0.7 feature. Moreover, the oscillations are completely gone at the higher temperature of 4 K, where the conductance traces are already quite smeared out, while the 0.7 feature remains visible, as one would expect.

Thus I could show that interaction effects indeed lead to visible features in narrow bilayer graphene quantum point contacts. The observed 0.7 anomaly can be modeled by a phenomenological model based on an effective spontaneous spin splitting, while valley remains degenerate. A similar behavior is expected in other materials that possess N_s spin and N_v valley degrees of freedom, that are all degenerate without interaction effects. This feature is stronger for a flatter dispersion. Coulomb interaction does not induce spin-flip processes but allows for valley flips, so that a spin-valley symmetry of the non-interacting model is broken down. As a result, spin splitting can occur, while valley remains degenerate.

7.1.2 Disorder dominated transport in a graphene Corbino disk

In Chapter 5 I consider the situation where both spatial dimensions are larger than the impurity scattering length, thus transport is dominated by disorder. In this regime, I investigated the two-terminal magnetoresistance in a graphene Corbino disk, which is special, since in this geometry the Hall conductivity does not enter into the resistance. The applied perpendicular magnetic field $B \leq 0.15$ T turned out to be small enough to disregard quantum effects due to Landau levels, since they were sufficiently smeared by disorder.

In this situation one may use a semiclassical analysis, based on the Boltzmann equation, to obtain the longitudinal conductivity, which, up to a geometric factor, completely determined the magnetoresistance of the device and leads to a simple quadratic dependence on B. The only information related to the disorder in the sample that enters the Boltzmann equation is the transport time τ_{tr}, which I determined for both short range scatterers and charged impurities, assuming that the total τ_{tr} is determined by the reciprocal sum, i.e. applying a mixed disorder model, where scattering events from different types of disorder are independent.

Since the two considered transport times show a different density dependence, one may extract details, like the concentration of the different types of disorder, by investigating the voltage dependence of the measured magnetoresistance, as was obtained from the experiment. Because the sample was very clean, the resistance was dominated by the contact resistance of the leads, which has to be subtracted to find the true bulk mobility, but is in general not known. Using the assumption that this contact resistance may depend on the gate voltage, but not on the magnetic field, I was able to extract the true bulk parameters and an estimate of said contact resistance, which indeed dominates the resistance. The true bulk mobility, obtained from the this procedure, is larger by a factor of up to two, than the naively determined mobility, which is typically used to characterize the sample.

In all of this, particular attention was aimed at the fact that the data includes densities very close to the Dirac point, where effects related to the saturation of the density of states have to be taken into account. These considerations where applied at zero temperature, so I considered the influence of finite temperature on the magnetoresistance curves, using the parameters obtained from the $T = 0K$ fit, which turned out to be very small, for the considered temperatures of 4 K and 27 K. The influence of electron-electron interaction leads to a diffusive logarithmic correction at $4K$, while at $27K$ finite temperature corrections dominate.

Thus I could show, that magnetotransport in a Corbino geometry is dominated by the

Drude-Boltzmann result in the considered regime, where it is important to consider a mixed disorder model. A similar conclusion is expected for other two-dimensional electron gases, although the density dependencies will be different. Because of this magnetoresistance measurements performed at different densities and small magnetic fields and low temperatures in a Corbino disk, can be used to accurately characterize the disorder in the sample, if one performs a careful analysis.

7.1.3 Hydrodynamic transport in a graphene Corbino disk

In Chapter 6 I considered a similar graphene Corbino disk but at elevated temperatures, without a magnetic field and at charge neutrality. In this regime, electron-electron interaction sets the smallest length scale and the hydrodynamic approach introduced in Sec. 2.4 is applicable. At charge neutrality and zero magnetic field, the transport of energy and charge completely decouple. While energy is carried by the hydrodynamic velocity $\mathbf{u}$, charge current becomes completely dissipative and should lead to a simple ohmic resistance of the device.

Nevertheless, hydrodynamics does influence the electric potential and the resistance of the device. In the considered setup, where highly doped graphene leads are attached to the inner and outer radius of the charge neutral graphene sample and a current is injected from the middle, I use the conservation of entropy, current and imbalance current at the interface to determine the hydrodynamic quantities, taking into account recombination processes, disorder and energy relaxation.

It turns out that in this geometry, the hydrodynamic velocity is characterized by a new Gurzhi length ℓ_{GE} that is renormalized by energy relaxation and effectively dominated over the viscosity. If this new length scale is smaller than the radii of the disk, the hydrodynamic velocity vanishes in the bulk. In all other cases it stays finite. The temperature profile within the disk is determined by this renormalized Gurzhi length ℓ_{GE} and a second length scale related to recombination processes and shows jumps in opposite directions at the two interfaces, which can be measured by modern imaging techniques.

Finally I argue that to find the potential profile and thus the resistance of the device, one has to take into account that there is viscous dissipation in the sample, which has to be balanced at the interface, to avoid an accumulation of dissipation there. To this end, I take a look at the dissipation and find that the joule heat at the interface exactly balances this dissipation and thus leads to a jump of potential there. Finally, one obtains the resistance of the device, which shows small, size dependent corrections to the ohmic result.

In summary, I find that electronic transport at charge neutrality is influenced by hydrodynamics, which leads to jumps of both the temperature and the electrochemical potential at the interface between the leads and the sample, which can be measured by modern imaging techniques. Contrary to the finite density case, the electronic fluid is compressible even in linear response. In the regime of applicability of hydrodynamics, energy relaxation will dominate and renormalize the effective viscosity.

7.2 Outlook

The popularity of graphene and untwisted bilayer graphene has recently been rivaled by the advent of twisted bilayer graphene but the reason for this is not that these systems are perfectly understood already. In the following, I will state additional predictions based on my findings and further possible directions.

7.2.1 Interaction effects in a bilayer graphene quantum point contact

While the main transport features in quantum point contacts (QPCs) can be described without taking into account interaction effects, the possible low density and high density of states enhance even these weak effects. This happens in all materials but screening due to the gates was shown to be largely unchanged for distances relevant to transport experiments in graphene and bilayer graphene [119], so these materials are especially interesting.

Predictions Using the extended phenomenological model, I would predict a similar behavior as in BLG in other materials with N_s spin degrees of freedom and N_v valley degrees of freedom, which are degenerate without interaction effects. Since Coulomb interaction allows for valley but not spin flipping processes, they should show an interaction induced shoulder, which appears close to the value of $0.7 \times N_s \times N_v \frac{e^2}{h}$. This feature is stronger the flatter the dispersion at the bottom of the lowest subband. If the material has strong spin orbit coupling of the Kane-Mele type, an additional, stronger plateau at $0.5 \times N_s \times N_v \frac{e^2}{h}$ should appear.

Future directions In the experiment considered in Chapter 4, these effects were an enhancement of the Landé g-factor and an additional shoulder in the conductance. Both of these effects were only treated on phenomenological grounds in this thesis. Except for the additional valley degree of freedom, interaction effects in bilayer graphene are expected to be similar to a more conventional two dimensional electron gas, so the enhanced Landé g-factor should be treatable similarly to Refs. [161–163], where one should however also include the effective one dimensional nature imposed by the quantum point contact. This effect should also be visible in quantum wires.

As discussed at length already, the second feature, the 0.7 anomaly has evaded an accepted microscopic theoretical explanation for more than 20 years and this is certainly not changed by this thesis. While the functional renormalization group treatment developed in Refs. [83, 84, 115] looks compelling to a large degree, the produced shoulder is much weaker than what is seen in experiment and analytical solutions exist not even in a perturbative limit.

There are several additional ingredients that could be combined with this sort of setup. In particular, in Ref. [238] it was observed that, at least if there is a substantial gap and the trigonal warping is relevant, electrons might predominately orient along the lattice directions and not take the shortest path, which is expected to affect the conductance of the QPC in the corresponding regime of gate voltages.

Further, while the intrinsic spin-orbit coupling in BLG is very weak, using an additional layer with strong spin-orbit coupling, e.g., a layer of a transition metal dichalcogenide, should induce noticeable proximity spin-orbit related effects [239, 240] and may lead to topologically nontrivial states.

In addition, the introduction of a finite twist between the layers may also lead, at certain fillings and twist angles, to topological states [43, 240]. In order to open a gap in such a system, spin-orbit coupling has to be added as well. To what extent these states can be manipulated with gates and external magnetic fields and what role interaction effects play in such engineered sample are questions worth exploring. The analysis presented here serves as the starting point for further studies in this direction.

7.2.2 Disorder dominated transport in a graphene Corbino disk

Electrical transport in the disorder dominated regime in graphene at low temperatures and low magnetic fields, as discussed in Chapter 5 seems to be largely understood.

Predictions A similar regime, where magnetoresistance is dominated by the Drude-Boltzmann result should exist in other two-dimensional electron gases. By using the transport scattering times calculated in Ref. [193] I would predict, that for a parabolic spectrum one can also characterize and distinguish short range and charged scatterers. For a parabolic spectrum, the product $\omega_c \tau_q$ does not depend on the energy, so tuning between the classical and the quantum regime is only possible by changing the disorder strength or the magnetic field.

Future directions If one keeps temperature low but increases the magnetic field, Landau level physics will become important and the semiclassical approach discussed in 5 will no longer work. Instead, one should use the perturbative results discussed in Sec. 2.2.5. There should however still be a regime, where this Kubo result dominates over interaction induced corrections.

When one instead increases the temperature, electron-electron interaction starts to dominate at some point and hydrodynamic transport should be observed. As shown in Chapter 6, this already leads to interesting effects, like viscosity induced jumps at the interfaces without an external magnetic field. If one does apply such a perpendicular magnetic field, the scenario becomes even more interesting, particularly, since the perpendicular components of currents do not enter the equations for charge, imbalance and energy conservation, so additional boundary conditions have to be found. Moreover, the viscosity induced jump at the interface will acquire a magnetic field dependence, which might lead to another way of measuring the viscosity. This is a direction I am already working on.

7.2.3 Hydrodynamic transport in a graphene Corbino disk

Predictions As already remarked, the expected jumps of temperature and electrochemical potential should be observable by modern imaging techniques (the local temperature variation can be measured using the approach of Refs. [234–236], while measurements of the local potential are at the heart of the technique proposed in Refs. [202, 237]). Since energy relaxation dominates the viscosity in the graphene sample, the jumps of the electrochemical potential are in the same direction at both interfaces, in contrast to the prediction of Refs. [220] and [232].

Future directions While the found solution in the vanishing magnetic field case is already interesting, the situation becomes more complex with a finite magnetic field. This field couples the energy and charge modes. Since I already argued that resistance measurements in a charge neutral graphene Corbino disk without a magnetic field are not well suited to determine quantities like the interaction induced viscosity and both the temperature and potential profile are dominated by energy relaxation over viscosity, magnetoresistance measurements might solve this problem. This is especially interesting, since the fitting experiment has already been realized.

Finally, one may extend this theory to the study of thermoelectric phenomena and find all thermoelectric coefficients. Since it was already found that the thermoelectric response is anomalous, i.e. violates the Matthiessen's rule, the Wiedemann-Franz law and the Mott relation in Ref. [220], it would be interesting to see how these conclusions change, if one treats the interface more carefully and considers energy relaxation processes.

A Appendix A

Mono- and bilayer graphene: Calculations

A.1 Eigensystem monolayer graphene

Following Ref. [56] we can also consider the system in the presence of a perpendicular magnetic field $\mathbf{B} = B\mathbf{e}_z$, where we have

$$\hat{\pi} = im\omega_B \left(\left[x + \frac{1}{m\omega_B}\hat{q}_y \right] - i\xi \frac{1}{m\omega_B}\hat{q}_x \right), \quad \hat{\pi}^\dagger = -im\omega_B \left(\left[x + \frac{1}{m\omega_B}\hat{q}_y \right] + i\xi \frac{1}{m\omega_B}\hat{q}_x \right), \tag{A.1}$$

$$\hat{q}_x = -i\hbar\partial_x, \quad \hat{q}_y = -i\hbar\partial_y, \quad m\omega_B = \frac{eB\hbar}{c}. \tag{A.2}$$

Defining raising and lowering operators

$$\hat{a} = \frac{i}{\sqrt{2\hbar m\omega_B}}\hat{\pi}^\dagger, \quad \hat{a}^\dagger = \frac{-i}{\sqrt{2\hbar m\omega_B}}\hat{\pi}, \tag{A.3}$$

which fulfill $[\hat{a}, \hat{a}^\dagger] = \xi$ leaves us with the Hamiltonian

$$\check{H}_0 = \xi \frac{v_g}{\hbar}\sqrt{2\hbar m\omega_B} \begin{pmatrix} 0 & -i\hat{a} \\ i\hat{a}^\dagger & 0 \end{pmatrix}, \tag{A.4}$$

and after decoupling the two components $\mathbf{F} = (u, v)$ we find for the first one

$$\left(\varepsilon^2 - 2\frac{v_g^2}{\hbar} m\omega_B \hat{a}\hat{a}^\dagger \right) u(x, y) = 0. \tag{A.5}$$

For $\xi = +1$ $\hat{a}$ and $\hat{a}^\dagger$ fulfill the requirements for ladder operators and we find the eigenenergies

$$\varepsilon_{+,s,n} = s\sqrt{2}v_g \sqrt{\frac{eB}{c}}\sqrt{n+1}, \tag{A.6}$$

where $s = \pm$ label two sets of bands and n is assumed to be integer. In general, eigenstates remain translationally invariant along y direction with a wave vector k_y, then the lowest mode fulfills

$$\hat{a}u_0(x,y) = 0, \tag{A.7}$$

$$\left(x - \frac{\hbar}{m\omega_B}k_y + \frac{i}{m\omega_B}q_x\right)e^{-ik_y y}\tilde{u}_0(x) = 0, \tag{A.8}$$

$$\Rightarrow \tilde{u}_0(x) = Ce^{-\frac{1}{2}\frac{m\omega_B}{\hbar}\left(x-\frac{\hbar k_y}{m\omega_B}\right)^2}, \tag{A.9}$$

and all higher states are found via

$$u_{n,k_y,+}(x,y) = \frac{(\hat{a}^\dagger)^n}{\sqrt{n!}}e^{-ik_y y}\tilde{u}_0(x). \tag{A.10}$$

The second component is then given by

$$v_{n,k_y,+}(x,y) = i\frac{v_g}{\hbar}\sqrt{2\hbar m\omega_B}\frac{i}{\varepsilon_{n,+}}\hat{a}^\dagger u_{n,k_y,+}(x,y). \tag{A.11}$$

A.2 Two band theory BLG

Here we state, how the four band Hamiltonian (1.11) can be used, to construct an effective low energy theory. In order to find an effective low-energy theory, which is defined by energies $|E| \ll \gamma_1$, we follow the derivation of Ref. [44]. First we reorder the basis states to $(\psi_{A1}, \psi_{B2}, \psi_{A2}, \psi_{B1}) \otimes (\uparrow, \downarrow)$, since then the first half corresponds to the low-energy, non-dimer states while the second half corresponds to the dimer states, that are coupled by the large energy γ_1. After this reordering, we can define the Green's function of the total Hamiltonian $\check{H} = \check{H}_i + \check{H}_Z + \check{H}_i^{\mathrm{so}}$ as follows:

$$\check{H} = \begin{pmatrix} H_{11} & H_{12} \\ H_{21} & H_{22} \end{pmatrix}, \tag{A.12}$$

$$\begin{aligned} \check{G} &= \begin{pmatrix} G_{11} & G_{12} \\ G_{21} & G_{22} \end{pmatrix} = (\check{H} - E)^{-1} \\ &= \begin{pmatrix} G_{11}^{(0)-1} & H_{12} \\ H_{21} & G_{22}^{(0)-1} \end{pmatrix}^{-1}, \end{aligned} \tag{A.13}$$

$$G_{\alpha\alpha}^{(0)} = (H_{\alpha\alpha} - E)^{-1}. \tag{A.14}$$

We now aim to find a closed expression for G_{11}, from which we define the new Hamiltonian $\check{H}_2$ according to

$$G_{11} = (\check{H}_2 - E)^{-1} \quad \Leftrightarrow \quad \check{H}_2 = G_{11}^{-1} + E. \tag{A.15}$$

We find

$$G_{11} = \left(1 - G_{11}^{(0)}H_{12}G_{22}^{(0)}H_{21}\right)^{-1}G_{11}^{(0)} \tag{A.16}$$

and, thus,

$$\check{H}_2 = G_{11}^{-1} + E = H_{11} - H_{12}G_{22}^{(0)}H_{21}. \tag{A.17}$$

Nest we expand $G_{22}^{(0)} = (H_{22}-E)^{-1}$ in $E/\gamma_1 \ll 1$. Then we obtain to linear order in $U, \Delta', \delta_{AB}, v_4, v_3, \lambda, \Delta E_Z$, the effective two-band Hamiltonian:

$$\check{H}_2 = \check{h_0} + \check{h}_U + \check{h}_3 + \check{h}_{\mathrm{AB}} + \check{h}_4 + \check{h}_{\Delta'} + \check{h}_Z + \check{h}_{\mathrm{so}}, \tag{A.18}$$

where

$$\check{h}_0 = -\frac{v^2}{\gamma_1}\begin{pmatrix} 0 & (\pi^\dagger)^2 \\ \pi^2 & 0 \end{pmatrix} \otimes \check{s}_0, \tag{A.19}$$

$$\check{h}_U = -\frac{U}{2}\left[\begin{pmatrix} 1 & 0 \\ 0 & -1 \end{pmatrix} - \frac{v^2}{\gamma_1^2}\begin{pmatrix} \pi^\dagger\pi & 0 \\ 0 & -\pi\pi^\dagger \end{pmatrix}\right] \otimes \check{s}_0, \tag{A.20}$$

$$\check{h}_3 = v_3\begin{pmatrix} 0 & \pi \\ \pi^\dagger & 0 \end{pmatrix} \otimes \check{s}_0, \tag{A.21}$$

$$\check{h}_{\mathrm{AB}} = \frac{\delta_{AB}}{2}\begin{pmatrix} 1 & 0 \\ 0 & -1 \end{pmatrix} \otimes \check{s}_0, \tag{A.22}$$

$$\check{h}_{\Delta'} = 2\Delta'\frac{v^2}{\gamma_1^2}\begin{pmatrix} \pi^\dagger\pi & 0 \\ 0 & \pi\pi^\dagger \end{pmatrix} \otimes \check{s}_0, \tag{A.23}$$

$$\check{h}_4 = 2v_4\frac{v^2}{\gamma_1^2}\begin{pmatrix} \pi^\dagger\pi & 0 \\ 0 & \pi\pi^\dagger \end{pmatrix} \otimes \check{s}_0, \tag{A.24}$$

$$\check{h}_Z = \frac{\Delta E_Z}{2}\begin{pmatrix} 1 & 0 \\ 0 & 1 \end{pmatrix} \otimes \check{s}_z, \tag{A.25}$$

$$\check{h}_{\mathrm{so}} = \xi\begin{pmatrix} \lambda_1+\lambda_2+\lambda_u & 0 \\ 0 & -\lambda_1-\lambda_2-\lambda_d \end{pmatrix} \otimes \check{s}_z. \tag{A.26}$$

B Appendix B

Perturbative calculations

B.1 Derivation Landauer-Büttiker formula

Let us assume, that we have two leads, that can be practically described as one dimensional metals with parabolic spectrum. Then the conductance G in linear response to an external field is given by

$$G = \lim_{\omega \to 0} \frac{ie^2}{\omega} C^R_{II}(\hbar\omega), \tag{B.1}$$

$$C^R_{II}(t-t') = -i\Theta(t-t') \left\langle [I(t), I(t')] \right\rangle, \tag{B.2}$$

where the one dimensional current operator is defined as

$$I(x,t) = \frac{\hbar}{2mi} \sum_\sigma \left[\Psi^\dagger(x,t) \left(\partial_x \Psi(x,t) \right) - \left(\partial_x \Psi^\dagger(x,t) \right) \Psi(x,t) \right]. \tag{B.3}$$

For all calculations we make use of the Matsubara formalism and compute $C_{II}(\tau - \tau')$ instead. After Fourier transforming we use the analytical continuation $C^R_{II}(\omega) = C_{II}(i\omega_n \to \omega + i\epsilon)$. In order to make a numerical solution easier, we keep track of all $\hbar$s. This means, that $\beta = \frac{\hbar}{k_B T}$ is an inverse frequency (or a time) and Matsubara frequencies $i\omega_n \propto \frac{1}{\beta}$ are actual frequencies instead of energies. This way the imaginary time τ is also an actual time. Greek symbols like ϵ and ω represent frequencies, energies are noted by upper case roman letters like E. Wavevectors are called k, but are not a good quantum number, since the system will not have translational invariance.

We consider the case, where we can express the field operators as

$$\hat{\Psi}_\sigma(x,\tau) = \sum_\eta \int \mathrm{d}\omega \frac{m}{2\pi\hbar} \psi_{\omega,\eta}(x) c_{\sigma,\omega,\eta}(\tau) = \sum_1 \psi_1(x) c_{1,\sigma}(\tau), \tag{B.4}$$

For consistency this requires the normalization

$$\psi_{\omega,\eta}(x) \to \frac{e^{ik(\omega)x}}{\sqrt{k(\omega)}}, \tag{B.5}$$

which lets us reexpress the current as

$$I(x,\tau) = \frac{\hbar}{2mi} \sum_\sigma \sum_{1,2} \left[\phi_1^*(x) \left(\partial_x \phi_2(x) \right) - \left(\partial_x \phi_1^*(x) \right) \phi_2(x) \right] c^\dagger_{1,\sigma}(\tau) c_{2,\sigma}(\tau) \tag{B.6}$$

$$= \sum_\sigma \sum_{1,2} \langle 1 | \hat{J}(x) | 2 \rangle c^\dagger_{1,\sigma}(\tau) c_{2,\sigma}(\tau), \tag{B.7}$$

where

$$\langle 1|\hat{J}(x)|2\rangle = \frac{\hbar}{2mi}\phi_1^*(x)\left(\partial_x\phi_2(x)\right) - \left(\partial_x\phi_1^*(x)\right)\phi_2(x). \tag{B.8}$$

The current-current correlator can thus be expressed as

$$\begin{aligned}
C_{II}(\tau-\tau') &= -\langle T_{\tau-\tau'} I(x,\tau)I(x,\tau')\rangle && \text{(B.9)}\\
&= -\sum_{\sigma,\sigma'}\sum_{1,2,3,4}\langle 1|\hat{J}(x)|2\rangle\langle 3|\hat{J}(x)|4\rangle\langle T_{\tau-\tau'}c^\dagger_{1,\sigma}(\tau)c_{2,\sigma}(\tau)c^\dagger_{3,\sigma'}(\tau')c_{4,\sigma'}(\tau')\rangle && \text{(B.10)}\\
&= -\sum_{\sigma,\sigma'}\sum_{1,2,3,4}\langle 1|\hat{J}(x)|2\rangle\langle 3|\hat{J}(x)|4\rangle\langle T_{\tau-\tau'}c_{2,\sigma}(\tau)c_{4,\sigma'}(\tau')c^\dagger_{3,\sigma'}(\tau')c^\dagger_{1,\sigma}(\tau)\rangle && \text{(B.11)}\\
&= -\sum_{\sigma,\sigma'}\sum_{1,2,3,4}\langle 1|\hat{J}(x)|2\rangle\langle 3|\hat{J}(x)|4\rangle G^{(2)}(2\tau,4\tau';1\tau,3\tau') && \text{(B.12)}
\end{aligned}$$

We would generally evaluate the two particle Greens function using a perturbative expansion for a pair interaction $W(x,y)$ using

$$\int_0^\beta \mathrm{d}\tau\hat{W}(\tau) = \frac{1}{2}\int \mathrm{d}x\int \mathrm{d}y\int_0^\beta \mathrm{d}\tau\int_0^\beta \mathrm{d}\tau'\Psi^\dagger(x,\tau+\delta)\Psi^\dagger(y,\tau'+\delta)W(x,y)\delta(\tau-\tau\prime)\Psi(y,\tau')\Psi(x,\tau) \tag{B.13}$$

$$= \int_0^\beta \mathrm{d}\tau\int_0^\beta \mathrm{d}\tau'\frac{1}{2}\sum_{1,2,3,4}W_{12,43}c_1^\dagger(\tau+\delta)c_2^\dagger(\tau'+\delta)c_3(\tau')c_4(\tau)\delta(\tau-\tau'), \tag{B.14}$$

$$W_{12,43} = \int \mathrm{d}x\int \mathrm{d}y\phi_1^*(x)\phi_2^*(y)W(x,y)\phi_4(x)\phi_3(y). \tag{B.15}$$

For the free case, we can immediately rewrite the the two particle Greens function using Wick's theorem

$$G_0^{(2)}(2\tau,4\tau';1\tau,3\tau') = G_0(2\tau;1\tau)G_0(4\tau';3\tau') - G_0(2\tau;3\tau')G_0(4\tau';1\tau). \tag{B.16}$$

The first term does not contribute for finite frequencies. Since Matsubara Green's function can only depend on the imaginary time difference, we can immediately write down the Fourier transform only keeping the second term

$$C_{II}(i\omega_n) = \sum_{\sigma,\sigma'}\sum_{1,2,3,4}\langle 1|\hat{J}(x)|2\rangle\langle 3|\hat{J}(x)|4\rangle\frac{1}{\beta}\sum_{iq_n}G_0(23,i\omega_n+iq_n)G_0(41,iq_n). \tag{B.17}$$

The free Matsubara Green's functions are given by

$$\begin{aligned}
G_0(x_1,\tau_1,\sigma_1;x_2,\tau_2,\sigma_2) &\overset{\text{def}}{=} -\left\langle T_\tau\hat{\Psi}(x_1,\tau_1,\sigma_1)\hat{\Psi}^\dagger(x_2,\tau_2,\sigma_2)\right\rangle && \text{(B.18)}\\
&= \delta_{\sigma_1,\sigma_2}\sum_{34}\psi_3(x_1)\psi_4^*(x_2)\frac{1}{\beta}\sum_{i\omega_n}e^{-i\omega_n(t_1-t_2)}\frac{\delta_{34}}{i\omega_n-\omega_3}, && \text{(B.19)}\\
G_0(3,4;i\omega_n) &\overset{\text{def}}{=} \frac{\delta_{34}}{i\omega_n-\omega_3}; \qquad G_0(3;i\omega_n) \overset{\text{def}}{=} \frac{1}{i\omega_n-\omega_3}. && \text{(B.20)}
\end{aligned}$$

One should further note, that

$$\delta_{12} = \frac{2\pi\hbar}{m}\delta(\omega_1 - \omega_2)\delta_{\eta_1,\eta_2}, \tag{B.21}$$

so $G_0(3,4;i\omega_n)$ and $G_0(3;i\omega_n)$ have actually different units. We can then evaluate the Matsubara sum as

$$\frac{1}{\beta}\sum_{iq_n} G_0(23, i\omega_n + iq_n)G_0(41, iq_n) = \frac{1}{\beta}\sum_{iq_n}\frac{\delta_{23}}{i\omega_n + iq_n - \omega_2} \times \frac{\delta_{14}}{iq_n - \omega_1} \tag{B.22}$$

$$= \delta_{23}\delta_{14}\frac{n_F(\omega_2) - n_F(\omega_2)}{i\omega_n - \omega_2 + \omega_1}, \tag{B.23}$$

$$n_F(\omega) = \frac{1}{1 + e^{\beta\omega}}. \tag{B.24}$$

Thus we get

$$C_{II}(i\omega_n) = \sum_{\sigma,\sigma'}\sum_{1,2}\langle 1|\hat{J}(x)|2\rangle\langle 2|\hat{J}(x)|1\rangle\frac{n_F(\omega_1) - n_F(\omega_2)}{i\omega_n - \omega_2 + \omega_1}. \tag{B.25}$$

Next up we realize that

$$\langle 2|\hat{J}(x)|1\rangle = \langle 1|\hat{J}(x)|2\rangle^*, \tag{B.26}$$

i.e.

$$C_{II}(i\omega_n) = \sum_{\sigma,\sigma'}\sum_{1,2}|\langle 1|\hat{J}(x)|2\rangle|^2\frac{n_F(\omega_1) - n_F(\omega_2)}{i\omega_n - \omega_2 + \omega_1}. \tag{B.27}$$

The real part of the conductance is thus given by

$$\mathrm{Re}(G) = -e^2\lim_{\omega\to 0}\frac{\mathrm{Im}(C_{II}(i\omega_n \to \omega + i\delta))}{\hbar\omega} \tag{B.28}$$

$$= \frac{e^2}{\hbar}\pi\sum_{1,2}\left|\langle 2|\hat{J}(x)|1\rangle\right|^2\lim_{\omega\to 0}\delta(\omega - \omega_2 + \omega_1)\frac{n_F(\omega_1) - n_F(\omega_2)}{\omega} \tag{B.29}$$

$$= -\frac{e^2}{\hbar}\pi\sum_{1,2}\left|\langle 2|\hat{J}(x)|1\rangle\right|^2\delta(-\omega_1 + \omega_2)\frac{\partial n_F(\omega_2)}{\partial\omega_2}. \tag{B.30}$$

As a next step we restore the integrals as

$$\sum_1 \to \sum_{\eta_1=\pm 1}\frac{m}{2\pi\hbar}\int \mathrm{d}\omega_1 \tag{B.31}$$

to get

$$\mathrm{Re}(G) = -\frac{e^2m^2}{4\pi\hbar^3}\sum_{\eta_1=\pm 1}\sum_{\eta_2=\pm 1}\int \mathrm{d}\omega_1\int \mathrm{d}\omega_2\left|\langle 2|\hat{J}(x)|1\rangle\right|^2\delta(-\omega_1 + \omega_2)\frac{\partial n_F(\omega_2)}{\partial\omega_2}. \tag{B.32}$$

Since the conductance is invariant under translations of x, we can chose a large x, where a scattering state approximation is well justified. For the particularly simple case of a delta barrier at $x = 0$ we get at $x = +\epsilon$

$$\phi_1(\epsilon) = \frac{1}{\sqrt{k_1}} \begin{cases} t_1 & \eta_1 = +1 \\ 1 + r_1 & \eta_1 = -1 \end{cases}, \quad \frac{\phi_1(x)}{x}(\epsilon) = \frac{ik_1}{\sqrt{k_1}} \begin{cases} t_1 & \eta_1 = +1 \\ -1 + r_1 & \eta_1 = -1 \end{cases} \tag{B.33}$$

Thus we find

$$\langle 1|\hat{J}(x)|2\rangle = \frac{\hbar}{2m\sqrt{k_1 k_2}} \left(k_1 \begin{pmatrix} t_1 t_2^* & t_1(1 + r_2^*) \\ t_2^*(-1 + r_1) & (1 + r_2^*)(-1 + r_1) \end{pmatrix} + k_2 \begin{pmatrix} t_1 t_2^* & t_1(-1 + r_2^*) \\ t_2^*(1 + r_1) & (-1 + r_2^*)(1 + r_1) \end{pmatrix} \right). \tag{B.34}$$

where $\eta_1 = \pm 1$ and $\eta_2 = \pm 1$ correspond to the rows and columns of the matrix, respectively. Alternatively one can evaluate this current at $x = -\epsilon$. Translation invariance of the current then leads to the following restrictions:

$$1 = t_1^* t_2 + r_1^* r_2, \quad \textbf{and} \quad 0 = t_1^* r_2 + r_1^* t_2 \tag{B.35}$$

and

$$(r_2 = r_1^* \quad \textbf{xor} \quad k_1 = k_2) \tag{B.36}$$

$$\textbf{and} \quad (t_2 = t_1^* \quad \textbf{xor} \quad k_1 = k_2). \tag{B.37}$$

For $k_1 \neq k_2$ this has the physical solution $r_1 = r_2 = 1$ and $t_1 = t_2 = 0$, i.e. there is no current between modes of different frequencies. Thus we can simplify this to

$$\langle 1|\hat{J}(x)|2\rangle = \delta_{E_1,E_2} \frac{\hbar}{m} \begin{pmatrix} T_1 & t_1 r_1^* \\ -t_1 r_1^* & -T_1 \end{pmatrix} = \delta_{E_1,E_2} J_{\eta_1 \eta_2}. \tag{B.38}$$

If both are at the same frequency we can simplify this as

$$\langle 1|\hat{J}(x)|2\rangle = \frac{\hbar}{m} \begin{pmatrix} T_1 & t_1 r_1^* \\ t_1^* r_1 & -T_1 \end{pmatrix} = J_{\eta_1 \eta_2} \tag{B.39}$$

and thus get

$$\mathrm{Re}(G) = -\frac{e^2 m^2}{4\pi\hbar^3} \int \mathrm{d}\omega_2 \frac{\partial n_F(\omega_2)}{\partial \omega_2} \sum_{\eta_1 = \pm 1} \sum_{\eta_2 = \pm 1} J_{\eta_1 \eta_2} J^*_{\eta_1 \eta_2} \tag{B.40}$$

$$= -\frac{e^2 m^2}{4\pi\hbar^3} \int \mathrm{d}\omega_2 \frac{\partial n_F(\omega_2)}{\partial \omega_2} \mathrm{Tr}(J^\dagger J) \tag{B.41}$$

$$= \frac{e^2}{h} \int \mathrm{d}\omega_2 \left(-\frac{\partial n_F(\omega_2)}{\partial \omega_2} \right) T(\omega_2), \tag{B.42}$$

where we used the unitarity of the S-matrix. This is the Landauer-Büttiker formula of conductance, which we will use to describe the conductance in quantum point contacts (see Chapter 4).

Bibliography

[1] *Wad: a shortened version of the chapter by dave bridge in lakeland's mining heritage*, `https://www.cumbria-industries.org.uk/wad/`, Accessed: 13.06.2022.

[2] P. R. Wallace, "The band theory of graphite," Phys. Rev. **71**, 622–634 (1947).

[3] M. S. Dresselhaus and G. Dresselhaus, "Intercalation compounds of graphite," Advances in Physics **51**, 1–186 (2002).

[4] K. S. Novoselov, A. K. Geim, S. V. Morozov, D. Jiang, Y. Zhang, S. V. Dubonos, I. V. Grigorieva, and A. A. Firsov, "Electric field effect in atomically thin carbon films," Science **306**, 666–669 (2004).

[5] A. H. Castro Neto, F Guinea, N. M. R. Peres, K. S. Novoselov, and A. K. Geim, "The electronic properties of graphene," Rev. Mod. Phys. **81**, 109 (2009).

[6] V. N. Kotov, B. Uchoa, V. M. Pereira, F. Guinea, and A. H. Castro Neto, "Electron-electron interactions in graphene: current status and perspectives," Rev. Mod. Phys. **84**, 1067–1125 (2012).

[7] E. McCann and M. Koshino, "The electronic properties of bilayer graphene," Reports on Progress in Physics **76**, 056503 (2013).

[8] E. McCann, "Asymmetry gap in the electronic band structure of bilayer graphene," Phys. Rev. B **74**, 161403 (2006).

[9] S. Datta, *Electronic transport in mesoscopic systems*, Cambridge Studies in Semiconductor Physics and Microelectronic Engineering (Cambridge University Press, 1995).

[10] H. Bruus and K. Flensburg, *Many-body quantum theory in condensed matter physics*, en, Oxford Graduate Texts (Oxford University Press, London, England, Sept. 2004).

[11] Y. V. Nazarov and Y. M. Blanter, *Quantum transport* (Cambridge University Press, Cambridge, England, June 2012).

[12] M. Kamada, V. Gall, J. Sarkar, M. Kumar, A. Laitinen, I. Gornyi, and P. Hakonen, "Strong magnetoresistance in a graphene corbino disk at low magnetic fields," Phys. Rev. B **104**, 115432 (2021).

[13] H. van Houten, C. W. J. Beenakker, J. G. Williamson, M. E. I. Broekaart, P. H. M. van Loosdrecht, B. J. van Wees, J. E. Mooij, C. T. Foxon, and J. J. Harris, "Coherent electron focusing with quantum point contacts in a two-dimensional electron gas," Phys. Rev. B **39**, 8556–8575 (1989).

[14] D Tobben, D. A. Wharam, G Abstreiter, J. P. Kolthaus, and F Schaffler, "Ballistic electron transport through a quantum point contact defined in a si/si0.7ge0.3heterostructure," Semiconductor Science and Technology **10**, 711–714 (1995).

[15] K. J. Thomas, J. T. Nicholls, M. Y. Simmons, M. Pepper, D. R. Mace, and D. A. Ritchie, "Possible spin polarization in a one-dimensional electron gas," Phys. Rev. Lett. **77**, 135–138 (1996).

[16] L. P. Pitaevskii, E. M. Lifshitz, and A. M. Kosevich, *Physical kinetics* (Butterworth-Heinemann, Oxford, England, Nov. 1981).

[17]A. V. Andreev, S. A. Kivelson, and B. Spivak, "Hydrodynamic Description of Transport in Strongly Correlated Electron Systems," Physical Review Letters **106**, 256804 (2011).

[18]A. Lucas, R. A. Davison, and S. Sachdev, "Hydrodynamic theory of thermoelectric transport and negative magnetoresistance in weyl semimetals," Proceedings of the National Academy of Sciences **113**, 9463–9468 (2016).

[19]V. Gall, R. Kraft, I. V. Gornyi, and R. Danneau, "Spin and valley degrees of freedom in a bilayer graphene quantum point contact: zeeman splitting and interaction effects," Phys. Rev. Research **4**, 023142 (2022).

[20]H. Bruus, V. V. Cheianov, and K. Flensberg, "The anomalous 0.5 and 0.7 conductance plateaus in quantum point contacts," Physica E: Low-dimensional Systems and Nanostructures **10**, Proceedings of the First International Conference on the Physics and Applications of Spin-Related Phenomena in Semiconductors, 97 –102 (2001).

[21]R. Kraft, I. V. Krainov, V. Gall, A. P. Dmitriev, R. Krupke, I. V. Gornyi, and R. Danneau, "Valley subband splitting in bilayer graphene quantum point contacts," Phys. Rev. Lett. **121**, 257703 (2018).

[22]V. Gall, B. N. Narozhny, and I. V. Gornyi, "Electronic viscosity and energy relaxation in neutral graphene," arXiv **2206.07414** (2022).

[23]P. Phillips, "Mottness," Annals of Physics **321**, July 2006 Special Issue, 1634–1650 (2006).

[24]K. S. Novoselov, A. K. Geim, S. V. Morozov, D. Jiang, M. I. Katsnelson, I. V. Grigorieva, S. V. Dubonos, and A. A. Firsov, "Two-dimensional gas of massless Dirac fermions in graphene," Nature **438**, 197–200 (2005).

[25]Y. Zhang, Y.-W. Tan, H. L. Stormer, and P. Kim, "Experimental observation of the quantum Hall effect and Berry's phase in graphene," Nature **438**, 201–204 (2005).

[26]A. Calogeracos and N. Dombey, "History and physics of the klein paradox," Contemporary Physics **40**, 313–321 (1999).

[27]C. Itzykson and J.-B. Zuber, *Quantum field theory*, Dover Books on Physics (Dover Publications, Mineola, NY, Feb. 2006).

[28]P. A. Lee and T. V. Ramakrishnan, "Disordered electronic systems," Rev. Mod. Phys. **57**, 287–337 (1985).

[29]D. Nelson, T Piran, and S. Weinberg, *Statistical mechanics of membranes and surfaces* (WORLD SCIENTIFIC, 1989).

[30]B. Fauser, J. Tolksdorf, and E. Zeidler, eds., *Quantum gravity*, en, 2007th ed. (Birkhauser Verlag AG, Basel, Switzerland, Dec. 2006).

[31]J. C. Meyer, A. K. Geim, M. I. Katsnelson, K. S. Novoselov, T. J. Booth, and S. Roth, "The structure of suspended graphene sheets," Nature **446**, 60–63 (2007).

[32]C. N. Lau, W. Bao, and J. Velasco, "Properties of suspended graphene membranes," Materials Today **15**, 238–245 (2012).

[33]I. V. Gornyi, V. Y. Kachorovskii, and A. D. Mirlin, "Rippling and crumpling in disordered free-standing graphene," Phys. Rev. B **92**, 155428 (2015).

[34]I. V. Gornyi, V. Y. Kachorovskii, and A. D. Mirlin, "Conductivity of suspended graphene at the Dirac point," Phys. Rev. B **86**, 165413 (2012).

[35]L. Lindsay, D. A. Broido, and N. Mingo, "Flexural phonons and thermal transport in graphene," Phys. Rev. B **82**, 115427 (2010).

[36]A. R. Akhmerov and C. W. J. Beenakker, "Boundary conditions for dirac fermions on a terminated honeycomb lattice," Phys. Rev. B **77**, 085423 (2008).

[37]A. Rycerz, J. Tworzydło, and C. W. J. Beenakker, "Valley filter and valley valve in graphene," Nature Physics **3**, 172–175 (2007).

[38]V. V. Cheianov and V. I. Fal'ko, "Selective transmission of dirac electrons and ballistic magnetoresistance of $n-p$ junctions in graphene," Phys. Rev. B **74**, 041403 (2006).

[39]M. M. Fogler, D. S. Novikov, L. I. Glazman, and B. I. Shklovskii, "Effect of disorder on a graphene $p-n$ junction," Phys. Rev. B **77**, 075420 (2008).

[40]H. B. Heersche, P. Jarillo-Herrero, J. B. Oostinga, L. M. K. Vandersypen, and A. F. Morpurgo, "Bipolar supercurrent in graphene," Nature **446**, 56–59 (2007).

[41]A. Varlet, M.-H. Liu, V. Krueckl, D. Bischoff, P. Simonet, K. Watanabe, T. Taniguchi, K. Richter, K. Ensslin, and T. Ihn, "Fabry-pérot interference in gapped bilayer graphene with broken anti-klein tunneling," Phys. Rev. Lett. **113**, 116601 (2014).

[42]A. Varlet, M. Mucha-Kruczynski, D. Bischoff, P. Simonet, T. Taniguchi, K. Watanabe, V. Fal'ko, T. Ihn, and K. Ensslin, "Tunable fermi surface topology and lifshitz transition in bilayer graphene," Synthetic Metals **210**, Reviews of Current Advances in Graphene Science and Technology, 19 –31 (2015).

[43]Y. Cao, V. Fatemi, S. Fang, K. Watanabe, T. Taniguchi, E. Kaxiras, and P. Jarillo-Herrero, "Unconventional superconductivity in magic-angle graphene superlattices," Nature **556**, 43–50 (2018).

[44]E. McCann and V. I. Fal'ko, "Landau-level degeneracy and quantum hall effect in a graphite bilayer," Phys. Rev. Lett. **96**, 086805 (2006).

[45]K. S. Novoselov, E. McCann, S. V. Morozov, V. I. Fal'ko, M. I. Katsnelson, U. Zeitler, D. Jiang, F. Schedin, and A. K. Geim, "Unconventional quantum hall effect and berry's phase of 2π in bilayer graphene," Nature Physics **2**, 177–180 (2006).

[46]A. Knothe and V. Fal'ko, "Influence of minivalleys and berry curvature on electrostatically induced quantum wires in gapped bilayer graphene," Phys. Rev. B **98**, 155435 (2018).

[47]T. Stauber, N. M. R. Peres, F. Guinea, and A. H. Castro Neto, "Fermi liquid theory of a fermi ring," Phys. Rev. B **75**, 115425 (2007).

[48]F. Guinea, A. H. Castro Neto, and N. M. R. Peres, "Electronic states and landau levels in graphene stacks," Phys. Rev. B **73**, 245426 (2006).

[49]R. Kraft, J. Mohrmann, R. Du, P. B. Selvasundaram, M. Irfan, U. N. Kanilmaz, F. Wu, D. Beckmann, H. von Löhneysen, R. Krupke, A. Akhmerov, I. Gornyi, and R. Danneau, "Tailoring supercurrent confinement in graphene bilayer weak links," Nature Communications **9**, 1722 (2018).

[50]E. McCann, "Electronic properties of monolayer and bilayer graphene," in *Graphene nanoelectronics: metrology, synthesis, properties and applications, nanoscience and technology*, edited by H. Raza (2012), p. 237.

[51]F Guinea, "Spin–orbit coupling in a graphene bilayer and in graphite," New Journal of Physics **12**, 083063 (2010).

[52]L. Banszerus, B. Frohn, T. Fabian, S. Somanchi, A. Epping, M. Müller, D. Neumaier, K. Watanabe, T. Taniguchi, F. Libisch, B. Beschoten, F. Hassler, and C. Stampfer, "Observation of the spin-orbit gap in bilayer graphene by one-dimensional ballistic transport," Phys. Rev. Lett. **124**, 177701 (2020).

[53]M. Van der Donck, F. M. Peeters, and B. Van Duppen, "Transport properties of bilayer graphene in a strong in-plane magnetic field," Phys. Rev. B **93**, 115423 (2016).

[54]A. Kamenev, *Field theory of non-equilibrium systems* (Cambridge University Press, Cambridge, England, Sept. 2011).

[55]J. M. Ziman, *Principles of the theory of solids*, 2nd ed. (Cambridge University Press, Cambridge, England, June 2013).

[56]N. Shon and T. Ando, "Quantum transport in two-dimensional graphite system," Journal of the Physical Society of Japan **67**, 2421–2429 (1998).

[57]P. M. Ostrovsky, I. V. Gornyi, and a. D. Mirlin, "Electron transport in disordered graphene," Physical Review B **74**, 235443 (2006).

[58]P. S. Alekseev, A. P. Dmitriev, I. V. Gornyi, and V. Y. Kachorovskii, "Strong magnetoresistance of disordered graphene," Physical Review B **87**, 165432 (2013).

[59]J. González, F. Guinea, and M. A. H. Vozmediano, "Marginal-fermi-liquid behavior from two-dimensional coulomb interaction," Phys. Rev. B **59**, R2474–R2477 (1999).

[60]O. Vafek, "Anomalous thermodynamics of coulomb-interacting massless dirac fermions in two spatial dimensions," Phys. Rev. Lett. **98**, 216401 (2007).

[61]D. E. Sheehy and J. Schmalian, "Quantum critical scaling in graphene," Phys. Rev. Lett. **99**, 226803 (2007).

[62]A. Lucas and K. C. Fong, "Hydrodynamics of electrons in graphene," Journal of Physics: Condensed Matter **30**, 053001 (2018).

[63]L. D. Landau, E. M. Lifshits, and E. M. Lifshitz, *Fluid mechanics: vol 6*, en, Course of Theoretical Physics (Butterworth-Heinemann, Oxford, England, Jan. 1987).

[64]B. N. Narozhny, I. V. Gornyi, A. D. Mirlin, and J. Schmalian, "Hydrodynamic approach to electronic transport in graphene," Annalen der Physik **529**, 1700043 (2017).

[65]B. N. Narozhny, "Electronic hydrodynamics in graphene," Annals of Physics **411**, 167979 (2019).

[66]D. A. Wharam, T. J. Thornton, R Newbury, M Pepper, H Ahmed, J. E. F. Frost, D. G. Hasko, D. C. Peacock, D. A. Ritchie, and G. A. C. Jones, "One-dimensional transport and the quantisation of the ballistic resistance," Journal of Physics C: Solid State Physics **21**, L209–L214 (1988).

[67]B. J. van Wees, H. van Houten, C. W. J. Beenakker, J. G. Williamson, L. P. Kouwenhoven, D. van der Marel, and C. T. Foxon, "Quantized conductance of point contacts in a two-dimensional electron gas," Phys. Rev. Lett. **60**, 848–850 (1988).

[68]M. Büttiker, "Quantized transmission of a saddle-point constriction," Phys. Rev. B **41**, 7906–7909 (1990).

[69]N. Menezes, V. S. Alves, E. C. Marino, L. Nascimento, L. O. Nascimento, and C. Morais Smith, "Spin g-factor due to electronic interactions in graphene," Phys. Rev. B **95**, 245138 (2017).

[70]Y. Meir, K. Hirose, and N. S. Wingreen, "Kondo model for the "0.7 anomaly" in transport through a quantum point contact," Phys. Rev. Lett. **89**, 196802 (2002).

[71]S. M. Cronenwett, H. J. Lynch, D. Goldhaber-Gordon, L. P. Kouwenhoven, C. M. Marcus, K. Hirose, N. S. Wingreen, and V. Umansky, "Low-temperature fate of the 0.7 structure in a point contact: a kondo-like correlated state in an open system," Phys. Rev. Lett. **88**, 226805 (2002).

[72]A. Golub, T. Aono, and Y. Meir, "Suppression of shot noise in quantum point contacts in the "0.7 regime"," Phys. Rev. Lett. **97**, 186801 (2006).

[73]E. J. Koop, A. I. Lerescu, J. Liu, B. J. van Wees, D. Reuter, A. D. Wieck, and C. H. van der Wal, "The influence of device geometry on many-body effects in quantum point contacts: signatures of the 0.7 anomaly, exchange and kondo," Journal of Superconductivity and Novel Magnetism **20**, 433–441 (2007).

[74]V Tripathi and N. R. Cooper, "Nuclear magnetic resonance probes for the kondo scenario for the 0.7 feature in semiconductor quantum point contact devices," Journal of Physics: Condensed Matter **20**, 164215 (2008).

[75]B. Brun, F. Martins, S. Faniel, B. Hackens, G. Bachelier, A. Cavanna, C. Ulysse, A. Ouerghi, U. Gennser, D. Mailly, S. Huant, V. Bayot, M. Sanquer, and H. Sellier, "Wigner and kondo physics in quantum point contacts revealed by scanning gate microscopy," Nature Communications **5**, 4290 (2014).

[76]V. V. Flambaum and M. Y. Kuchiev, "Possible mechanism of the fractional-conductance quantization in a one-dimensional constriction," Phys. Rev. B **61**, R7869–R7872 (2000).

[77]O. P. Sushkov, "Conductance anomalies in a one-dimensional quantum contact," Phys. Rev. B **64**, 155319 (2001).

[78]K. M. Liu, H. I. Lin, V. Umansky, and S. Y. Hsu, *Spin incoherent transport in density-modulated quantum wires*, 2009.

[79]O. P. Sushkov, "Restricted and unrestricted hartree-fock calculations of conductance for a quantum point contact," Phys. Rev. B **67**, 195318 (2003).

[80]C. Sloggett, A. I. Milstein, and O. P. Sushkov, "Correlated electron current and temperature dependence of the conductance of a quantum point contact," The European Physical Journal B **61**, 427–432 (2008).

[81]A. M. Lunde, A. D. Martino, A Schulz, R Egger, and K Flensberg, "Electron–electron interaction effects in quantum point contacts," New Journal of Physics **11**, 023031 (2009).

[82]O. A. Tkachenko and V. A. Tkachenko, "Temperature dependence of conductance and thermopower anomalies of quantum point contacts," JETP Letters **96**, 719–723 (2013).

[83]F. Bauer, J. Heyder, E. Schubert, D. Borowsky, D. Taubert, B. Bruognolo, D. Schuh, W. Wegscheider, J. von Delft, and S. Ludwig, "Microscopic origin of the '0.7-anomaly' in quantum point contacts," Nature **501**, 73–78 (2013).

[84]J. Heyder, F. Bauer, E. Schubert, D. Borowsky, D. Schuh, W. Wegscheider, J. von Delft, and S. Ludwig, "Relation between the 0.7 anomaly and the kondo effect: geometric crossover between a quantum point contact and a kondo quantum dot," Phys. Rev. B **92**, 195401 (2015).

[85]A. Iagallo, N. Paradiso, S. Roddaro, C. Reichl, W. Wegscheider, G. Biasiol, L. Sorba, F. Beltram, and S. Heun, "Scanning gate imaging of quantum point contacts and the origin of the 0.7 anomaly," Nano Research **8**, 948–956 (2015).

[86]K. J. Thomas, J. T. Nicholls, N. J. Appleyard, M. Y. Simmons, M. Pepper, D. R. Mace, W. R. Tribe, and D. A. Ritchie, "Interaction effects in a one-dimensional constriction," Phys. Rev. B **58**, 4846–4852 (1998).

[87]A. Kristensen, H. Bruus, A. E. Hansen, J. B. Jensen, P. E. Lindelof, C. J. Marckmann, J. Nygård, C. B. Sørensen, F. Beuscher, A. Forchel, and M. Michel, "Bias and temperature dependence of the 0.7 conductance anomaly in quantum point contacts," Phys. Rev. B **62**, 10950–10957 (2000).

[88]A. C. Graham, K. J. Thomas, M. Pepper, N. R. Cooper, M. Y. Simmons, and D. A. Ritchie, "Interaction effects at crossings of spin-polarized one-dimensional subbands," Phys. Rev. Lett. **91**, 136404 (2003).

[89]D. J. Reilly, T. M. Buehler, J. L. O'Brien, A. R. Hamilton, A. S. Dzurak, R. G. Clark, B. E. Kane, L. N. Pfeiffer, and K. W. West, "Density-dependent spin polarization in ultra-low-disorder quantum wires," Phys. Rev. Lett. **89**, 246801 (2002).

[90]P. Roche, J. Ségala, D. C. Glattli, J. T. Nicholls, M. Pepper, A. C. Graham, K. J. Thomas, M. Y. Simmons, and D. A. Ritchie, "Fano factor reduction on the 0.7 conductance structure of a ballistic one-dimensional wire," Phys. Rev. Lett. **93**, 116602 (2004).

[91]L. DiCarlo, Y. Zhang, D. T. McClure, D. J. Reilly, C. M. Marcus, L. N. Pfeiffer, and K. W. West, "Shot-noise signatures of 0.7 structure and spin in a quantum point contact," Phys. Rev. Lett. **97**, 036810 (2006).

[92]F. Sfigakis, C. J. B. Ford, M. Pepper, M. Kataoka, D. A. Ritchie, and M. Y. Simmons, "Kondo effect from a tunable bound state within a quantum wire," Phys. Rev. Lett. **100**, 026807 (2008).

[93]A. M. Burke, O. Klochan, I. Farrer, D. A. Ritchie, A. R. Hamilton, and A. P. Micolich, "Extreme sensitivity of the spin-splitting and 0.7 anomaly to confining potential in one-dimensional nanoelectronic devices," Nano Letters **12**, 4495–4502 (2012).

[94]M. J. Iqbal, R. Levy, E. J. Koop, J. B. Dekker, J. P. de Jong, J. H. M. van der Velde, D. Reuter, A. D. Wieck, R. Aguado, Y. Meir, and C. H. van der Wal, "Odd and even kondo effects from emergent localization in quantum point contacts," Nature **501**, 79–83 (2013).

[95]L. W. Smith, H. Al-Taie, A. A. J. Lesage, F. Sfigakis, P. See, J. P. Griffiths, H. E. Beere, G. A. C. Jones, D. A. Ritchie, A. R. Hamilton, M. J. Kelly, and C. G. Smith, "Dependence of the 0.7 anomaly on the curvature of the potential barrier in quantum wires," Phys. Rev. B **91**, 235402 (2015).

[96]L. W. Smith, H. Al-Taie, A. A. J. Lesage, K. J. Thomas, F. Sfigakis, P. See, J. P. Griffiths, I. Farrer, G. A. C. Jones, D. A. Ritchie, M. J. Kelly, and C. G. Smith, "Effect of split gate size on the electrostatic potential and 0.7 anomaly within quantum wires on a modulation-doped GaAs/AlGaAs heterostructure," Phys. Rev. Applied **5**, 044015 (2016).

[97]L. P. Rokhinson, L. N. Pfeiffer, and K. W. West, "Spontaneous spin polarization in quantum point contacts," Phys. Rev. Lett. **96**, 156602 (2006).

[98]R. Danneau, W. R. Clarke, O. Klochan, A. P. Micolich, A. R. Hamilton, M. Y. Simmons, M. Pepper, and D. A. Ritchie, "Conductance quantization and the 0.7×2e2/h conductance anomaly in one-dimensional hole systems," Applied Physics Letters **88**, 012107 (2006).

[99]O. Klochan, W. R. Clarke, R. Danneau, A. P. Micolich, L. H. Ho, A. R. Hamilton, K. Muraki, and Y. Hirayama, "Ballistic transport in induced one-dimensional hole systems," Applied Physics Letters **89**, 092105 (2006).

[100]R. Danneau, O. Klochan, W. R. Clarke, L. H. Ho, A. P. Micolich, M. Y. Simmons, A. R. Hamilton, M. Pepper, and D. A. Ritchie, "0.7 structure and zero bias anomaly in ballistic hole quantum wires," Phys. Rev. Lett. **100**, 016403 (2008).

[101]Y. Komijani, M. Csontos, I. Shorubalko, T. Ihn, K. Ensslin, Y. Meir, D. Reuter, and A. D. Wieck, "Evidence for localization and 0.7 anomaly in hole quantum point contacts," EPL (Europhysics Letters) **91**, 67010 (2010).

[102]O. Klochan, A. P. Micolich, A. R. Hamilton, K. Trunov, D. Reuter, and A. D. Wieck, "Observation of the kondo effect in a spin-$\frac{3}{2}$ hole quantum dot," Phys. Rev. Lett. **107**, 076805 (2011).

[103]K. L. Hudson, A. Srinivasan, O. Goulko, J. Adam, Q. Wang, L. A. Yeoh, O. Klochan, I. Farrer, D. A. Ritchie, A. Ludwig, A. D. Wieck, J. von Delft, and A. R. Hamilton, "New signatures of the spin gap in quantum point contacts," Nature Communications **12**, 5 (2021).

[104]J. F. von Pock, D. Salloch, G. Qiao, U. Wieser, T. Hackbarth, and U. Kunze, "Quantization and anomalous structures in the conductance of si/sige quantum point contacts," Journal of Applied Physics **119**, 134306 (2016).

[105]A. P. Micolich, "What lurks below the last plateau: experimental studies of the $0.7 \times 2e2/h$conductance anomaly in one-dimensional systems," Journal of Physics: Condensed Matter **23**, 443201 (2011).

[106]K. S. Pyshkin, C. J. B. Ford, R. H. Harrell, M. Pepper, E. H. Linfield, and D. A. Ritchie, "Spin splitting of one-dimensional subbands in high quality quantum wires at zero magnetic field," Phys. Rev. B **62**, 15842–15850 (2000).

[107]D. J. Reilly, "Phenomenological model for the 0.7 conductance feature in quantum wires," Phys. Rev. B **72**, 033309 (2005).

[108]P. E. Lindelof, "Effect on conductance of an isomer state in a quantum point contact," in Optical organic and inorganic materials, Vol. 4415, edited by S. P. Asmontas and J. Gradauskas (International Society for Optics and Photonics, 2001), pp. 77 –85.

[109]K. Hirose, Y. Meir, and N. S. Wingreen, "Local moment formation in quantum point contacts," Phys. Rev. Lett. **90**, 026804 (2003).

[110]P. S Cornaglia and C. A Balseiro, "On the magnetic nature of quantum point contacts," Europhysics Letters (EPL) **67**, 634–640 (2004).

[111]T. Rejec and Y. Meir, "Magnetic impurity formation in quantum point contacts," Nature **442**, 900–903 (2006).

[112]B. Spivak and F. Zhou, "Ferromagnetic correlations in quasi-one-dimensional conducting channels," Phys. Rev. B **61**, 16730–16735 (2000).

[113]K. A. Matveev, "Conductance of a quantum wire in the wigner-crystal regime," Phys. Rev. Lett. **92**, 106801 (2004).

[114]K. A. Matveev, "Conductance of a quantum wire at low electron density," Phys. Rev. B **70**, 245319 (2004).

[115]D. H. Schimmel, B. Bruognolo, and J. von Delft, "Spin fluctuations in the 0.7 anomaly in quantum point contacts," Phys. Rev. Lett. **119**, 196401 (2017).

[116]D. Miserev, J. Klinovaja, and D. Loss, "Exchange intervalley scattering and magnetic phase diagram of transition metal dichalcogenide monolayers," Phys. Rev. B **100**, 014428 (2019).

[117]D. Miserev, J. Klinovaja, and D. Loss, "Magnetic phase transitions in two-dimensional two-valley semiconductors with in-plane magnetic field," Phys. Rev. B **103**, 024401 (2021).

[118]R. Du, M.-H. Liu, J. Mohrmann, F. Wu, R. Krupke, H. von Löhneysen, K. Richter, and R. Danneau, "Tuning anti-klein to klein tunneling in bilayer graphene," Phys. Rev. Lett. **121**, 127706 (2018).

[119]M. Kim, S. G. Xu, A. I. Berdyugin, A. Principi, S. Slizovskiy, N. Xin, P. Kumaravadivel, W. Kuang, M. Hamer, R. Krishna Kumar, R. V. Gorbachev, K. Watanabe, T. Taniguchi, I. V. Grigorieva, V. I. Fal'ko, M. Polini, and A. K. Geim, "Control of electron-electron interaction in graphene by proximity screening," Nature Communications **11**, 2339 (2020).

[120]Y. Lee, A. Knothe, H. Overweg, M. Eich, C. Gold, A. Kurzmann, V. Klasovika, T. Taniguchi, K. Wantanabe, V. Fal'ko, T. Ihn, K. Ensslin, and P. Rickhaus, "Tunable valley splitting due to topological orbital magnetic moment in bilayer graphene quantum point contacts," Phys. Rev. Lett. **124**, 126802 (2020).

[121]S. A. Wolf, D. D. Awschalom, R. A. Buhrman, J. M. Daughton, S. von Molnár, M. L. Roukes, A. Y. Chtchelkanova, and D. M. Treger, "Spintronics: a spin-based electronics vision for the future," Science **294**, 1488 (2001).

[122]D. D. Awschalom and M. E. Flatté, "Challenges for semiconductor spintronics," Nature Physics **3**, 153–159 (2007).

[123]J. R. Schaibley, H. Yu, G. Clark, P. Rivera, J. S. Ross, K. L. Seyler, W. Yao, and X. Xu, "Valleytronics in 2d materials," Nature Reviews Materials **1**, 16055 (2016).

[124]H. van Houten, C. Beenakker, and B. van Wees, "Chapter 2: quantum point contacts," in , Vol. 35, edited by M. Reed, Semiconductors and Semimetals (Elsevier, 1992), pp. 9–112.

[125]M. T. Allen, J. Martin, and A. Yacoby, "Gate-defined quantum confinement in suspended bilayer graphene," Nature Communications **3**, 934 (2012).

[126]A. S. M. Goossens, S. C. M. Driessen, T. A. Baart, K. Watanabe, T. Taniguchi, and L. M. K. Vandersypen, "Gate-defined confinement in bilayer graphene-hexagonal boron nitride hybrid devices," Nano Letters **12**, 4656–4660 (2012).

[127]H. Overweg, H. Eggimann, X. Chen, S. Slizovskiy, M. Eich, R. Pisoni, Y. Lee, P. Rickhaus, K. Watanabe, T. Taniguchi, V. Fal'ko, T. Ihn, and K. Ensslin, "Electrostatically induced quantum point contacts in bilayer graphene," Nano Letters **18**, 553–559 (2018).

[128]H. Overweg, A. Knothe, T. Fabian, L. Linhart, P. Rickhaus, L. Wernli, K. Watanabe, T. Taniguchi, D. Sánchez, J. Burgdörfer, F. Libisch, V. I. Fal'ko, K. Ensslin, and T. Ihn, "Topologically nontrivial valley states in bilayer graphene quantum point contacts," Phys. Rev. Lett. **121**, 257702 (2018).

[129]L. Banszerus, B. Frohn, A. Epping, D. Neumaier, K. Watanabe, T. Taniguchi, and C. Stampfer, "Gate-defined electron–hole double dots in bilayer graphene," Nano Letters **18**, 4785–4790 (2018).

[130]K. Sakanashi, N. Wada, K. Murase, K. Oto, G.-H. Kim, K. Watanabe, T. Taniguchi, J. P. Bird, D. K. Ferry, and N. Aoki, "Valley polarized conductance quantization in bilayer graphene narrow quantum point contact," Applied Physics Letters **118**, 263102 (2021).

[131]D. Terasawa, S. Norimoto, T. Arakawa, M. Ferrier, A. Fukuda, K. Kobayashi, and Y. Hirayama, "Large zeeman splitting in out-of-plane magnetic field in a double-layer quantum point contact," Journal of the Physical Society of Japan **90**, 024709 (2021).

[132]C. L. Kane and E. J. Mele, "Quantum spin hall effect in graphene," Phys. Rev. Lett. **95**, 226801 (2005).

[133]J. Sichau, M. Prada, T. Anlauf, T. J. Lyon, B. Bosnjak, L. Tiemann, and R. H. Blick, "Resonance microwave measurements of an intrinsic spin-orbit coupling gap in graphene: a possible indication of a topological state," Phys. Rev. Lett. **122**, 046403 (2019).

[134]J. González, F. Guinea, and M. A. H. Vozmediano, "Electron-electron interactions in graphene sheets," Phys. Rev. B **63**, 134421 (2001).

[135]J. González, "Kohn-luttinger superconductivity in graphene," Phys. Rev. B **78**, 205431 (2008).

[136]W.-S. Wang, Y.-Y. Xiang, Q.-H. Wang, F. Wang, F. Yang, and D.-H. Lee, "Functional renormalization group and variational monte carlo studies of the electronic instabilities in graphene near $\frac{1}{4}$ doping," Phys. Rev. B **85**, 035414 (2012).

[137], M. O. Goerbig, "*d*-wave superconductivity on the honeycomb bilayer," Phys. Rev. B **86**, 214505 (2012).

[138]J. M. D. Coey, M. Venkatesan, C. B. Fitzgerald, A. P. Douvalis, and I. S. Sanders, "Ferromagnetism of a graphite nodule from the canyon diablo meteorite," Nature **420**, 156–159 (2002).

[139]T. C. Lang, Z. Y. Meng, M. M. Scherer, S. Uebelacker, F. F. Assaad, A. Muramatsu, C. Honerkamp, and S. Wessel, "Antiferromagnetism in the hubbard model on the bernal-stacked honeycomb bilayer," Phys. Rev. Lett. **109**, 126402 (2012).

[140]R. Dillenschneider and J. H. Han, "Exciton formation in graphene bilayer," Phys. Rev. B **78**, 045401 (2008).

[141], "Fractionalization in dimerized graphene and graphene bilayer," Phys. Rev. B **78**, 245424 (2008).

[142]R. Nandkishore and L. Levitov, "Dynamical screening and excitonic instability in bilayer graphene," Phys. Rev. Lett. **104**, 156803 (2010).

[143]H. Wang, D. N. Sheng, L. Sheng, and F. D. M. Haldane, "Broken-symmetry states of dirac fermions in graphene with a partially filled high landau level," Phys. Rev. Lett. **100**, 116802 (2008).

[144]B. Valenzuela and M. A. H. Vozmediano, "Pomeranchuk instability in doped graphene," New Journal of Physics **10**, 113009 (2008).

[145]J. Jung, M. Polini, and A. H. MacDonald, "Persistent current states in bilayer graphene," Phys. Rev. B **91**, 155423 (2015).

[146]F. Guinea, B. Horovitz, and P. Le Doussal, "Gauge fields, ripples and wrinkles in graphene layers," Solid State Communications **149**, Recent Progress in Graphene Studies, 1140–1143 (2009).

[147]D. A. Abanin, A. V. Shytov, and L. S. Levitov, "Peierls-type instability and tunable band gap in functionalized graphene," Phys. Rev. Lett. **105**, 086802 (2010).

[148]O. L. Berman, R. Y. Kezerashvili, and Y. E. Lozovik, "Bose–einstein condensation of quasiparticles in graphene," Nanotechnology **21**, 134019 (2010).

[149]J. Wang, H. A. Fertig, and G. Murthy, "Critical behavior in graphene with coulomb interactions," Phys. Rev. Lett. **104**, 186401 (2010).

[150]M. L. Kiesel, C. Platt, W. Hanke, D. A. Abanin, and R. Thomale, "Competing many-body instabilities and unconventional superconductivity in graphene," Phys. Rev. B **86**, 020507 (2012).

[151]M. M. Scherer, S. Uebelacker, and C. Honerkamp, "Instabilities of interacting electrons on the honeycomb bilayer," Phys. Rev. B **85**, 235408 (2012).

[152]C. Platt, W. Hanke, and R. Thomale, "Functional renormalization group for multi-orbital fermi surface instabilities," Advances in Physics **62**, 453–562 (2013).

[153]B. Roy and J. D. Sau, "Competing charge-density wave, magnetic, and topological ground states at and near dirac points in graphene in axial magnetic fields," Phys. Rev. B **90**, 075427 (2014).

[154]R. E. Throckmorton and S. Das Sarma, "Quantum multicriticality in bilayer graphene with a tunable energy gap," Phys. Rev. B **90**, 205407 (2014).

[155]V. Cvetkovic, R. E. Throckmorton, and O. Vafek, "Electronic multicriticality in bilayer graphene," Phys. Rev. B **86**, 075467 (2012).

[156]N. K. Patel, L Martin-Moreno, M Pepper, R Newbury, J. E. F. Frost, D. A. Ritchie, G. A. C. Jones, J. T. M. B. Janssen, J Singleton, and J. A. A. J. Perenboom, "Ballistic transport in one dimension: additional quantisation produced by an electric field," Journal of Physics: Condensed Matter **2**, 7247–7254 (1990).

[157]N. K. Patel, J. T. Nicholls, L. Martn-Moreno, M. Pepper, J. E. F. Frost, D. A. Ritchie, and G. A. C. Jones, "Evolution of half plateaus as a function of electric field in a ballistic quasi-one-dimensional constriction," Phys. Rev. B **44**, 13549–13555 (1991).

[158]L Martin-Moreno, J. T. Nicholls, N. K. Patel, and M Pepper, "Non-linear conductance of a saddle-point constriction," Journal of Physics: Condensed Matter **4**, 1323–1333 (1992).

[159]R. Danneau, O. Klochan, W. R. Clarke, L. H. Ho, A. P. Micolich, M. Y. Simmons, A. R. Hamilton, M. Pepper, D. A. Ritchie, and U. Zülicke, "Zeeman splitting in ballistic hole quantum wires," Phys. Rev. Lett. **97**, 026403 (2006).

[160]J. B. Oostinga, H. B. Heersche, X. Liu, A. F. Morpurgo, and L. M. K. Vandersypen, "Gate-induced insulating state in bilayer graphene devices," Nature Materials **7**, 151–157 (2008).

[161]J. F. Janak, "g Factor of the two-dimensional interacting electron gas," Phys. Rev. **178**, 1416–1418 (1969).

[162]G. Zala, B. N. Narozhny, and I. L. Aleiner, "Interaction corrections at intermediate temperatures: magnetoresistance in a parallel field," Phys. Rev. B **65**, 020201 (2001).

[163]G.-H. Chen and M. E. Raikh, "Exchange-induced enhancement of spin-orbit coupling in two-dimensional electronic systems," Phys. Rev. B **60**, 4826–4833 (1999).

[164]K. Zollner, M. Gmitra, and J. Fabian, "Heterostructures of graphene and hbn: electronic, spin-orbit, and spin relaxation properties from first principles," Phys. Rev. B **99**, 125151 (2019).

[165]M. Eich, F. c. v. Herman, R. Pisoni, H. Overweg, A. Kurzmann, Y. Lee, P. Rickhaus, K. Watanabe, T. Taniguchi, M. Sigrist, T. Ihn, and K. Ensslin, "Spin and valley states in gate-defined bilayer graphene quantum dots," Phys. Rev. X **8**, 031023 (2018).

[166]A. F. Young and P. Kim, "Quantum interference and klein tunnelling in graphene heterojunctions," Nature Physics **5**, 222–226 (2009).

[167]A. V. Shytov, M. S. Rudner, and L. S. Levitov, "Klein backscattering and fabry-pérot interference in graphene heterojunctions," Phys. Rev. Lett. **101**, 156804 (2008).

[168]P. Rickhaus, R. Maurand, M.-H. Liu, M. Weiss, K. Richter, and C. Schönenberger, "Ballistic interferences in suspended graphene," Nature Communications **4**, 2342 (2013).

[169]A. Varlet, M.-H. Liu, D. Bischoff, P. Simonet, T. Taniguchi, K. Watanabe, K. Richter, T. Ihn, and K. Ensslin, "Band gap and broken chirality in single-layer and bilayer graphene," physica status solidi (RRL) – Rapid Research Letters **10**, 46–57 (2016).

[170]R. Kraft, M.-H. Liu, P. B. Selvasundaram, S.-C. Chen, R. Krupke, K. Richter, and R. Danneau, "Anomalous cyclotron motion in graphene superlattice cavities," Phys. Rev. Lett. **125**, 217701 (2020).

[171]F. Mireles and J. Schliemann, "Energy spectrum and landau levels in bilayer graphene with spin–orbit interaction," New Journal of Physics **14**, 093026 (2012).

[172]N. M. R. Peres, "Colloquium: the transport properties of graphene: an introduction," Rev. Mod. Phys. **82**, 2673–2700 (2010).

[173]K. Bolotin, K. Sikes, Z. Jiang, M. Klima, G. Fudenberg, J. Hone, P. Kim, and H. Stormer, "Ultrahigh electron mobility in suspended graphene," Solid State Communications **146**, 351–355 (2008).

[174]M. Kumar, A. Laitinen, and P. Hakonen, "Unconventional fractional quantum hall states and wigner crystallization in suspended corbino graphene," Nature Communications **9**, 2776 (2018).

[175]S. Das Sarma, S. Adam, E. H. Hwang, and E. Rossi, "Electronic transport in two-dimensional graphene," Rev. Mod. Phys. **83**, 407–470 (2011).

[176]B. Zhou, K. Watanabe, T. Taniguchi, and E. A. Henriksen, "Extraordinary magnetoresistance in encapsulated monolayer graphene devices," Applied Physics Letters **116**, 053102 (2020).

[177]R. P. Tiwari and D. Stroud, "Model for the magnetoresistance and hall coefficient of inhomogeneous graphene," Phys. Rev. B **79**, 165408 (2009).

[178]J. Ping, I. Yudhistira, N. Ramakrishnan, S. Cho, S. Adam, and M. S. Fuhrer, "Disorder-Induced Magnetoresistance in a Two-Dimensional Electron System," Physical Review Letters **113**, 047206 (2014).

[179]D. V. Nomokonov, A. V. Goran, and A. A. Bykov, "Anisotropic corbino conductivity in a magnetic field," Journal of Applied Physics **125**, 164301 (2019).

[180]Y. Zheng and T. Ando, "Hall conductivity of a two-dimensional graphite system," Phys. Rev. B **65**, 245420 (2002).

[181]M. Müller, L. Fritz, and S. Sachdev, "Quantum-critical relativistic magnetotransport in graphene," Phys. Rev. B **78**, 115406 (2008).

[182]J. Jobst, D. Waldmann, I. V. Gornyi, A. D. Mirlin, and H. B. Weber, "Electron-electron interaction in the magnetoresistance of graphene," Phys. Rev. Lett. **108**, 106601 (2012).

[183]M. Kamada, A. Laitinen, W. Zeng, M. Will, J. Sarkar, K. Tappura, H. Seppä, and P. Hakonen, *Electrical low-frequency* $1/f^{\gamma}$ *noise due to surface diffusion of scatterers on an ultra low noise graphene platform*, 2021.

[184]A. Laitinen, G. S. Paraoanu, M. Oksanen, M. F. Craciun, S. Russo, E. Sonin, and P. Hakonen, "Contact doping, Klein tunneling, and asymmetry of shot noise in suspended graphene," Physical Review B **93**, 1–14 (2016).

[185]E. H. Hwang, S. Adam, and S. D. Sarma, "Carrier transport in two-dimensional graphene layers," Phys. Rev. Lett. **98**, 186806 (2007).

[186]F. M. D. Pellegrino, I. Torre, and M. Polini, "Nonlocal transport and the hall viscosity of two-dimensional hydrodynamic electron liquids," Phys. Rev. B **96**, 195401 (2017).

[187]A. A. Kozikov, A. K. Savchenko, B. N. Narozhny, and A. V. Shytov, "Electron-electron interactions in the conductivity of graphene," Phys. Rev. B **82**, 075424 (2010).

[188]G. Vasileva, P. Alekseev, Y. Vasilyev, A. Dmitriev, V. Kachorovskii, D. Smirnov, H. Schmidt, and R. Haug, "Magnetoresistance of monolayer graphene with short-range disorder," physica status solidi (b) **256**, 1800525 (2019).

[189]G. Y. Vasileva, P. S. Alekseev, Y. B. Vasil'ev, A. P. Dmitriev, V. Y. Kachorovskii, D. Smirnov, H. Schmidt, and R. Haug, "Temperature-Dependent Magnetoresistance of Single-Layer Graphene," Journal of Experimental and Theoretical Physics **129**, 438–443 (2019).

[190]A. Rycerz, "Magnetoconductance of the Corbino disk in graphene," Physical Review B **81**, 121404 (2010).

[191]A. Laitinen, M. Kumar, and P. J. Hakonen, "Weak antilocalization of composite fermions in graphene," Physical Review B **97**, 075113 (2018).

[192]I. V. Gornyi and A. D. Mirlin, "Interaction-induced magnetoresistance in a two-dimensional electron gas," Phys. Rev. B **69**, 045313 (2004).

[193]E. H. Hwang and S. Das Sarma, "Single-particle relaxation time versus transport scattering time in a two-dimensional graphene layer," Phys. Rev. B **77**, 195412 (2008).

[194]D. A. Bandurin, I. Torre, R. Krishna Kumar, M. Ben Shalom, A. Tomadin, A. Principi, G. H. Auton, E. Khestanova, K. S. Novoselov, I. V. Grigorieva, L. A. Ponomarenko, A. K. Geim, and M. Polini, "Negative local resistance caused by viscous electron backflow in graphene," Science **351**, 1055–1058 (2016).

[195]J. Crossno, J. K. Shi, K. Wang, X. Liu, A. Harzheim, A. Lucas, S. Sachdev, P. Kim, T. Taniguchi, K. Watanabe, T. A. Ohki, and K. C. Fong, "Observation of the Dirac fluid and the breakdown of the Wiedemann-Franz law in graphene," Science **351**, 1058–1061 (2016).

[196]R. Krishna Kumar, D. A. Bandurin, F. M. D. Pellegrino, Y. Cao, A. Principi, H. Guo, G. H. Auton, M. Ben Shalom, L. A. Ponomarenko, G. Falkovich, K. Watanabe, T. Taniguchi, I. V. Grigorieva, L. S. Levitov, M. Polini, and A. K. Geim, "Superballistic flow of viscous electron fluid through graphene constrictions," Nat. Phys. **13**, 1182–1185 (2017).

[197]F. Ghahari, H.-Y. Xie, T. Taniguchi, K. Watanabe, M. S. Foster, and P. Kim, "Enhanced thermoelectric power in graphene: violation of the mott relation by inelastic scattering," Phys. Rev. Lett. **116**, 136802 (2016).

[198]D. A. Bandurin, A. V. Shytov, L. S. Levitov, R. Krishna Kumar, A. I. Berdyugin, M. Ben Shalom, I. V. Grigorieva, A. K. Geim, and G. Falkovich, "Fluidity onset in graphene," Nat. Commun. **9**, 4533 (2018).

[199]A. I. Berdyugin, S. G. Xu, F. M. D. Pellegrino, R. Krishna Kumar, A. Principi, I. Torre, M. B. Shalom, T. Taniguchi, K. Watanabe, I. V. Grigorieva, M. Polini, A. K. Geim, and D. A. Bandurin, "Measuring hall viscosity of graphene's electron fluid," Science **364**, 162 (2019).

[200]P. Gallagher, C.-S. Yang, T. Lyu, F. Tian, R. Kou, H. Zhang, K. Watanabe, T. Taniguchi, and F. Wang, "Quantum-critical conductivity of the dirac fluid in graphene," Science **364**, 158 (2019).

[201]M. J. H. Ku, T. X. Zhou, Q. Li, Y. J. Shin, J. K. Shi, C. Burch, L. E. Anderson, A. T. Pierce, Y. Xie, A. Hamo, U. Vool, H. Zhang, F. Casola, T. Taniguchi, K. Watanabe, M. M. Fogler, P. Kim, A. Yacoby, and R. L. Walsworth, "Imaging viscous flow of the dirac fluid in graphene using a quantum spin magnetometer," Nature **583**, 537–541 (2020).

[202]J. A. Sulpizio, L. Ella, A. Rozen, J. Birkbeck, D. J. Perello, D. Dutta, M. Ben-Shalom, T. Taniguchi, K. Watanabe, T. Holder, R. Queiroz, A. Stern, T. Scaffidi, A. K. Geim, and S. Ilani, "Visualizing poiseuille flow of hydrodynamic electrons," Nature **576**, 75 (2019).

[203]A. Jenkins, S. Baumann, H. Zhou, S. A. Meynell, D. Yang, T. T. K. Watanabe, A. Lucas, A. F. Young, and A. C. B. Jayich, *Fractionalization in dimerized graphene and graphene bilayer*, version 1, Mar. 2020.

[204]P. J. W. Moll, P. Kushwaha, N. Nandi, B. Schmidt, and A. P. Mackenzie, "Evidence for hydrodynamic electron flow in PdCoO2," Science **351**, 1061–1064 (2016).

[205]B. A. Braem, F. M. D. Pellegrino, A. Principi, M. Röösli, C. Gold, S. Hennel, J. V. Koski, M. Berl, W. Dietsche, W. Wegscheider, M. Polini, T. Ihn, and K. Ensslin, "Scanning gate microscopy in a viscous electron fluid," Phys. Rev. B **98**, 241304(R) (2018).

[206]A. Jaoui, B. Fauqué, C. W. Rischau, A. Subedi, C. Fu, J. Gooth, N. Kumar, V. Süß, D. L. Maslov, C. Felser, and K. Behnia, "Departure from the Wiedemann-Franz law in WP_2 driven by mismatch in T-square resistivity prefactors," npj Quantum Materials **3**, 64 (2018).

[207]M. S. Steinberg, "Viscosity of the electron gas in metals," Phys. Rev. **109**, 1486–1492 (1958).

[208]R. N. Gurzhi, "Hydrodynamic Effects in Solids At Low Temperature," Soviet Physics Uspekhi **11**, 255–270 (1968).

[209]B. Bradlyn, M. Goldstein, and N. Read, "Kubo formulas for viscosity: hall viscosity, ward identities, and the relation with conductivity," Phys. Rev. B **86**, 245309 (2012).

[210]P. S. Alekseev, "Negative magnetoresistance in viscous flow of two-dimensional electrons," Phys. Rev. Lett. **117**, 166601 (2016).

[211]T. Scaffidi, N. Nandi, B. Schmidt, A. P. Mackenzie, and J. E. Moore, "Hydrodynamic electron flow and hall viscosity," Phys. Rev. Lett. **118**, 226601 (2017).

[212]B. N. Narozhny and M. Schütt, "Magnetohydrodynamics in graphene: shear and hall viscosities," Phys. Rev. B **100**, 035125 (2019).

[213]L. S. Levitov and G. Falkovich, "Electron viscosity, current vortices and negative nonlocal resistance in graphene," Nat. Phys. **12**, 672–676 (2016).

[214]P. S. Alekseev, A. P. Dmitriev, I. V. Gornyi, V. Y. Kachorovskii, B. N. Narozhny, M. Schütt, and M. Titov, "Magnetoresistance in two-component systems," Phys. Rev. Lett. **114**, 156601 (2015).

[215]P. S. Alekseev, A. P. Dmitriev, I. V. Gornyi, V. Y. Kachorovskii, B. N. Narozhny, M. Schütt, and M. Titov, "Magnetoresistance of compensated semimetals in confined geometries," Phys. Rev. B **95**, 165410 (2017).

[216]P. S. Alekseev, A. P. Dmitriev, I. V. Gornyi, V. Y. Kachorovskii, B. N. Narozhny, and M. Titov, "Nonmonotonic magnetoresistance of a two-dimensional viscous electron-hole fluid in a confined geometry," Phys. Rev. B **97**, 085109 (2018).

[217]P. S. Alekseev, A. P. Dmitriev, I. V. Gornyi, V. Y. Kachorovskii, B. N. Narozhny, and M. Titov, "Counterflows in viscous electron-hole fluid," Phys. Rev. B **98**, 125111 (2018).

[218]C. Kumar, J. Birkbeck, J. A. Sulpizio, D. J. Perello, T. Taniguchi, K. Watanabe, O. Reuven, T. Scaffidi, A. Stern, A. K. Geim, and S. Ilani, "Imaging hydrodynamic electrons flowing without landauer-sharvin resistance," Phys. Rev. B **78**, 245424 (2021).

[219]A. Hui, V. Oganesyan, and E.-A. Kim, "Beyond ohm's law: bernoulli effect and streaming in electron hydrodynamics," Phys. Rev. B **103**, 235152 (2021).

[220]S. Li, A. Levchenko, and A. V. Andreev, "Hydrodynamic thermoelectric transport in corbino geometry," Phys. Rev. B **105**, 125302 (2022).

[221]A. Stern, T. Scaffidi, O. Reuven, C. Kumar, J. Birkbeck, and S. Ilani, "Spread and erase – how electron hydrodynamics can eliminate the landauer-sharvin resistance," Phys. Rev. B **78**, 245424 (2021).

[222]O. E. Raichev, "Superballistic boundary conductance and hydrodynamic transport in microstructures," Phys. Rev. B **78**, 245424 (2022).

[223]G. Y. Vasileva, D. Smirnov, Y. L. Ivanov, Y. B. Vasilyev, P. S. Alekseev, A. P. Dmitriev, I. V. Gornyi, V. Y. Kachorovskii, M. Titov, B. N. Narozhny, and R. J. Haug, "Linear magnetoresistance in compensated graphene bilayer," Phys. Rev. B **93**, 195430 (2016).

[224]A. B. Kashuba, "Conductivity of defectless graphene," Phys. Rev. B **78**, 085415 (2008).

[225]M. Müller and S. Sachdev, "Collective cyclotron motion of the relativistic plasma in graphene," Phys. Rev. B **78**, 115419 (2008).

[226]M. S. Foster and I. L. Aleiner, "Slow imbalance relaxation and thermoelectric transport in graphene," Phys. Rev. B **79**, 085415 (2009).

[227]M. Schütt, P. M. Ostrovsky, I. V. Gornyi, and A. D. Mirlin, "Coulomb interaction in graphene: relaxation rates and transport," Phys. Rev. B **83**, 155441 (2011).

[228]B. N. Narozhny, I. V. Gornyi, M. Titov, M. Schütt, and A. D. Mirlin, "Hydrodynamics in graphene: linear-response transport," Phys. Rev. B **91**, 035414 (2015).

[229]U. Briskot, M. Schütt, I. V. Gornyi, M. Titov, B. N. Narozhny, and A. D. Mirlin, "Collision-dominated nonlinear hydrodynamics in graphene," Phys. Rev. B **92**, 115426 (2015).

[230]J. M. Link, B. N. Narozhny, E. I. Kiselev, and J. Schmalian, "Out-of-bounds hydrodynamics in anisotropic dirac fluids," Phys. Rev. Lett. **120**, 196801 (2018).

[231]B. N. Narozhny, I. V. Gornyi, and M. Titov, "Anti-poiseuille flow in neutral graphene," Phys. Rev. B **104**, 075443 (2021).

[232]M. Shavit, A. Shytov, and G. Falkovich, "Freely flowing currents and electric field expulsion in viscous electronics," Phys. Rev. Lett. **123**, 026801 (2019).

[233]B. N. Narozhny and I. V. Gornyi, "Hydrodynamic approach to electronic transport in graphene: energy relaxation," Frontiers in Physics **9**, 108 (2021).

[234]D. Halbertal, J. Cuppens, M. Ben Shalom, L. Embon, N. Shadmi, Y. Anahory, H. R. Naren, J. Sarkar, A. Uri, Y. Ronen, Y. Myasoedov, L. S. Levitov, E. Joselevich, A. K. Geim, and E. Zeldov, "Nanoscale thermal imaging of dissipation in quantum systems," Nature **539**, 407–410 (2016).

[235]D. Halbertal, M. Ben Shalom, A. Uri, K. Bagani, A. Y. Meltzer, I. Markus, Y. Myasoedov, J. Birkbeck, L. S. Levitov, A. K. Geim, and E. Zeldov, "Imaging resonant dissipation from individual atomic defects in graphene," Science **358**, 1303–1306 (2017).

[236]A. Aharon-Steinberg, A. Marguerite, D. J. Perello, K. Bagani, T. Holder, Y. Myasoedov, L. S. Levitov, A. K. Geim, and E. Zeldov, "Long-range nontopological edge currents in charge-neutral graphene," Nature **593**, 528–534 (2021).

[237]L. Ella, A. Rozen, J. Birkbeck, M. Ben-Shalom, D. Perello, J. Zultak, T. Taniguchi, K. Watanabe, A. K. Geim, S. Ilani, and J. A. Sulpizio, "Simultaneous voltage and current density imaging of flowing electrons in two dimensions," Nat. Nanotechnol. **14**, 480 (2019).

[238]C. Gold, A. Knothe, A. Kurzmann, A. Garcia-Ruiz, K. Watanabe, T. Taniguchi, V. Fal'ko, K. Ensslin, and T. Ihn, "Coherent jetting from a gate-defined channel in bilayer graphene," Phys. Rev. Lett. **127**, 046801 (2021).

[239]Z. Wang, D.-K. Ki, H. Chen, H. Berger, A. H. MacDonald, and A. F. Morpurgo, "Strong interface-induced spin–orbit interaction in graphene on ws2," Nature Communications **6**, 8339 (2015).

[240]A. Thomson, I. Sorensen, S. Nadj-Perge, and J. Alicea, *Gate-defined wires in twisted bilayer graphene: from electrical detection of inter-valley coherence to internally engineered majorana modes*, 2021.